CRANFIELD UNIVERSITY

Krishan Parmar

The Aerodynamic Effects of Runback Ice

SCHOOL OF ENGINEERING
Department of Power and Propulsion – Optimisation Group

PhD THESIS
Initial Registration: 30th January 2009

Supervisor: Professor M. Savill
20th September 2013

CRANFIELD UNIVERSITY

SCHOOL OF ENGINEERING
Department of Power and Propulsion – Optimisation Group

PhD THESIS
Initial Registration: January 30th 2009

Krishan Parmar

The Aerodynamic Effects of Runback Ice

Supervisor: Professor M. Savill
September 2013

This thesis is submitted in fulfilment of the requirements for the degree of Doctor of Philosophy.

I would like to dedicate this work to my sister, Beejal Parmar. Her support and encouragement throughout my academic career has been fundamental to my achievements. I would like to take this opportunity to thank her for being a selfless, kind and caring sister.

Krishan Parmar
18th September 2013

Abstract

The objectives of this PhD were to investigate the aerodynamic performance effects due to runback ice accretion with particular interest on the EASA 45 minute hold case in icing conditions. The sponsors, Airbus and Cranfield University collaboratively identified this aim as a result of the successful creation and capture of full-scale runback ice using the Cranfield Icing Tunnel.

The hold phase represents typical icing conditions but with increasing demands on airports and subsequent knock-on effects to increased holding times has led to airliners paying more attention to this phase of flight. Typical icing conditions occur during the hold phrase of flight and place increasing demands on airports. A further challenge is that the EASA 45 minute hold case fails to take into account the large supercooled liquid droplets (SLD) when certifying the airplane. Published literature open to the public domain on flowfield interaction with realistic runback ice shapes, force coefficient losses and heat transfer interaction is limited. This is despite the fact that these parameters play a significant role in the examination of ice accretion. Inspection of the runback ice casting highlighted regions of two-dimensional features which were used for aerodynamic analysis. These high-fidelity two-dimensional runback ice shapes were utilised throughout this project.

A single hex-core hybrid mesh from an ANSYS ICEMCFD script was designed and served the dual purpose of assisting the process of optimisation and validation. The numerical validation procedure analysed three separate studies with differing airfoils. The three studies examined were B737-700, B737-200ADV and NACA 23012. The first two studies were in clean cruise configuration and the third simulated forward-facing quarter-round ridge ice. The experimental validation process investigated the drag associated for the three run back ice shapes. Tests were conducted in the atmospheric boundary layer wind tunnel. A multi-objective Tabu Search optimiser was coupled with ANSYS FLUENT solver for investigations on ice location, shape optimisation using free-form deformation, vertical tail plane shape optimisation and leading edge heat-transfer effects.

The primary finding in relation to ice location optimisation was an observed sensitivity to chord location. Further exploration of this data identified two district characteristics for this sensitivity. These characteristics are the variation of run back ice height relative to the size of boundary layer thickness. More specifically, if the boundary layer thickness is smaller than the runback ice height, trends identified from this project are adhered to. However, if the boundary layer thickness is larger than the run back ice height, no visible trends

are observed. The ice location study found optimum chord locations closer to the leading edge of the airfoil and sensitivity to small chord movements. The B737 shape study was conducted as a preliminary optimisation test to highlight best practices for shape optimisation using free-form deformation. The results showed more stringent requirements for geometrical constraint handling when dealing with shape optimisation. Small changes to the NACA vertical plane improved both clean and iced performance. This was attributed to the leading edge design producing a lower velocity around the airfoil. This was a highly constrained optimisation problem where improved results required an exhaustive and competent search mechanism. The MOTS code was best placed to conduct this search and was therefore used throughout this study. Anti-Icing optimisation incorporated heat transfer providing a more complete runback ice optimisation study. This more complete design comprised a multipoint optimisation code with three objectives and one variable; to minimise leading edge temperature output, maximise lift and minimise drag with variable heat input. The findings corroborate the results seen in the ice location optimisation study.

The ice location study would benefit from an increased range of variability to observe the development of the trends found. Solver prediction capabilities for ice accretion studies would benefit from experimental data on roughness parameters associated with icing. The two-dimensional airfoil simulations would benefit from further CFD runs using three-dimensional swept wings. The Pareto-optimal designs are ideal candidates to compare the flowfield inadequacies alluded to by literature. As an interim study before three-dimensional simulations are conducted, an extension to the cruise configuration airfoil study would be to deploy high-lift profiles. It would provide insight into ice accretion scaling methods by running a second NACA tail plane optimisation run using runback ice shapes scaled based on boundary layer thickness. Findings would provide invaluable information on the interaction of the two scaling methods with the boundary layer and how changes to flowfield characteristics effect force coefficients. Finally, further aerodynamic investigations with wind tunnel testing of representative full-scale runback ice shapes on a sectioned full-scale swept wing would be beneficial. This would complete the years of commitment and innovation by Cranfield University, sponsors and various students on the issue of ice accretion, particularly runback ice.

Acknowledgements

I would like to thank my supervisor, Professor Mark Savill, for his support, encouragement and guidance. This project would never have been a success without his kindness, care and expertise. Professor Savill's ability to listen, calm and help me keep a level head has proved invaluable.

Thank you to my second supervisor, Professor Kevin Garry for giving me the opportunity to study at Cranfield and advising me on the experimental aspects of this project.

Thank you to my advisor Dr Timoleon Kipouros, wind tunnel technician, Jenny Holt and the industrial contact from Airbus UK, Nick Dart.

A special thanks to Dr Nathalie Alégre, a special friend, flatmate and exceptional predecessor in the field runback ice accretion.

Big thanks to Luca Camosi and Michael Corsar for laughs, support and invaluable expertise in their respective fields.

Thanks to former colleagues at Cranfield library. A special thanks to Anita Beal for the fond memories and friendly chats.

Special thanks to all the friends I have made and people from the optimisation group for allowing me to explore ideas with you.

I would like to thank Teresa Townsend for keeping me sane and helping me grow into a better person.

Huge thanks to Marion Dearlove and Maria Smith for the endless cups of tea in my favourite mug and catering to my fussy eating habits.

Thanks to my parents for money, food, shelter and love. Thanks to my puppy Jinko for company and sanity whilst writing up.

Last but not least, thanks to my uncle, Captain Sanjay Parmar for letting me waffle on about runback ice and never getting bored.

Contents

List of Figures

List of Tables

List of Equations

Nomenclature

Roman Letters

a	Area of control volume, m
a_p	Linearised coefficients for ϕ
a_{nb}	Linearised coefficients for ϕ_{nb}
$\vec{a}$	Specified vector force, N
A	Area of force balance, m^2
c	Chord length, m
C_d	Drag coefficient
C_{dmin}	Minimum drag coefficient
c_{FB}	Length of force balance, m
C_l	Lift coefficient
C_{lmax}	Maximum lift coefficient
C_m	Moment coefficient
d	Maximum thickness of runback ice ridge, m
D	Drag force, N
$\vec{F}_p$	Pressure force component, N
F_s	Safety factor for Richardson extrapolation
$\vec{F}_v$	Viscous Force Component, N
G_v	Production of turbulent viscosity
h	Heat transfer coefficient, $m^2 s^{-1}$
l	Wind tunnel boundary layer thickness height, m
l, m, n	Dimensions of the FFD lattice
k	Turbulent kinetic energy, $m^2 s^{-2}$
k_a	Air thermal conductivity, $W m^{-1} K^{-1}$
L	Lift force, N
M	Mach number
M_w	Molecular weight, Kg
nb	Neighbouring cells (used for discretisation)
Nu	Nusselt Number
Pr	Prandtl Number
P_s	Static pressure, Pa
P_t	Total pressure, Pa

q_w	Convective and radiative wall heat flux, Wm^{-2}
r	Grid refinement ratio
R	Universal gas constant, $m^2s^{-2}K^{-2}$
Re	Reynolds number
Re_x	Reynolds number at position x
s, t, u	Coordinates of a generic point before FFD
s	Span of the force balance, m
S	Area of the skin friction balance, m
St	Stanton Number
T_s	Static temperature, °Celsius
T_t	Total temperature, °Celsius
T_w	Wall temperature, °Celsius
T_∞	Freestream temperature at Inlet, °Celsius
T^+	Reference temperature, °Celsius
$u^{'}$	Root mean square of the turbulent velocity fluctuations, ms^{-1}
U	Mean velocity, ms^{-1}
u^*	Frictional velocity, ms^{-1}
V_∞	Freestream velocity, ms^{-1}
y^+	Non-dimensional distance to wall
Y_v	Destruction of turbulent viscosity that occurs in near-wall region due to wall blocking and viscous damping
$3D\ C_d$	Uncorrected three-dimensional drag for wake survey method
X_{FFD}	Vector containing the Cartesian coordinates of the displaced point

Greek Letters

α	Thermal diffusivity, m^2s^{-1}
γ_r	Ratio of specific heats
δ	Boundary layer thickness, m
ε	Turbulent dissipation rate, m^2s^{-3}
ε_r	Relative error defined as $\frac{f_2-f_1}{f_1}$
ρ	Density, kgm^{-3}
σ_t	Turbulent Prandlt (Schmidt) Number
τ_w	Wall Shear Stress, $kgm^{-1}s^{-2}$

v	Molecular kinematic viscosity, $m^2 s^{-1}$
v_t	Kinematic Turbulent Viscosity, $m^2 s^{-1}$
ϕ	Scalar Variable

Acronyms

ABLWT	Atmospheric Boundary Layer Wind Tunnel
AOA	Angle of Attack
CIT	Cranfield Icing Tunnel
CRM	Common Research Model
EASA	European Aviation Safety Agency
EWT	Enhanced Wall Treatment
FAA	Federal Aviation Admission
FB	Force Balance
LWC	Liquid Water Content
MOTS	Multi-Objective Tabu Search
RANS	Reynolds-Averaged Navier-Stokes
S-A	Spalart-Allmaras
SLD	Supercooled Liquid Droplets
SST	Shear Stress Transport
WSM	Wake Survey Method

1. Introduction

"A journey of a thousand miles must begin with a single step."
- Lao-Tsu

Commercial airplanes must cope with a vast range of meteorological conditions. Safety therefore is of upmost importance, especially for commercial airplane manufacturers. In addition to strong winds, turbulence and the more recent ash clouds from volcanic eruptions, icing is one of the fundamental weather conditions airplanes are exposed to. This chapter will outline the main aims and objectives of the study combined with some context of ice accretion. Particular focus will be paid to runback ice accretion.

1.1. Atmospheric Icing condition

The atmospheric conditions in which icing occurs are linked with the presence of supercooled liquid water droplets. Water can exist as a liquid well below 0°C. The melting point of water is 0°C and water in liquid form below this value is termed supercooled liquid water. The liquid molecules require a presence of a crystal seed or nucleus to disrupt the droplet and freeze. In icing conditions, the airplane acts as this disturbance typically in stratus and cumulus clouds. The supercooled liquid water droplet sizes are usually between 10μm and 50μm in diameter with ambient temperatures no lower than 20°C [1]. However instances have been observed where the size of the droplets are larger; ranging from 50μm to 400μm [2]. These larger Supercooled Liquid Droplets (SLD) are not tested under the design and certification phase and thus require further study alongside pilot training and awareness.

1.2. Anti-Icing Systems

Ice protection is required at engine nacelles, wings and tail surfaces. The aerodynamic performance loss at the wing surfaces can be significant. The protected region on the wings can typically extend up to 10% to 15% chord length but can vary depending on airplane specification [3].

The two classifications of ice protection systems are anti-icing systems and de-icing systems. Anti-icing systems prevent or alleviate ice growth whereas de-icing systems remove ice after growth. Common anti-icing systems are thermal systems whereas de-icing systems are usually mechanically operated (pneumatic boots) but can also use heating systems. The energy source for

thermal systems is usually found from typical bleed air systems. Thermal anti-icing systems can be either fully evaporative or a wet system. A fully evaporative system ensures enough heat is provided to the system to evaporate all impinged water. A wet system provides just enough energy to ensure the critical surface temperatures are above freezing. These circumstances allow water to run back and refreeze in the unprotected region. This type of ice accretion is known as runback ice.

In reality, most airplanes will experience both regimes. Atmospheric conditions, engine regime and efficiency of heating system are just a few examples of the contributing factors leading to either a fully evaporative or wet system. As a result the thermal protection systems may fully evaporate water in one instance but only keep the surface above freezing in other instance causing runback ice accretion.

1.3. Runback Ice

Icing conditions where supercooled large droplets or when engine performance hinders the efficiency of bleed air systems, ice protections systems may not fully evaporate the impinged water. Consequently water runs beyond the heated region where the temperature of the wing surface falls low enough and this excess water begins to freeze. This leaves the streamwise leading edge free from ice formation and allow ridge like ice features to form aft of the heated section. A schematic of the runback ice shape at the experimental location (0.023x/c) and comparison of the boundary layer thickness relative to the runback ice height is shown in Figure 1.1.

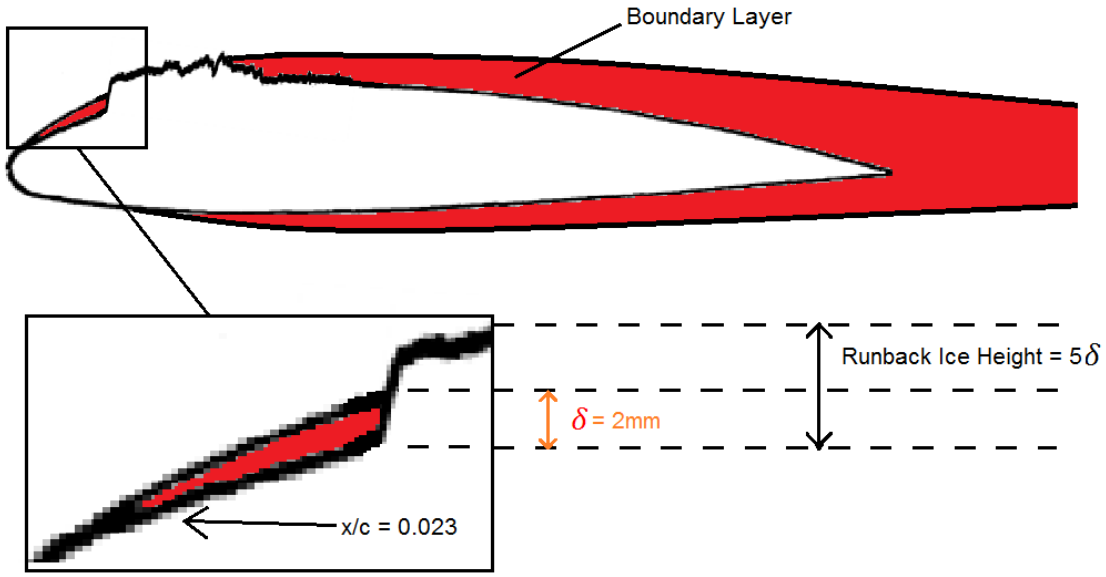

Figure 1.1: Schematic of Runback Ice on Airfoil

There are a number of images available for runback ice and Figure 1.2 to Figure 1.4 depicts representative full-scale runback ice images and casting created at the Cranfield icing Tunnel [1].

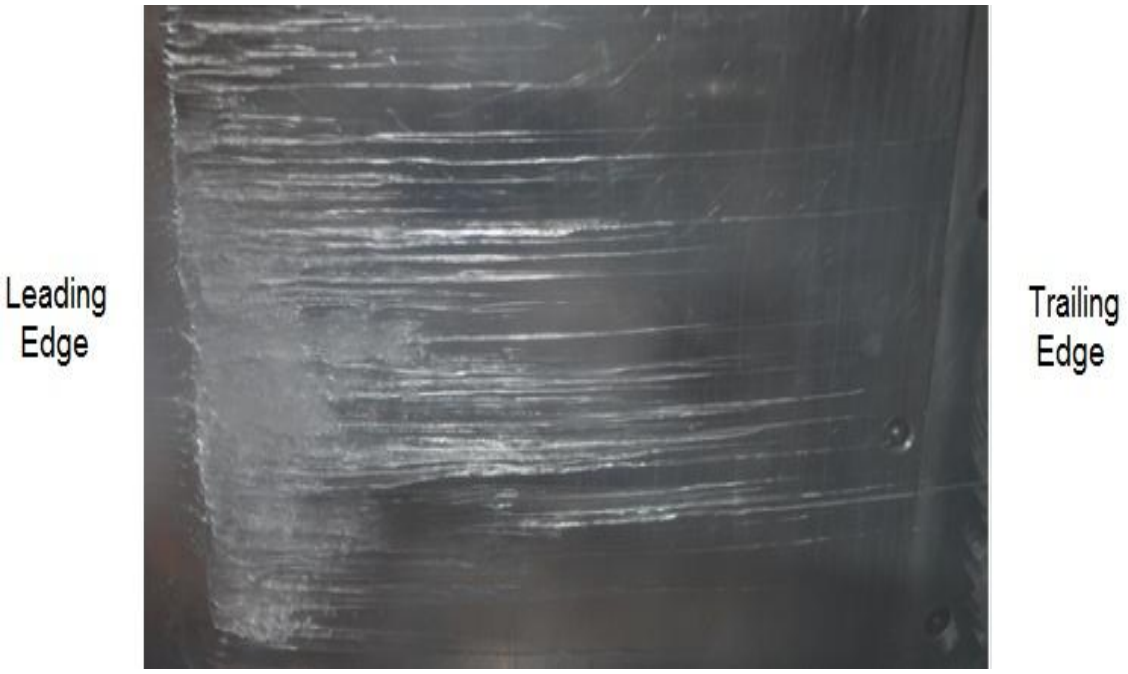

Figure 1.2: 10 Minute Ice Build Up in Continuous Icing Conditions [1]

Figure 1.3: Top View of Thin Cast of Typical Runback Ice Shape for Continuous Maximum Icing Conditions [1]

Figure 1.4: Side View of Thin Cast Typical Runback Ice Shape for Continuous Maximum Icing Conditions [1]

1.4. Context

With increasing demand of passenger air travel, airplane manufacturers must accommodate the busy airports. A consequence of this directly affects airplane holding times. The holding phase of the flight occurs at a critical altitude where ice formation is likely to occur. The largest liquid water content and conditions ripe for icing occur between 5000ft and 15000ft [4]. Additionally the envelope for icing encounters in stratiform clouds (clouds with extensive horizontal development and small water droplets) rarely occur at temperatures below -18°C as shown Figure 1.5 [2]. The altitude range for encounters ranges from ground level up to 22,000ft. The cumuliform cloud (clouds with vertical development allowing transport of large water droplets) envelope for icing encounters is narrower than for stratiform clouds. The icing encounter altitude range is 4000ft to 24000ft. The most frequent encounters (40% of the time) occur within the temperature range of 0°C to -10°C. This corresponds to an altitude region of 4000ft to 17000ft. The frequency of freezing at lower temperatures (-30°C) is much lower at around 6%.

Clearly the altitude regions where ice accretion is more likely to occur are in line with typical holding phase altitudes.

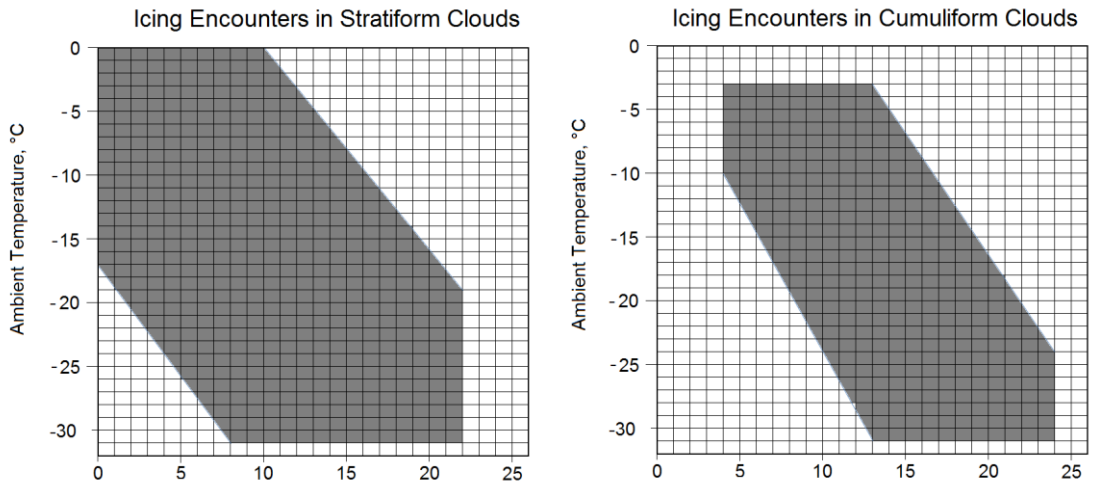

Figure 1.5: Icing Encounters for Stratiform and Cumuliform Clouds [2]

There is very little information for full-scale runback ice and airplane performance due to the cost and difficulty in acquiring this data. Realistic runback ice accretion at full-scale must be separately tested in an aerodynamic wind tunnel, again at full-scale. This has meant that there is very little research into the dynamics of runback ice.

A number of runback ice publications on ice location only select a few chord locations and consider the aerodynamic effects. However, there is no in-depth

study on how the location of runback ice along the chord impacts the flowfield and consequent force coefficients. Comprehensive analysis of the effects of ice location movements along the chord was conducted to provide a better understanding of the effects of ice and interaction with respect to boundary layer thickness.

There are also a number of issues surrounding runback ice which remain unclear:

- Evaluation of anti-icing power and runback ice accretion. This is a complex relationship and both directly affect each other. The advantages of understanding these interactions provide an opportunity to reduce the power or dependence on anti-icing protection.
- Simplistic runback ice shapes are still favoured by airplane manufacturers. With significant variation in ice shapes, heights and different reaction to flowfields based on blunt and streamline shapes, continuous efforts are required to better understand runback ice accretion.
- Very little information is available on full-scale runback ice on full-scale geometries.

1.5. Objectives

Ice accretion studies range from experimental to computational with the focus lying on ice accretion, aerodynamic testing, flowfield disruptions and many more. Runback ice represents a type of ice accretion where very little information is available due to the complexities involved with collecting experimental data. To this end Cranfield University and Airbus set out to study the effects of full-scale runback ice. Previous work at Cranfield University allowed successful production of full-scale runback ice accretions at the Cranfield Icing Tunnel and outlined the need for aerodynamic testing of these representative runback ice shapes [1]. The following objectives were set for thorough aerodynamic testing and optimisation using realistic runback ice:

- Aerodynamic study of the Boeing 737 airfoil for atmospheric conditions outlined by the EASA 45 minute hold case.

- Aerodynamic performance impact for representative full-scale runback ice used on two-dimensional full scale Boeing 737 airfoil.

- Understand interaction of clean and iced Boeing 737 airfoil

- Consider relationship between realistic runback ice shapes and simple shapes observed throughout the literature survey.

- Consider high-fidelity two-dimensional runback ice airfoil optimisation of:
    - Ice location aerodynamic penalties
    - Shape optimisation for fixed ice location
    - NACA 0012 tail plane optimisation using geometric scaling methods
    - Anti-icing heat transfer optimisation

1.6. Structure of thesis

The thesis contains the following chapters:

Chapter two surveys the literature surrounding runback ice accretion studies.

Chapter three outlines the methods used throughout the thesis with emphasis placed on commercial numerical solver methods.

Chapter four provides the models used to validate the runback ice CFD efforts.

Chapter five provides the initial analysis of the Boeing 737 airfoil. The performance effects due to runback ice at the experimental datum location and insight into the effects of runback ice shapes are also shown.

Chapter six provides insight into the aerodynamic effects of runback ice via wind tunnel testing with computational comparison and a modified version of Jones wake survey method.

Chapter seven considers a four-part optimisation study on ice location, shape optimisation, NACA tail plane shape optimisation and finally anti-icing optimisation.

Chapter eight outlines the conclusions from the research efforts as well as the recommendations and future work.

2. Literature Review

“Google' is not a synonym for 'research'.”

- Dan Brown

An airplane flying through clouds containing super-cooled water droplets can accrete ice on its aerodynamic surfaces. Small disturbances on the airfoil surfaces can have significant impact on the aerodynamic performance [5].

Ice accretion in normal icing conditions can occur on the leading edge of the wing. Typical hot-air systems use jets of hot gas to fully evaporate the liquid water droplets on the leading edge. In conditions where super cooled large droplets are present, some water is not 100% evaporated and impinges behind the heating system; runback ice. The size and shape of these ice accretions are mainly dependent on:

- Airspeed
- Temperature
- Water Droplet Size (WDS)
- Liquid Water Content (LWC)
- Time

Runback ice presents a significant problem during holding and decent phases in adverse icing conditions. The holding phase of flight is held at critical altitudes conducive to runback ice accretion. Portions of bleed air from the turbine engine compressor provide the hot gases which reduce engine power availability.

With deteriorating condition, lower temperatures and higher water-catch rates exaggerate the problem. During the decent phase engine power is reduced which directly affects the hot-air temperature and flow rate available in icing conditions and represents an equally challenging runback ice problem as highlighted for the hold phase of flight.

Research into runback ice and anti-icing systems can be found well over half a century ago [6]. A two-hour flight test was conducted in freezing conditions. During these tests runback ice and subsequent freezing was observed beyond the heated region. A performance loss for both lift and drag was noticed but the degradation was not enough to cause loss of control. By the 1950s, runback ice was considered a genuine problem and research into the flow dynamics was undertaken.

Bowden (1952) considered the characteristics and requirements of cyclic de-icing of an airfoil using an external electric heater [7]. The experiment was conducted at NASA Lewis icing research tunnel. Their aim was to evaluate how much energy and time was required to sufficiently de-ice the wing. Runback ice was observed during their runs. What became clear was the necessity to de-ice the wings in an efficient manner whilst considering the runback ice penalty. These early works provided the foundations to understanding and optimising current de-ice systems.

Experiments were conducted by Gray and von Glahn (1953) on the influence of high-fidelity runback ice using a NACA 65-212 airfoil equipped with hot-air anti-icing system at the NASA Lewis icing tunnel [8]. In continuous icing conditions the runback ice shape size and location was recorded. Approximately 28% to 44% of the impinged water was evaporated and pictures of the typical runback ice characteristics were captured. The drag was measured using an electrically heated pressure rake. They found the AOA significantly affected the drag increase. The key finding was that the atmospheric conditions for the icing tunnel required significantly higher turbulence level than that would be observed in typical external icing conditions. As a result the authors recommended the need for two separate testing arrangements; one to fully capture the runback ice (in an icing tunnel) and second to test the aerodynamic penalties (in a wind tunnel).

To fully understand the aerodynamic penalties associated with realistic runback ice the following was suggested:

- Formation of realistic runback ice on a representative wing
- Means to capture the runback ice shape's structure and create castings
- Transfer runback ice onto wing for aerodynamic wind tunnel testing

2.1. Experimental Survey

Research up until the mid 2000s was mainly based on airfoil wind tunnel tests using single generic ice shapes placed on the upper surface of the airfoil or wing. Calay, et al., [9], Lee and Bragg [10] and Papadikas, et al., [3] conducted aerodynamic tests using simplistic ice shapes. Calay, et al., [9] used the NACA 0012 airfoil, Lee and Bragg [10] tested the NACA 23012 and NLF 0414 airfoils while the test model used by Papadikas, et al., [3] was a 22% scale model of a 65% semispan regional/large business jet wing. A number of simplistic shapes were considered by the selected publications and Figure 2.1 very broadly separates the simulated shapes into three categories also described in Table 2.1.

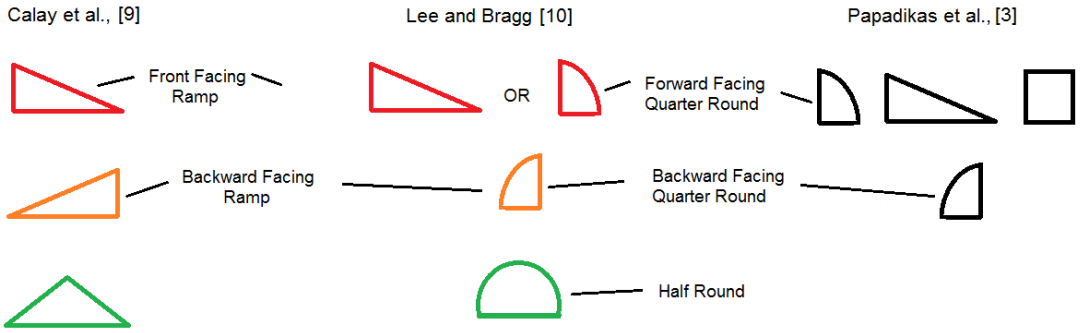

Figure 2.1: Simplistic Runback Ice Shapes found in Literature

Ice Shape Colour	Geometrical Description	Performance Losses
Red	Blunt face	Largest performance loss regardless of chord location
Orange	Ramp	Varying performance loss based on chord location
Green	Hump	Least adverse in terms of drag coefficient at all chord locations

Table 2.1: Simple Ice Shape Categories

The categories in Table 2.1 hold well for airfoil case studies by Calay, et al., [9] and Lee and Bragg [10] but trends from simple ice shapes on a wing by Papadikas, et al., [3] were not clear as the wing aerodynamic performance was found to be sensitive to ice shape geometry and the reason why the shapes are not colour coded in Figure 2.1.

The non-dimensional height of the simplistic ice shapes against the mean aerodynamic chord is given in Table 2.2:

Author	Calay, et al., [9]	Lee and Bragg [10]	Papadikas, et al., [3]
Ice Height to Chord Ratio (k/c)	3.5%	1.38%	1.07% & 2.67%

Table 2.2: Non-Dimensional Simple Ice Shapes Heights

The publications surveyed used different ice to chord heights (k/c) for different airfoils of differing chord lengths which made comparison complicated. Lee and Bragg [10] compared the NACA 23012 and NLF 0414 for the same set of simplistic runback ice shapes fixed at 10% upper chord location. The findings showed the effects on performance. The geometrical shape changes were of particular interest as realistic three-dimensional castings do exhibit features

which could be recreated as lower-fidelity castings easing the experimental fabrication time and costs. The authors found the more streamline backward-facing quarter-round shapes only performed slightly better than the blunter forward-facing quarter-round ice shape. The comparison against the half-round shape, which had identical geometric features facing the flow as the backward-facing quarter-round ice shape, performed significantly better. This signified that the geometry downstream of the point of separation affects the lift characteristics of the ice accreted airfoil. In contrast to these observations, the blunt faced shapes examined, front-facing ramp and front-facing quarter-round, did not exhibit any significant variation in lift curves. The author concluded that the downstream geometrical features do not have a significant effect on aerodynamic performance relative to the more streamline shapes. Other findings indicated the simulated ice shapes were dependent on the airfoil geometry. Their findings indicated that pressure distributions of a given airfoil dictate how a disturbance affects performance along the chord. To further complicate the matter the shape and chord location of the ice also had a significant effect. Alègre [1] conducted a number of CFD runs for aerodynamic shape study on a flat plate. Triangles and rectangles were used with both sharp and smoothed edges. The purpose of the study was to investigate shapes suitable for wind tunnel testing. The results indicated the sharp edged shapes caused the flow to detach more severely than the corresponding smoothed edge shape (Figure 2.2).

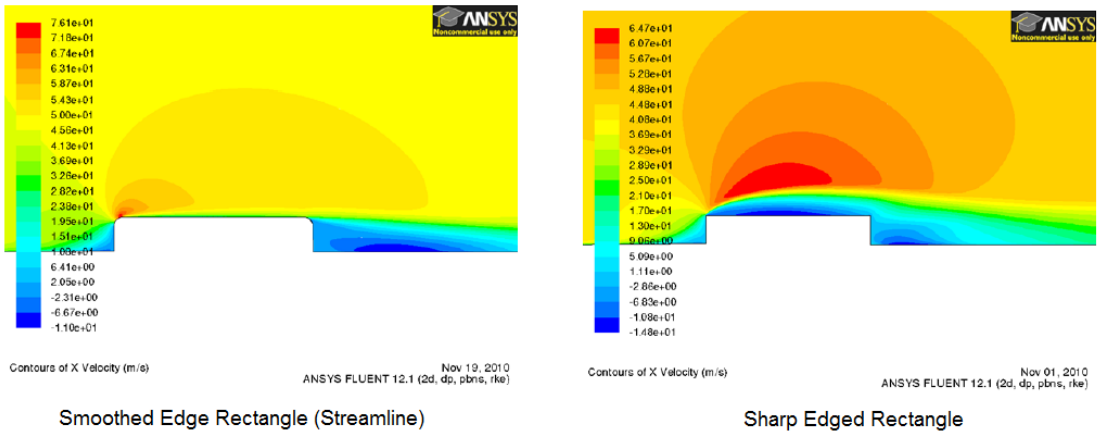

Figure 2.2: Comparison of Sharp and Smoothed Edge Shapes on Flow Detachment [1]

Reynolds number investigations revealed an upper limit where the effects on C_{lmax} are insignificant relative to the degradation due to the presence of runback ice. Broeren, et al., [11] conducted a study using three different airfoils to evaluate ice accretion performance effects at the University of Illinois Subsonic Aerodynamics Laboratory using a low-speed, low-turbulence wind tunnel. The airfoils used were the NACA 23012, NACA 3415 and NLF 0414

where ice casting from a previous study by Broeren, et al., [12] were utilised. The original castings were produced on a 0.91m NACA 23012 airfoil and were scaled down by a factor of two. The author conceded the ice shape features may not be accurate for the NACA 3415 and NLF 0414 airfoils but the purpose of this study was to consider performance effects and thus did not impact on the validity of the results. The chord-based scaling was considered valid for this study as the height of the ice accretion was not comparable with the boundary layer thickness. The authors found there was virtually no change in C_{lmax} for Reynolds numbers larger than $3.5x10^6$. These trends were also observed by Morgan, et al., [13] for large glaze ice on a super critical multi-element airfoil. They performed tests in cruise configuration and observed very little variation for C_{lmax} over a range of Reynolds numbers from $3x10^6$ to $12x10^6$. These observations were also seen on the NLF 0414 airfoil by Andy and Chung [14]. Both authors found the transition to turbulence for the iced airfoil runs was dictated by the location of the ice shape whereas in the clean airfoil cases, the Reynolds number dictated the location for transition.

Calay, et al., [9] noted the contaminated NACA 0012 airfoil produced a greater C_{lmax} than the clean airfoil at the 15% and 25% chord locations. Although further insight into this phenomenon was not detailed, the author attributed the result to increased turbulence in the flow due to the ridge shape. The work of Papadikas, et al., [3] using the representative modern business and regional jet airplane also found the contaminated wing produced a higher C_{lmax} than the clean wing for a particular ice shape. One of the conclusions found was the need to do more experimental tests exploring a range of runback ice shapes.

Previous runback ice studies consider a few locations along the chord for a fixed ice height followed by different runback ice shapes or simple shapes with different height to chord ratios. To this end Lyncha and Khodadoust [15] conducted an extensive review of the literature available and found runback ice protuberances smaller than 0.0020k/c on airfoils were sensitive to chord location and the largest C_{lmax} losses were found at the leading edge (or very close to leading edge). However their findings indicated the height of ridge ice on the leading edge would be smaller than typical leading edge ice accretions. The authors found that these trends were no longer observed when the chord ratio height of the ice shape increased. Larger disturbances ($0.005 < k/c < 0.0139$) produce their largest C_{lmax} at more aft locations between 5% and 15% chord locations.

To this end Whalen, et al., [16] set out to investigate runback ice accretions due to hot-air ice protection systems and scaling of external flow parameters for testing thermal systems. The authors grew thermodynamically scaled runback

ice on a full-scale typical business jet (Figure 2.3 & Figure 2.4). Castings of the ice shapes were successfully captured with the aim of running aerodynamic performance tests.

The process to apply realistic ice casting to the wing for aerodynamic testing is both time consuming and costly. Accordingly, geometrically scaled (ratio based on chord length) and boundary layer scaled (ratio to local boundary layer thickness) simplistic two-dimensional shapes were used to develop a three-dimensional runback ice profile for the NACA 23012 and NACA 3415 (Figure 2.5 & Figure 2.6).

Figure 2.3: Representative Business Jet Thermal Model Installed in the NASA Glenn Icing Research Tunnel [16]

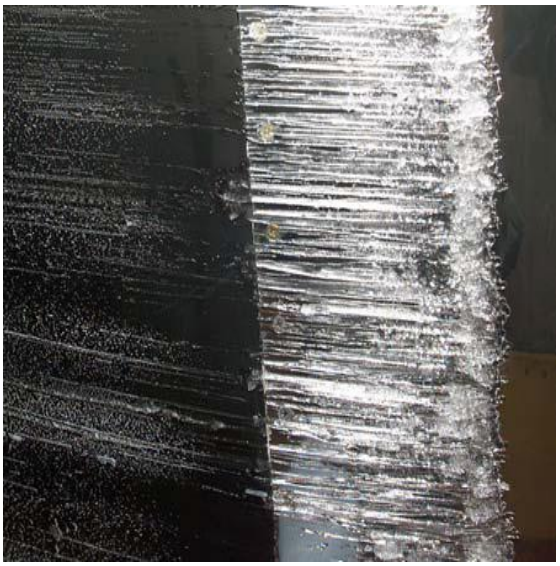

Figure 2.4: Overall Photograph (Suction Surface) of a Warm Hold Runback Accretion [16]

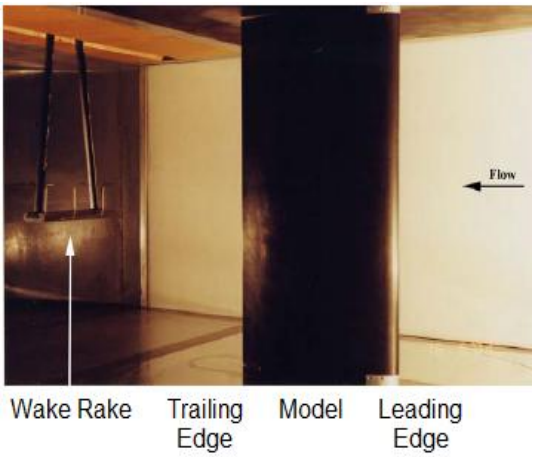

Figure 2.5: Experimental Setup in University of Illinois at Urbana-Champaign 3'x4' Wind Tunnel [16]

Figure 2.6: Upper Surface Simulated Warm Hold Accretion [16]

The Reynolds and Mach number for the aerodynamic run was $1.8x10^6$ and 0.18 respectively. They found the geometrically scaled runback ice shapes enhanced the aerodynamic performance when the boundary layer size was comparable to the ice height. They also found the boundary layer scaled runback ice shapes never enhanced the aerodynamic performance of the airfoil. This result was not understood and further testing was called upon.

The heat and mass transfer changes with altitude are difficult to replicate in an icing tunnel. Whalen, et al., [16] attempted to thermodynamically scale the runback ice shapes to assess the methods plausibility. However without any reference to full scale ice accretion setup, be it simplistic shapes or realistic, the author concluded that there is a strong need for full scale aerodynamic tests along with further studies on geometrical scaling.

Questions about the validity of runback ice scaling required some answers. Lee and Bragg [17] and Broeren and Bragg [11] demonstrated that geometrical scaling was an accurate method for runback ice predictions using experimental data from wind tunnel testing. However, in both cases the runback ice height was over 20 times taller than the boundary layer. In these instances, scaling with respect to chord length was a sensible option. However when the boundary layer thickness is comparable with the runback ice height, geometrical scaling may not be appropriate. Calay, et al., [9] also found that the C_{lmax} increased for the iced case, and attributed the flow remaining attached to be due to extra turbulence but the mechanism for this to occur was not discussed.

The variations observed for geometric and boundary layer shape scaling was significant and led to a joint effort by NASA, Onera and the University of Illinois to investigate aerodynamic simulations on airfoil ice accretion [18]. A summary of their objectives, consequent publications and key findings over a number of years is presented.

Phase 1:
Brag, et al., [19] presented a detailed literature review on icing aerodynamics broken down into three chronological time periods; up to 1978, 1978-1994 and 1994-2005. The authors presented the identification of four classes of ice formation; roughness, horn ice (large horn type shapes appearing from leading edge ice), streamwise ice, and spanwise-ridge ice (Figure 2.7).

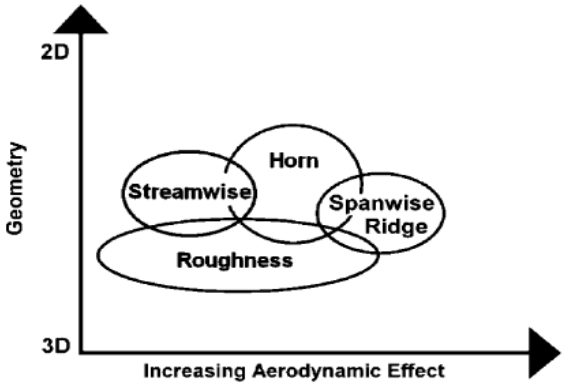

Figure 2.7: Qualitative Description of Aerodynamic Effects for Various Iced Airfoil Flow-fields [19]

Runback ice falls under the latter class. Each of the four types of ice accretion flowfield parameters were discussed and the spanwise-ridge ice analysis highlighted four critical factors associated with runback ice; height, location, geometry and spanwise uniformity. For runback ice it was found that location and height were key parameters, but the geometry of the ridge was also shown to be important.

The effect of ice accretions on Reynolds number was also covered. They found that the sensitivity for ice accreted airfoils relative to clean airfoils was much less. This was attributed to the fixed ice location dictating the point of separation. For a clean airfoil, the transition to turbulence is highly dependent on Reynolds number hence the higher sensitivity to changes in Reynolds number. These finding were also confirmed by Diebold, et al., [20].

Phase 2:

With the key ice features categorised the next objective was to accrete runback ice (as well as the other three types of ice accretion) with geometrical features typical of their individual ice classification. A NACA 23012 sub-scale airfoil was used in the NASA Icing Research Tunnel for ice accretion tests. Successful three-dimensional castings were acquired along with tracing and pictures. Although the set of castings were formed on a sub-scale airfoil, the aim here was simply to gather ice castings representative in shape rather than size.

Figure 2.8: Subscale NACA 23012 Ice Accretion Model Installation in NASA Icing Research Tunnel for Phase 2 [18]

Phase 3:

A total of sixteen moulds were produced representing the four categories outlined in phase 1. Of particular interest were spanwise ridge shapes shown in Figure 2.9. These high-fidelity castings were compared with two-dimensional smoothed ice shapes and simple geometrical shapes. Along with a performance comparison for all types of ice accretion, a spanwise ridge shape fidelity test was conducted (Figure 2.10). The authors found the two-dimensional smooth shapes were the better match to the casting rather than the simple shapes. This suggested the cross-sectional area of the ice shape was more important when considering the aerodynamic affect of ridge/runback ice. The results showed an alarming increase in drag coefficient of 250% when comparing the clean and two-dimensional smooth run around 3° AOA.

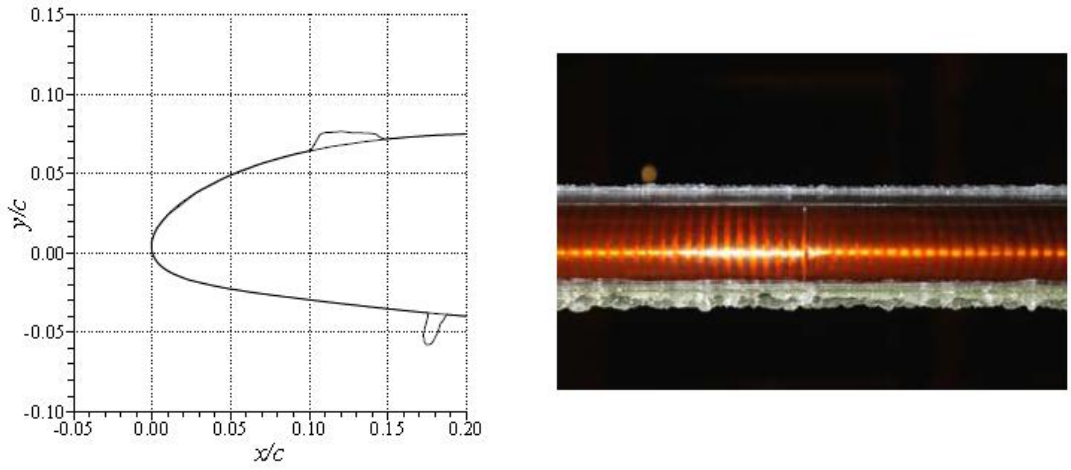

Figure 2.9: Tracing and Photograph of Spanwise-Ridge Shape for Sub-Scale Model [18]

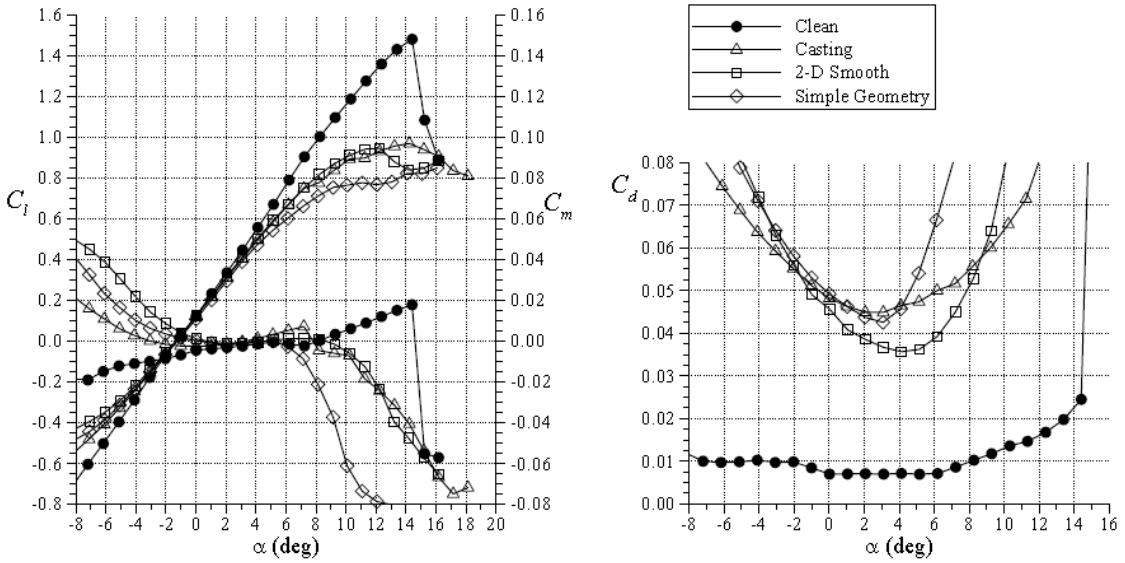

Figure 2.10: Aerodynamic Performance Comparison of Simulation Fidelity for Spanwise-Ridge Ice Shape on the NACA 23012 Model [18]

Phase 4:

This phase of the study focused on the full-scale ice accretion testing. As outlined in phase 2, the aim was to capture the geometrical features typical of the four ice categories and of particular interest was the full-scale spanwise ridge ice shape (Figure 2.11).

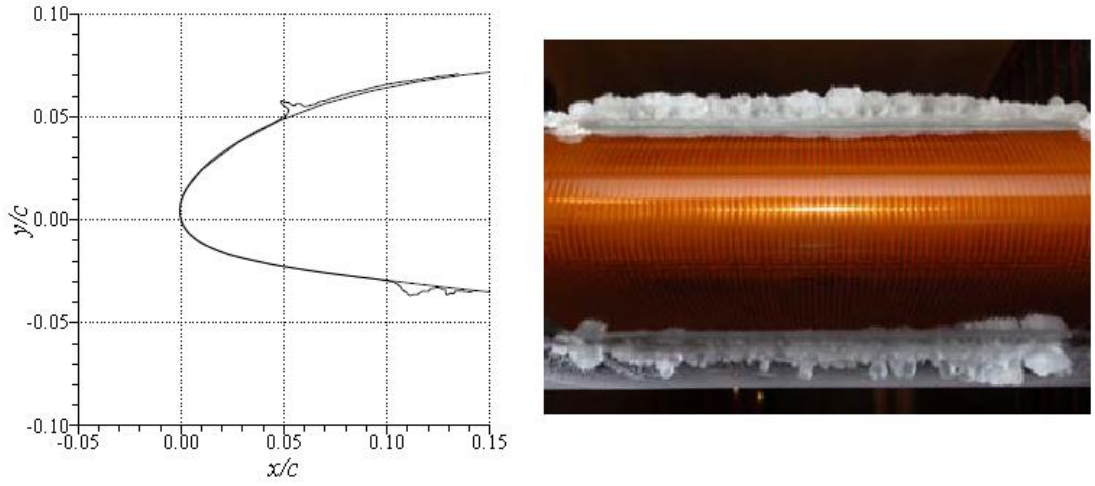

Figure 2.11: Tracing and Photograph of Spanwise Ridge Shape for Full-Scale Model [18]

Phase 5:

Phase 5 considered the aerodynamic penalties associated with full scale ice accretion. The Onera F1 pressurised wind tunnel was used with the NACA 23012 airfoil of chord length of 1.828m. Alongside the full-scale runback ice shown in Figure 2.11, Broeren, et al., [21] presented the results for other

runback ice shapes which were deemed representative of typical runback ice formation in the hold phase on airplane equipped with bleed-air thermal ice protection system (Figure 2.12 & Figure 2.13). The representative shapes by Broeren, et al., [21] shows remarkable similarities with the runback ice shape used for the aerodynamic studies presented in this thesis which were created at the Cranfield Icing Tunnel by Alègre [1] and shown in Figure 2.14 and Figure 2.15.

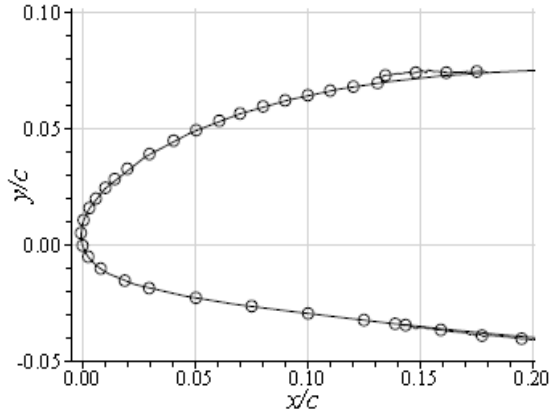

Figure 2.12: Representative Full-Scale Runback Ice [21]

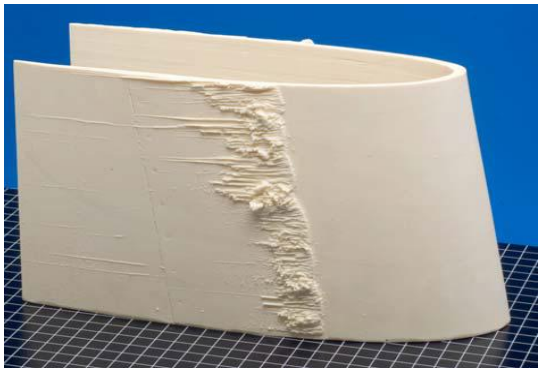

Figure 2.13: Photograph of Runback Ice Accretion Casting for Upper-Surface Ridge [21]

Figure 2.14: Closer Examination of Representative Full-Scale Runback Ice [21]

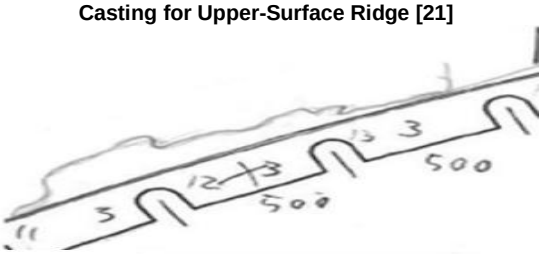

Figure 2.15: Representative Full-Scale Runback Ice Shape for Boeing 737-700 Hybrid Airfoil [1]

The icing condition in which the two runback ice shapes (Figure 2.11 & Figure 2.12) were accreted is shown in Table 2.3. The icing conditions for the runback ice accretion by Alègre [1] are also shown.

Runback Ice Shape	Freestream Velocity (ms^{-1})	Angle of Attack	MVD (μm)	LWC (gm^{-3})	Total Temperature (Celsius)	Accretion Time (minutes)
[18]	77	1.5	20	0.81	-6.7	15
[21]	72	1.1	28	0.91	-5.05	22.5
[1]	85	8	17	0.42	-9	20

Table 2.3: Icing Conditions for Representative Runback Ice Shapes Accretion

Broeren, et al., [22] work provided data for clean full-scale NACA 23012 airfoil which was used to analyse the performance degradation associated with their representative runback ice. The high fidelity runback ice aerodynamic wind tunnel test found:

Runback ice accretion by Bragg, et al., [18] shown in Figure 2.11 found a C_{lmax} drop of 70%, stall reduction by 69% and the minimum drag increased by over a factor of 4.

Runback ice accretion by Broeren, et al., [21] shown in Figure 2.12 found a C_{lmax} drop of 17%, stall reduction by 17% and the minimum drag increased by a factor of 2.

These startling variations once again highlight the variability in performance losses based on geometrical shape, location and airfoil to name a few.

Phase 6:

The final experimental stage of this collaboration placed attention on the aerodynamic scaling of runback ice accretions [23]. As previously stated, the uncertainly involved when the runback ice shape height is similar to the boundary layer thickness required investigation. With the 5 phases of this collaboration complete, aerodynamic data on full-scale and sub-scale airfoils with representative runback ice was available; thorough analysis of runback ice scaling methods was discussed. Two airfoils were considered; NACA 3415 and NACA 23012. The two airfoils were chosen due to their distinctly different pressure loading mechanism. Lee and Bragg [24] found runback ice was particularly sensitive to the chord-wise loading.

Three cases were examined by Whalen, et al., [23]; cold hold, decent ice and warm hold. Airbus follow the EASA requirements for worst icing conditions and of particular interest was the 45 minute hold case in maximum icing; warm hold.

For each case, high and medium fidelity runs were conducted. The high fidelity castings are similar to Figure 2.13. The medium fidelity shapes used were simple squares or rectangle cross-sections representing ridge ice.

For the cold and decent case, the height of the runback ice shapes was ten times the size of the boundary layer. For this size, Whalen, et al., [23] used the chord length to scale the height but for the warm hold case the boundary layer size was comparable with average runback ice height. Therefore both boundary layer and chord ratio scaling was applied and evaluated. One of the main

differences noticed was the boundary layer scaling produced a much larger separation bubble (Figure 2.16) and trailing-edge separation was found to move forward with angle of attack.

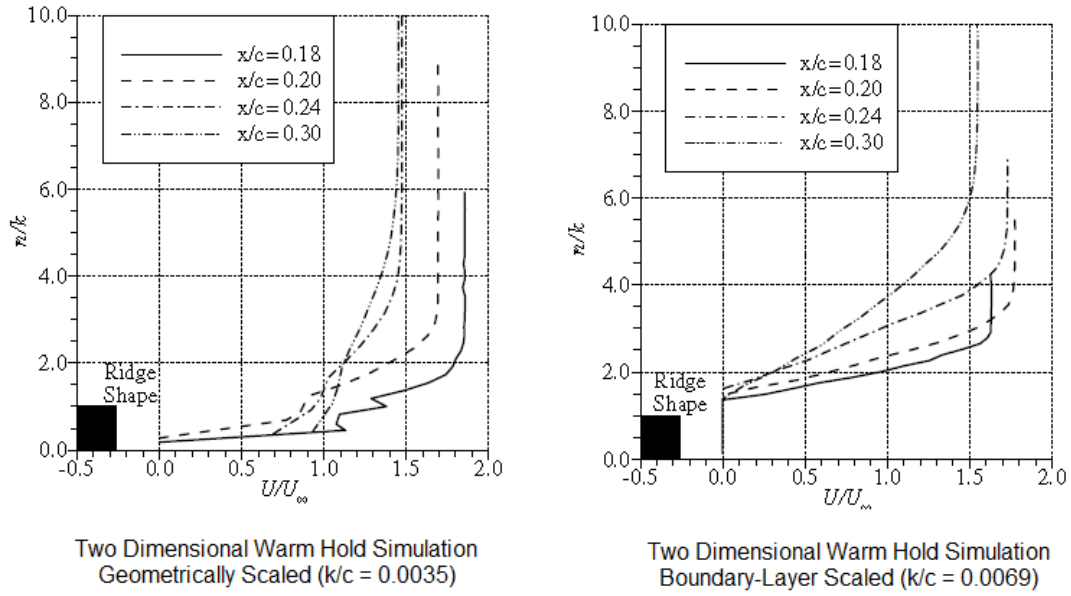

Figure 2.16: Boundary Layer Profile Measurements for Two-dimensional Warm Hold Ice Simulation [23]

The geometrically scaled cold hold and decent ice cases performed well and found effects due to Reynolds number were negligible. The author concluded geometrical scaling of these two cases was representative of full scale runback ice.

The warm hold case did not exhibit good agreement between the two fidelity runs. The high-fidelity run showed a detrimental effect on both airfoils while the medium-fidelity run improved the C_{lmax} and stall for the NACA 3415 and had very little effect on the NACA 23012. The warm hold case ice accretion forms further along the chord relative to the cold hold and decent ice case; the boundary layer size becomes comparable to the height of the ice shape. The scaling effects here become important, hence the reason why Whalen, et al., [23] attempted to provide some insight into the appropriate scaling method; boundary-layer scaling methods.

Large differences between the geometrical and boundary layer scaling methods were found. The maximum lift was increased by 14.7% for the geometrical scaled ice but decreased by 34.5% for the boundary layer scaled ice.

A small separation bubble was seen with the geometrically scaled runs with delayed trailing edge separation. The increase in maximum lift and stalling angle of attack was credited to this delay. Conversely the boundary layer scaling method was found to cause significant losses with separation bubble sizes over 30% larger than observed for geometrically scaled ice shapes. They found at angles of attack over 8°, the flow separated directly from the ice shape.

The findings by Whalen, et al., [23] showed there was some interaction with the boundary layer when the heights of the ice accretion were increased from 0.0035k/c to 0.0065k/c. The position where the runback ice formed during a warm hold case coupled with the accretion heights leads to a situation where the boundary layer height was comparable to accretion height and geometrical scaling results compared to boundary layer scaling provided poor agreement. The need for further testing and insight into the mechanism controlling this discrepancy was required. This problem was magnified for ice location optimisation where the boundary layer thickness relative to ice height varied for each design vector. Therefore selecting the appropriate scaling technique bearing in mind the discrepancies highlighted deem the use of scaling and ice location optimisation questionable.

Broeren, et al., [21] paper provided a further discussion on the aerodynamic effects from the full scale NACA 23012 over a range of Reynolds number from 4.7×10^6 to 16.0×10^6 and Mach number range of 0.1 to 0.28. High-fidelity runback ice castings on both surfaces were used for performance tests. The C_{lmax} was reduced by 17% with a reduction in stall angle of 3.1°. With these full-scale results a second sub-scale test using NACA 23012 model (0.45m) with corresponding Reynolds number of 1.8×10^6 and Mach number of 0.18 was conducted. Two tests using low and high fidelity, geometrically-scaled, castings from full-scale ice shapes were used. The authors concluded the low-fidelity two-dimensional ridge ice shapes produced the best result with the full-scale, high-Reynolds number run. The authors study using high-fidelity, geometrically-scaled runback ice shapes lead to a new classification within the spanwise-step accretion category; short and tall ridges. This proposal was based upon the flowfield characteristics which were evidently different for tall and short ridge type runback ice. Tall shapes were found to significantly disrupt the flowfield around the airfoil with large unsteady regions of separated flow. These were exaggerated with increasing angle of attack and lead to earlier stall and lower maximum lift coefficient. The short ridge ice shapes produce small separation bubbles very close to the ice shape. These small regions were found not to disrupt the overall pressure distribution. The authors concluded the need to investigate the appropriate aerodynamic simulation methods for short ridges, particularly for Reynolds numbers less than 1.8×10^6.

2.2. Computational Survey

Numerical simulations allow further insight into the flow dynamics associated with ice accretion, This survey focussed on runback ice accretion using RANS turbulence modelling.

Numerical simulations for iced airfoils can be found as early as 1985 with Potapczuk and Gerhart [25] using the RANS equation for external flows. A NACA 0012 airfoil with glaze and rime ice accretions was simulated. Numerical simulations directed towards runback ice were conducted by Dunn, et al., [26] on the NACA 23012 using the NSU2D flow code and the one-equation Spalart-Allmaras turbulence model. The results were compared with experimental data from Lee, et al., [27] and predicted the flow features quite well. The discrepancies arose when flow separation was large. It was noted the Spalart-Allmaras model pressure recovery was much faster relative to the experimental data in the separated flow region. They also found the model prediction for fully separated flow was similar in magnitude to large flow separations and was attributed to the fact that the reattachment point was fixed to the trailing edge for both cases.

Pan, et al., [28] conducted RANS simulations for a number of turbulence models. The study investigated the effects of simulated ridge ice shapes on a NACA 23012, NLF 0414 and NACA 3415 for a range of Reynolds and Mach numbers. The study also considered performance effects due to ice height and shape features. The computational results were compared with the experimental data acquired at the NASA Langley low turbulence pressure tunnel and the University of Illinois Low-Speed wind tunnel. Their findings were consistent with published experimental data in terms of insensitivity to Reynolds number and non-linear relationships for lift and drag with respect to runback ice heights. The angle of attack study by Dunn, et al., [26] showed that when the region of separated flow was large and up to fully separated flow, the RANS model was unable to accurately predict the force coefficients. The authors concluded the unsteady characteristics associated with iced airfoils near and post stall cannot be reasonably captured by the RANS models. Pan, et al., [28] also considered the two-dimensional airfoil simulations against three-dimensional wing simulations. The authors found the increase in drag due to ice accretions was large relative to the increase from induced drag deficit by simulating two-dimensional airfoils. They suggested the critical ice location trends seen for the two-dimensional airfoil simulation may be quantitatively extended to three-dimensional wings.

An enhancement of this study was conducted using the Detached Eddy Simulation (DES) approach alongside a Large Eddy Simulation (LES) / RANS

hybrid model [29]. The aim here was to improve the predictive ability of the stall behaviour. Clearly the numerical prediction for low angles of attack iced airfoils simulations was not of concern after the well predicted results seen in the previous RANS study. The authors found the DES model predicted a more obvious stall which was of similar incidence as the experimental data but failed to accurately predict the force coefficients. The authors suggested the already computationally intensive DES model required an even higher gird resolution to improve the numerical simulation results.

Marques and Badcock [30] considered the validation of two airfoils for ridge ice accretion; NACA 23012 and generic multi-element airfoil. The one-equation Spalart-Allmaras and two-equation Menter $k-\omega$ turbulence models were compared. They found both the lift and drag comparison up to 5° AOA (where separation occurred) was well predicted and that both turbulence model predictions were similar (Figure 2.17). The turbulence levels produced by the $k-\omega$ model at 0° AOA was larger than the Spalart-Allmaras model and was due to the production terms reacting to flow gradients. This was one of the flaws associated with Wilcox's $k-\omega$ model and led to the creation of Menter's Shear Stress Transport $k-\omega$ turbulence model. Turbulence modelling and its appropriate selection are discussed in detail in Section 3.4. Overall the authors concluded the general trends were well captured by CFD.

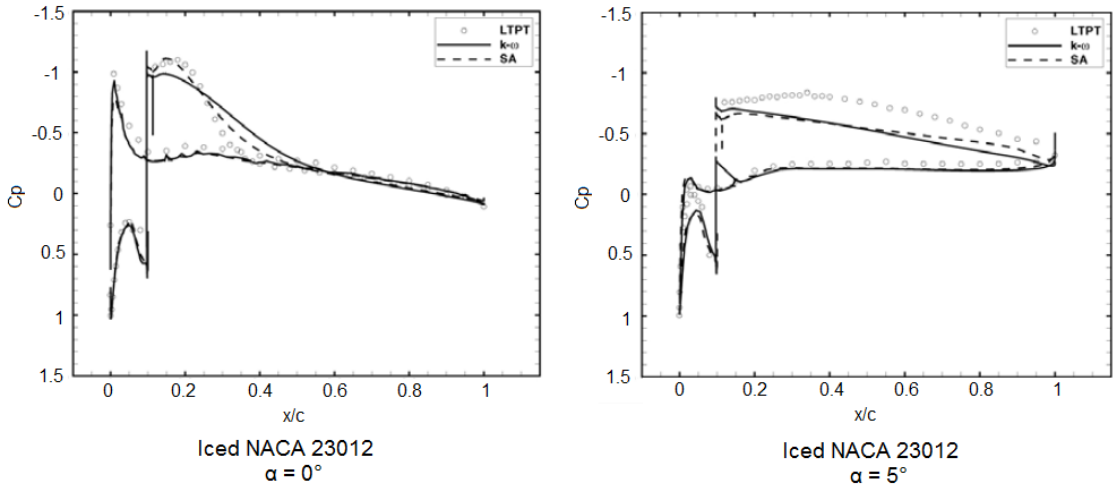

Figure 2.17: NACA 23012 Surface Pressure Coefficient Comparisons for Iced Surface [28]

More recent publications are geared towards wing ice accretion testing and computation validation of commercial codes. The need to understand whether two-dimensional airfoil ice accretion prediction from numerical solvers could be used instead of computationally expensive three-dimensional high fidelity simulations was considered [31]. A two-dimensional hybrid grid was used for clean and leading edge iced NACA 23012 airfoil. The mesh consisted of

quadrilaterals around the airfoil and triangles in the rest of the domain totalling 90,000 cells. The volume mesh consisted of prism layers near the viscous region and tetrahedral cells in the farfield (Figure 2.18). The three-dimensional ice shapes were developed using the LEWIS3D software and reduced for two-dimensional study. CFD++ was used as the commercial solver utilising the realizable $k-\varepsilon$ turbulence model. The author compared the two-dimensional NACA 23012 CFD results against the data published by Broeren, et al., [22]. The author found the CFD predictions for the clean airfoil was comparable with experimental data. The iced airfoil numerical lift coefficient predicted an earlier drop in angle of attack relative to the experimental data. The drag was slightly over predicted for the clean airfoil but the overall trends were well observed. In iced configuration the drag was slightly under predicted up to 4° AOA but also captured the drag increase quite well. These variations observed between the numerical and experimental data were attributed to the unsteady effects associated with ice accretion flows, particularly leading edge ice. The author considered the computational costs and found the three-dimensional simulations took 35 hours utilising 24 processors, where the two-dimensional simulations took 1 hour using 2 processors. The author concluded the general trends captured by the two-dimensional simulations proved to be good initial estimates of the change in airfoil aerodynamics. The ability for accurate prediction using two-dimensional simulations with only 90,000 cells for separated flows highlighted the robustness of turbulence models available in commercial codes for low angles of attack where flow separation was kept minimal. When considering the implication of high-fidelity three-dimensional optimisation, CFD run times of 24 hours are not feasible. The literature suggests two-dimensional airfoil simulations capture the general trends well and thus were deemed appropriate to conduct high-fidelity two-dimensional CFD simulations coupled with optimisation algorithms.

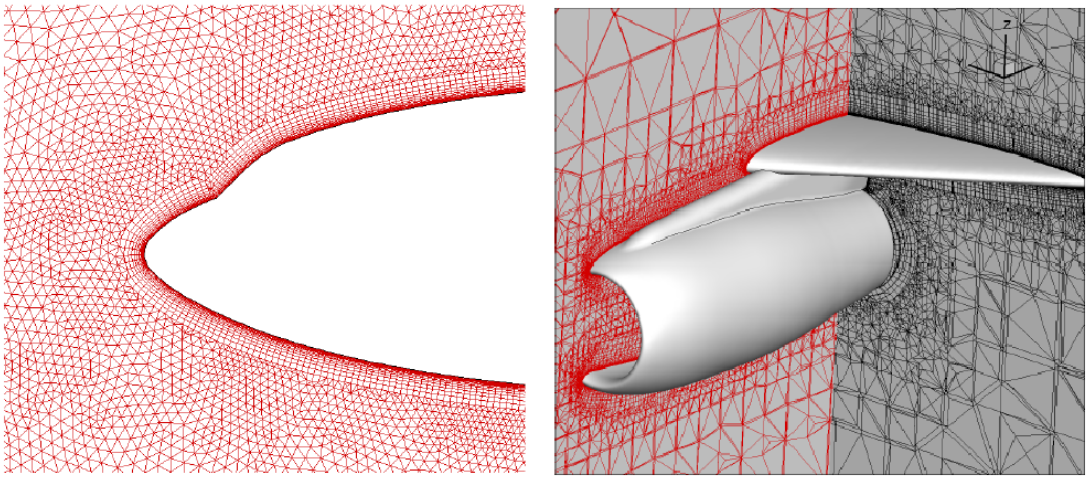

Figure 2.18: Symmetry Plane and Volume Mesh Highlighting Hybrid Nature [31]

Three dimensional CFD analysis on a reflection plane wing with laminar flow section and a mean aerodynamic chord of 1.2192m was conducted [32].The results were compared with wind tunnel data from the Wichita State University Walter H. Beech Wind Tunnel. ANSYS FLUENT was the commercial software package. A pressure-based solver and SIMPLE pressure velocity coupling algorithm was used. The Spalart-Allmaras turbulence model was used with all results converged to second-order accuracy. The angle of attack for the simulations was set to 7° to allow a large enough separated region to form and test the prediction capabilities of the ANSYS FLUENT solver. A hybrid volume consisting of prism layer elements near the walls and tetrahedral elements for the rest of the domain was utilised using ANSYS ICEMCFD as shown in Figure 2.19. The authors performed computational simulations using a 4mm forward-facing quarter-round ice shape and further simulations including roughness. Wall function modification for rough surfaces was used to simulate sandpaper roughness which meant two hybrid meshes of differing first cell size were required. ANSYS FLUENT required the first cell size to be larger than the roughness height which increased the y+ by two to three magnitudes and significantly reducing the number of cells in the mesh.

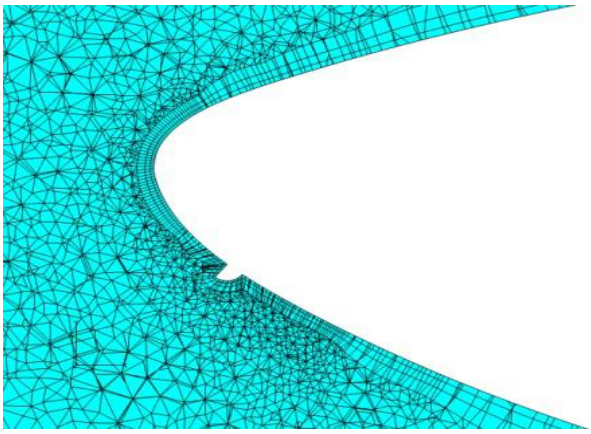

Figure 2.19: Hybrid Mesh [32]

Comparison of the experimental and computation pressure profile data for the clean and iced runs showed good correlation (Figure 2.20). The discrepancies observed only occurred at high angles of attack due to large separated regions. For the simulations tested the lift coefficient varied from the experimental results by -6.2% and 4.9% and the drag coefficient results were under predicted by 1.5% to 7.4%. The author concluded that ANSYS FLUENT captured the flow behaviour of the iced airfoils well.

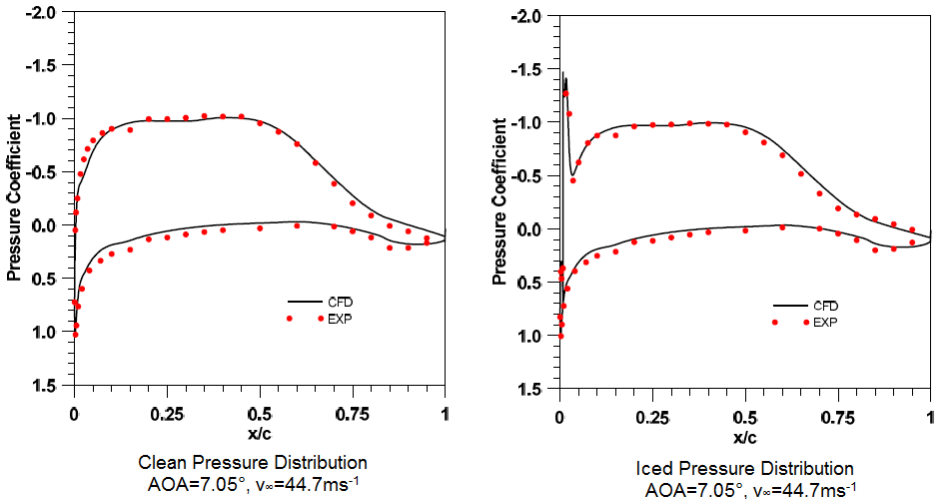

Figure 2.20: Comparison of Chordwise Pressure Distribution from CFD and Experiments [32]

Performance tests for three-dimensional CFD simulation on conjugate heat transfer was conducted by Wong, et al., [33]. ANSYS FLUENT was the commercial package considered with ANSYS ICEMCFD used for hybrid volume mesh creation. The authors investigated the performance of bleed air ice systems for warm and cold hold dry external flow conditions. The computational mesh was significant with approximately 308 million cells modelling a 1.8m span and 1.5m chord wing. The CFD simulation modelled laminar and turbulent flow over the wing surfaces. A transitional $k-\omega$ SST model was used. This model included two additional transport equations; intermittency and onset of transition. The authors found the bleed air system temperatures and pressures trends were generally well predicted with their respective magnitudes in good agreement with experimental data. The leading edge skin temperatures were over predicted around the upper surface 3% chord station. Apart from this, the computed and experimental leading edge skin temperatures were in good agreement.

Similar to the three year/six phase study run by Bragg, et al., [18] a second study comprising seven phases outlining technical challenges faced with icing on large scale and on three-dimensional swept wings was presented by Broeren and Potapczuk [34]. This is an ongoing collaborative study by NASA, FAA, ONERA, the University of Illinois and Boeing at the time of writing and all seven phases are illustrated in Figure 2.21.

This collaboration entails the use of wings rather than airfoils and subsequent techniques not entirely relevant to this study. However the findings are included as they represent the more recent studies and publications for icing over the past three years.

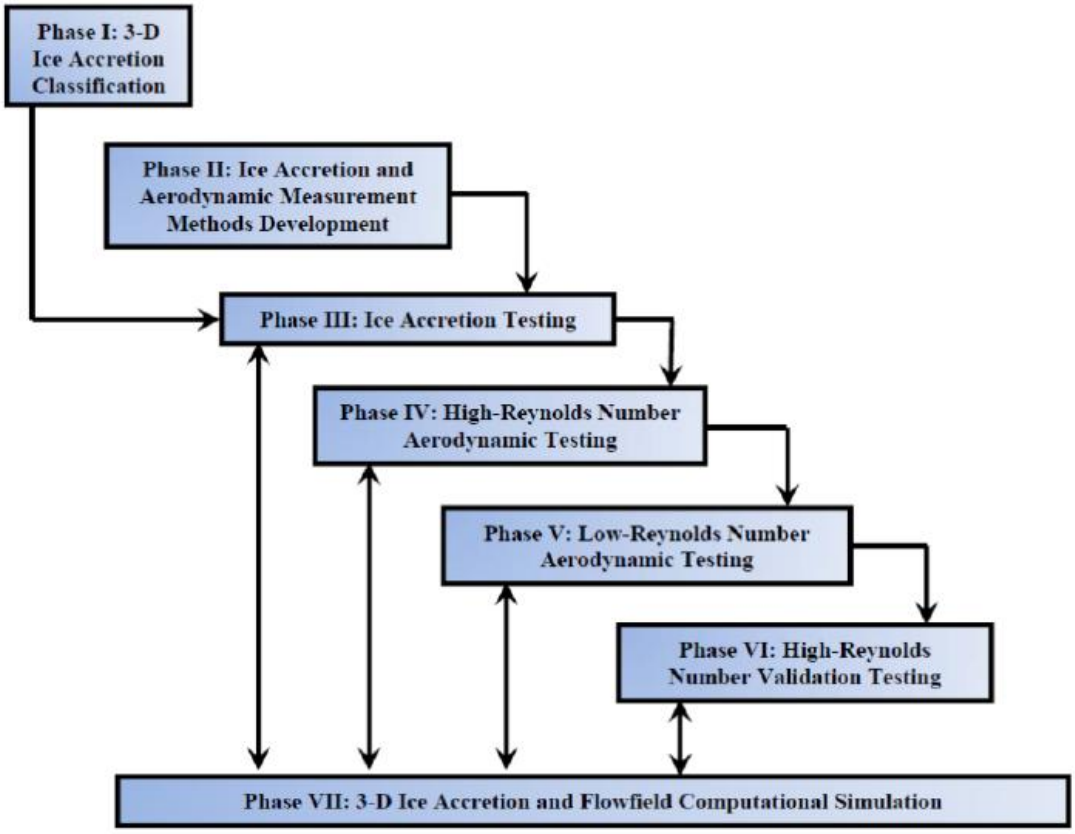

Figure 2.21: Flow Diagram Outlining Seven Phase Study [34]

Phase one provided an extensive review of ice accretion for swept wings and identified areas of improvement in our understanding [35]. The literature surveys lead the author to conclude very little information on spanwise ridge ice exists and there is a need for further testing. This phase of the research was ongoing at the time of writing and may evolve as more data is acquired.

Phase two defined the methods and necessary work for the experimental and computational work conducted in phases three and four. This part was broken down into three sections:

Define baseline, full-scale, swept-wing geometry

A 65% scale version of the Common Research Model wing (CRM) geometry was selected as the baseline reference geometry (Figure 2.22). The author designated the wing as CRM 65 to identify the scaling factor. This design of the CRM was motivated by a number of interested parties approaching NASA to enhance the current experimental data available to perform CFD validations [36].

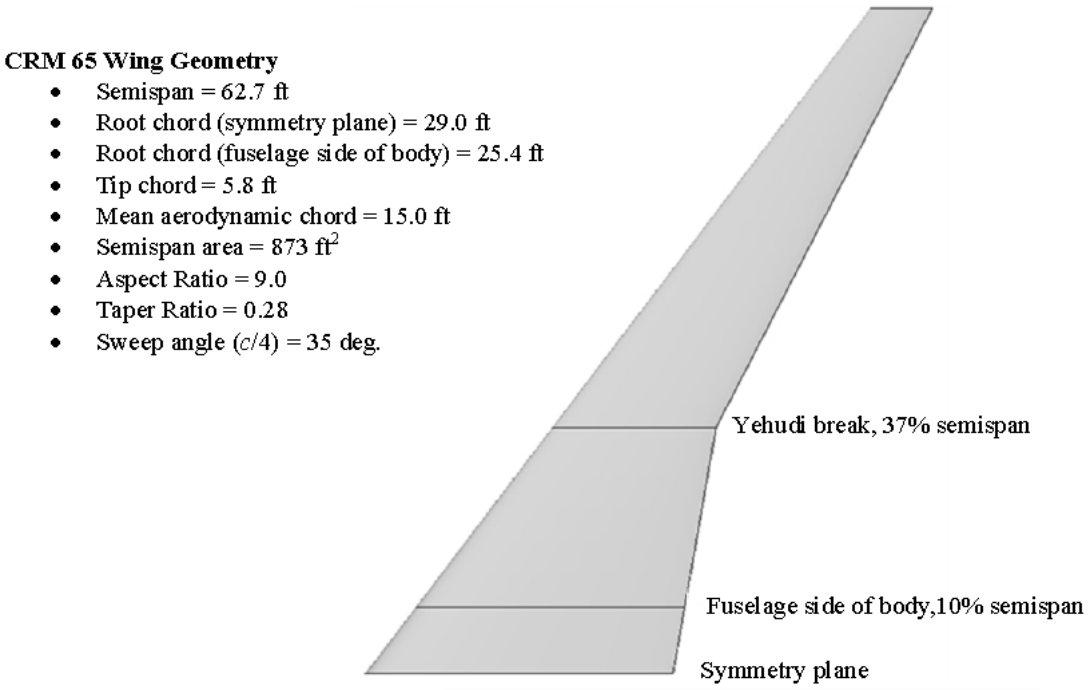

Figure 2.22: Summary of CRM65 Wing Geometric Characteristics [34]

Develop and validate method to measure three-dimensional ice castings

The current leading technology for capturing three-dimensional ice shapes is via molds and casting. Although this method captures excellent detailed features, these cannot be readily digitised. An alternative method was presented in phase two with ongoing efforts (at the time of writing) by NASA to adapt a commercial laser-based scanning method to capture three-dimensional ice accretion features. Deibold, et al., [37] described the significant progress already made in this area. The paper outlined two phases of the study. Firstly to identify the most suitable laser scanning hardware and software (phase 1) followed by research on implemention of the system and validation of its capability to record all of the aerodynamically relevant features (phase 2). Sample data from the scanner shown in Figure 2.23 highlights the ability to digitise the ice features with tremendous detail. Phase one was complete when the paper was publisished and phase two is currently underway (2013).

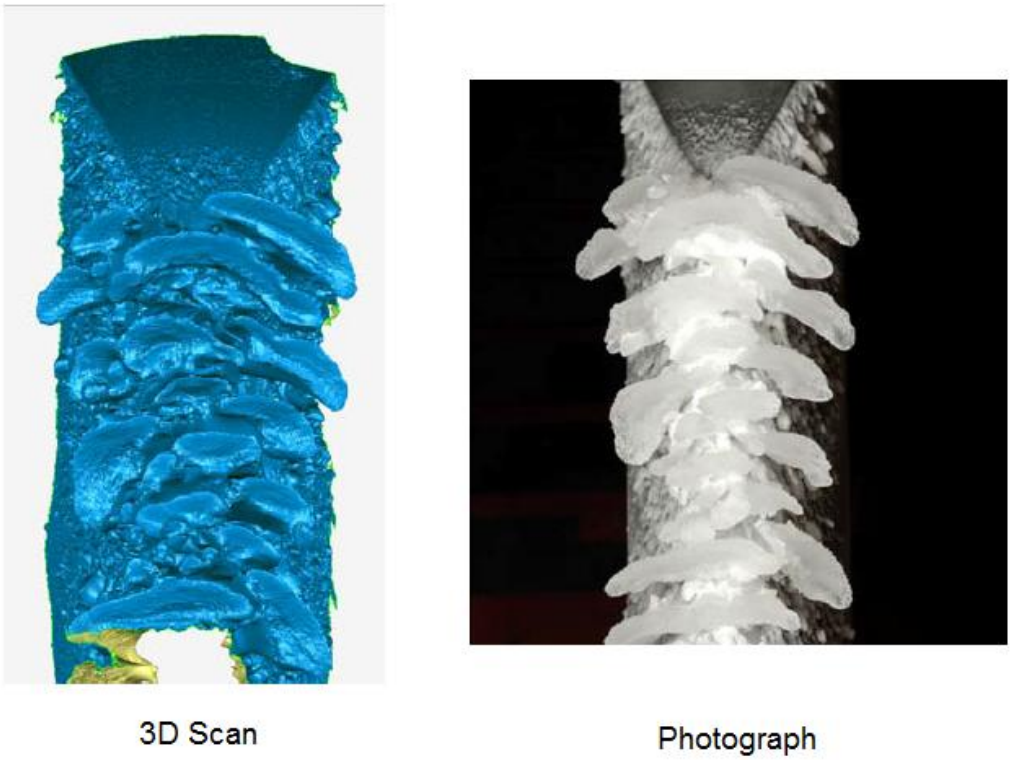

Figure 2.23: Sample Data from Scanner Evaluation [37]

Develop appropriate measurement methods to quantify iced swept wing aerodynamics

Two methods were outlined for aerodynamic measurements; pressure sensitive paint and wake survey techniques. The pressure sensitive paint coupled with surface oil flow visualisation was considered in detail by Deibold, et al., [20] on the CRM. The study investigated the aerodynamic performance and flowfield characteristics of a modern swept wing with leading edge ice. The visualisation of the flowfield was important as the ability to characterise and understand how these changes effected performance was considered paramount for airplane safety and to strengthen/validate current numerical solvers. The iced wing flow visualisation showed some similarities with two-dimensional iced airfoils for trends such as increasing separation bubble size with angle of attack. However at higher angles of attack, the unstable flowfield was highly three-dimensional; the initial vortex due to flow separation was three-dimensional. This is where the two-dimensional CFD simulations fail to accurately predict the flowfield. However at lower angles of attack, a number of publications suggest two-dimensional simulations provided good prediction of flowfield trends and force coefficients relative to costly three-dimensional high-fidelity simulations.

Ice accretion testing for three hybrid-swept wings modelling the 20%, 64% and 83% semispan stations of the baseline wing have been outlined after a four stage study:

- Selection of flight and icing conditions
- Full-scale icing conditions simulation
- Design and simulation of hybrid model wing sections in 2-D
- Design and simulation of hybrid model wing sections in 3-D

Stage two ran flow simulations using 3-D RANS code OVERFLOW for flowfield solutions used for input on the LEWIS3D code [38]. The authors consider the S-A, $k-\omega$ SST and a number of transitional models incorporating addition transport equations for transition prediction. Although for low angles of attack all models provided good predictions, at high angles of attack, the both transitional models exhibit early signs of stall and require further study. Roughness was not considered throughout this study.

Stages three and four were based upon earlier work by Saeed, et al., [39] and a number of others publication by the same authors. A more detailed and current analysis of the use of hybrid wings can be found by Fujiwara, et al., [40].The key aspect of this part of the study was to create a hybrid airfoil which accurately represented the full-scale local catch efficiency and leading edge flow field to allow for representative full-scale ice accretions. With these four stages complete future work to produce the hybrid-swept wings for testing at the NASA Icing Research Tunnel was planned.

Phase four and five was outlined for the development of artificial ice shapes of varying fidelity for aerodynamic testing for a large range of Reynolds numbers using the ONERA F1 pressurised wind tunnel. The impact of ice shape fidelity and Reynolds number was to be considered in phase six. The final phase of this collaborative research was to explore and further develop the use of CFD for iced wing aerodynamics.

Optimisation using CFD has become an important tool in recent years. Parameterisation tools can readily be found and integrated into the process to perform shape optimisation. A Multi-Objective Tabu Search (MOTS) optimiser developed by Jaeggi, et al., [41] was used to optimise the design of an iced airfoil using a simple forward-facing quarter-round shape [42]. The parameterisation tool used was Free Form Deformation (FFD). The CFD tool used was both OpenFOAM and XFoil. The ice shape and location used represented the worst case scenario for the NACA 23012 airfoil.

Their findings indicated improvements to iced airfoil performance can be found without excessive penalty to clean performance when considering airfoil shape optimisation. The authors noted how the position of the ice shape was one of the critical determining factors to iced airfoil performance. Airplane manufacturers invest heavily on wing design. The feasibility to implement a wing optimised for ice condition is not practical for airplane manufacturers. The design philosophy for an efficient clean wing still remains the logical route. However the design philosophy for its heating system could benefit from some form of optimisation relating directly to runback ice position. A more detailed discussion on optimisation codes and appropriate selection can be found in Section 3.5.

2.3. Summary

The literature survey highlighted a number of fundamental flow traits associated with runback ice.

A number of authors concluded the pressure distribution of the clean airfoil was directly related to the magnitude of performance loss. An identical ice shape at chord positions ranging from 3-15% show significant variation in force coefficients and found that critical regions are located near the point of maximum pressure gradient. To this end, the numerical simulations used in this study were restricted to the B737-700 airfoil to remain consistent with the airfoil used to create ice accretions. Airfoil shape optimisation for iced airfoils represents an opportunity to consider how the pressure distribution could impact on fixed chord ice accretion.

Geometrical features have been considered by numerous authors. Leading edge properties of the ice accretion significantly changed the flow characteristics for a range of similar height shapes. Sharp faced edges in the direction of the flow produce larger performance losses and the downstream geometrical features have very little influence on the flow. On the other hand, shapes with leading edges that are more streamline are more favourable in terms of aerodynamic performance but the geometrical features aft of the point of separation have a larger effect on force coefficients. This represented a problem for the validation of the runback ice shapes used throughout this study. No experimental aerodynamic data for a full scale Boeing 737-700 airfoil with ice casting was available. A geometrical shape study based on the representative runback ice shapes created at the Cranfield Icing Tunnel was undertaken to highlight any possible similarities with other published data and confirm the observations for blunt and streamline accretions (Chapter 5.5).

Ice location and ice height are considered together. The performance variation has been shown to be linked with pressure distribution but boundary layer interaction was also shown to be important. Height of the runback ice was shown to be important and distinctions were made between tall and short ridges based on the size of the observed separated region. The chord location dictates the size of the boundary layer; Extensive studies suggest when the size of the boundary layer is comparable to the size of the ice height, Reynolds number becomes significant and boundary layer scaling techniques (if scaled) may be required. However further studies on the boundary layer scaling technique and its validity need to be ascertained as the only comprehensive analysis found on scaling methods for both geometrical and boundary layer scaling methods provided significantly different results and the mechanism for this required further work. The runback ice location optimisation study shown in Chapter 7.1 was run at full scale due to these observed scaling discrepancies. The optimisation process also offers the opportunity to provide some insight on boundary layer interaction with ice height. The optimiser surveyed the domain space which for ice location optimisation was the chord location of runback ice. The thickness of the boundary layer height changed with different chord locations. As the runback ice height remained constant, comparison of force coefficients against boundary layer thickness allowed observation of any obvious changes to flow properties.

Ice accretion aerodynamic tests on the validity of two-dimensional airfoil simulations relative to three-dimensional wing simulations were tested. The increase in induced drag from airfoil to wing was insignificant in comparison to the observed drag increase due to runback ice accretion. The results suggested the critical ice location trends seen for the two-dimensional airfoil simulation may be quantitatively extended to three-dimensional wings. More recent work also highlighted the prediction capabilities of two-dimensional airfoils to represent three-dimensional cases and found the force coefficient magnitudes are well predicted at low angles of attack; typically below 4° or before the separation bubble becomes large and unsteady. At higher angles of attack the literature suggested the flow was highly three-dimensional and detailed examination of an iced airfoil case would require high-fidelity analysis of the wing. This was attributed to the three-dimensional nature of vortices at the point of separation. The discrepancy with experimental data increased as the angle of attack was increased. For iced airfoil simulations at large angles of attack where the separation bubble can be characterised as unsteady, an unsteady RANS or LES/DES type solver are necessary to capture the complex flow. In the case of this study, the small separated regions at 3° angle of attack have been shown to be well predicted by CFD solvers.

Aerodynamic scaling of runback ice lead to a further categorisation of spanwise-ridge ice based on ice height relationships with separation bubble size. Tall and short ridge ice types were defined. Tall ice shapes depict large separated regions of flow whereas short ice shapes produce small separation bubbles very close to the ice shape.

Reynolds number effects were found to be less significant for iced airfoil flows. The transition to turbulence for a clean airfoil is dependent on Reynolds number. For iced airfoils, the location where separation occurs dictates transition and as such changes in Reynolds number do not yield a different separation point; having a small effect on the force coefficients.

3. Methods

"We must conduct research and then accept the results. If they don't stand up to experimentation, Buddha's own words must be rejected."

- Dalai Lama XIV

This chapter outlines the methods and general practises concerning the numerical modelling and optimisation. The chapter is broken down into the following sections:

- Pre-Processor
- Solver
- Post-Processor
- Turbulence Modelling
- Optimisation

3.1. Pre-Processor

The pre-processing stage consists of the inputs which define the flow problems. The numbers of steps to accurately define a problem for solvers are outlined below:

Computational Domain:

The environmental conditions dictate the size, shape and orientation of the computational domain. The dimensions of the computational domain required to simulate the Boeing 737-700 airfoil was 20c by 12c (Figure 3.1). The distance between the inlet and leading edge was 5c while the outlet was set 15c from the trailing edge of the airfoil.

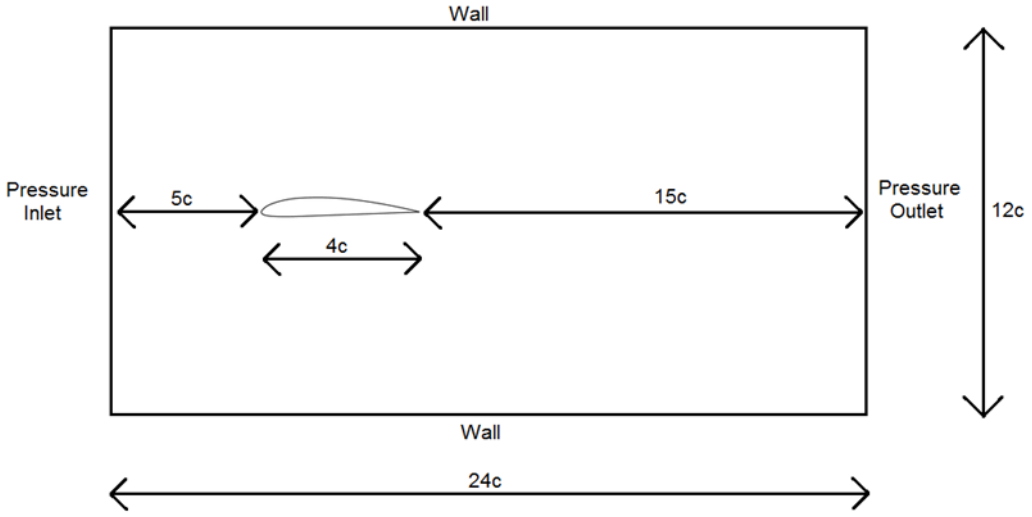

Figure 3.1: Boeing 737-700 Computational Domain

The computation domain size for a specific type of boundary condition, “pressure-far-field” is given by (FLUENT, 2009). However for other boundary condition types no precise values were available. Works by four authors were used to consider the extent of the computational domain, particularly the distance from the trailing edge of the airfoil to the outlet boundary normalised by chord lengths, c:

Works Title	T.E Outlet Boundary (c)	Reference
Robust Design Optimization of Airfoils with Respect to Ice Accretion	10	Ghisu, et al., [43]
Full-Scale Runback Ice: Accretion and Aerodynamic Study	10	Alègre [1]
RANS Simulations of Airfoils with Ice Shapes	20	Pan, et al., [44]
Detached Eddy Simulations for Iced Airfoils	20	Pan, et al., [29]

Table 3.1: Extent of Computational Domain Comparison

The average distance between the trailing edge of the ice shape the outlet boundary condition was 15 chord lengths with a range of 10 chord lengths. As such the distance between the trailing edge of the airfoil and the outlet boundary condition used was set to 15 chord lengths for all validation and optimisation runs.

Grid Generation:

In Computation Fluid Dynamics (CFD) the most important step in the overall process is grid generation. Partial Differential Equations (PDEs) are solved via discretisation methods using a mesh or grid. Although the regular mesh can be considered ideal, the quality of commercial solvers can cope with a variety of mesh types ranging from structured single blocks, multiblocks, hexcore hybrid and non-conformal interface. ANSYS FLUENT only accepts grid files using unstructured data storage algorithms. Although ANSYS ICEMCFD can create structured multiblock grids, when creating a mesh file specifically for ANSYS FLUENT, the data is stored using an unstructured algorithm.

A large proportion of time was invested in grid generation. The accuracy of the solver is dependent on the mesh quality and density particularly in key areas such as the boundary layer, separated zone behind the runback ice shape and trailing edge of the airfoil are very important. Increasing grid density improves the solver results (up to a limit) but at the cost of computational resource. The overall aim when developing the mesh was to achieve a grid independent

solution but to remain mindful that the size of the mesh would impact on the time taken to achieve a converged solution. This compromise was further intensified for this project as the mesh was to be implemented into an optimisation process. A typical optimisation process may run thousands of iterations exploring the global search space.

To accurately model the boundary layer around the airfoil, the grid was dense. The boundary layer thickness at the experimental location where the runback ice shape was placed was 2mm thick. Figure 3.2 demonstrates the mesh used to adequately modelled and capture the detailed geometrical features of the runback ice shape and the region of separated flow. The height of the hexcore was 80δ at the experimental runback ice chord location to allow for boundary layer growth and effects of airfoil shape changes.

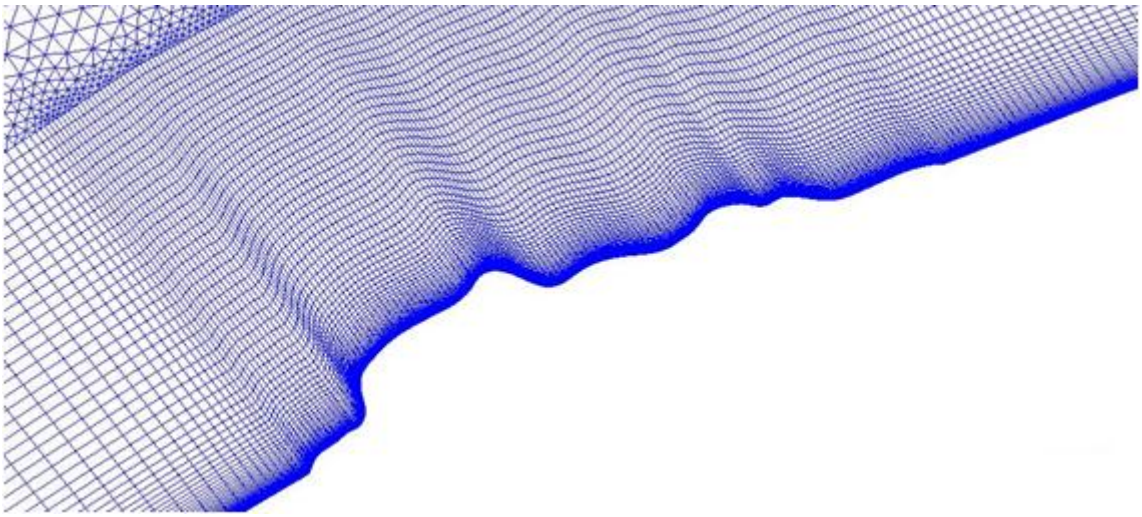

Figure 3.2: Hex-Core Mesh around Runback Ice

A number of grid types were available when considering the nature of the cell rather than the storage of the cell data; structured, unstructured and hybrid. Current grid generation tools allow the use of multiblock structured grids. For simple external flows, the structured multiblock grids produce accurate results. A downfall of multiblock type meshes were arbitrarily linked blocks which did not provide the flexibility required for complex geometries. For complicated geometries an unstructured or hybrid mesh was considered to be more appropriate.

The runback ice on the 4m Boeing 737-700 airfoil was five times larger than the boundary layer thickness. The representative runback ice produced complex shape and the local mesh density was refined to capture these minute changes in geometry. However, as stated, the multiblock structured grids were connected and the localised mesh density around the runback ice shape

propagated throughout the linked blocks. For ANSYS FLUENT to appropriately model the boundary layer and regions of separated flow, a structured quadrilateral (known as Hexa in ANSYS ICEMCFD) mesh was required. To appropriately model the boundary layer and overcome the propagation of cell density using a structured multiblock grid, a hex-core hybrid mesh was used. A hex-core hybrid mesh utilised a structured quadrilateral grid in the region around the airfoil and regions of separated flow with unstructured triangular cells to fill the remainder of the domain (Figure 3.3).

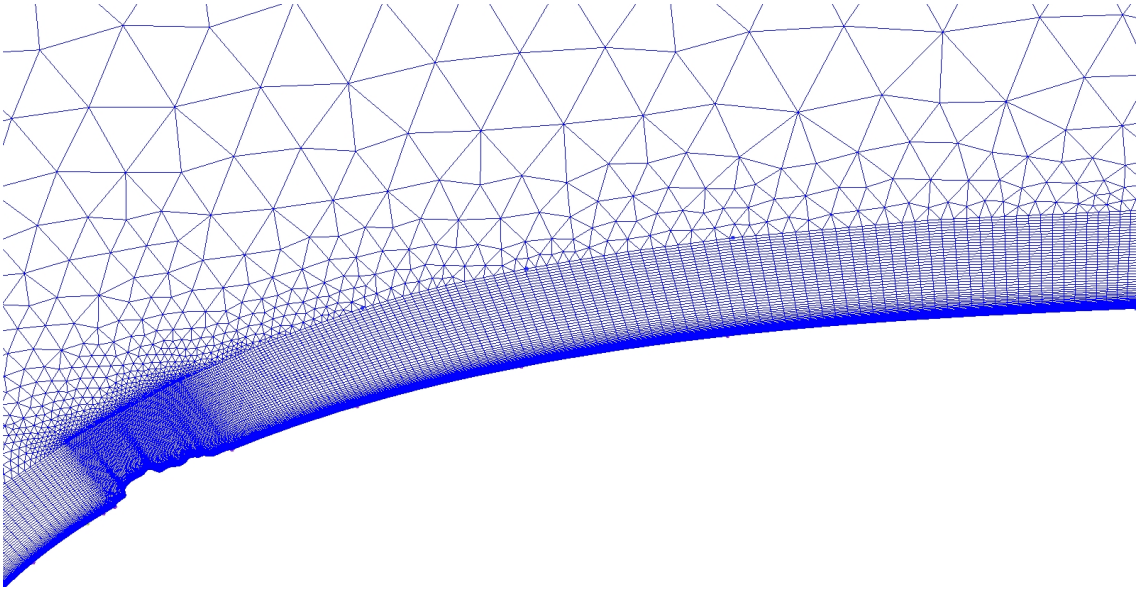

Figure 3.3: Hex-Core Hybrid Mesh Interface

During the mesh creation process an automated scripting file was required for use with the multi-objective Tabu Search optimiser (MOTS). ANSYS ICECFD utilised text files known as replay files (.rpl) to script the mesh creation process. Each user input was recorded and replayed at any given time. The MOTS code manipulated the replay file at each iterative step.

Careful creation and subsequent manipulation of a replay script was used to create a structured quadrilateral grid core. This process represented a significant amount of time. However the work done by Shaw [45] showed the model efficiency gained from investing time into creating a multiblock hybrid mesh was justified.

The entire replay script and ICEMCFD block creation was tailored to easily accept location changes for runback ice, airfoil shape changes and heat transfer input when introduced into the optimisation process.

The Hexa core was setup as a block of vertex points which were dependent on the runback ice location parameter input at the start of the script. This allowed the runback ice geometry to be placed anywhere along the airfoil. From this point the runback ice vertex points were rotated until the alignment of the ice shape matched the geometry of the airfoil (Figure 3.4).

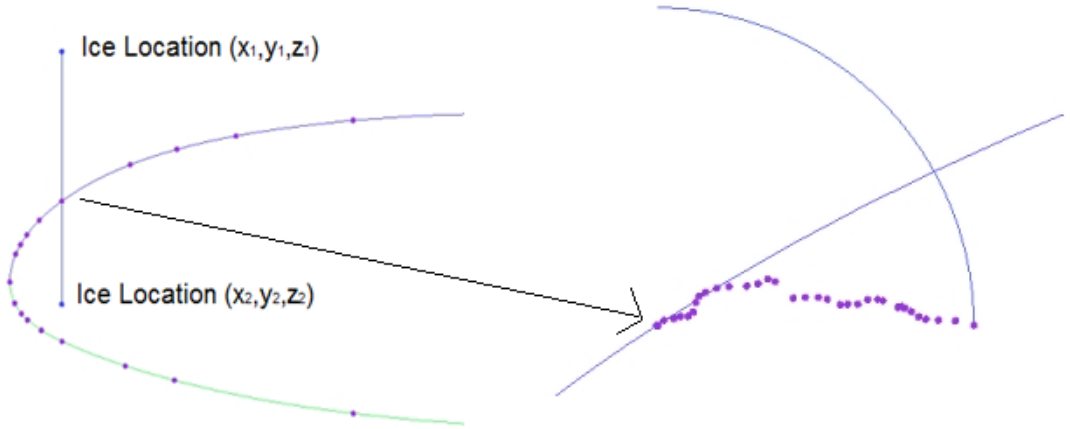

Figure 3.4: ANSYS ICEMCFD Replay Meshing Strategy 1

Once the runback ice shape was attached, the perimeter used to enclose the Hexa core was manipulated to create an isolated block around the runback ice shape. A secondary perimeter was created to control the changing density for the range of movement allowed (Figure 3.5).

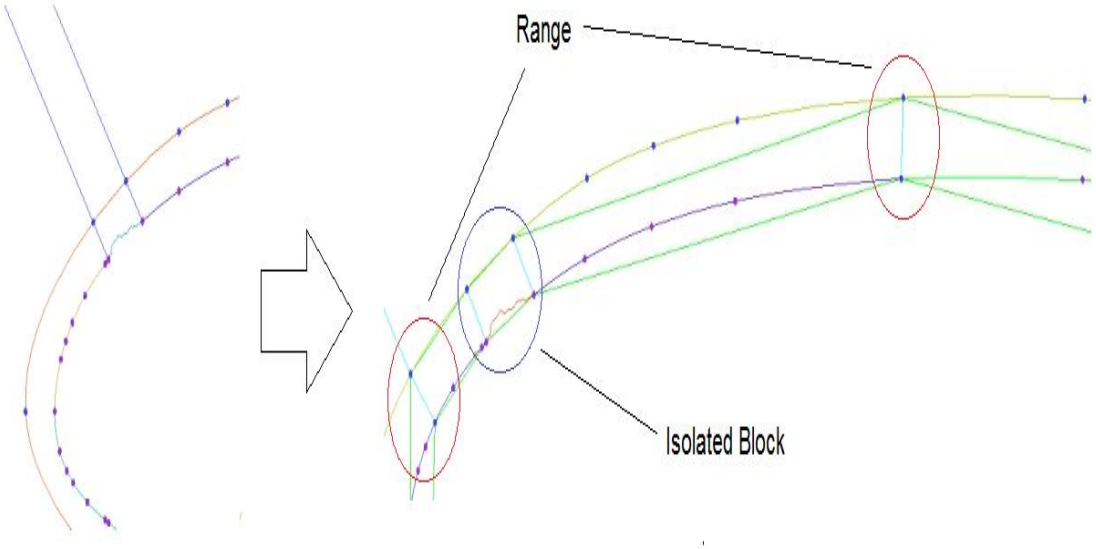

Figure 3.5: ANSYS ICEMCFD Replay Meshing Strategy 2

The original replay script required significant modification. The robustness of the script for a number of different optimisation projects was a methodical process which required testing of all variable extremes systematically during the replay

script creation. The accuracy of the type of mesh was also considered and the use of a structured and unstructured hybrid mesh was known to be particularly suited with the ANSYS FLUENT finite-volume solver [46].

Complicated geometries and near wall modelling required attention to detail when creating a structured grid. This region where the velocity gradients reach their maximum was the region of interest. The flow near the wall compromises laminar flow, a blending region where the flow is going through a transitional state followed by a fully turbulent region (Figure 3.6).

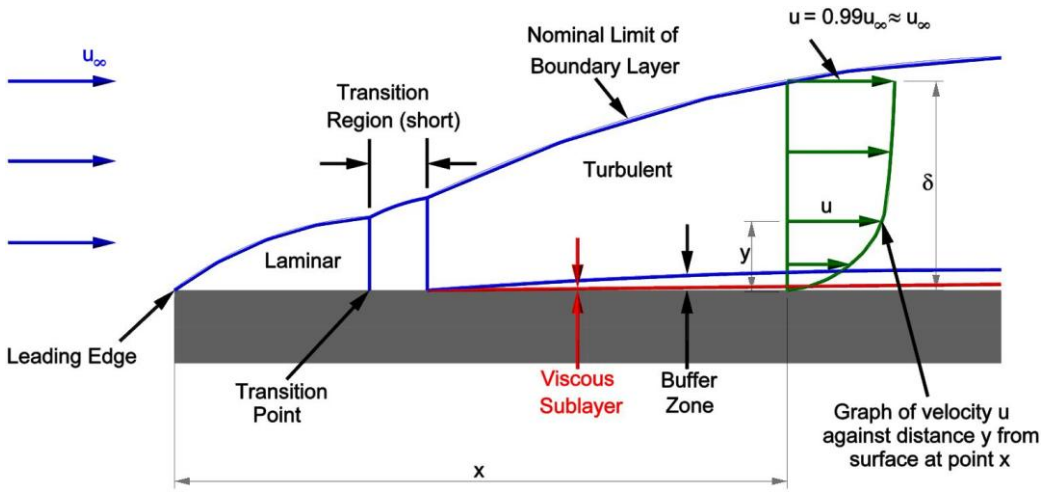

Figure 3.6: Transition to Turbulent Flow [47]

Correct development of structured mesh near the wall requires consideration of:

- Viscous Scale (y^+)
- Boundary Layer Thickness (δ)
- Geometrical Stretching Ratio (SR)

ANSYS FLUENT offers enhanced wall functions where the traditional two-layer model (low-Reynolds number meshes) can be combined with wall-function models where the mesh is not sufficiently fine. This type of near-wall modelling is particularly suitable for large three-dimensional meshes where refinement of the mesh up to the viscous sublayer is not possible. For this study the y^+ was set to be less than 1. It was deemed appropriate to model flow up to the viscous sublayer to fully capture the flowfield changes in the region of separated flow.

The $k-\omega$ SST turbulence model was used throughout the project and the boundary layer to be fully resolved. According to Menter [48] the first grid position must yield a y^+ value of less than 3 where the ANSYS FLUENT manual

[49] states a y^+ of less than 5. For all simulations conducted in this thesis, the y^+ was set to 1 and less than 3 at all times.

The size of the first cell was calculated using Equation 3.1:

$$y = \frac{y^+ \gamma}{u^*}$$

Equation 3.1: Wall Law

Where
$y^+ =$ Non-dimensional distance to wall
$\gamma =$ Kinematic viscosity (m^2s^{-1})
$u^* =$ Frictional Velocity (ms^{-1})

The frictional velocity u^* is unknown before the solution is solved and represented by Equation 3.2.

$$u^* = \left(\frac{\tau_w}{\rho}\right)^{1/2}$$

Equation 3.2: Frictional Velocity

Where
$\tau_w =$ Wall Shear Stress ($kgm^{-1}s^{-2}$)
$\rho =$ Density (kgm^{-3})

The wall shear stress is given by Equation 3.3:

$$\tau_w = \frac{1}{2} C_f^* \rho_\infty V_\infty^2$$

Equation 3.3: Wall Shear Stress

The compressible skin friction coefficient, c_f^*, using the reference temperature method is given below:

$$C_f^* = \frac{0.074}{(Re_x^*)^{1/5}}$$

Equation 3.4: Skin Friction Coefficient using Reference Temperature Method

Equation 3.4 represents the skin friction drag for an incompressible turbulent boundary layer on a flat plate. This was the appropriate correlation to use when working with airfoil boundary layers. An approximate engineering method for predicting skin friction for laminar compressible flow was developed in 1994 [50]. Essentially the incompressible flow formulas are utilised with a modification to the reference temperature. By extension, these approximations are also valid for turbulent incompressible to compressible flows [51].

With the ability to calculate the first cell size y^+ the geometrical boundaries needed to create an adequate structure encompassing the entire near wall region can be realised with and the boundary layer thickness δ:

$$\delta = \frac{0.37x}{Re_x^{1/5}}$$

Equation 3.5: Boundary Layer Thickness for Turbulent Flows

For optimum grid distribution within the boundary layer Spalart [52] states the stretching ratio (SR) should not exceed 1.2 because the Baldwin-Lomax model was shown to be sensitive to grid spacing. Although the $k-\omega$ SST model does not specifically require a stretching ratio of 1.2, it has become the standard for near wall treatment grid spacing. The key parameters to correctly model the near wall region were acquired. Table 3.2 highlights the values used to create the boundary layer hexa-mesh for the datum Boeing 737-700 airfoil in Chapter 5.

Reynolds Number (Re)	First Cell Size (y)	Stretching Ratio (SR)	Boundary Layer Thickness (δ)	Number of Grid Nodes in Boundary Layer
$2x10^7$	0.005mm	1.2	0.002m	46768

Table 3.2: Near Wall Modelling Meshing Parameters

A mesh dependency study was conducted to determine which mesh density provided the optimum grid where no significant change in the solution variables was found. For this project the force coefficient variations were observed with changing grid density. Quantitative analysis on the discretisation error associated with various meshes of different grid densities was found using the Grid Convergence Index (GCI) [53]. An overview and implementation of the GCI with a full mesh dependency study is outlined in Chapter 5.

Define Fluid Properties:

A critical parameter characterising the flow when simulating external aerodynamic flows was the freestream velocity. For this project the flow properties were defined by the EASA 45 minute hold case (Table 3.3):

Velocity (ms^{-1})	118
Altitude (m)	5181.6
Temperature (Celsius)	-9
Angle of Attack (degrees)	3

Table 3.3: Freestream Conditions for EASA 45 Minute Hold Case

The freestream velocity expressed in terms of Mach number was defined as the ratio of airplane speed and the speed of sound at altitude as shown in Equation 3.6.

$$M = \frac{V_\infty}{\left(\gamma R_{specific} T\right)^{1/2}}$$

Equation 3.6: Mach number for a Given Altitude

Where
V_∞ = Airplane Velocity
$R_{specific}$ = Gas Constant
T = Static Temperature

For the EASA 45 minute hold case the dimensionless Mach number was 0.347. When considering the compressibility of a fluid, the Mach number is the dominant parameter. For various ranges of Mach numbers, the following classifications are commonly used as a rough guide [54]:

Ma < 0.3 ⟶ Incompressible Flow ⟶ Density is negligible
0.3<Ma<0.8 ⟶ Subsonic Flow ⟶ Density effect important, no shock waves
0.8<Ma<1.2 ⟶ Transonic Flow ⟶ Shockwaves – Subsonic & Supersonic regions
1.2<Ma<3 ⟶ Supersonic Flow ⟶ Shockwaves with no subsonic region

The velocity defined Mach number for this project was categorised as high subsonic.

Specification of Boundary Conditions:

The numerical solver required the boundary conditions to be specified. ANSYS FLUENT provides 10 boundary zone types to specify the flow at the inlet and outlet. A pressure inlet and pressure outlet boundary condition was throughout this study. The pressure inlet boundary condition is one of many inlet conditions suitable for modelling compressible flow. A number of parameters must be defined in ANSYS FLUENT. The total pressure and total temperature for a compressible fluid is given by Equation 3.7 and Equation 3.8 respectively.

$$p_t = p_s \left(1 + \frac{\gamma - 1}{2} M^2\right)^{\gamma/(\gamma-1)}$$

Equation 3.7: Stagnation Pressure for a Compressible Fluid

$$\frac{T_t}{T_s} = 1 + \left(\frac{\gamma - 1}{2}\right) M^2$$

Equation 3.8: Total Temperature for a Compressible Fluid

Where
p_t = total pressure
p_s = static pressure
M = Mach number

T_t = total temperature
T_s = static temperature
γ = Ratio of specific heats $\left[\frac{c_p}{c_v}\right] = 1.4$

The numerical round-off problem for pressure calculations in ANSYS FLUENT arise when the overall pressure drop is small compared to absolute static pressure. As a consequence FLUENT avoids this problem by subtracting the operating pressure from the absolute pressure and using the result termed gauge pressure (Equation 3.9).

$$p_{abs} = p_{op} + p_{gauge}$$

Equation 3.9: ANSYS FLUENT Round-off Pressure Correction

For higher Mach number compressible flow the pressure changes are larger and no real round-off problem occurs. As FLUENT always uses gauge pressure the operating pressure is set to zero making the gauge pressure and absolute pressure equivalent.

The final parameter required to fully represent the pressure inlet boundary condition were the transported turbulence quantities. These quantities vary according the chosen turbulence model. The $k-\omega$ SST turbulence model required two terms to be solved; turbulent kinetic energy, k, and turbulent dissipation rate, ω.

The turbulent intensity parameter required as a percentage is defined in Equation 3.10.

$$I = \frac{u'}{U}$$

Equation 3.10: Turbulent Intensity Parameter [49]

Where
u'= root mean square if the turbulent velocity fluctuations
U = mean velocity

The turbulent length scale for boundary layer flows is given by Equation 3.11.

$$l = 0.4\delta_{gg}$$

Equation 3.11: Turbulent Length Scale for Boundary Layer Flows [49]

The following inputs were provided to describe the pressure outlet boundary condition used in ANSYS FLUENT:

- Static Pressure
- Static Temperature
- Backflow Conditions (Not required for this study)

The size of the computation domain modelled for the 4m Boeing 737-700 airfoil was sufficiently large and the inputs used for the pressure inlet were used to outline the pressure outlet fluid properties values.

3.2. Solver

The CFD software used dictates how the governing equations of fluid and heat transfer are solved. There are four mainstream numerical solutions techniques:

- Finite Difference
- Finite Element
- Finite Volume
- Spectral Methods

ANSYS FLUENT utilises the well known and thoroughly validated finite volume method [55]. The governing equations of fluid flow stipulate the following conservation equations:

Conservation of Mass: The mass of the fluid must be conserved.

Rate of increase of mass in fluid element	=	Net rate of flow of mass into the fluid element

The unsteady, three-dimensional mass conservation or continuity equation at any point in a compressible fluid is given by Equation 3.12.

$$\underbrace{\frac{\partial \rho}{\partial t}}_{\text{Rate of change in time of the}} + \underbrace{div(\rho u)}_{\text{Convective Term: Net flow of mass out of the element across its}} = 0$$

Equation 3.12: Unsteady Three-Dimensional Mass Conservation at a Point in a Compressible Fluid

Where:

$$div(\rho u) = \frac{\partial(\rho u)}{\partial x} + \frac{\partial(\rho v)}{\partial y} + \frac{\partial(\rho w)}{\partial z}^{1}$$

Equation 3.13: Divergence theorem Longhand Expression

Newton's Second Law: Rate of change of momentum of a fluid particle equals the sum of the force on the particle.

Rate of increase of momentum of fluid particle	=	Sum of all forces on fluid particle

It is common practise to present the conservative form of the momentum governing equation at any point in a compressible fluid as separate terms to highlight their individual contributions.

By considering the value of a property per unit mass φ, the total derivative with respect to time following a fluid is given by Equation 3.14.

$$\frac{D\varphi}{Dt} = \frac{\partial\varphi}{\partial t} + \frac{\partial\varphi}{\partial x}\frac{\partial x}{\partial t} + \frac{\partial\varphi}{\partial y}\frac{\partial y}{\partial t} + \frac{\partial\varphi}{\partial z}\frac{\partial z}{\partial t}$$

Equation 3.14: Total Derivative with Respect to Time for Property φ

Where $\frac{\partial x}{\partial t} = u$, $\frac{\partial y}{\partial t} = v$ and $\frac{\partial z}{\partial t} = z$ which reduces Equation 3.14 to:

$$\frac{D\varphi}{Dt} = \frac{\partial\varphi}{\partial t} + u.grad\ \varphi$$

Equation 3.15: Total Derivative with Respect to Time for Property φ

Using Equation 3.12 (Continuity equation) for an arbitrary conserved property provides an expression for the rate of change of φ per unit volume plus the net rate of φ out of the fluid volume element per unit volume:

$$\frac{\partial(\rho\varphi)}{\partial t} + div(\rho\varphi u) = 0$$

Equation 3.16: Continuity Equation for an Arbitrary Conserved Property

[1] The final component was not used throughout this project as all CFD simulations were two-dimensional. However for a full description of the governing equations and their subsequent transformation, the three dimensional terms are included.

The relationship between Equation 3.15 and Equation 3.16; between a fluid particle and a fluid element, is shown below:

$$\frac{\partial(\rho\varphi)}{\partial t} + div(\rho\varphi u) = \underbrace{\rho\left[\frac{\partial\varphi}{\partial t} + u.\,grad\,\varphi\right]}_{\frac{D\varphi}{Dt}} + \underbrace{\rho\left[\frac{\partial\varphi}{\partial t} + u.\,div(\rho u)\right]}_{=0}$$

Equation 3.17: Relationship between Fluid Particle and Fluid Element Expressed with Substantial Derivative

Equation 3.17 reduced to:

$$\underbrace{\frac{\partial(\rho\varphi)}{\partial t}}_{\text{Rate of increase of φ of fluid element}} + \underbrace{div(\rho\varphi u)}_{\text{Net rate of flow of φ out of fluid element}} = \underbrace{\rho\frac{D\varphi}{Dt}}_{\text{Rate of increase of φ of fluid particle}}$$

Equation 3.18: Relationship between Fluid Particle and Fluid Element Expressed with Substantial Derivative

Expression for momentum variant rather than just transported quantity in the x, y and z component in the generally used conservative form is given below.

$$\frac{\partial(\rho u)}{\partial t} + div(\rho u\boldsymbol{u}) = -\frac{\partial p}{\partial x} + div(\mu\ grad\ u) + S_{Mx}$$

Equation 3.19: Governing Equation for Momentum in Compressible Flow (x - Component)

$$\frac{\partial(\rho v)}{\partial t} + div(\rho v\boldsymbol{u}) = -\frac{\partial p}{\partial y} + div(\mu\ grad\ v) + S_{My}$$

Equation 3.20: Governing Equation for Momentum in Compressible Flow (y - Component)

$$\frac{\partial(\rho w)}{\partial t} + div(\rho w\boldsymbol{u}) = -\frac{\partial p}{\partial z} + div(\mu\ grad\ w) + S_{Mz}$$

Equation 3.21: Governing Equation for Momentum in Compressible Flow (z - Component)

First Law of Thermodynamics: Rate of change of energy equals the sum of the rate of heat addition to the work done on a fluid.

Rate of increase of energy of fluid particle	=	Net rate of heat added to a fluid particle	+	Net rate of work done on the fluid particle

The internal energy equation is solved when the temperature of a fluid must be computed, as in the case for compressible flow, and shown in conservative form in Equation 3.22.

$$\frac{\partial(\rho i)}{\partial t} + div(\rho i \boldsymbol{u}) = -p\ div\ \boldsymbol{u} + div(k\ grad\ T) + \phi + S_i$$

Equation 3.22: Governing Equation for Energy in Compressible Flow

With the governing differential equations established, the domain is broken up into small control volumes where the variable concerned is stored at the cell centre (Figure 3.7).

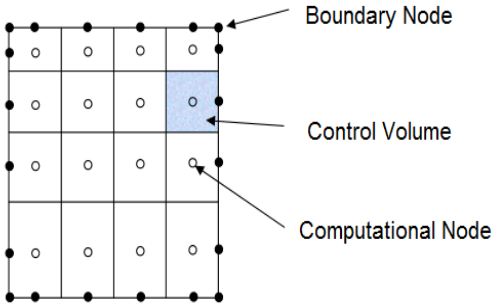

Figure 3.7: Control Volume Schematic [56]

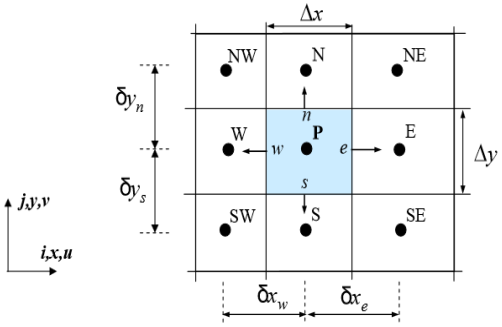

Figure 3.8: Control Volume Net Flux Illustration [56]

Figure 3.8 illustrates that the net flux through the control volume, P, is the sum of the integrals (for governing differential equations) over the control volume faces (four or six for two-dimensions and three-dimensions respectively). At this point the evaluation of the variables concerned is at the cell centre whereas the finite volume method requires variable values at the control volume faces.

ANSYS FLUENT offers a number of numerical schemes to interpolate the integrand value from the cell centre to the control volume faces:

- First-Order Upwind Scheme
- Power-Law Scheme
- Second-Order Upwind Scheme
- QUICK Scheme
- Central-Differencing Scheme

The differencing scheme accuracy used throughout this project was the second-order upwind scheme. All CFD solutions were started as first-order but solutions were converged to second-order accuracy.

The first-order upwind scheme is the simplest of numerical schemes. Leading on from Figure 3.8, the cell-centre can be assumed to hold a value, φ. This scheme assumes the value at the face of the control volume cell is the same as the cell-centre value of the upstream cell (Figure 3.9).

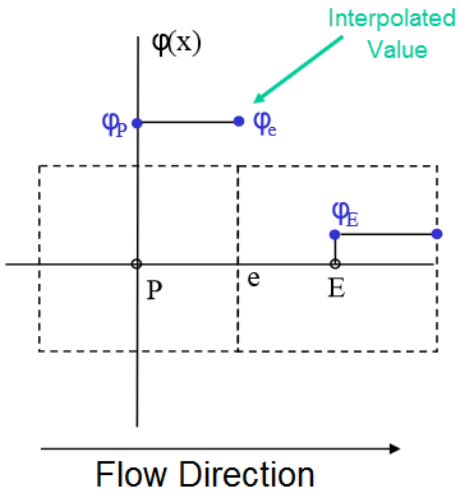

Figure 3.9: First-Order Upwind Scheme Illustration [56]

The advantages of this type of numerical scheme are easy implementation and solution stability. The disadvantages are the diffusive nature of solution caused by large gradients in the flow field being smoothed out [56].

When the domain allows for simple meshes where the flow is aligned with the cells; first-order accuracy can be deemed acceptable. However when the cells are not aligned with the mean flow (tri/tet meshes are never aligned with mean flow) the first-order convective discretisation increases the numerical discretisation error (numerical diffusion).

ANSYS FLUENT implements a multidimensional linear reconstruction approach as the second-order spatial discretisation scheme [57]. The higher order accuracy was achieved by using a Taylor series expansion on the cell-centre value. The cell face value φ_e, is found by computing the average of φ from the two adjacent cell-centres ($\varphi_e$and φ_w) as shown in Figure 3.10.

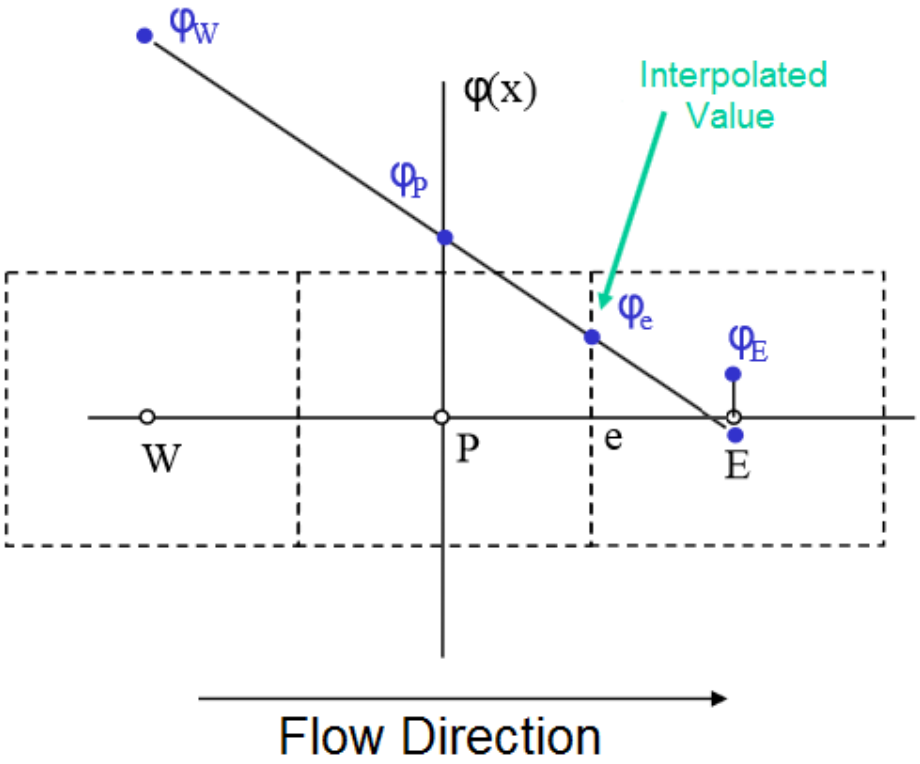

Figure 3.10: Second-Order Upwind Scheme Illustration [56]

Upon application of the upwind numerical scheme, the integral is converted into a system of linear algebraic equations. The discretisation process yields the general transport equation for an unknown variable in linearised form (Equation 3.23):

$$a_p \phi = \sum_{nb} a_{nb} \phi_{nb} + b$$

Equation 3.23: Linearised Form of General Transport Equation for Unknown Variable

Where
ϕ= Scalar Variable
nb= Neighbouring cells
a= Area of Control Volume
a_p and a_{nb}= linearised Coefficients for ϕ and ϕ_{nb}
With the fluid properties specified and a system of algebraic equations, ANSYS FLUENT offers two solvers suitable for compressible ideal gas:

- Pressure-Based Solver
- Density-Based Solver

Traditionally the choice of solver was dependent on the fluid compressibility. However current commercial solvers are now applicable for a broad range of flows from incompressible to highly compressible.

Pressure-based solvers were originally intended for incompressible and mildly compressible flows, whereas density-based approach was originally intended for high-speed compressible flows.

Since the flow properties associated with the EASA 45 minute hold condition were considered as a mildly compressible flow, the pressure-based solver was used throughout this study.

When using a pressure-based solver, ANSYS FLUENT options for pressure-velocity coupling algorithms are:

- SIMPLE
- SIMPLEC
- PISO
- Fractional Step

} Segregated

- Coupled

The flow chart in Figure 3.11 illustrates the difference between the segregated and coupled solver. In the case of the coupled solver, there is no need for the separate pressure correction step, as the continuity, momentum and energy equations are solved simultaneously.

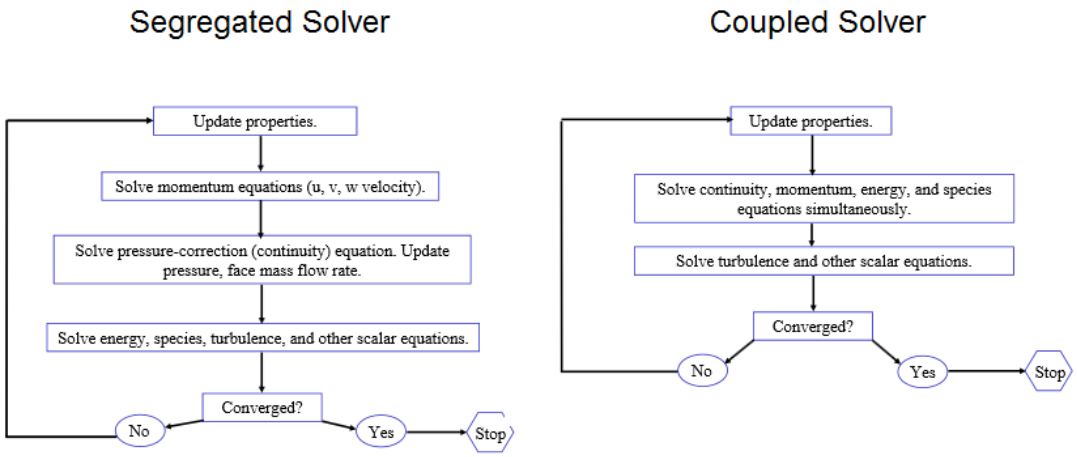

Figure 3.11: Comparison of Pressure-Velocity Coupling Algorithms [56]

Section 18.4.3 of the ANSYS FLUENT Theory Guide shows that solving the momentum and pressure-based continuity equations together (coupled-solver) rather and in a semi-implicit manner results in faster convergence times [58]. To this end a coupled pressure-velocity algorithm was used throughout this study.

ANSYS FLUENT utilises an Algebraic multigrid (AMG) to achieve full implicit coupling. An algebraic multigrid is used in conjunction with iterative solver which has a tendency to stall. Since convergence is a function of the gradient in error from node to node (or control volume to control volume), a fine mesh error distribution has a high frequency which has fast convergence for the first few iterations and as the error field is smoothed out the convergence rate deteriorates (stall). To alleviate this problem, the algebraic multigrid code, coarsens the mesh so the low frequency error of the fine mesh would then be seen as a high frequency error.

The advantages of using an AMG are faster convergence rates and effectiveness of the iterative solver is improved with each coarsening step. This is especially true for Jacobi and Gauss-Seidel solvers. The rate of convergence is further improved as the coarse level equations are generated without the need of the geometry or re-discretisation from the previous levels. This is particularly useful for unstructured grids as a coefficient matrix is used to perform the agglomeration (a combination of several control volumes from the original grid) instead of at the node on a geometrical level.

The stability and final solution is found using relaxation factors and monitoring the changes in a variable with each successive iteration (convergence) respectively.

When using a pressure-based coupled algorithm, ANSYS FLUENT offers both explicit (variables) and implicit (equations) under-relaxation. The use of explicit relaxation is required as the change in ϕ needs to be controlled due to the non-linearity of the equation being solved. Equation 3.24 simply reduced the change in ϕ with each iteration. Therefore the new value of ϕ is dependent on the old value of ϕ, ϕ_{old} and the computed change in ϕ, $\Delta\phi$.

$$\phi = \phi_{old} + \Delta\phi$$

Equation 3.24: ANSYS FLUENT Explicit Relaxation for Pressure-Velocity Coupled Algorithm

The implicit under-relaxation is used to stabilise the convergence behaviour of the outer non-linear iterations by introducing selective amounts of ϕ in the system of discretised equations with the introduction of the under-relaxation factor $\propto$.

$$\frac{a_p \phi}{\propto} = \sum_{nb} a_{nb} \phi_{nb} + b + \frac{1-\propto}{\propto} a_p + \phi_{old}$$

Equation 3.25: ANSYS FLUENT Implicit Relaxation for Pressure-Velocity Coupled Algorithm

The criteria for a converged solution vary significantly. Factors such as accuracy required, initial guess of flow field and the environment the variable of interest to name a few. The final solution was found via an iterative process. For a steady state simulation, the initial flow field is based on the boundary conditions. As the simulation starts, flow field parameters fluctuate and a solution is found when these fluctuations stop. The definition of a scaled residual for a pressure-based solver is shown in Equation 3.26.

$$R^{\emptyset} = \frac{\sum_{cell\ P} \left| \sum_{nb} a_{nb} \emptyset_{nb} + b - a_p \emptyset_p \right|}{\sum_{cells\ P} \left| a_p \emptyset_p \right|}$$

Equation 3.26: Scaled Residuals equation for ANSYS FLUENT Pressure Based Solver

Where $\emptyset$ is the general variable, a_p is the centre coefficient, a_{nb} are the influences for the neighbouring cells. The denominator is the scaling factor used to represent the flow rate of the general variable through the domain. ANSYS FLUENT allows users to monitor scales residuals of equations such as continuity (Figure 3.12).

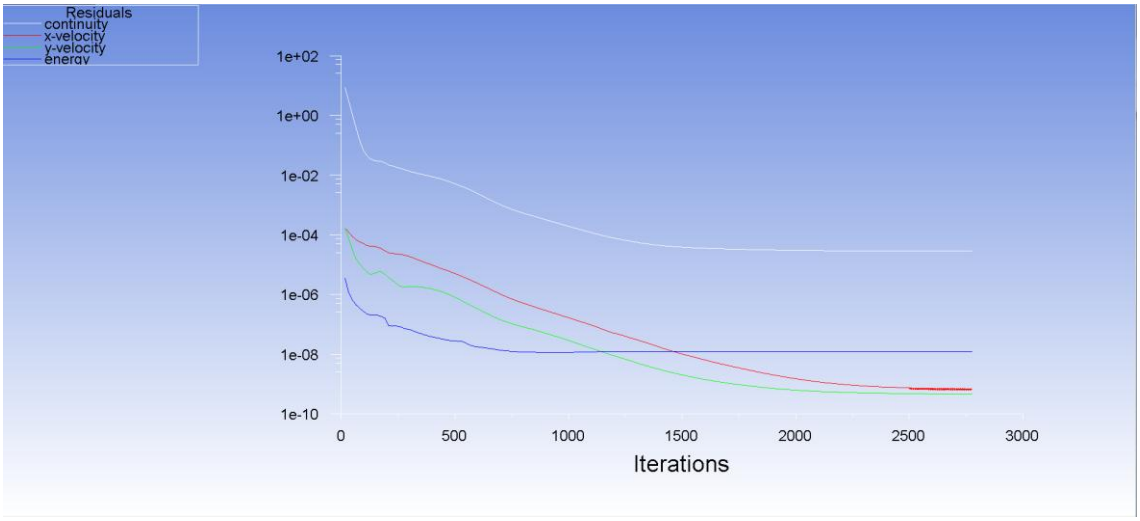

Figure 3.12: ANSYS FLUENT Scaled Residuals for B737-700 Clean Configuration

As a guideline for aerodynamic flows a reduction of the order of 3 - 4 magnitudes is deemed sufficient. This can be taken as one of the indicators that a solution has converged however, as stated earlier, a good initial guess may not yield 3-4 orders of reduction from an initial starting point. An aerodynamic study generally entails the output of force coefficients such as lift, drag and

moment. A good indicator of a converged solution can be found by monitoring the fluctuations in the force coefficients (Figure 3.13).

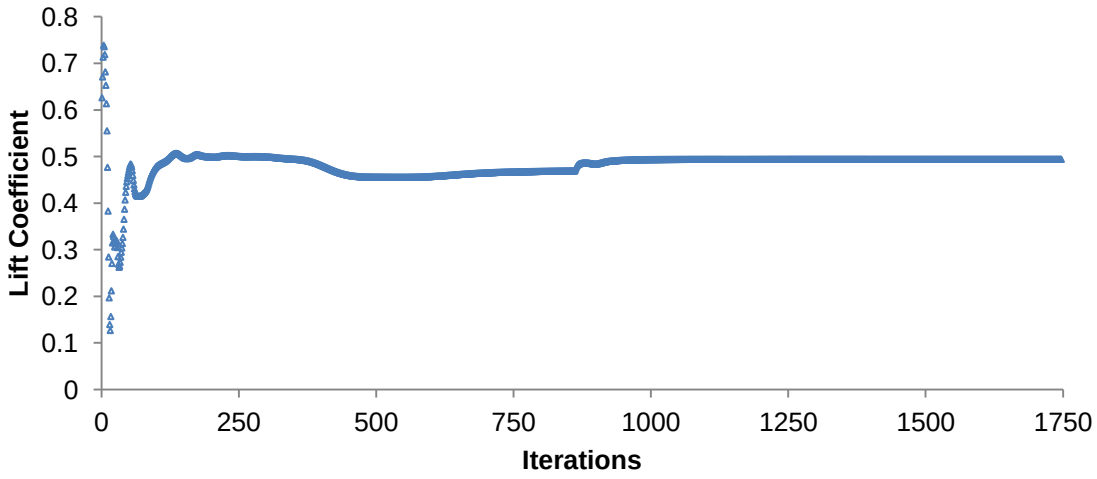

Figure 3.13: Lift Coefficient Fluctuations for B737-700 Clean Configuration

3.3. Post-Processor

Post-processing capabilities built into the ANSYS FLUENT package have improved dramatically with excellent graphical capabilities and a number of visual tools. Alongside the abundant options for qualitative data, ANSYS FLUENT offers quantitative reports on:

- Fluxes
- Forces
- Projected areas
- Surface and volume integrals

The lift, drag and moment coefficients are of particular interest for airfoil external aerodynamic flows. Section 20.2.1 of the ANSYS FLUENT Theory Guide outlines the procedure for computing forces and moments. The total force component along the specified force vector, $\vec{a}$, on a wall zone are calculated by summing the dot product of the pressure and viscous forces. For lift and drag coefficients, the total force component for the respective forces is divided by $1/2\,\rho A V^2$ where ρ, V and A are density, velocity and area respectively. The specifications of these variables are set in the ANSYS FLUENT reference value GUI panel.

The total moment is specified using the cross product of pressure and viscous forces at each face using the moment vector, $\overrightarrow{r_{AB}}$. The moment vector is the vector for the specified moment centre,A, to the force origin, B (Equation 3.27).

$$\underbrace{M_A}_{\text{Total Moment}} = \underbrace{\overrightarrow{r_{AB}} \times \vec{F}_p}_{\text{Pressure Moment}} + \underbrace{\overrightarrow{r_{AB}} \times . \vec{F}_v}_{\text{Viscous Moment}}$$

Equation 3.27: Total Moment Component Extrapolation [58]

The moment coefficient is defined as the moment divided by $1/2\,\rho ALV^2$ where the additional variable of length, L is added.

The Anti Icing Optimisation study in Chapter 7.4 used the heat transfer coefficient for comparison. Neale, et al., [59] provided a validation and comparative study of heat transfer coefficients calculated using different turbulence models implemented in ANSYS FLUENT. All heat transfer simulations conducted in this study followed the published methods by [59]. Accordingly the key parameter was the dimensionless heat transfer coefficient temperature used by ANSYS FLUENT shown in Equation 3.28.

$$T^+ = \frac{T_w - T_\infty}{T^*}$$

Equation 3.28: Dimensionless Heat Transfer Coefficient Temperature

Where

T_w = Wall Temperature
T_∞ = Freestream Temperature at Inlet

$$T^* = \frac{\alpha q_w}{k u^*}$$

Equation 3.29: Reference Temperature

Where
α = Thermal Diffusivity
q_w = Convective and Radiative Wall Heat Flux
k = Thermal Conductivity

$$u^* = \sqrt{\frac{\tau_w}{\rho}}$$

Equation 3.30: Reference Velocity

Equation 3.31 defines the surface heat transfer coefficient as computed by ANSYS FLUENT:

$$h = \frac{q_W}{T_W - T^+}$$

Equation 3.31: Heat Transfer Coefficient

where

T^+ = Reference Temperature given in Equation 3.28.

The application of the reference temperature can be found in the Anti Icing Optimisation Chapter 7.4.

3.4. Turbulence Modelling

This section outlines the physical process of turbulence with some historical perspective and how this effects the governing equations of flow. A discussion on the turbulence models used throughout this project alongside a critical overview of the turbulence model robustness is also provided.

3.4.1. Introduction

Turbulent behaviour is arguably the most important unresolved problem of classical physics[2]. The need to fully understand the nature of turbulent flows must be considered paramount as most fluid flow problems are turbulent and in many cases represent the dominant physics. The problem can be considered universal affecting all macroscopic scales from the interior of biological cells through to stellar physics; used to predict stellar boundary layer turbulent entrainment [60].

Since then many great physicist and engineers of the 19th and 20th century contributed to the turbulence problem but no complete understanding of how or why turbulence occurs has been found. However a vast improvement in modelling turbulent behaviour provides a platform to build upon. According to Sinobar, [61], there is no good definition of turbulence and this may remain the case until turbulent flows are more fully described. However the properties associated with turbulent flows are well documented and outlined:

Irregularity:
Turbulent flows are irregular with respect to space and time.

Unpredictability:
Turbulent flows display unpredictable and random patterns.

[2] Richard Feynman, the great *Nobel* Prize-winning physicist of 1965, called *turbulence* "the most important *unsolved* problem of *classical* physics."

Wide Range of Active Length Scales:

Turbulent flows exhibit rotational flow structures (turbulent eddies) with a wide range of length scales.

Vortex stretching:

The largest eddies interact with the mean (freestream) flow and extract energy. This interaction causes the fluid portion to thin down and become elongated; hence the name vortex stretching. This portion of the fluid folds and intertwines with other eddies within the boundary layer. The largest eddies characteristic velocity and length can be considered to be the same order as the mean flow. Accordingly the Reynolds number for the mean flow and the largest eddies is similar:

$$Reynolds\ Number = \frac{UL}{v}$$

Equation 3.32: Reynolds Number

$$'Large\ Eddy'\ Reynolds\ Number = \frac{\vartheta l}{v}$$

Equation 3.33: 'Large Eddy' Reynolds number

Where $U \approx \vartheta$ and $L \approx l$.

From the above relation, it becomes clear the largest eddies are dominated by inertia effects and viscous effects are negligible. This means we can consider the larger eddies as effectively inviscid and thus angular momentum is conserved. For angular momentum to remain conserved, the increased velocity the larger eddies 'absorbed' from the mean flow requires a reduction in the radius of their cross-sections. When considering this effect on the bulk motion of turbulent flow, these larger eddies intrinsically take swirling motions with reducing radius and smaller time scales.

Figure 3.14: Image of Turbulence from Tip Vortex [47]

The larger turbulent eddies transfer their kinetic energy to somewhat smaller eddies, which in turn pass their kinetic energy into even smaller eddies. This process continues until the characteristic length/velocity reduces the Reynolds number to 1. At this point viscous forces dominate the flow and the kinetic

energy becomes dissipated and converted into thermal internal energy (Figure 3.15). This accounts for the increases losses due to turbulent flow.

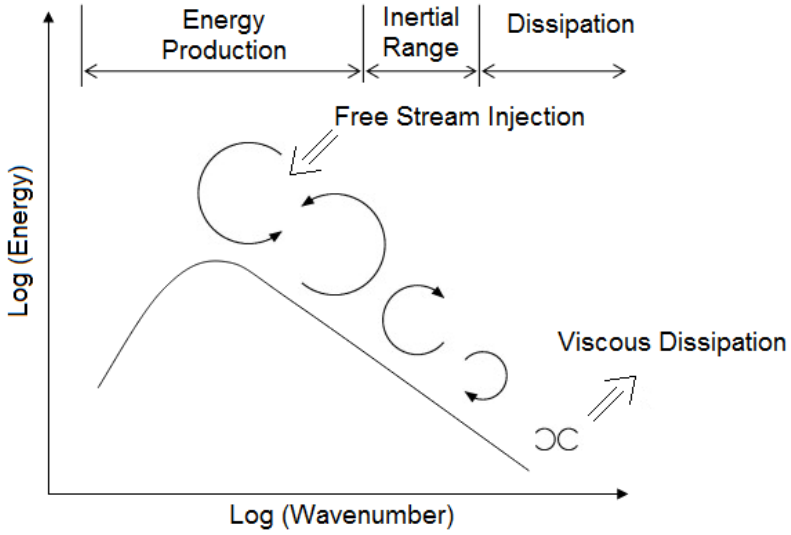

Figure 3.15: Turbulent Eddy Energy Transfer

3.4.2. Transition to Turbulence

The circumstance under which a steady laminar flow becomes unstable and develops into unsteady turbulent flow is of great interest for practical applications of flow phenomenon. This extraordinarily complex process is covered very briefly and a detailed guide can be found by Schlichting, [62]. The delaying of laminar to turbulent transition can be of considerable advantage as the skin friction drag for laminar flow can be up to an order of magnitude less than in a turbulent state [63]. Conversely, turbulent flows exhibit efficient mixing useful for heat exchangers in combustors and enhanced heat transfer. The theory behind laminar-turbulent transition is not fully understood. The engineering benefits to be had from careful manipulation of the transition point has lead to years of exhaustive research culminating in a series of stages outlining the transition to turbulence for a flat plate [64]:

Distortion of T-S waves: Linear instability occurs around $Re_{x,crit} = 91000$. Unstable two-dimensional disturbances called Tollmien-Schlichling (T-S) waves occur. Larger, secondary, non-linear instabilities cause T-S waves to become three-dimensional.
Hairpin Vortices: K-type transition is common where hairpin vortices are aligned.
Emmons Spots: Small triangular shapes turbulent spots burst.

Merging of Emmons Spots: The Emmons spots convect in wedge shape regions downstream and eventually fuse together to encompass the entire boundary layer.
Fully Turbulent Flow: The above process leads to fully turbulent flow.
The complexity associated with modelling the laminar- turbulent transition was not the objective of the project. After discussions with the sponsors (Airbus), the numerical models were assumed to be fully turbulent. For runback ice simulations, one can consider that the upstream disturbances due to liquid droplets would trip early transition to turbulent flow. For a Reynolds number typical of subsonic flight the free-shear layer, when flow separation has occurred, can be considered fully turbulent in a small fraction of step height downstream [65]. To this end, the assumption for a fully turbulent regime was deemed reasonable. For commercial CFD codes, general practices assume the errors incurred by neglecting the transitional region are small considering the size of the transitional zone relative to the size of the domain [62].

3.4.3. Turbulence and Governing Equations

The characteristics and onset of turbulent flows have been outlined. The governing (Navier-Stokes) equations represent the transport equations for instantaneous flow quantities. Experimental data on turbulent flows revealed complex motions are due to vortex stretching and an extensive range of turbulent eddy length scales. It is not feasible to resolve all length scales with current computing resources and is sometimes unnecessary. Instead the time-averaged properties of the mean flow can be resolved and incorporated into the existing governing equations; Reynolds averaging of the Navier-Stokes equation.

The typical velocity measurements using a hotwire probe for turbulent flows exhibits the form shown in Figure 3.16.

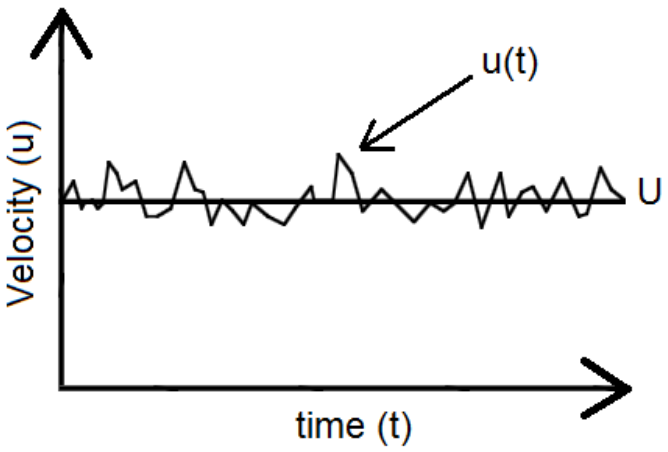

Figure 3.16: Typical Hotwire Probe Turbulent Velocity Fluctuation

Instead of trying to capture the complete description of the flow Reynolds, [66] suggested that the variables in the Navier-Stokes equations could be decomposed into steady mean values with a fluctuating term. The velocity components and by extension other scalar components are shown in Equation 3.34 and Equation 3.35:

$$u = U + u'$$

Equation 3.34: Mean and Fluctuating Velocity Components

$$\phi = \bar{\phi} + \phi'$$

Equation 3.35: Mean and Fluctuating Scalar Components

Substitution of these expressions into the continuity and momentum equations and taking the time (or ensemble) average yields the Reynolds Averaged Navier-Stokes (RANS) equation:

$$\frac{\partial \rho}{\partial t} + \ div(\rho U)$$

Equation 3.36: Continuity Equation for Turbulent Compressible Flow

$$\frac{\partial(\rho U)}{\partial t} + div(\rho U \boldsymbol{U}) = -\frac{\partial P}{\partial x} + div(\mu \ grad\ U) + \underbrace{\left[-\frac{\partial\left(\rho\overline{u'^2}\right)}{\partial x} - \frac{\partial\left(\rho\overline{u'v'}\right)}{\partial y} - \frac{\partial\left(\rho\overline{u'w'}\right)}{\partial z} \right]}_{\text{Reynolds Stress Tensor}} + S_{Mx}$$

Equation 3.37: Governing Equation for Momentum in Turbulent Compressible Flow (x - Component)

$$\frac{\partial(\rho V)}{\partial t} + div(\rho V \boldsymbol{U}) = -\frac{\partial P}{\partial y} + div(\mu \ grad\ V) + \left[-\frac{\partial(\rho\overline{u'v'})}{\partial x} - \frac{\partial\left(\rho\overline{v'^2}\right)}{\partial y} - \frac{\partial(\rho\overline{v'w'})}{\partial z} \right] + S_{My}$$

Equation 3.38: Governing Equation for Momentum in Turbulent Compressible Flow (y - Component)

$$\frac{\partial(\rho W)}{\partial t} + div(\rho W \boldsymbol{U}) = -\frac{\partial P}{\partial z} + div(\mu \ grad\ W) + \left[-\frac{\partial(\rho\overline{u'w'})}{\partial x} - \frac{\partial(\rho\overline{v'w'})}{\partial y} - \frac{\partial\left(\rho\overline{w'^2}\right)}{\partial z} \right] + S_{Mz}$$

Equation 3.39: Governing Equation for Momentum in Turbulent Compressible Flow (z - Component)

Where

$$\boldsymbol{u} = \boldsymbol{U} + \boldsymbol{u}';\ \ u = U + u';\ \ v = V + v';\ \ \ w = W + w';\ \ \ p = P + p'$$

The addition term relative to the compressible Navier-Stokes equations represents the effects of the turbulence Reynolds stresses. For compressible flow the velocities are representing mass averaged values and can be interpreted as Favre-averaged Navier-Stokes equations [67].

The instantaneous Navier-Stokes equation required additional information to form a closed set of four equations with 4 unknowns, u, v, w and p. These were provided by the equation of state (for compressible flow).

When incorporating the Reynolds averaging for turbulent compressible flow, the Reynolds stress tensor term appears in the Navier-Stokes equation. The Reynolds Stress tensor is a symmetrical equation incorporating six unknowns allowing the turbulent stresses to enhance the momentum transport in the mean flow. This leads to a new closure problem and the development of turbulence models to provide a mathematical framework to determine these Reynolds stresses.

3.4.4. Turbulence Models

A turbulence model is essentially a computational procedure to provide expressions for the Reynolds stresses and turbulent scalar transport terms. The RANS approach requires Reynolds stresses to be appropriately modelled. Solving the transport equation for each term in the Reynolds stress tensor would add five addition transport equations in two-dimensions and seven transport equations in three-dimensions. A common method employed by the S-A, $k-\varepsilon$ and $k-\omega$ models is the Boussinesq hypothesis which relates the Reynolds stresses to the mean rate of deformation. It was experimentally observed that:

- Turbulence decays unless there is shear in isothermal incompressible flows
- Turbulence was found to increase as the mean rate of deformation increases

Based on these observations the hypothesis states the Reynolds stresses are proportional to the mean flow strain rate with the introduction of a proportionality factor; turbulent viscosity also known as eddy viscosity. Using this approximation negates the need to solve six turbulent stresses (in two-dimensions).

It should be noted that turbulent viscosity is a property of flow and not the fluid. The turbulence viscosity assumes a relationship between the molecular and turbulent motion. However the turbulent viscosity is assumed to be isotropic; the relationship between the Reynolds stresses and the mean rate of deformation is the same in all directions. Based on the constraints of kinetic gas theory, the turbulent eddies cannot be considered as rigid bodies nor their mean free paths small compared to the size of the eddy. Even though these assumptions cast

doubt on the turbulent viscosity concept, reasonable results for a large range of flow problems can be found. These assumptions become apparent for flows with strong separation or swirls and in these cases all Reynolds stresses must be solved. The turbulent viscosity parameter allows the momentum equations to be closed.

Similar to the concept of turbulent viscosity, the turbulent heat or mass transport can be assumed to be proportional to the gradient of the transported quantity with a proportionality factor; Turbulent diffusivity. The turbulent diffusivity is also a function of the flow and not the fluid. The Reynolds analogy suggests the turbulent diffusivity is a function of turbulent viscosity:

$$\Gamma = \frac{\nu_t}{\sigma_t}$$

Equation 3.40: Turbulent Diffusivity

Where:

ν_t= Kinematic Turbulent Viscosity

σ_t= Turbulent Prandlt (Schmidt) Number

There are a number of turbulence models available to predict the turbulent viscosity. The following models are discussed due to their use in this thesis:

- Spalart-Allmaras one-equation turbulence model
- Shear Stress Transport (SST) $k-\omega$ Model

Spalart-Allmaras one-equation Turbulence Model

Spalart-Allmaras is a one-equation turbulence model developed mainly for aerodynamic flows [68]. This model is well known for accurate prediction of airfoil aerodynamics with good prediction of separated flows due to adverse pressure gradients.

The S-A model solves a single transport equation for turbulent viscosity. This transport equation contains convective and diffusive transport terms as well as expressions for the production and dissipation of the kinematic eddy (turbulent) viscosity:

$$\frac{\partial}{\partial t}(\rho\tilde{\nu}) + \frac{\partial}{\partial x_i}(\rho\tilde{\nu}u_i) = G_\nu + \frac{1}{\sigma\tilde{\nu}}\left[\frac{\partial}{\partial x_i}\left\{(\mu+\rho\tilde{\nu})\frac{\partial\tilde{\nu}}{\partial x_j}\right\} + C_{b2}\rho\left(\frac{\partial\tilde{\nu}}{\partial x_j}\right)^2\right] - Y_\nu + S_{\tilde{\nu}}$$

Equation 3.41: Transport Equation for the Spalart-Allmaras Model

Where
G_v =Production of turbulent viscosity
Y_v = Destruction of turbulent viscosity that occurs in near-wall region due to wall blocking and viscous damping
$\sigma\tilde{v}$ and C_{b2} = Constants
v = Molecular kinematic viscosity

SST Transport Equation for $k-\omega$ Model

The shear-stress transport (SST) $k-\omega$ model was developed to blend two existing two-equation turbulence models by Menter, [48]. The $k-\omega$ model by Wilcox, [69] is utilised near the wall and the well established and robust $k-\varepsilon$ model by Launder and Spalding, [70] in the freestream. The turbulence kinetic energy, k, and specific dissipation rate, ω, are obtained from the transport equations shown in Equation 3.42 and Equation 3.43.

$$\frac{\partial}{\partial t}(\rho k)+\frac{\partial}{\partial x_i}(\rho k u_i)=\frac{\partial}{\partial x_j}\left(\Gamma_{\mathrm{k}}\frac{\partial k}{\partial x_j}\right)+\widetilde{\mathrm{G}}_{\mathrm{k}}+\mathrm{Y}_{\mathrm{k}}+\mathrm{S}_{\mathrm{k}}$$

Equation 3.42: SST Transport Equation for Turbulence Kinetic Energy

$$\frac{\partial}{\partial t}(\rho\omega)+\frac{\partial}{\partial x_i}(\rho\omega u_i)=\frac{\partial}{\partial x_j}\left(\Gamma_{\omega}\frac{\partial \omega}{\partial x_j}\right)+\mathrm{G}_{\omega}+\mathrm{Y}_{\omega}+\mathrm{D}_{\omega}+\mathrm{S}_{\omega}$$

Equation 3.43: SST Transport Equation for Specific Dissipation Rate

Where
$\widetilde{\mathrm{G}}_{\mathrm{k}}$ = The generation of turbulent kinetic energy due to mean velocity gradients
Y_{k} = The dissipation of k due to turbulence
S_{k}= A user defined source term for k
G_{ω}= The generation of ω
Y_{ω}= The dissipation of ω due to turbulence
D_{ω}= The cross-diffusion term
S_{ω}= A user defined source term for ω

3.4.5. Turbulence Model Selection

The turbulence model selection process is unique to each end user and their specific physical problem. For external flows, particularly airfoils, the Spalart-Allmaras and the SST Transport Equation $k-\omega$ model are among the most favoured.

The S-A model was specifically designed for robust and fast solutions for aerodynamic flows. A study by Pettersson and Rizzi, [71] compared two different CFD solvers and two different turbulence models against wind tunnel measurements of a flat plate with swept bump. They found the furthest positions upstream of the bump, where no pressure gradients and three-dimensional effects were introduced, the S-A model produced the best results. Further studies by Pan and Loth, [72], Morongin, et al., [73], Badcock, [74] and Ghisu, et al., [43] all show the S-A turbulence model provides satisfactory results.

A comparison by Johansen, [75] of the already well defined one-equation S-A model against the two-equation $k-\varepsilon$ realisable and SST $k-\omega$ models using the NACA 0012 airfoil at Reynolds number of three million was conducted. The boundary layer was assumed fully turbulent for numerical simulations and compared with experimental data also for a fully turbulent boundary layer. The most accurate model was the SST $k-\omega$, followed by S-A and finally the $k-\varepsilon$ realisable model.

A presentation on various turbulence model performances was conducted by Rahimi, et al., [76] for two airfoils; FX 79-W-151A and NACA 63-430. The S-A model was found to perform well up to stall. From the point of stall the S-A model failed to accurately predict force coefficients. The SST $k-\omega$ was found to perform well in both pre- and post-stall regimes.

A large study was conducted by Nichols, [77] where turbulence models are compared relative to each other for a number of flow conditions. This extensive study provided an insight into the turbulence models strengths and weaknesses with regards to grid sensitivity. The SST $k-\omega$ model was found to be less sensitive (especially for pressure) to cell elongation relative to the S-A model.

The SST $k-\omega$ model utilises the benefits from the $k-\varepsilon$ and $k-\omega$ models. For many years the $k-\varepsilon$ model has been the tried and tested industry choice [58]. However for aerodynamics, the $k-\varepsilon$ model limitations lie with its lack of sensitivity to adverse pressure gradients [78]. Work by Kline, et al., [79] found the $k-\varepsilon$ model delayed or completely suppressed flow separation due to the significant over-prediction of shear stress. Further inspection of the $k-\varepsilon$ model attributed these shortcomings to over-prediction of the turbulent length scale near the wall [80].

The $k-\omega$ turbulence model by Wilcox, [69] was developed for aeronautical flows, particularly aerofoil flows which require accurate prediction of strong adverse pressure gradients and separation. The Wilcox $k-\omega$ model is substantially more accurate for near-wall modelling with moderate adverse

pressure gradients. However in the presence of flows where the pressure induced separation occurs, the model fails [81].

This was one of the key motivations behind the development of the SST model; utilise the best features from both the $k-\varepsilon$ and $k-\omega$ turbulence models. With small modifications the model has been improved to provide the same levels of convergence as the standard $k-\varepsilon$ model with wall functions [82].

The validity for the SST model was its performance on flow prediction in strong adverse pressure gradients against the $k-\varepsilon$ and $k-\omega$ turbulence models. The SST model was found to be superior from three sources:

- Menter, [48]
- Menter, [81]
- Eleni, et al., [83]

Recent work on numerical optimisation high-lift devices was considered by Trapani, et al., [84] utilising the MOTS code developed by Jaeggi, et al., [41]. The performance in high-lift configuration was the objective and shape optimisation of the slat, flap gaps and deflection angles was considered. The ANSYS CFX solver was used with the $k-\omega$ SST model as the force coefficient results were superior to the Spalart-Allmaras model. Both the Spalart-Allmaras and $k-\omega$ SST models were evaluated. A noticeable feature at high angles of attack was the Spalart-Allmaras model produced particularly large regions of separated flow which were considered unrealistic. The author found the $k-\omega$ SST model performed particularly well for separated flow enough to warrant the extra computational costs.

Selection of the turbulence model based on the literature was carefully considered. For runback ice simulations, the key parameter was the results found from the Backward-Facing-Step (BFS), i.e. separation and reattachment by Shur, et al., [85] and by extension the work done by Trapani, et al., [84] highlighting the differences observed for regions of separated flow. The S-A model proved to be a robust and accomplished turbulence model. The performance of the SST model warranted the increased PDE complexity and computational costs and was the turbulence model of choice.

3.5. Optimisation

This section introduces the concept of a design optimisation process. The following description focuses on a metaheuristic Multi-Objective Tabu Search (MOTS) type optimiser developed by [86].

3.5.1. Introduction

Product design/development cycles represent significant costs. Tools and techniques to reduce the engineering process cycle, particularly for computational aerodynamic design processes bought forward the development of numerical optimisation [87].

The use of optimisation in aerodynamics can be seen as early as the 1970s [88]. With huge advancements in both CFD and optimisation algorithms, authors now publish books rather than chapters dealing with optimisation relying on evaluations obtained from computational fluid dynamics; CFD-based optimisation or CFD-O [89].

Numerical optimisation aims at locating the minima of a function (objective function) on a finite design space while satisfying a number of constraints (inequality verified by a constraint function).

For single objective optimisation, the goal is to find the vector $\bar{x}$ such that the function $f(\bar{x})$ attains its minimum value. $\bar{x}$ is called a vector of design variables or design vector. A point $\bar{x}_1$ in a given design space can be considered better than another point $\bar{x}_2$ if the inequality $f(\bar{x}_1) < f(\bar{x}_2)$ is satisfied. With only one objective, a global search of the design space yields one optimum design (multiple optimum designs are possible). Practical optimisation to find a feasible optimum design is rarely satisfied by a single objective function. For complex aerodynamic flows a number of objectives are usually required to be satisfied.

Modern offering for multi-objective optimisation algorithms are:

- Genetic Algorithms (GA)
- Simulated Annealing (SA)
- Ant Colony Optimisation (ACO)
- Particle Swarm Optimisation (PSO)
- Neural Networks (NN)
- Tabu Search (TS)

At the turn of the century, a TS algorithm for multi-objective optimisation was compared to other published TS algorithms and an alternative SA algorithm

[90]. The authors used a TS algorithm developed and presented in two stages by Glover, [91] and Glover, [92] where adapted intensification and diversification moves called Enhanced Continuous Tabu Search (ECTS) were implemented. They found the proposed modifications to the intensification and diversification moves promising. Using less than ten variables, ECTS was found to be similar or better than other algorithms tested. However the author conceded that at the time of writing, only three other published works related to TS optimisation were available.

Although the TS algorithm showed promise, the research efforts at the time (early 2000s) were directed towards the GA and SA algorithms [93]. In 2002 work done by Harvey, [94] found that a single objective TS algorithm coupled with a highly constrained aerodynamic problem performed very well. Other approaches to TS algorithms were discussed by Jaeggi, et al., [41] and found most other TS algorithms suffer from problems common to all weighted-sum approaches; where the entire Pareto-optimal set may not be realised.

The introduction of a new MOTS algorithm by Jaeggi, et al., [86] was compared against leading multi-objective GA algorithms of the time. Exhaustive testing displayed the codes ability to successfully tackle realistic problems for a highly-constrained and non-linear search space [95]. It was noted that the identification of a Pareto-optimal set of results allowed the engineer to make a well informed assessment of how the variation of the design vector affects the trade-off between competing objectives.

Nearly a decade had passed since the introduction of the MOTS variant by Jaeggi, et al., [86] and the algorithm has now been used for a vast range of highly constrained aerodynamic optimisation problems. From 2008 to 2013, a number of the studies using this MOTS variant for aerodynamic and structural optimisation problems were considered.

According to Yang, [96] the correct selection of an algorithm is dependent on the type of problem, algorithm nature, solution quality, computing resource capacity, implementation and integration.

The MOTS algorithm developed by Jaeggi, et al., [86] was chosen because it has:

- Proven to be a robust optimisation tool particularly for airfoil and shape optimisation [84]
- Excellent results found with both single and multi-objective TS algorithms in highly constrained problems by Harvey, [94] and Jaeggi, et al., [41]

- Sophisticated memory allocation and search moves to ensure an entire Pareto-optimal set are provided
- Ease of implementation as a result of previous relationship with similar optimisation setup at Cranfield University
- Ease of integration with existing Operating System and parallel execution again due to done previous work at Cranfield University using MOTS

3.5.2. MOTS Overview

The MOTS algorithm was implemented to conduct a four-part CFD based optimisation study on runback ice. An outline of the code is presented here but a detailed study of the MOTS code with extensive testing of the key TS features can be found by Kipouros, [97].

The MOTS code was built upon the promise shown for a single-objective TS algorithm. With the introduction of another objective the concept of Pareto-dominance was introduced instead of using a weighted function to characterise objectives. Consider the multi-objective optimisation of n objective functions:

$$f_1(\bar{x}), \ldots\ldots, f_n(\bar{x}) \text{ where } n \geq 2$$

Taking the first objective function:

$$\bar{F}(\bar{x}) = \{f_1(\bar{x}), \ldots\ldots, f_n(\bar{x})\}$$

A point can be considered Pareto-dominant if:

"*A point $\bar{x}_1$, with an objective function vector $\bar{F}_1$, is said to dominate point $\bar{x}_2$, with an objective function vector $\bar{F}_2$, if no component of $\bar{F}_1$ is greater than its corresponding component in $\bar{F}_2$, and at least one component is smaller.*" [41]

Similarly a point can be considered Pareto-equivalent if:

"*$\bar{x}_1$ can be said to be Pareto-equivalent to $\bar{x}_2$ if some components of $\bar{F}_1$ are greater than $\bar{F}_2$ and some are smaller.*" [41]

As stated earlier, the MOTS algorithm employed in this thesis is a multi-objective variant of the single-objective TS implementation by Conner & Tilley, [98]. Their work effectively provided the starting point by using a Hooke and Jeeves (H&J) local search algorithm [99].

The TS algorithm operates in a sequential and iterative manor based on the implementation of the H&J search. It becomes apparent the performance of the TS algorithm will be tied closely to the search space selection process.

The TS algorithm search space selection process follows the work prescribed by Glover and Laguna, [100] which is based on the premise that an intelligent TS algorithm must incorporate:

"*Adaptive Memory*": Local search choices are guided by the collected search history

"*Responsive Exploration*": Using stored memories to exploit good solutions and exploit new promising regions.

To implement an intelligent TS algorithm, two highly important components are used; intensification and diversification strategies.

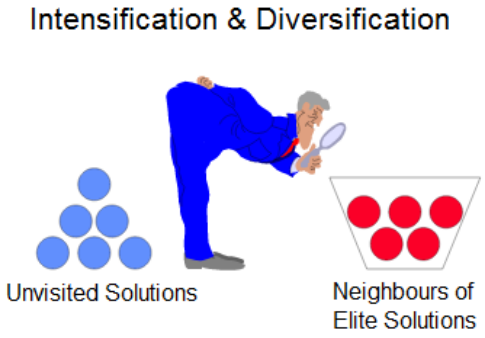

Figure 3.17: Comical Illustration of Intensification and Diversification Strategies [100]

Figure 3.17 illustrates the main differences between intensification and diversification moves.

Intensification:
Strategies based on modifying the search choice using a stored set of elite solutions to encourage a closer evaluation of the design space. The set of elite solutions are populated by historically found good solutions.

Diversification:
Strategies based on modifying the search choice to promote examination of the unvisited regions of the design space. The problem associated with local/multiple minima of a function are negated due to diversification ability to jump to a new unexplored design space.
To implement these two strategies, the need to store visited points efficiently was required; Short, Medium and Long term memories.

Short Term Memory (STM): Recently visited points are stored in the STM and are not allowed to be revisited.
Medium Term Memory (MTM): Optimal or near-optimal points are stored in the MTM and used for the intensification procedure.
Long Term Memory (LTM): Records regions of space explored. Used in diversification procedure to direct search in unvisited areas.

A final feature linking all the H&J search procedures to memories was a local iteration counter, i_local. Figure 3.18 provides a flow diagram of the TS algorithm. The initial starting point was the datum design. With each successful search added to the MTM, the i_local counter is reset. When the algorithm fails to find an improved solution, the i_local counter is incremented by one. When a user-specified i_local value is reached, the algorithm will intensify, diversify or restart with a Step Size Reduction (SSR).

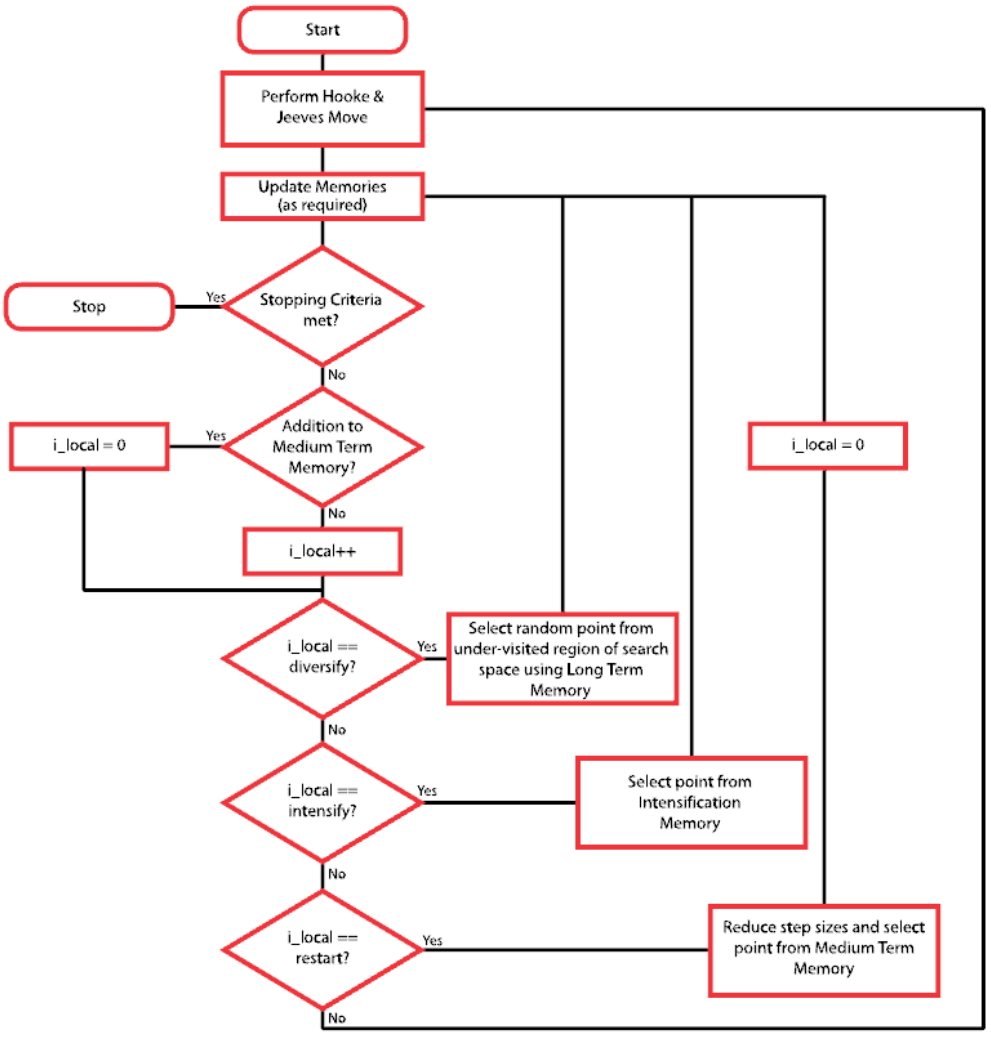

Figure 3.18: Flow Diagram for Multi-Objective Tabu Search Algorithm [41]

The MOTS code had incorporated parallelisation features. Numerical optimisation coupled with numerical modelling for complex external flow problems results in high computational costs. The ability to parallelise the code and execute multiple CFD evaluations simultaneously provides dividends for strict deadlines. The code is parallelised at the H&J move. This is a Functional Decomposition strategy where lower level operations within a sequential (TS) algorithm are executed in parallel. An excellent illustration by Saddawi, [101] is shown in Figure 3.19.

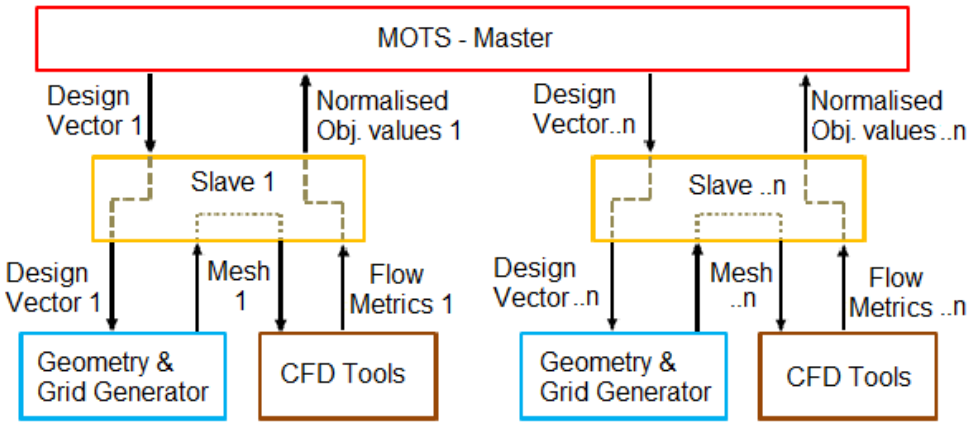

Figure 3.19: Parallelisation of MOTS Framework [101]

4. Computational Validation against CFD Model

"An expert is one who knows more and more about less and less until he knows absolutely everything about nothing."

- Nicholas Murray Butler

Computational validation against published data is one of the key aspects when experimental data is not available. Three validations were performed:

1. Boeing 737-700 airfoil against [1]
2. Boeing 737-200 Midspan airfoil against [102]
3. NACA 23012 Ridge Ice against [30]

An ICEMCFD mesh script was developed for the multi-objective Tabu Search optimisation code. A prerequisite was a robust script which allowed variable input of airfoil geometry, ice location and shape optimisation. Although the publications considered for this validation use different airfoils, the same meshing script was utilised which not only tested the ANSYS FLUENT solver capabilities but validated the method used to create a hex-core hybrid mesh for high-fidelity two-dimensional CFD analysis.

Solver scripts for ANSYS FLUENT were also created for optimisation purposes and utilised for validation in the same manner as the meshing script outlined above. Validation runs were solved as steady-state. The $k-\omega$ SST turbulence model was used and all results presented were converged to second order accuracy.

4.1. Boeing 737-700 Airfoil Validation

The aim of this validation was to corroborate the clean configuration datum Boeing 737-700 airfoil with the numerical study conducted by Alègre, [1].

This study was conducted at a lower speed than that specified by the EASA for the 45 minute hold case. The mesh was created using the same script utilised throughout this thesis including the optimisation studies.

Parameter	Alègre, [1]	B737-700 Airfoil in Datum Configuration
Airfoil	B737 - 4m	B737 - 4m
AOA	3°	3°
Grid	Structured	Hex-Core Hybrid
Solver	Coupled	Coupled
Turbulence Model	$k-\varepsilon$ (EWT)	$k-\omega$ SST
Mach Number	0.137	0.137

Table 4.1: B737-700 Solver Parameter Comparison

Results

Force coefficient data was not published as this was a parametric study to provide insight on the pressure distribution effects for full-scale and hybrid truncated airfoils.

Two vastly different grid designs were used for this validation study. For the parametric study by Alègre, [1], a typical c-grid multiblock structured mesh was used. A hex-core hybrid mesh, with a structured quadrilateral elements around the airfoil and triangular elements for the rest of the domain was used to perform the validation (Figure 4.1). The option to create a simple c-grid was available but the hex-core strategy was used heavily throughout this project and required validation in some form. Arguably the mesh used for a simple clean configuration airfoil was slightly overkill without the presence of high-fidelity runback ice but the need to validate the hex-core mesh deemed its use appropriate.

The parametric study was conducted using ANSYS FLUENT solver with $k-\varepsilon$ Enhanced Wall Treatment (EWT) turbulence model [1]. The y^+ value of less than three was specified. The $k-\omega$ SST model used for comparison required a y^+ of less than one.

The upper surface pressure and skin-friction coefficients were available for comparison and shown in Figure 4.2 and Figure 4.3. Contour plots were also available for comparison and shown in Figure 4.4 and Figure 4.5.

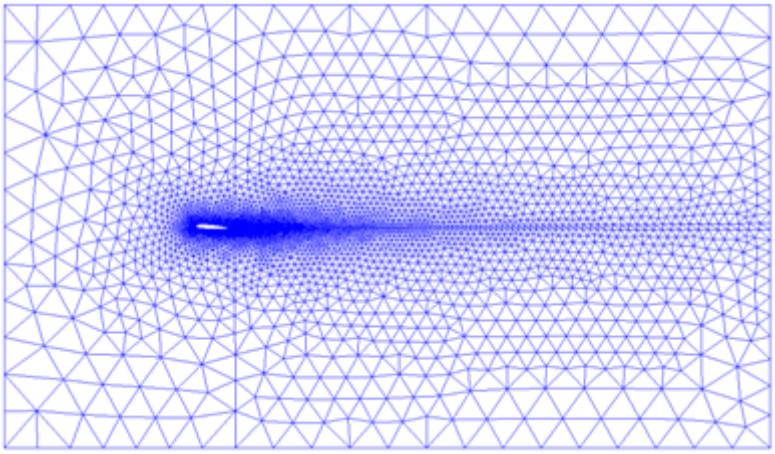

Figure 4.1: Hex-Core Hybrid Mesh for the Datum Boeing 737-700 in Clean Configuration

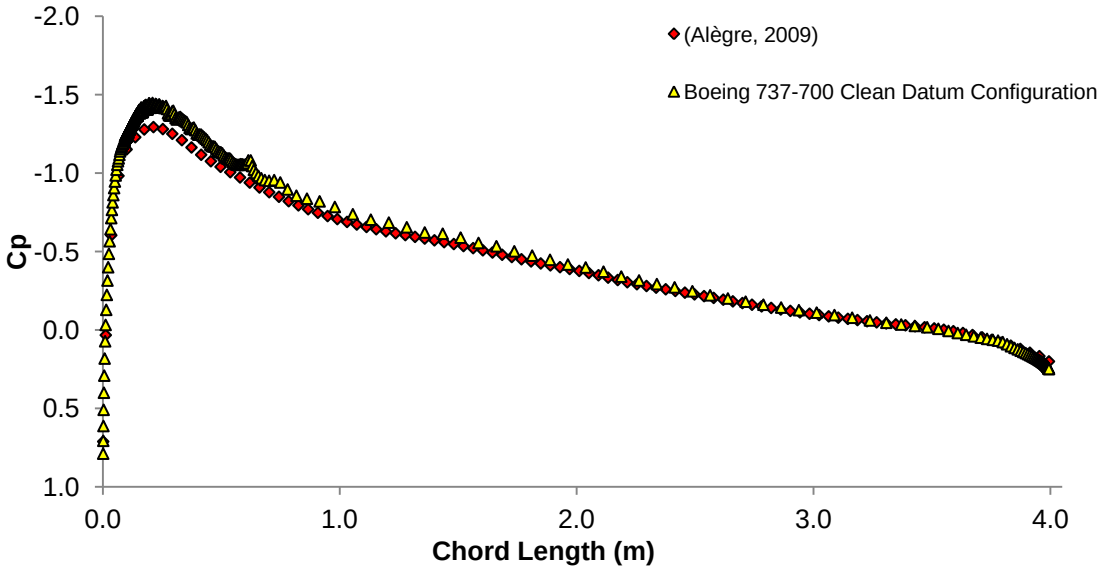

Figure 4.2: B737-700 Clean Upper Surface Pressure Coefficient Comparison

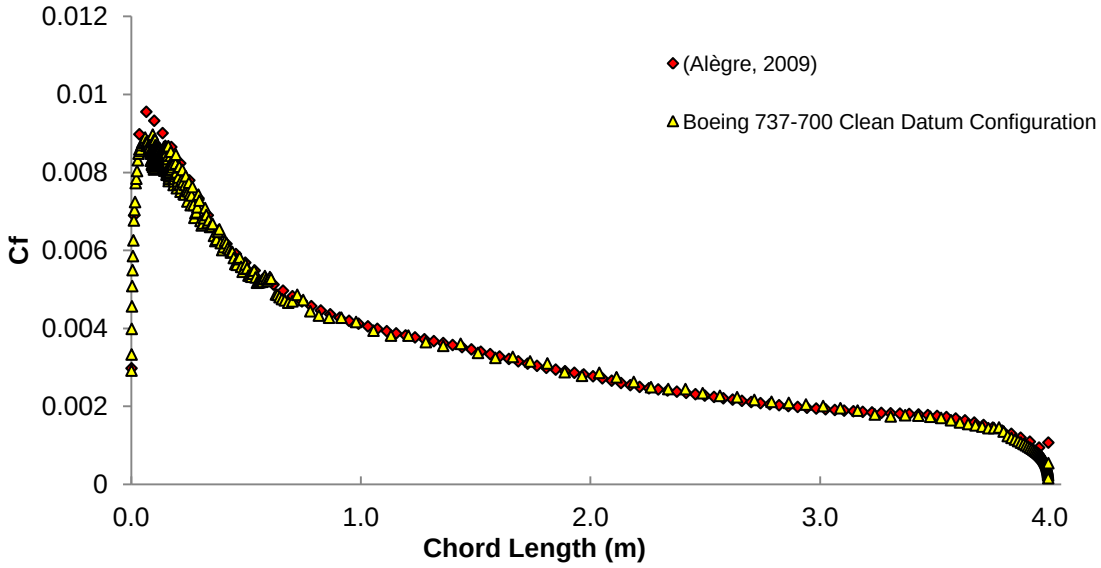

Figure 4.3: B737-700 Clean Upper Surface Skin Friction Coefficient Comparison

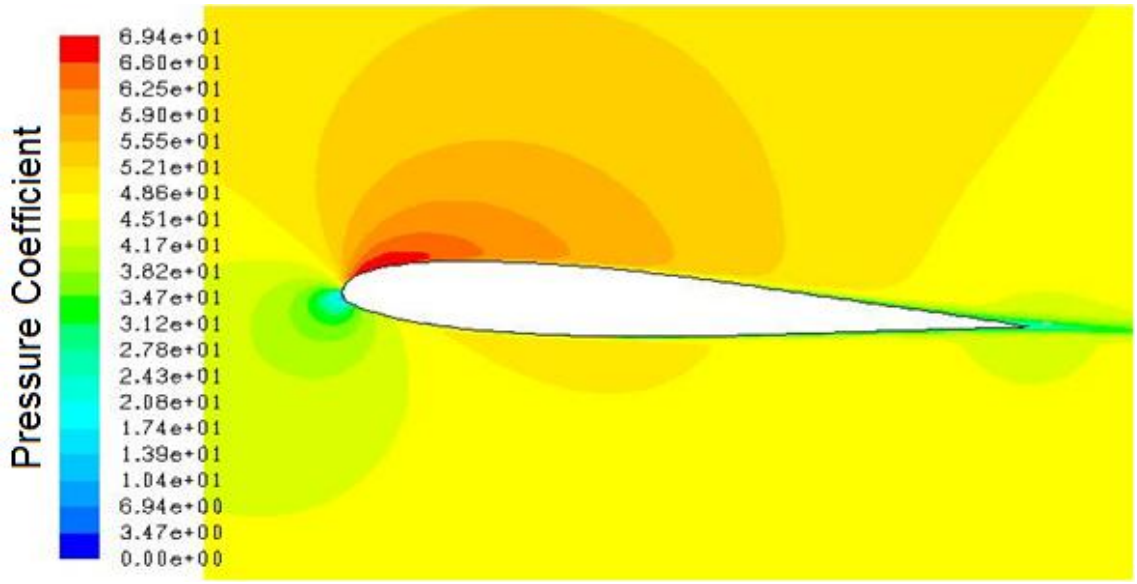

Figure 4.4: B737-700 Clean Pressure Contour plot [1]

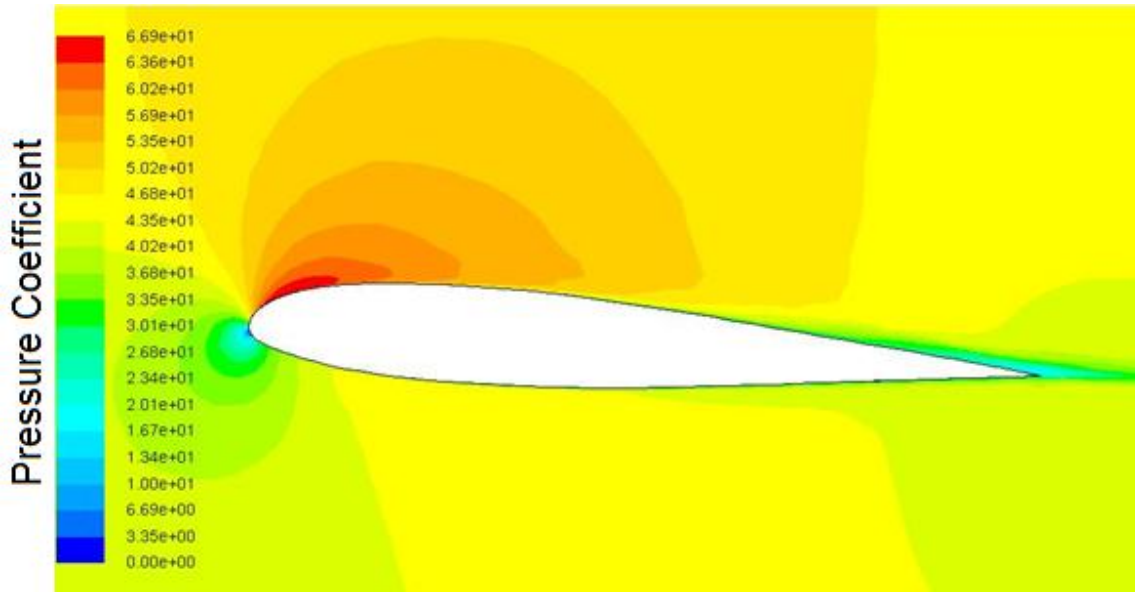

Figure 4.5: Boeing 737-700 Datum Configuration Pressure Contour plot

The variations observed between the two contour plots are due to the difference in the number of contour levels and maximum range. The results for the pressure and skin friction coefficients were in good agreement across the airfoil chord for two distinctly different numerical models with small variations observed at the location of peak suction pressure.

4.2. Boeing 737-200ADV Midspan Airfoil Validation

Experimental ice accretion tests were carried out at the NASA Lewis 6ft by 9ft Icing Research tunnel. The research efforts were geared towards multi-element airfoil ice accretion rather than in cruise configuration. A Boeing designed three-component force balance was used for direct drag measurements. The test conditions were based on cruise and approach conditions for the Boeing 737-200 ADV multi-element wing. A number of tests were run for the Boeing 737-200ADV in cruise configuration and are used for this validation (Figure 4.6). These tests are outlined in Figure 4.7. Run 8 (highlighted in red) was the closest match to the 45 minute EASA hold case shown in Table 4.2.

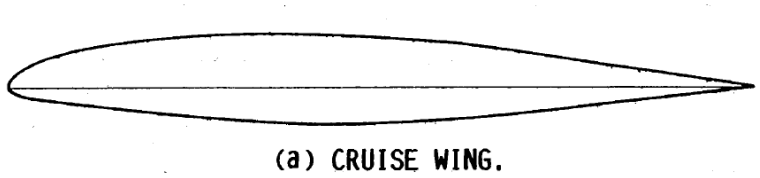

Figure 4.6: Boeing 737-200ADV in Cruise Configuration [102]

Run number	Duration (mins)	Temperature (°F)	Velocity (fts^{-1})	LWC (gm^{-3})	MVD (μm)
1	5	20	158	1.49	14
2b	5	28	158	1.4	17
3	5	13	158	0.9	14
4b	5	10	158	1.13	17
5	2	20	158	0.7	14
6	13	20	240	0.7	14
7	5	16	235	1.0	12.5
8	8	15	236	0.8	14
9	5	-16	154	0.87	17.1
10	8	-19	152	1.38	16

Figure 4.7: Table of Test Conditions for Cruise Wing Configuration [102]

Run/Case	Temperature (°C)	Velocity (ms^{-1})
Run 8 [102]	-9.4	72
EASA 45 minute Hold	-9	118

Table 4.2: EASA 45 Minute Hold Case Compared to Selected Run used for B737-200ADV Midspan Airfoil Validation

A hex-core hybrid mesh was used to emulate the experimental results (Figure 4.8). The force coefficient trends for run number 8 clean and iced B737-220ADV wings are shown in Figure 4.9. The numerical lift and drag profiles from ANSYS FLUENT showed good agreement with the experimental trends up to an angle of attack of 8°. Beyond this point the flow separation was large/unsteady and poorly predicted by RANS model as noted by a number of publications discussed in the literature review.

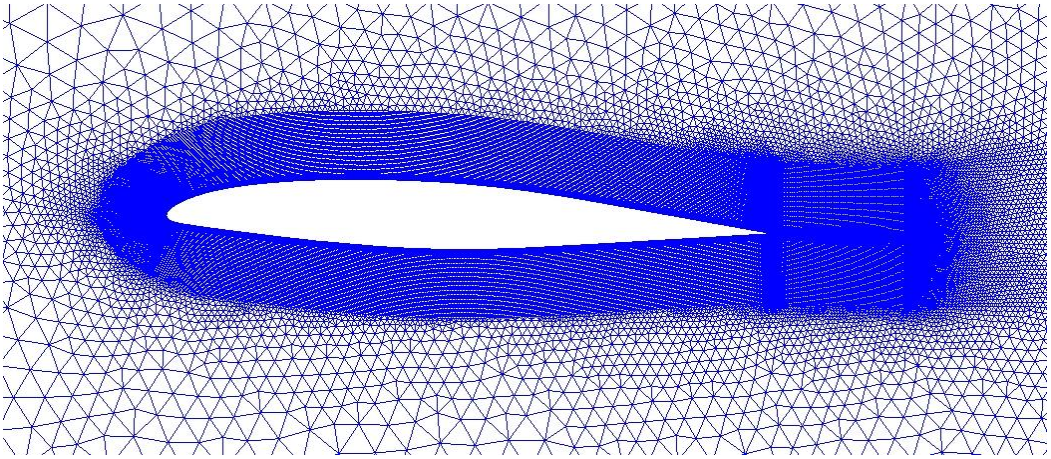

Figure 4.8: Hybrid-Hexcore Mesh for B737-200ADV Validation

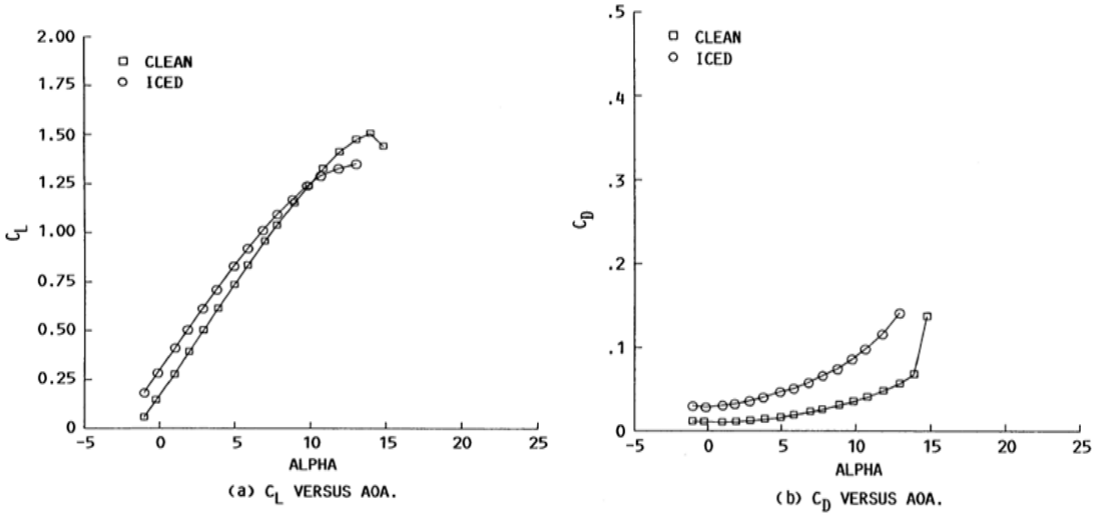

Figure 4.9: Force Coefficient Trends for Boeing 737-200ADV Midspan Validation [102]

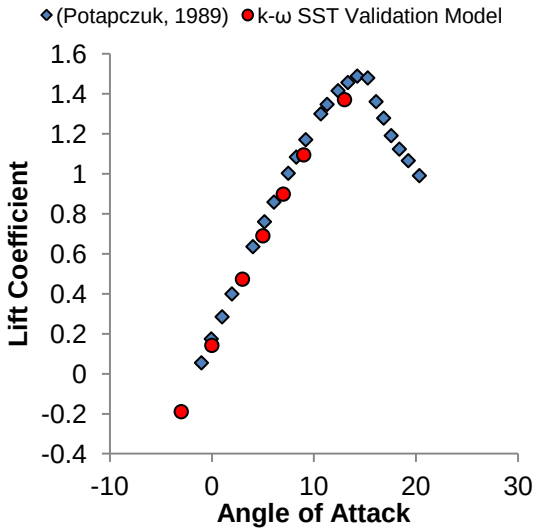

Figure 4.10: B737-200ADV Experimental and Numerical Lift Coefficient Curve

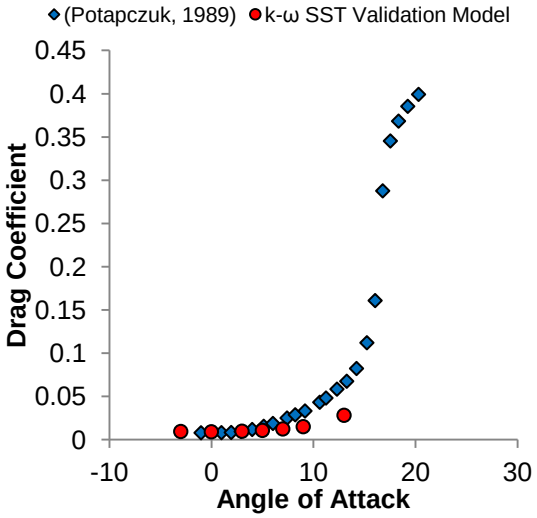

Figure 4.11: B737-200ADV Experimental and Numerical Drag Coefficient Curve

4.3. NACA 23012 Ridge Ice CFD Validation

Marques, et al., [30] presented a ridge ice CFD validation study for two airfoils; NACA 23012 and generic multi-element configuration. The RANS equations were implemented using a curvilinear multi-block body conforming grids. The $k-\omega$ model and Spalart-Allmaras turbulence models were examined. The results for the pressure profiles along the chord were compared against experimental data collected from the Langley Research Centre using the Low Turbulence Pressure Tunnel (LTPT) [17]. The force coefficient results were compared against the numerical model results published by Marques, et al., [30]. The mesh close to the ridge ice required some modification to the hexa blocks around ice shape (Figure 4.12).

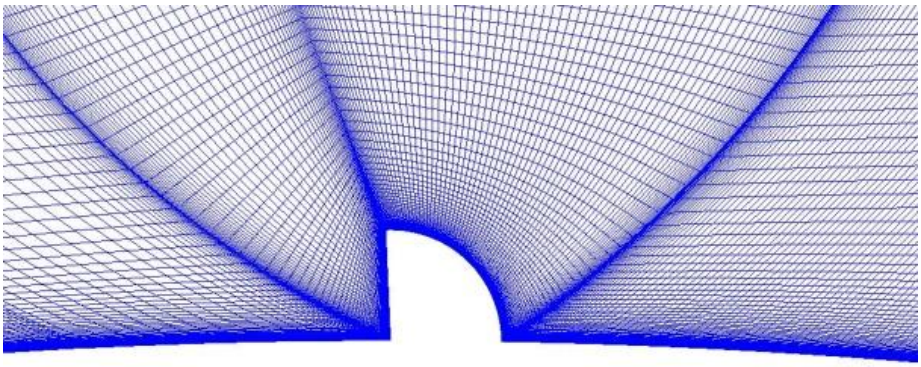

Figure 4.12: Ridge Ice Hybrid Mesh for NACA 23012 Study

Pressure coefficient profiles for the NACA 23012 airfoil at angles of attack of 0° and 5° were compared with two ANSYS FLUENT turbulence models; $k-\omega$ SST model and Spalart-Allmaras turbulence. Results for the airfoil in both clean and ridge-iced configurations are presented.

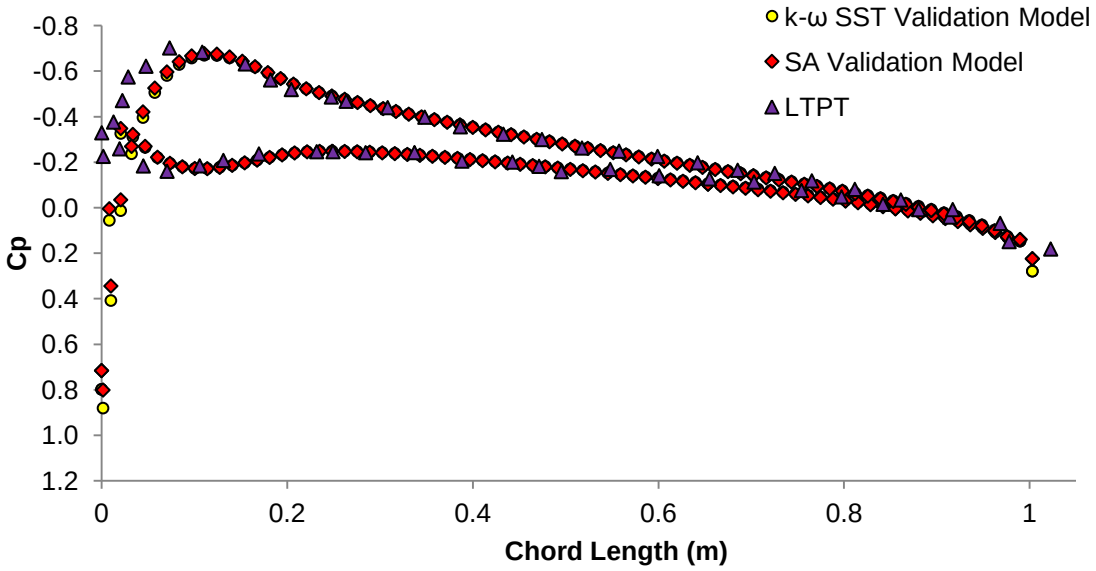

Figure 4.13: Clean NACA 23012 Surface Pressure Coefficient Comparison at 0° AOA

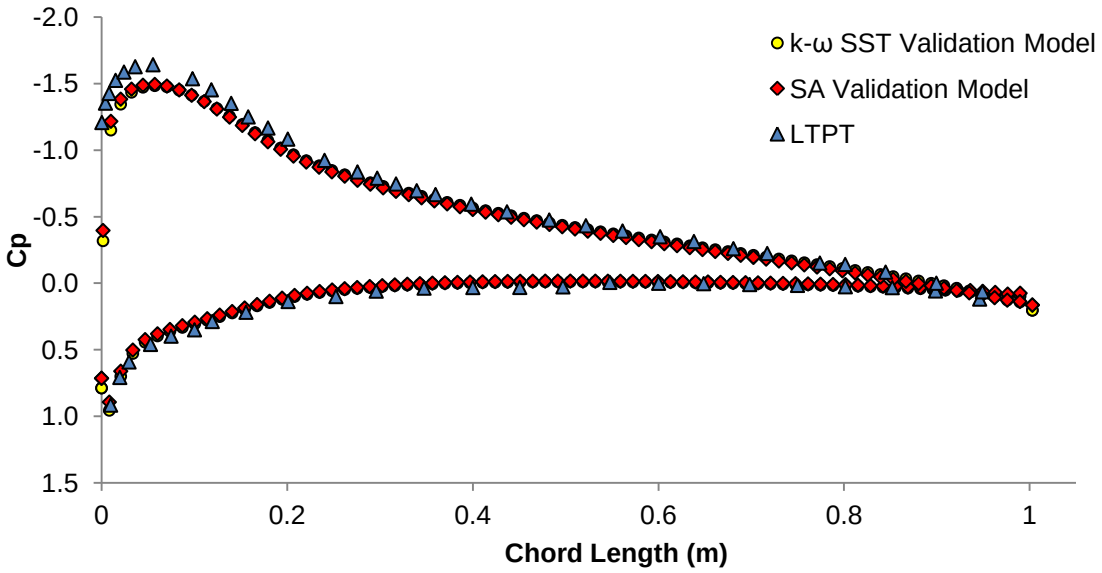

Figure 4.14: Clean NACA 23012 Surface Pressure Coefficient Comparison at 5° AOA

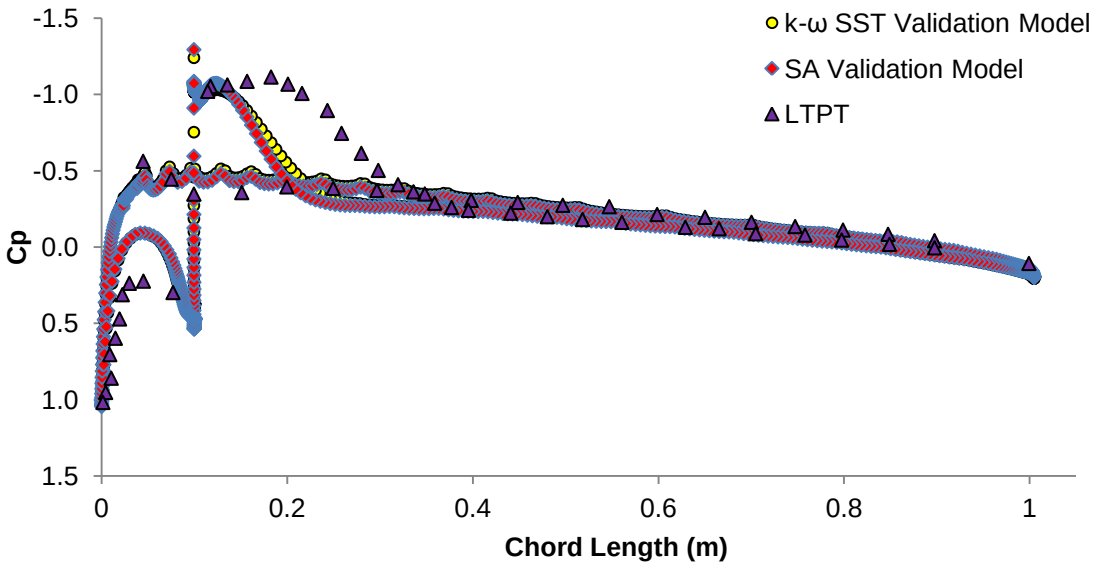

Figure 4.15: Ridge Ice NACA 23012 Surface Pressure Coefficient Comparison at 0° AOA

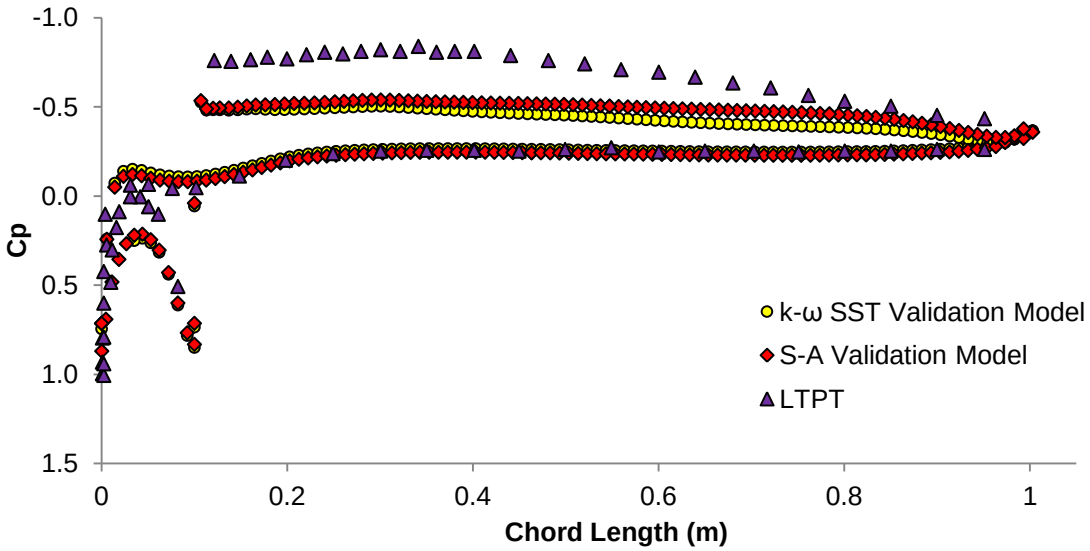

Figure 4.16: Ridge Ice NACA 23012 Surface Pressure Coefficient Comparison at 5° AOA

The pressure profiles for the clean airfoil were in good agreement with experimental data. Both turbulence models under-predicted the suction peak relative to the experimental data.

The iced configuration runs for the validation paper consistently produced larger regions of separated flow. A much less prominent suction peak was observed relative to the validation paper. The authors highlighted the RANS model predicted larger separated regions.

Comparison of the force coefficient results for clean and iced configurations at 0° and 5° angle of attack are presented in Figure 4.17 through to Figure 4.20. The force coefficient trends are consistent and comparable across all turbulence models.

Clean airfoil results and iced airfoil results at 0° were essentially identical to the results obtained by Marques, et al., [30] using the $k-\omega$ model and Spalart-Allmaras turbulence models.

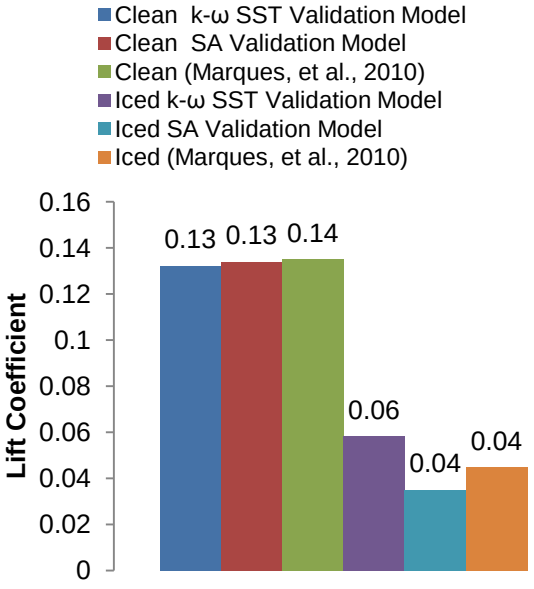

Figure 4.17: Ridge Ice 0° AOA Lift Comparison

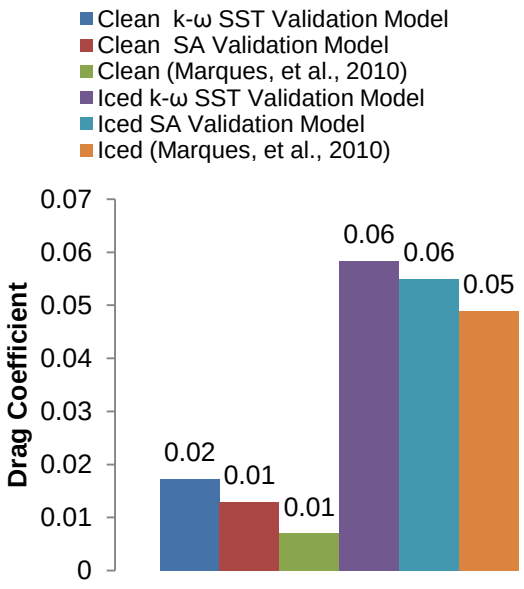

Figure 4.18: Ridge Ice 0° AOA Drag Comparison

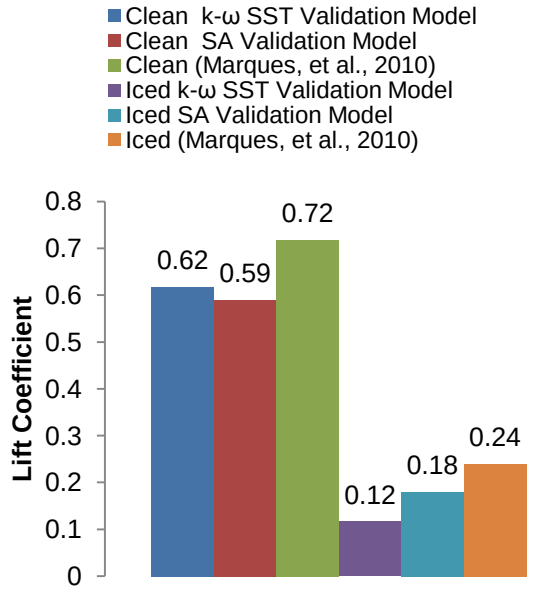

Figure 4.19: Ridge Ice 5° AOA Lift Comparison

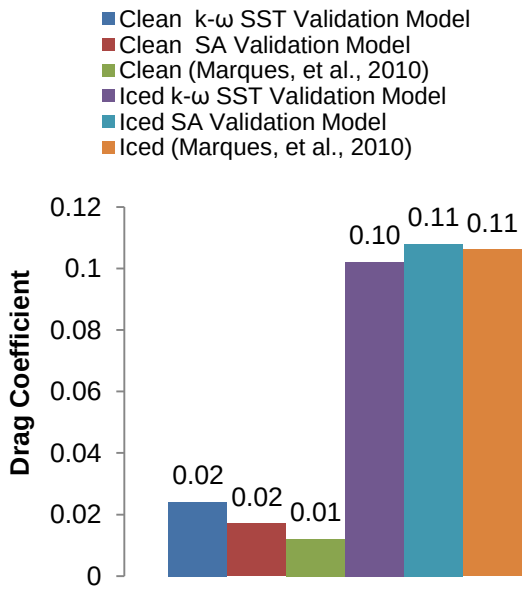

Figure 4.20: Ridge Ice 5° AOA Drag Comparison

4.4. Summary

- The general trends for all three validation studies were well predicted. The force coefficients results were important and comparable with studies considered.
- The B737-200ADV airfoil angle of attack comparison showed the models capability to accurately predict force coefficients up to 7° AOA.
- The outcome of the validation study highlighted the robust nature of the script files and hex-core hybrid mesh implementation.

5. Boeing 737-700 Airfoil Numerical Study

"Never regard study as a duty, but as the enviable opportunity to learn to know the liberating influence of beauty in the realm of the spirit for your own personal joy and to the profit of the community to which your later work belongs."

- Albert Einstein

A number of different Boeing 737 wing coordinates are available to the public domain including the B737-700 profile [103]. Alègre, [104] use of the Cranfield Icing Tunnel to produce realistic runback ice on a full scale B737-700 leading edge provided the ideal datum configuration for multi-objective Tabu Search (MOTS) studies.

Airbus recommended the use of the B737-700 airfoil and suggested it was sufficiently close to their airfoil profile. Airbus also provided the specific conditions to match the worst icing condition directed by the EASA; 45 minute hold case in continuous icing conditions with a calibrated speed of 118ms^{-1} at 17000 ft for a static temperature of -9°C. The sponsors provided a target lift coefficient range of 0.4 to 0.6 at an AOA of 3° as representative values for this hold configuration.

The B737-700 wing is used throughout the MOTS studies and this chapter is dedicated to the validation and performance analysis of a clean and iced cruise airfoil configuration.

5.1. Clean Configuration Boeing 737-700 Cruise Airfoil Verification and Validation

This verification and validation procedure served a number of purposes:

- Find minimum computational costs
- Analysis of Airfoil Properties
- Provides datum force coefficients used in MOTS

One of the critical considerations was the computational cost for an optimisation project. The aim of the optimisation process was to yield an improved design variable in a time that was significantly faster than a trial and error approach. A mesh dependency study allowed accurate judgement on the quality of the mesh by the fluctuation on the force monitors with each iteration; coefficients of lift and drag as well as total mass flow rate. The stability of the force values was critical as these values would dictate the progression of the optimiser. However

the time taken to find a converged solution was a critical parameter and was of concern at all times during this phase of the study. To this end a compromise between mesh quality and computational time was paramount.

The verification and validation process are both important factors for any simulation requiring the use of computational fluid dynamics. The method applied to quantify competent CFD modelling was from a 6 year debate across academia and industry culminating in an AIAA publication Guide for the Verification and Validation of Computational Fluid Dynamics Simulations [105].

Accordingly there are two aspects to verification:

- Verification of the code
- Verification of the calculation (CFD model)

Commercial codes are used throughout this thesis and therefore examination of the code was not conducted. A verification assessment was applicable for this study and comprised of the following:

1. Examine Iterative Convergence
2. Examine Consistency
3. Examine Mesh Quality and Associated Discretisation Error
4. Compare CFD Results to Highly Accurate Solutions

Examine Mesh Quality and Associated Discretisation Error

Mesh quality was examined using the tools provided within ANSYS ICEM CFD Mesh Generation Software. Discussions on Mesh strategy and methods can be found in Chapter 3 . ANSYS ICEM CFD tools quantify the quality of the different elements and offer a visual aid to gauge the location within the domain. The mesh used was a hybrid hex-core mesh comprised of a structured boundary layer around the airfoil and unstructured for the rest of the domain.

The Tri (ICEM CFD terminology for triangular elements) and Hexa (ICEM CFD terminology for rectangular elements) elements have different quality criterion:

1. Tri Quality Criteria:
   The aspect ratio of the triangular elements was used as the basis for the quality criterion shown in Equation 5.1**Error! Reference source not found.**. The quality value represented a scaled quantity where 1 equates to a perfectly regular element and 0 represents a highly skewed element with no area.

$$Tri\ Quality\ Criteria = \frac{\left|\frac{Area}{Max\ Edge\ Length}\right|_{actual}}{\left|\frac{Area}{Max\ Edge\ Length}\right|_{ideal}}$$

Equation 5.1: ANSYS ICEM CFD Triangle Elements Quality Criteria

2. Hexa Quality Criteria:
   The aspect ratio of the rectangular elements are used as the basis for the quality criterion but calculated differently. According to the ANSYS ICEM CFD user manual:

   "The vectors for each of the 4 quad nodes span a parallelogram. The area of each parallelogram is divided by the length of each component vector squared, to give 8 possible aspect ratios. The minimum ratio is taken as the aspect ratio for the quad element" [106]

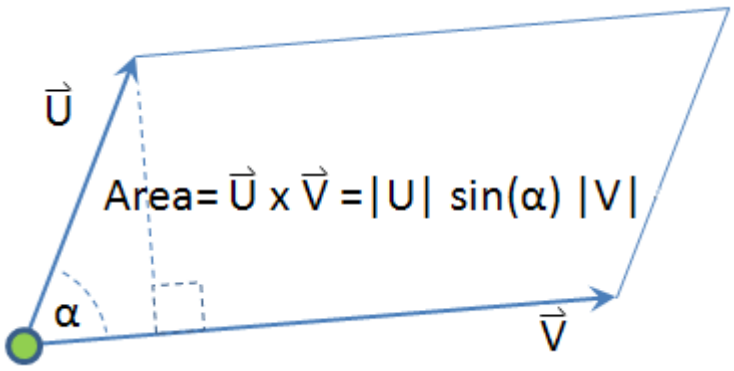

Figure 5.1: Hexa Element Aspect Ratio [106]

$$Area\ of\ Parallelogram = \vec{U}.\vec{V} = |U|Sin(\alpha)|V|$$

Equation 5.2: ANSYS ICEM CFD Calculation for Rectangular Element Parallelogram

$$Hexa\ Aspect\ Ratio = \frac{Size\ of\ Minimum\ Element\ Edge}{Size\ of\ Maximum\ Element\ Edge}$$

Equation 5.3: ANSYS ICEM CFD Calculation for Rectangular Element Aspect Ratio

Equation 5.3 defines the Hexa aspect ratio. Eight sets of aspect ratio were calculated and the minimum was used as the quality criterion.

The quality of the mesh could have been improved via a number of tools available in the Mesh Edit menus. However, these tools were found to be unreliable and on a number of occasions reduced the quality of the mesh in

critical areas close to the airfoil but improved the quality of a few elements in the free stream. The goal was to produce a robust script which ruled out the use of such quality improvement techniques.

The output of the lift and drag coefficients from the grid dependency study were used as the datum condition for the optimiser. Figure 5.2 shows the hybrid nature of the mesh. The blocking strategy within ICEMCFD proved an excellent means of producing a uniform quadrilateral mesh around the airfoil (Figure 5.3). This was extremely useful around the runback ice shape (Figure 5.4).

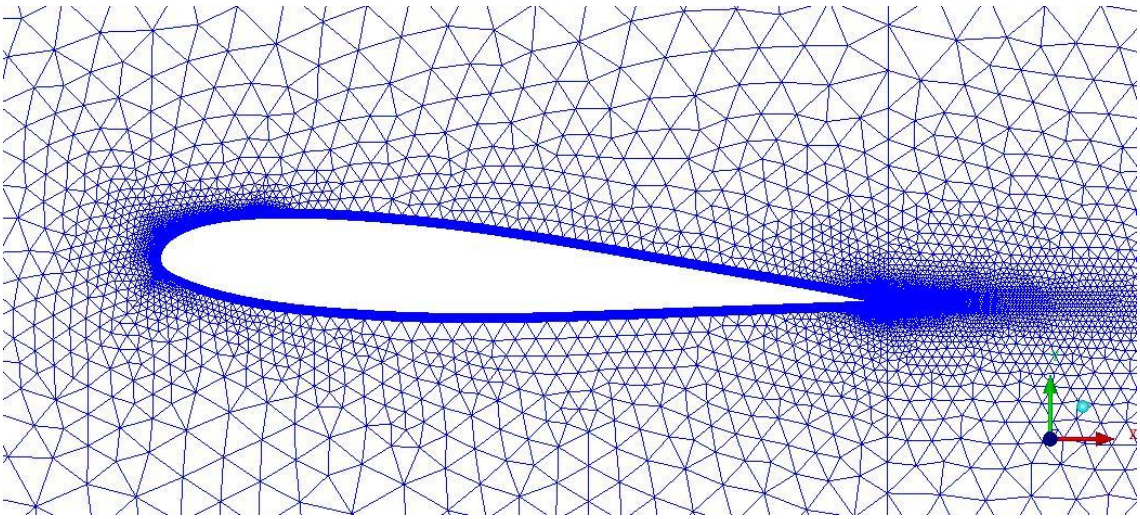

Figure 5.2: Clean Cruise Configuration Airfoil Section Mesh

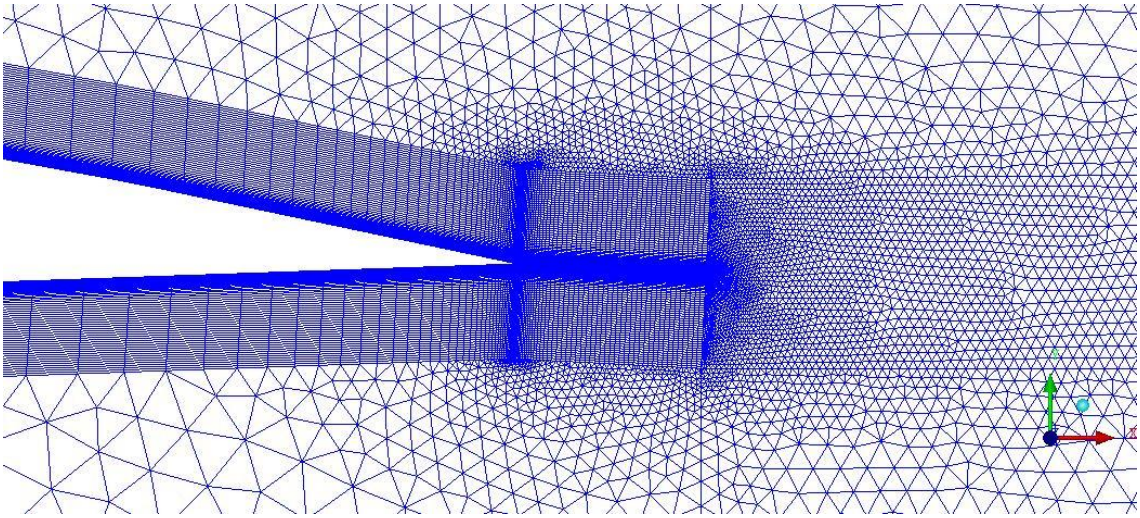

Figure 5.3: Mesh Node Clustering at Trailing Edge for Clean Cruise Configuration

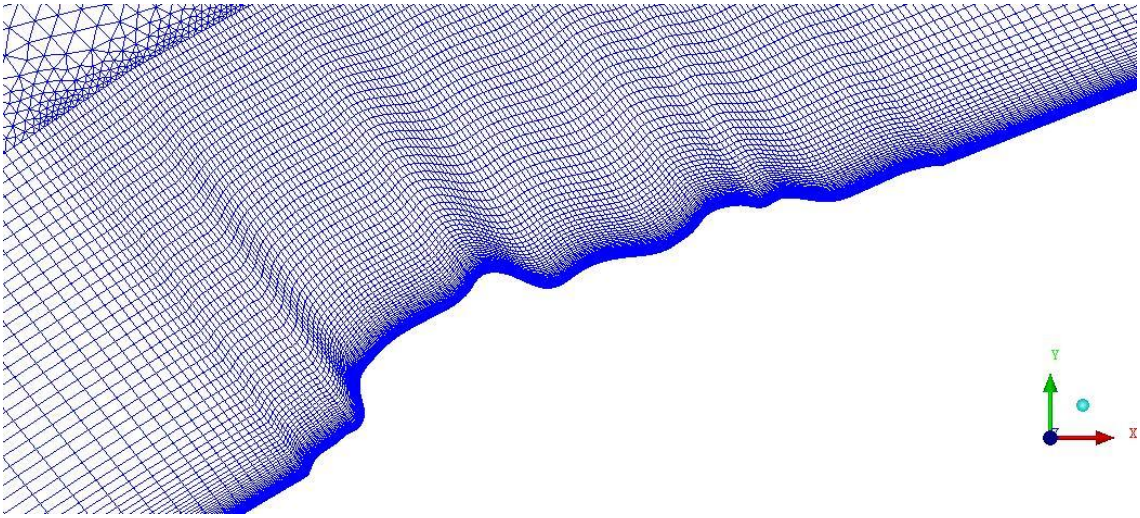

Figure 5.4: B737-700 Iced Cruise Configuration Mesh Close Up Around Ice Shape

Roache, [53] proposed use of a Grid Convergence Index (GCI) is now a well known method for estimating discretisation error. The GCI is based on the use of the Richardson Extrapolation [107]. Traditional convergence error analysis depended on a relation between the exact solution, f_{exact}, and the approximate solution $f(h)$:

$$f_{exact} = f(h) + Ah^p + HOT$$

Equation 5.4: Discretisation Approximate Numerical Solution

Where
h = measure of mesh dicretisation
A = constant
p = order (rate) of convergence
HOT = higher order terms involving h

If the mesh is sufficiently refined, the higher order terms can be neglected. When the exact solution is available, the discretisation error can be approximated using:

$$E(h) = f_{exact} - f(h) = Ah^p$$

Equation 5.5: Discretisation Error

Where
$E(h)$ = Discretisation error as a function of mesh discretisation parameter h

The order of convergence can be seen by plotting Equation 5.5 and taking the logarithmic for each side:

$$\log E(h) = \log A + p \log h$$

Equation 5.6: Order of Convergence

For most practical problems the exact solution is unknown. In this case there are three unknowns (based on Equation 5.4):

- The exact solution, f_{exact}
- The constant, A
- The observed order of convergence, p

To solve these three unknowns, three meshes are required:

- Fine mesh
- Medium Mesh
- Coarse Mesh

Constant Grid Refinement Ratio

For cases where the three meshes are constructed with a constant grid refinement ratio ($r = h_3/h_2 = h_2/h_1 = constant$) then Equation 5.6 can be written three times and solved in closed form:

$$\frac{f_{exact} - f_1}{f_1} = \frac{f_1 - f_2}{r_{21}^p - 1}\frac{1}{f_1} = \frac{\varepsilon_{21}}{r_{21}^p - 1}$$

Equation 5.7: Error Estimate between Fine Grid and Unknown Exact Solution

Where the relative error between the two finest meshes are given by:

$$\varepsilon_{21} = \left|\frac{f_2 - f_1}{f_1}\right|$$

Equation 5.8: Relative Error between the Two Finest Meshes

Equation 5.7 gives an estimate of the exact relative error with respect to the fine grid solution. This error is calculated based on the finest meshes ($f_1$and f_2), the mesh refinement ratio (r_{21}) and observed order of convergence (p).

Constant mesh refinements can become problematic in producing hybrid meshes.

Non-uniform Grid Refinement Ratio

Similar to the constant grid refinement ratio, Equation 5.6 can be rewritten three times and solved relaxing the requirement for the constant refinement ratio:

$$p = \frac{|ln|f_{32}/f_{21}| + q(p)|}{\ln r_{21}}$$

Equation 5.9: Error Estimate between Fine Grid and Unknown Exact Solution (Non-Uniform)

Where:

$q(p) = \ln\left(\frac{r_{21}^{p} - s}{r_{32}^{p} - s}\right)$

$s = sign\,(f_{32}/f_{21})$

$f_{ij} = f_i - f_j$

$r_{ij} = h_i/h_j$

The GCI becomes particularly useful for non-uniform grid refinement as complex three-dimensional cases can become a computation strain.

$$GCI_{fine} = F_s \frac{|\varepsilon|}{r^P - 1}$$

Equation 5.10: GCI Index for Fine Mesh

Where F_s is the safety factor, ε is the relative error defined as $\frac{f_2 - f_1}{f_1}$, r is grid refinement ratio.

General examination of GCI was conducted on the fine mesh. However as the underlining goal was to prepare a test bed for multi-objective optimisation studies, a GCI of the coarsest grid was also considered. The discretisation error for the coarser mesh is shown in Equation 5.11.

$$GCI_{coarse} = F_s \frac{|\varepsilon| r^P}{r^P - 1}$$

Equation 5.11: GCI Index for Coarse Mesh

When three or more grid comparisons are made, a safety factor value of 1.25 should be used [53]. The addition of the safety factor provides a 95% confidence band on the estimated relative error. A final modification was made to the grid refinement ratio to account for the unstructured grid (Equation 5.12). This ratio was calculated using the number of grid points as a reference:

$$r = \left(\frac{N_1}{N_2}\right)^{1/D}$$

Equation 5.12: Grid Ratio Refinement Factor

Where N is the total number of grid points and D is the dimension of the flow domain. Estimates on the numerically converged solution can be found using Equation 5.13.

$$f_{21} = \frac{r_{21}^{P} f_1 - f_2}{r_{21}^{P} - 1}$$

Equation 5.13: GCI Index for Intermediate Mesh Step

Equation 5.13 & Equation 5.11 provide an estimate for the numerically converged solution and quantify the discretisation error with a 95% confidence band.

CFD Solver Setting

The ANSYS FLUENT software packages offered an array of options for aerodynamic numerical modelling. Some of the fundamental setup options and values which dictated the solution accuracy and efficiency are declared for the clean cruise configuration Boeing 737 case study. A more detailed study of numerical modelling, particularly compressible flows and turbulence modelling can be found in Chapter 3.4. Turbulence Modelling).

The initial conditions were based on the EASA 45 minute hold case in continuous icing conditions. The computed to a Mach number was 0.347. ANSYS FLUENT provides 10 different inlet and outlet conditions. For compressible flow the pressure inlet and pressure outlet boundary conditions were used throughout this project.

Boundary and Initial Conditions:

The stagnation or total pressure was a required field when the Pressure Inlet boundary condition was applied. Atmospheric pressure at 17000ft equated to 52723Pa.

Throughout this study the ideal gas law was used. Although the ideal gas law was used and density was computed, the initial value for density was an important parameter.

Total Pressure:	57717Pascals
Gauge Pressure:	52723Pascals
Total Temperature:	264.176Kelvin
Turbulent Intensity	5%
Turbulent Length Scale:	0.0025metres
Initial Density:	0.721759kgms^{-2}

Table 5.1: ANSYS FLUENT Solver Variables

5.2. Boeing 737-700 Clean Cruise Configuration Mesh Dependency Study

Three meshes were produced for the clean cruise configuration airfoil geometry.

The observed variations in lift and drag coefficients for each of the three meshes was for the mesh dependency study. Review of these variations can be seen in Table 5.2. Equation 5.13 & Equation 5.11 gave the estimated numerical solution for the lift and drag coefficient as 0.492±0.013 and 0.0106±0.164 with 95% confidence level (Table 5.3).

Clean B737 Mesh Dependency Study	Total Number of Elements	Elements in Boundary Layer	Run Time (minutes)	Coefficient of Lift	Coefficient of Drag	Coefficient of Lift Variation Against Clean Mesh 1 (%)	Coefficient of Drag Variation Against Clean Mesh 1 (%)
Clean 1	72756	46768	9	0.494	0.0101	0.00%	0.00%
Clean 2	130684	101178	12	0.497	0.0097	0.63%	3.49%
Clean 3	351212	242048	39	0.498	0.0099	0.75%	1.48%

Table 5.2: Clean Configuration Boeing 737-700 Mesh Dependency Force Coefficient Variation

Clean B737 Mesh Dependency Study	Coefficient of Lift Variation Against Estimated Numerical Solution (%)	Coefficient of Drag Variation Against Estimated Numerical Solution (%)
Clean 1	0.80%	2.13%
Clean 2	0.18%	5.54%
Clean 3	0.06%	3.58%

Table 5.3: Clean Configuration Boeing 737-700 Mesh Dependency GCI Variation

The variation for drag coefficient against the estimated numerical solution of 2.13%, 5.54% and 3.58% was found for clean meshes 1, 2 and 3 respectively and did not converge to a specific value as seen with the lift coefficients in Table 5.2. This variation produced a large GCI and with a safety factor which multiplied the relative error term leading to a large error range. Another factor to consider was that the actual drag coefficient values were very small and when compared against an exact function; this quantified value becomes large.

The lift coefficient error range in contrast was one order of magnitude smaller and a clear indication that all three clean cruise configurations meshes were converging towards a stable lift coefficient value. The two final columns in Table 5.2 show the force coefficient variation from the estimated numerical solution.

The clean wing results in Figure 5.5 highlighted a maximum variation from the estimated numerical force coefficients of 0.80% and 5.54% for the lift coefficient and drag coefficient respectively. The time for a converged solution ranged from 9 minutes to 39 minutes. The Clean Run 2 mesh (130684 elements) provided a result within 3.49% and 0.62% of Clean Run 1 for lift and drag coefficient

respectively. This CFD run time was 12 minutes, an increase of 33.3% relative to Clean Run 1. The lift coefficient for this run offered the largest variation compared to all clean runs. No difference was found in any aspect of the CFD case to account for this variation. The variation between Clean Run 1 (72756 elements) and Clean Run 3 (351212) was 0.74% and 1.03% for the lift and drag coefficients respectively which equated to an element number increase of 382%. The time taken for Clean Run 3 was 333% longer than Clean Run 1 and did not offer a significant improvement in force values to warrant its usage.

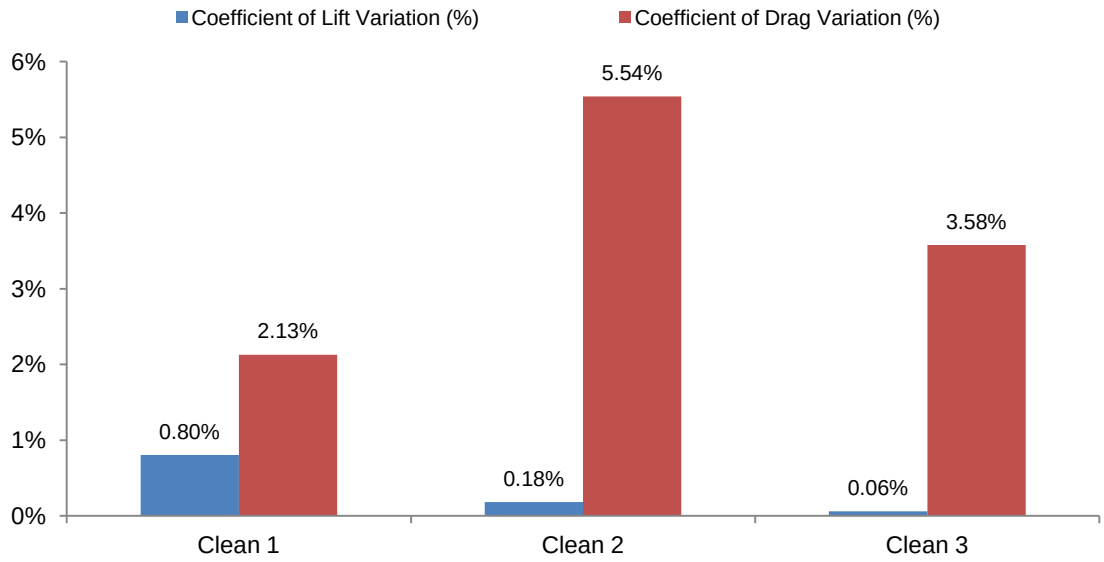

Figure 5.5: Boeing 737-700 Clean Cruise Configuration Lift & Drag Coefficient Variation against Estimated Numerical Solution

To conclude all three clean run meshes were within the confidence level defined by Roache, [53]. The maximum variation in the force coefficients for the coarsest and finest meshes was too small to justify the increased computation costs. Therefore the chosen clean mesh for the optimisation process and datum considerations was Clean Run 1.

5.3. B737-700 Iced Cruise Configuration Mesh Dependency Study

The iced mesh was more important as this was the main datum mesh used for all runback ice cases. The mesh was again a compromise between the force coefficient variations for different mesh densities compared to computational run times. The hexcore structured boundary layer was created to allow for boundary layer grown and effect of airfoil shapes changes. A schematic of the runback ice shape location along the chord and runback ice height relative to boundary layer thickness was shown in Figure 1.1. Three iced configuration meshes of

different densities were evaluated. The force coefficient results are shown Table 5.4.

Iced B737 Mesh Dependency Study	Total Number of Elements	Elements in Boundary Layer	Run Time (minutes)	Coefficient of Lift	Coefficient of Drag	Coefficient of Lift Variation Against Iced Mesh 1 (%)	Coefficient of Drag Variation Against Iced Mesh 1 (%)
Iced Run 1	74404	50560	12	0.466	0.0121	0.00%	0.00%
Iced Run 2	109582	81760	14	0.473	0.0121	1.47%	0.20%
Iced Run 3	340524	242048	37	0.474	0.0121	1.62%	0.29%

Table 5.4: Iced Configuration Boeing 737-700 Mesh Dependency Force Coefficient Variation

The estimated numerical solution for the lift and drag coefficient was 0.473±0.00181 and 0.0121±0.03709 with 95% confidence level. All runs were within the estimated error band. The variation in the force coefficients for all three iced configurations meshes against the estimated numerical solution are shown in Table 5.5.

Iced B737 Mesh Dependency Study	Coefficient of Lift Variation Against Iced Mesh 1 (%)	Coefficient of Drag Variation Against Iced Mesh 1 (%)
Iced Run 1	1.63%	0.45%
Iced Run 2	0.18%	0.26%
Iced Run 3	0.04%	0.17%

Table 5.5: Iced Configuration Boeing 737-700 Mesh Dependency GCI Variation

All three iced configuration meshes produced consistent results and compared well with the estimated numerical solution. Iced Run 2 and Iced Run 3 had an element number increase of 47% and 357% against iced run 1 respectively. The extra computational cost (run time) relative to Ice Run 1 was 16% and 208% for Ice Run 2 and Ice Run 3 respectively. The variation in force values for Ice Run 2 was 1.45% and 0.2% for lift and drag coefficient respectively. The variation in force values for Ice Run 3 was 1.59% and 0.29% (Figure 5.6).The maximum variation for Ice Run 2 and 3 force coefficients were very small. These small variations did not merit the extra computational costs when the Ice Run 1 mesh produced near identical results. Consequently the chosen mesh for the optimisation process and datum considerations is Ice Run 1.

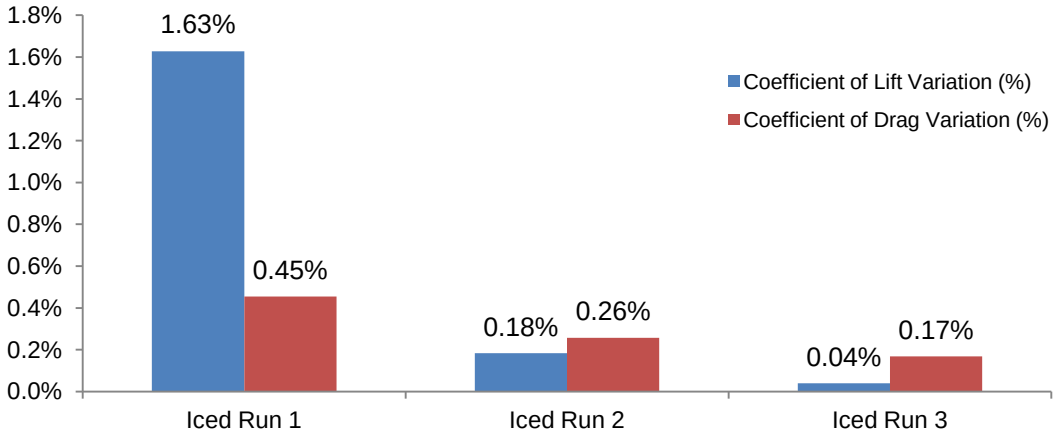

Figure 5.6: Boeing 737-700 Iced Cruise Configuration Lift & Drag Coefficient Variation against Estimated Numerical Solution

The iced meshes provide a more consistent result with respect to mesh density as a result of smaller grid density variations. This was because the total number of elements for clean mesh 1 and 2 was larger than for the iced meshes. However the actual force coefficient difference between all three clean meshes was small.

5.4. 2D CFD Boeing 737-700 Runback Ice Study

A study on the performance degradation is considered in this section. Table 5.6 shows the percentage losses for lift and drag coefficients for each corresponding mesh case. The datum ice location ($^{x}/_{c} = 0.0023$) provided a consistent loss in lift of around 5-6% for all three mesh densities. The drag loss for all three meshes ranged from 17-20%.

Run Comparison	Coefficient of Lift Decrease (%)	Coefficient of Drag Increase (%)
Clean Run 1 & Ice Run 1	5.73%	16.92%
Clean Run 2 & Ice Run 2	4.95%	19.97%
Clean Run 3 & Ice Run 3	4.92%	18.00%

Table 5.6: Performance Loss Comparison Grid Dependency Study

From this point onwards comparison of the chosen datum runs from the validation section in this chapter are considered, i.e. Clean Run 1 and Ice Run 1. The performance loss for the lift and drag coefficients are shown in Figure 5.7 & Figure 5.8.

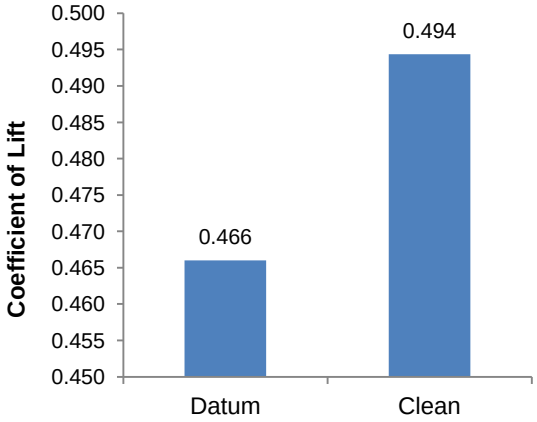

Figure 5.7: Lift Coefficient Comparison of Clean Run against Datum Run

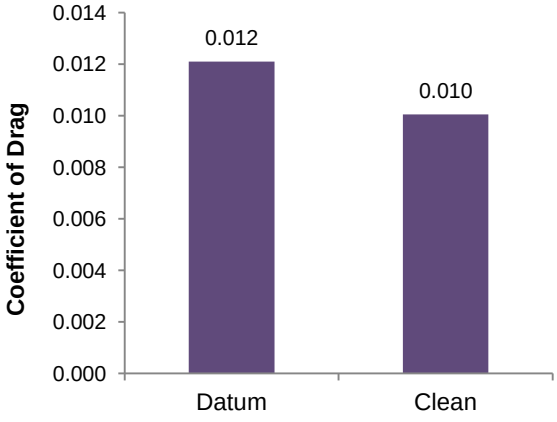

Figure 5.8: Drag Coefficient Comparison of Clean Run against Datum Run

There was a significant increase in the drag coefficient with the ice location set at 0.0915m along the chord (x/c= 0.023). However the lift coefficient reduction was smaller than drag coefficient increase.

The available literature on runback/ridge ice studies offer an understanding on which factors may affect the performance reductions. Authors such as Pan, et al., [108] and Broeren, et al., [109] found the runback/ridge ice size at critical locations along the chord on the airfoil are key variables that affect the performance degradation.

Pan, et al., [108] found a non-linear relationship between ice shape size and reduction in lift. Comparison with published data for force coefficients was not an option as a suitable ice height to chord ratio (k/c), ice location with respect to chord position (x/c) and airfoil (Boeing 737-700 in cruise configuration) was non-existent. However parametric finding and trends with regards to flow interaction highlighted flow features and key contributors to force coefficient degradation.

Figure 5.9 provides a pressure coefficient comparison for both the clean and iced configuration airfoil case.

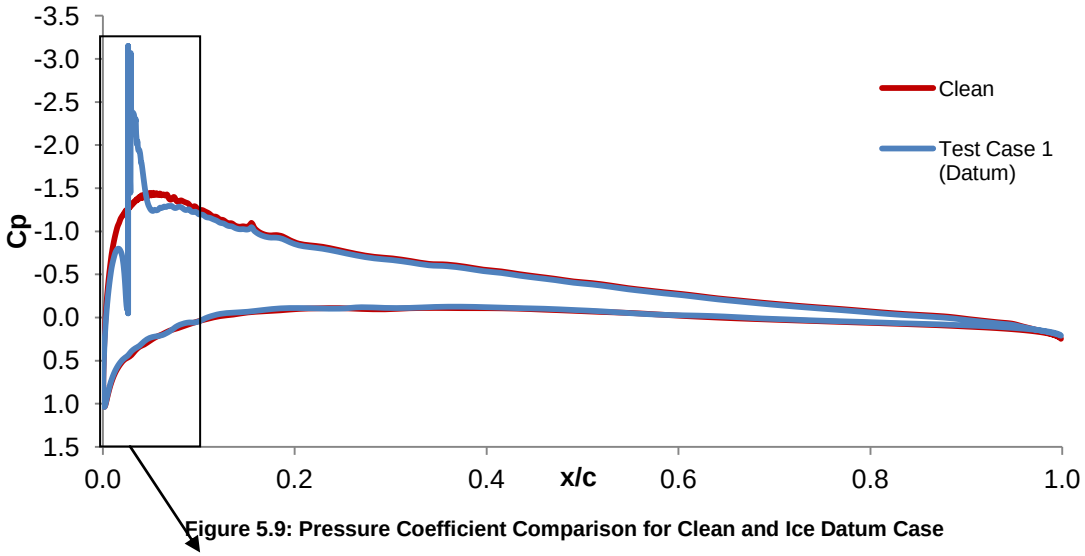

Figure 5.9: Pressure Coefficient Comparison for Clean and Ice Datum Case

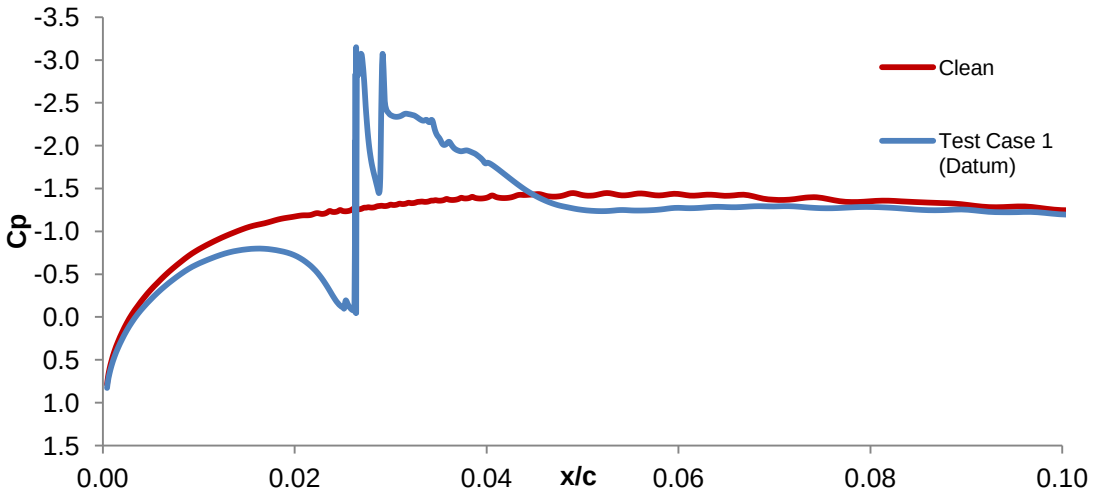

Figure 5.10: Pressure Coefficient Comparison Close to Ice Region for Clean and Datum Case

The pressure coefficient comparison close to the leading edge (Figure 5.10) showed the sharp change in pressure when in contact with the runback ice. There was an increase in the pressure at the leading edge of the runback ice shape; this was due to the front face blockage creating a localised stagnation point. This was followed by a sharp drop in pressure as the flow over the ice shape was accelerated to its maximum velocity causing a low pressure zone above the ice shape. A sharp feature where the pressure suddenly increased and decreased was observed. This feature was due to a small recirculation zone close to the highest point of the runback ice shape (Figure 5.11 & Figure 5.12). Just before x/c = 0.03 the flow was observed to detach and the separation bubble began to form. During this region a more aggressive adverse pressure gradient was observed up to x/c=0.05 and from then onwards the iced configuration Cp distribution was similar to the clean configuration (

Figure 5.9).

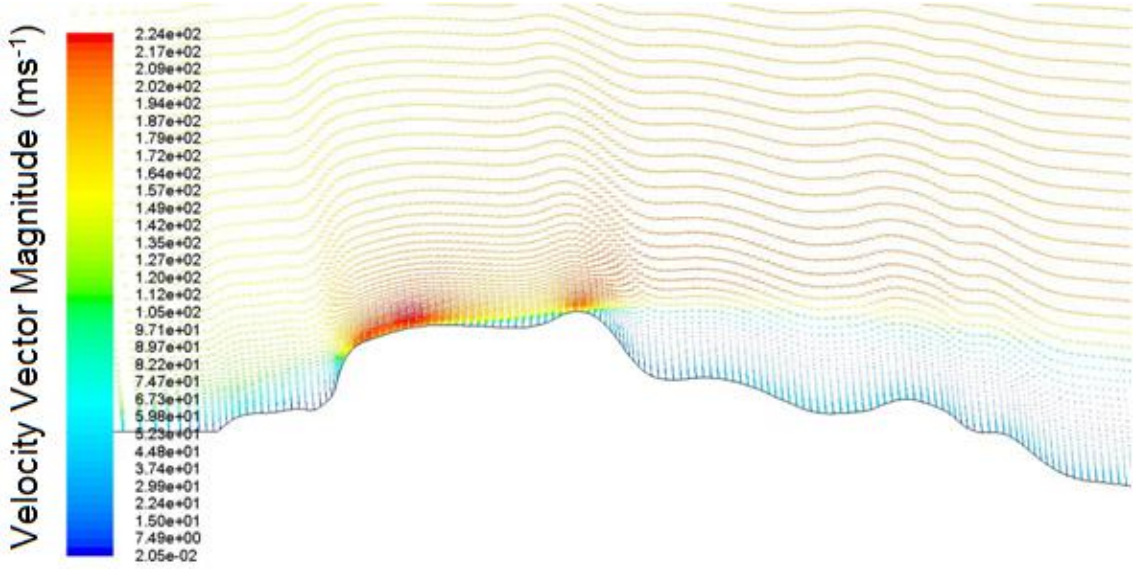

Figure 5.11: Velocity Vectors for Datum Runback Ice Case

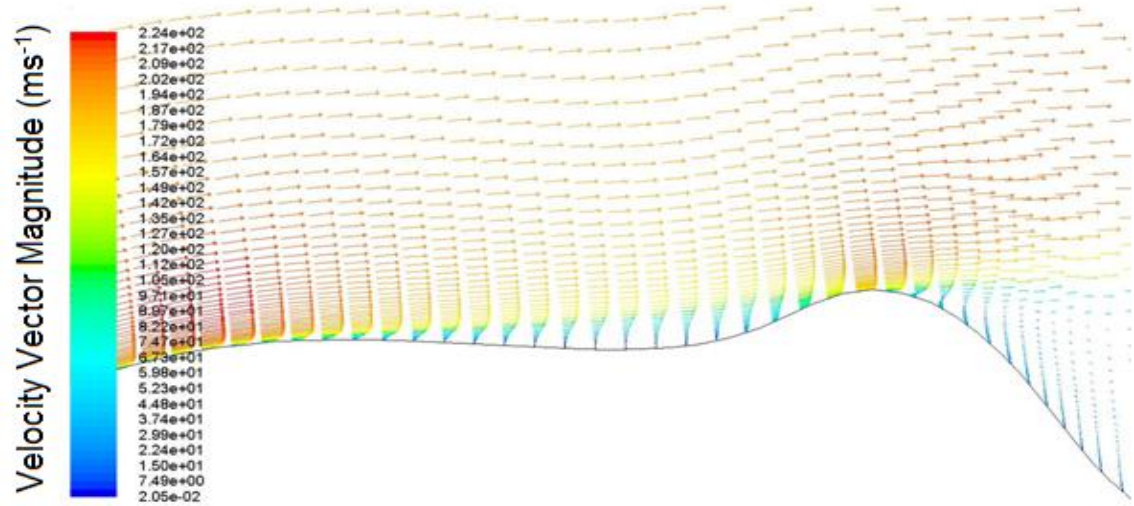

Figure 5.12: Velocity Vectors for Datum Runback Ice Case Depicting Recirculation Zone

Lee, et al., [110] identified that the critical location for runback ice shape was near (but upstream of) the location of the largest adverse pressure gradient of the clean airfoil and downstream of the location of minimum surface pressure. However for this study the runback ice was located at x/c=0.023. At this location the suction surface velocity was accelerating to reach maximum velocity and peak minimum pressure. Since the location was not within the critical location the runback ice did not stop the flow achieving its minimum Cp. The lower surface remained undisturbed and the overall pressure variation across the upper and lower surface was very similar to the clean configuration. The velocity and pressure contour plot in Figure 5.13 and Figure 5.14 respectively help visualise the change in velocity and pressure.

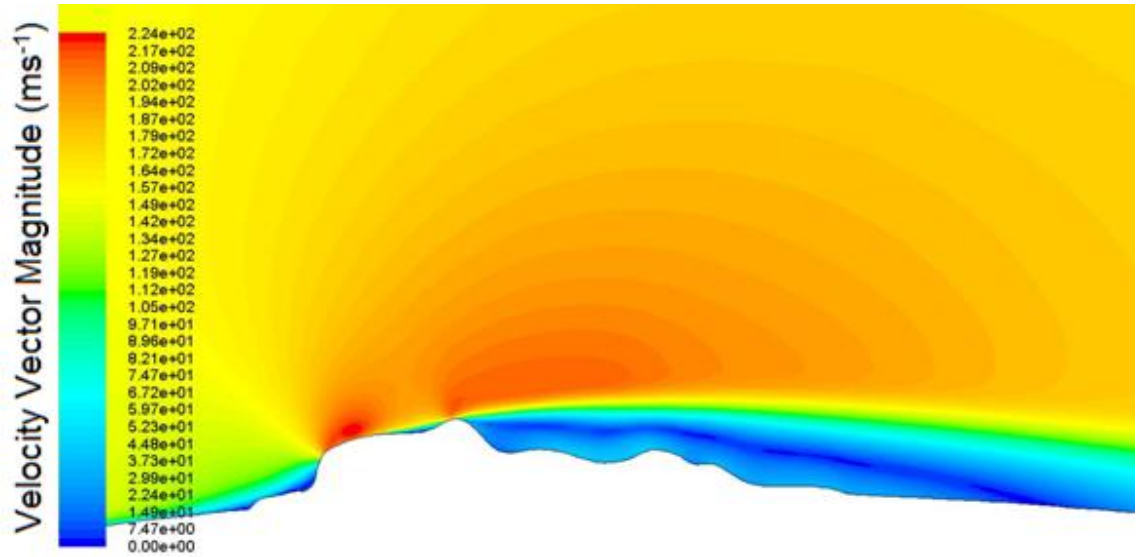

Figure 5.13: Steady State Velocity Contour Plot for Ice Run 1

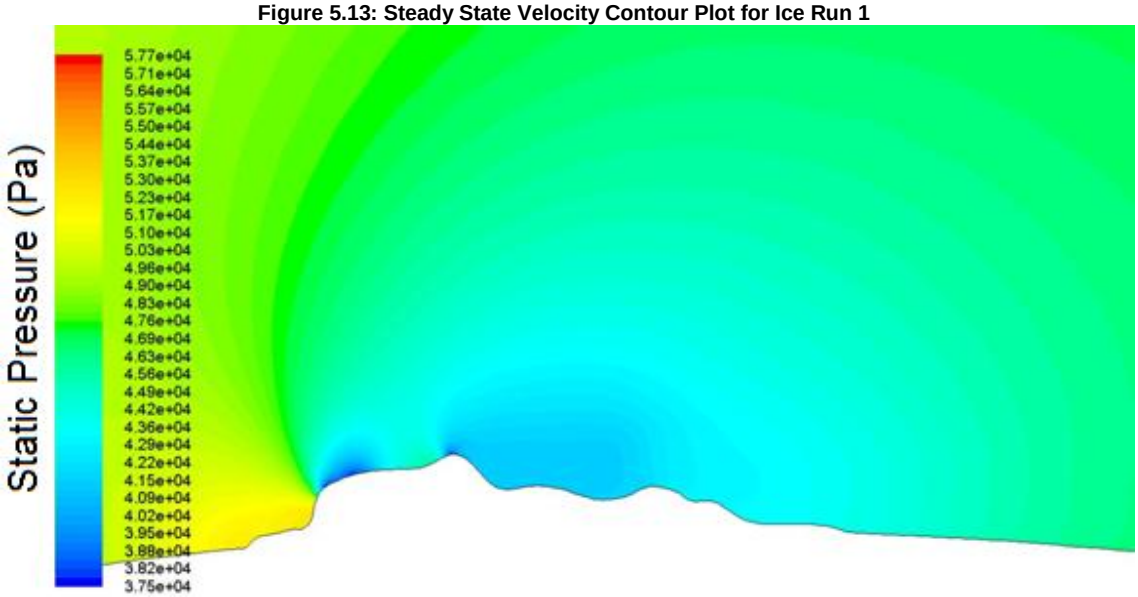

Figure 5.14: Static Pressure Contour Plot for Ice Run 1

The separation and reattachment zone was observed via the shear stress along the direction of the flow shown in Figure 5.15. The location where the shear stress became negative indicated flow separation (x/c = 0.024). Reattachment was indicated when the shear stress became positive (x/c = 0.046). The wake region produced an increase in form drag. Figure 5.16 shows the full chord extent of the shear stress. A more aggressive adverse pressure gradient observed in iced datum configuration relative to the clean configuration reduced the shear stress on the airfoil but increased form drag.

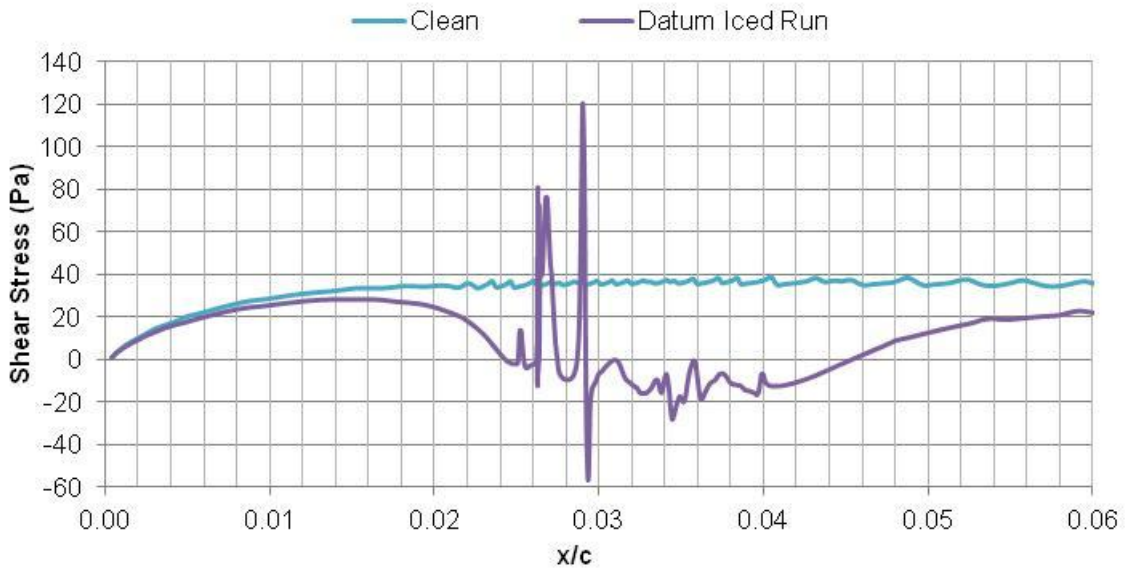

Figure 5.15: Shear Stress Plot for Clean and Iced Datum Configuration at Runback Ice Location

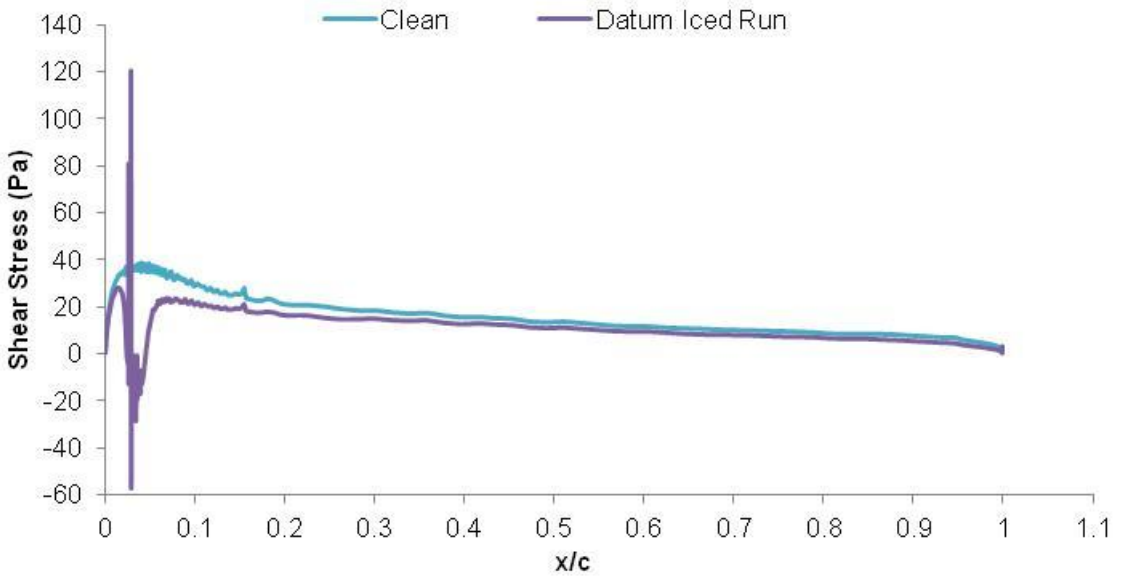

Figure 5.16: Shear Stress Plot for Clean and Iced Datum Configuration

The 16.9% increase in drag for the iced configuration was attributed to the form drag created by the separated flow aft of the ice shape and the more aggressive adverse pressure gradient.

5.5. Runback Ice Structure Geometrical Analysis

Numerical simulation studies for complex flows require validation with published literature. In this section further attempts to find suitable means of validating the iced configuration results are sought. Much data available on runback ice phenomena entails the use of generic quarter-circle ice shapes called ridge ice.

A parametric study on the flow features brought about by different runback ice and ridge ice geometries were examined to determine if the ridge ice studies or simplified shapes could emulate the geometry of a detailed runback ice profile. Four different ice geometries were evaluated (Table 5.7). This study provided some insight into how the flow behaves with harsh steps as shown in Figure 5.19 and Figure 5.20.

Datum Iced Run	Figure 5.17	Full runback ice geometry (datum) reported in Section 5.3
Test Case 2	Figure 5.18	Leading edge of datum runback ice up to peak height
Test Case 3	Figure 5.19	Trailing edge of datum runback ice starting from peak height
Test Case 4	Figure 5.20	Ridge ice with height equal to runback ice peak height

Table 5.7: Description of Tested Ice Shapes

Figure 5.17: Datum Iced Run- Geometry for Full Runback Ice Geometry (datum)

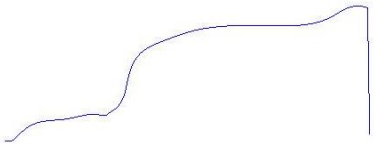

Figure 5.18: Test Case 2 – Geometry for Leading Edge of Datum Runback Ice

Figure 5.19: Test Case 3 – Geometry for Trailing Edge of Datum Runback Ice

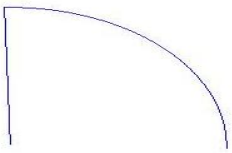

Figure 5.20: Test Case 4 - Geometry for Ridge Ice Shape

The validated iced configuration mesh from Section 5.3 was used for test cases 2, 3 and 4. Small variations to the blocking structure were required. Although a mesh dependency study was not conducted an extensive verification and validation for the datum iced run was deemed acceptable in terms of mesh quality and validity of results. The mesh changes made are shown in Figure 5.21 through to Figure 5.24. Test Cases 2, 3 and 4 required denser grid spacing around the sharp edges. The abrupt changes in the flow required an adequately denser grid spacing to capture these changes.

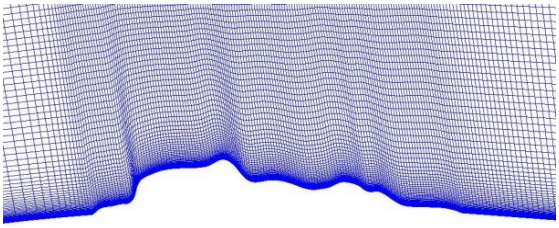

Figure 5.21: Datum Iced Run- Mesh for Full Runback Ice Geometry (Datum)

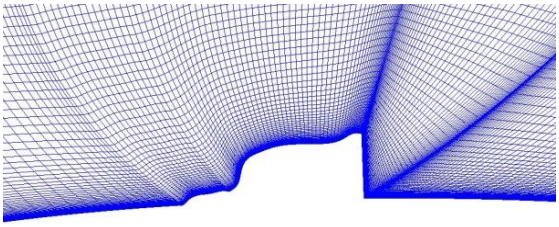

Figure 5.22: Test Case 2 – Mesh for Leading Edge of Datum Runback Ice

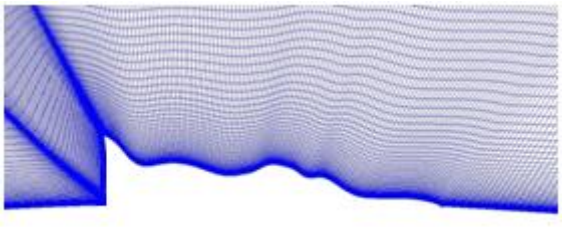

Figure 5.23: Test Case 3 – Mesh for Trailing Edge of Datum Runback Ice

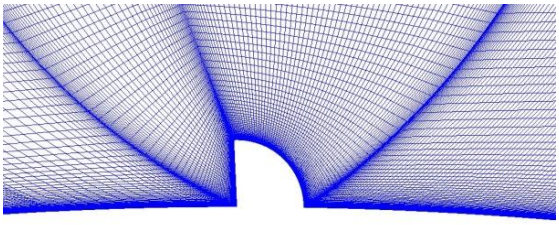

Figure 5.24: Test Case 4 - Mesh for Ridge Ice Shape

The force coefficients for each run are presented and provided an opportunity to compare the effects of high-fidelity geometrical features on the lift and drag coefficient.

Figure 5.25 and Figure 5.26 showed the datum iced run and test case 2 produced similar force coefficients with a variation between them of 1.13% and 8.68% for lift and drag coefficient respectively.

Test Case 3 and 4 produced similar force coefficient results with a variation between them of 0.39% and 2.78% for lift and drag coefficient respectively.

The variation in the lift and drag coefficient for test cases 2, 3 and 4 are shown in Figure 5.27. The comparison was against the datum iced run. The ridge ice shapes for test case 3 and 4 modify the flow field enough for a significant variation in force coefficients.

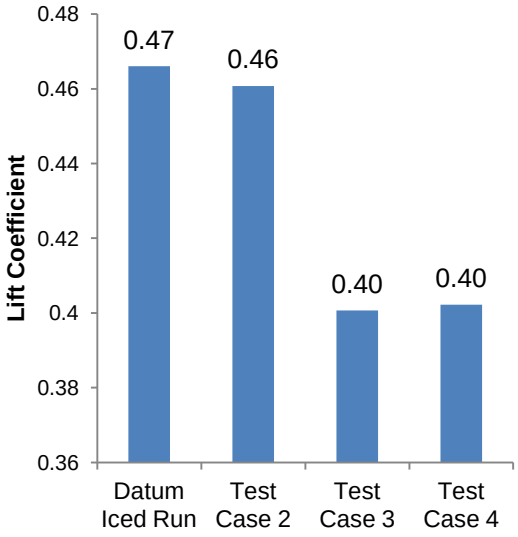

Figure 5.25: Lift Coefficient Comparison for Ice Structure Analysis

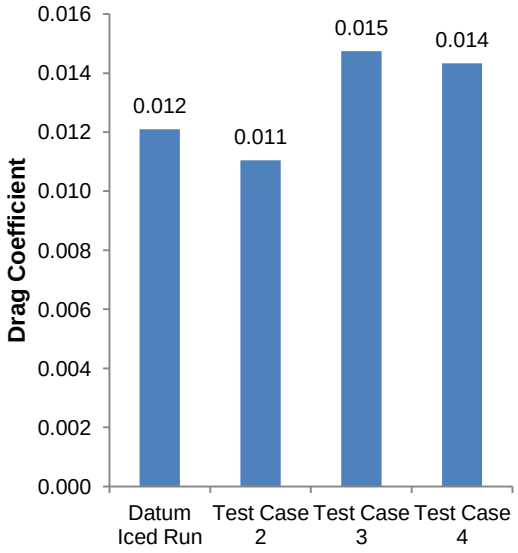

Figure 5.26: Drag Coefficient Comparison for Ice Structure Analysis

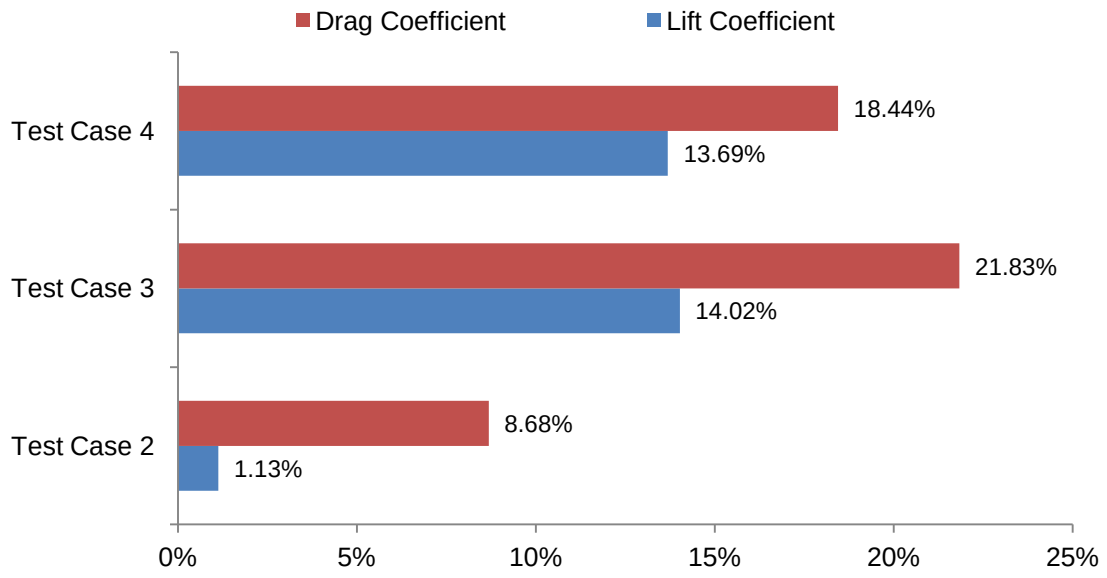

Figure 5.27: Force Coefficient Variation against Test Case 1 for Ice Structure Analysis

The runback ice profiles with 'streamline-type' leading edges showed strong similarities in lift but less for drag (8.7% variation). The sharp ridge type ice profiles show very strong force coefficient agreements. From this point onwards the datum iced run and 2 will be categorised as streamline ice shapes. Test case 3 and 4 will be categorised as ridge ice shapes.

The pressure coefficient profiles for the test cases are shown in Figure 5.28. From $^{x}/_{c} = 0.14$ onwards the pressure profiles for the suction surface were very similar. The ridge ice profiles (test case 3 & 4) produced a slightly higher

pressure coefficient across the chord length. The loss of suction pressure across the upper surface had a direct impact on the overall lift produced. There was no noticeable change to the lower surface for any of the four cases. Figure 5.29 allows a closer inspection of the pressure profiles up to 0.07x/c.

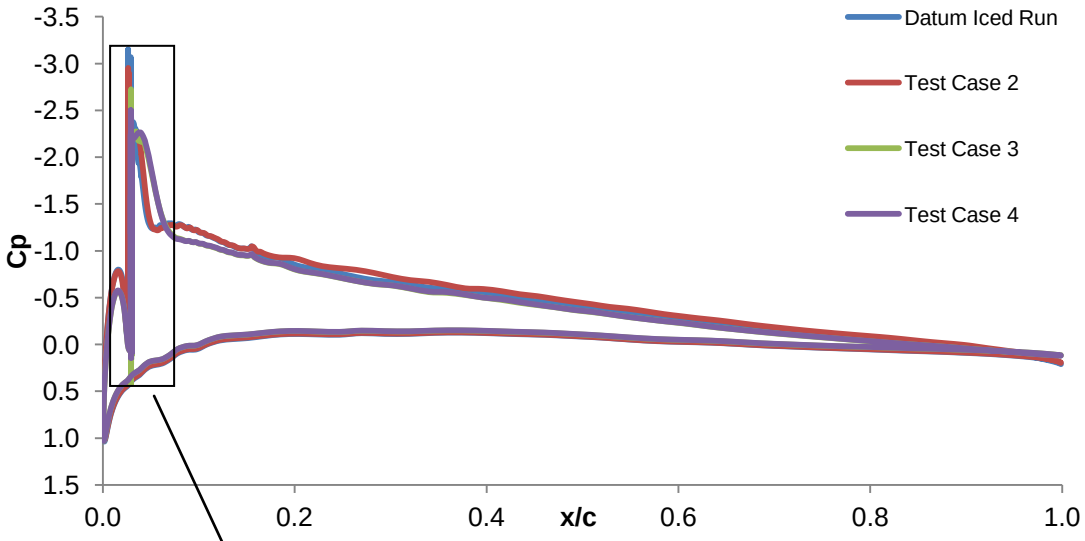

Figure 5.28: Pressure Coefficient Comparison for Ice Structure Analysis

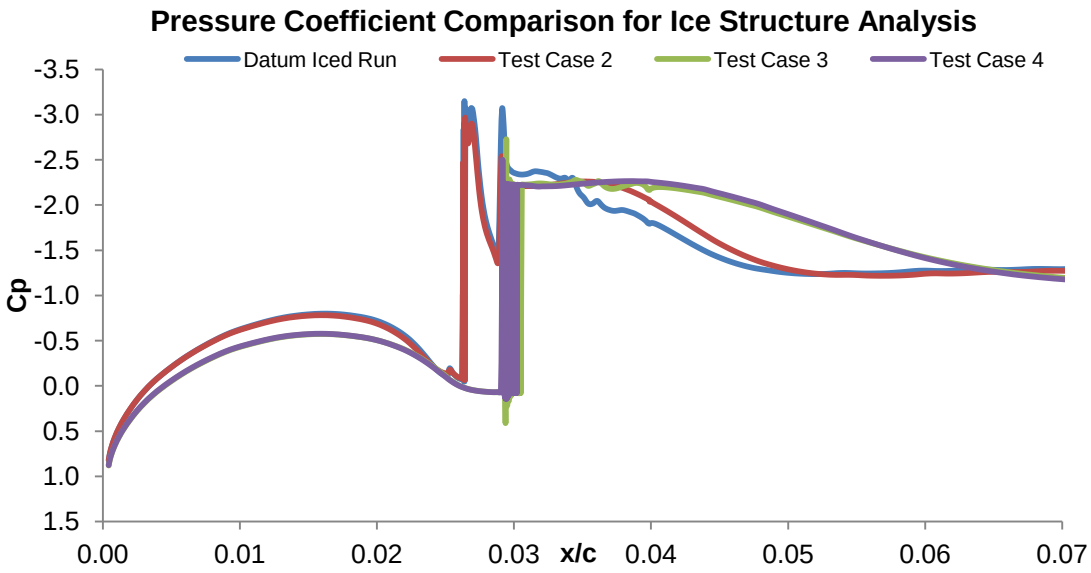

Figure 5.29: Pressure Coefficient Comparison for Ice Structure Analysis at Runback Ice Location

The initial drop in pressure as flow was accelerated along the suction surface from the stagnation point for the streamline type ice shapes (datum iced run & test case 2) showed a stronger minimum pressure coefficient curve up to the local stagnation point (increase in Cp) of the runback ice. This suggested the flow was not decelerated as rapidly as the ridge ice type shapes. This seemed

intuitive as the blockage from the streamline type ice shapes allowed for a ‘softer’ deceleration zone rather than an abrupt blockage in flow similar to the ridge ice shape.

A closer inspection of Figure 5.28 and Figure 5.29 at the leading edge showed the vertical step (blockage) produced a substantial reduction in velocity and a local stagnation point (increase in dynamic pressure). This was followed by the first minimum Cp peak where the flow was accelerated over the ice shape. The peak value in minimum Cp for the datum iced run & test case 2 was not observed for the ridge type runback ice shapes.

There was a sudden increase in pressure as a very small recirculation zone appeared in the uppermost dip in the runback ice.

The second peak in minimum Cp was due to accelerated velocity over the highest point of the streamline type runback ice shapes. The ridge ice shapes produced a single minimum peak in Cp and was observed at the same position as the maximum height of the streamline type ice shapes. This was deliberately done to allow the length of the recirculation zone for the two types of ice shapes to be comparable.

The wake produced by the obstacle in all four cases began at 0.03x/c. The pressure recover region for the streamline type runback ice shapes was more aggressive relative to the ridge type ice shapes. The adverse pressure gradient for the ridge type ice shapes was spread across a larger chord length; a consequence of a larger separation bubble.

A stronger adverse pressure gradient was observed for the datum iced run relative to test case 2 which resulted in a shorter reattachment position. Extensive work on flow separation and the mechanism for reattachment was conducted by Jovic, [111] and found:

“*The separated shear layer is influenced by the strong adverse pressure gradient, the short development length, the presence of a highly turbulent recirculating flow beneath it and a sheared turbulent boundary layer above it, and possibly by the streamline curvature.*” [111]

The development length and to a large extent the streamline curvature remain unchanged for the datum iced run and test case 2. A possible reason for the variation observed in the reattachment position for the datum iced run and test case 2 could be attributed to the difference in pressure recovery and the variation in the recirculation flow properties. It was postulated; due to the

presence, or lack of, trailing edge of runback ice shape, the adverse pressure gradient for the datum iced run allowed greater entrainment for the local recirculation zone and therefore quicker recovery and reattachment.

The velocity profiles for each test case around the separation bubble are shown in Figure 5.30 through to Figure 5.33. Only the two ridge type ice shapes visibly exhibit similar recirculation zones.

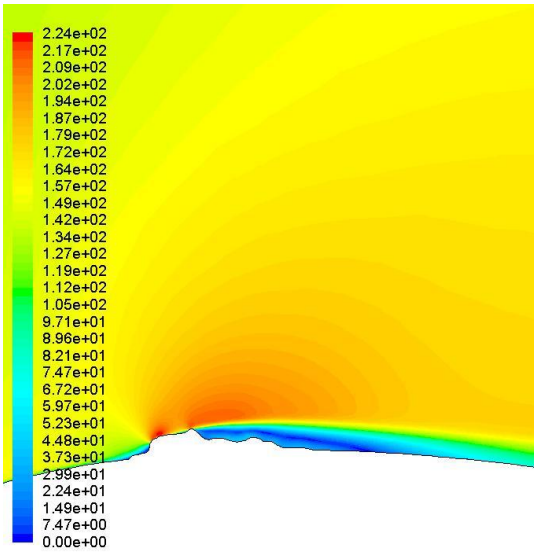

Figure 5.30: Velocity Contour for Datum Iced Run in Ice Structure Analysis

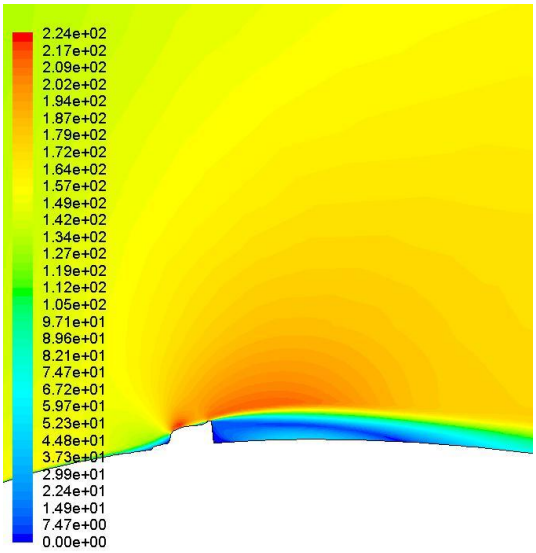

Figure 5.31: Velocity Contour for Test Case 2 in Ice Structure Analysis

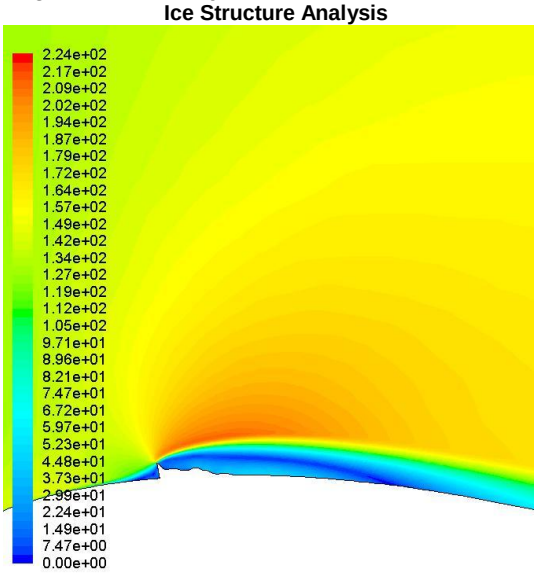

Figure 5.32: Velocity Contour for Test Case 3 in Ice Structure Analysis

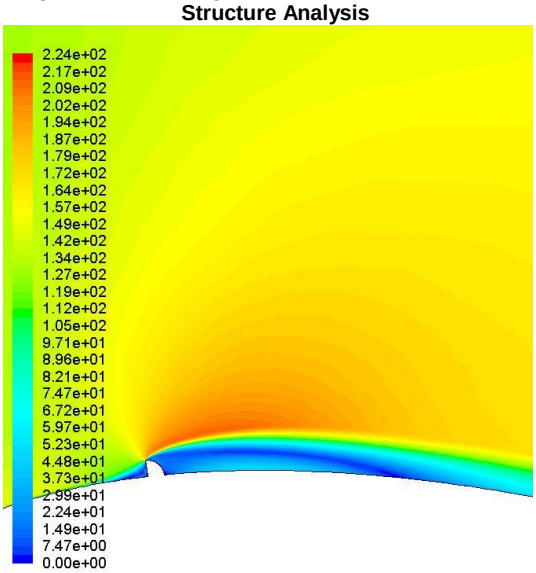

Figure 5.33: Velocity Contour for Test Case 4 in Ice Structure Analysis

A more quantitative inspection on the length of the separated region was considered from the shear stress profile across the chord. The shear stress profiles for all test cases are shown in Figure 5.35 and provided the location of

reattachment. The streamline type ice shapes reattached at 0.0453x/c and 0.0473x/c for the datum iced run and test case 2 respectively.

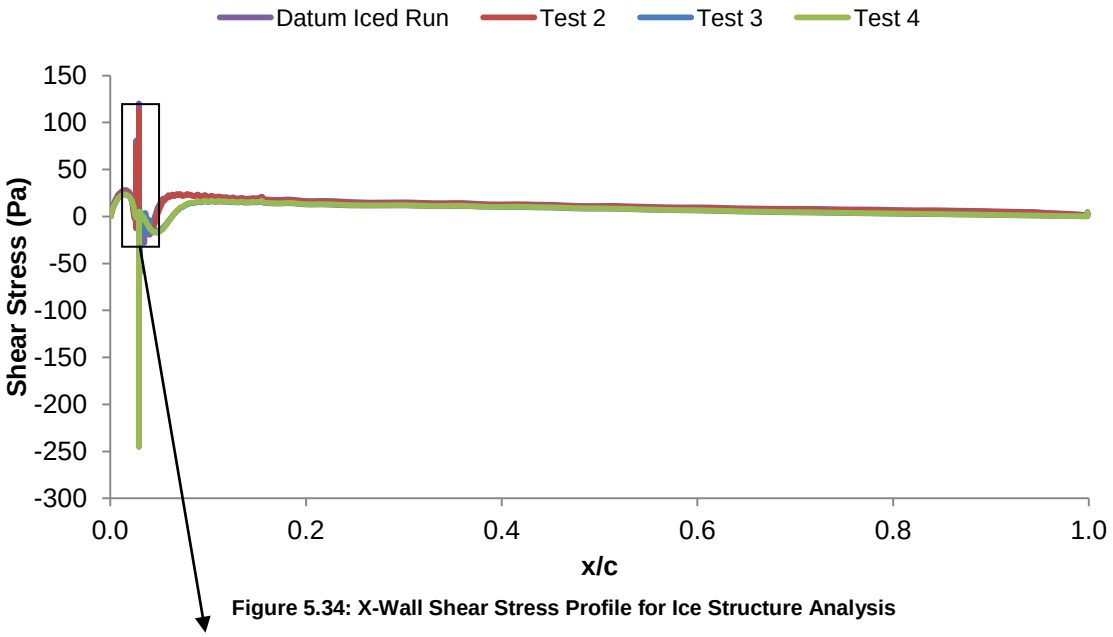

Figure 5.34: X-Wall Shear Stress Profile for Ice Structure Analysis

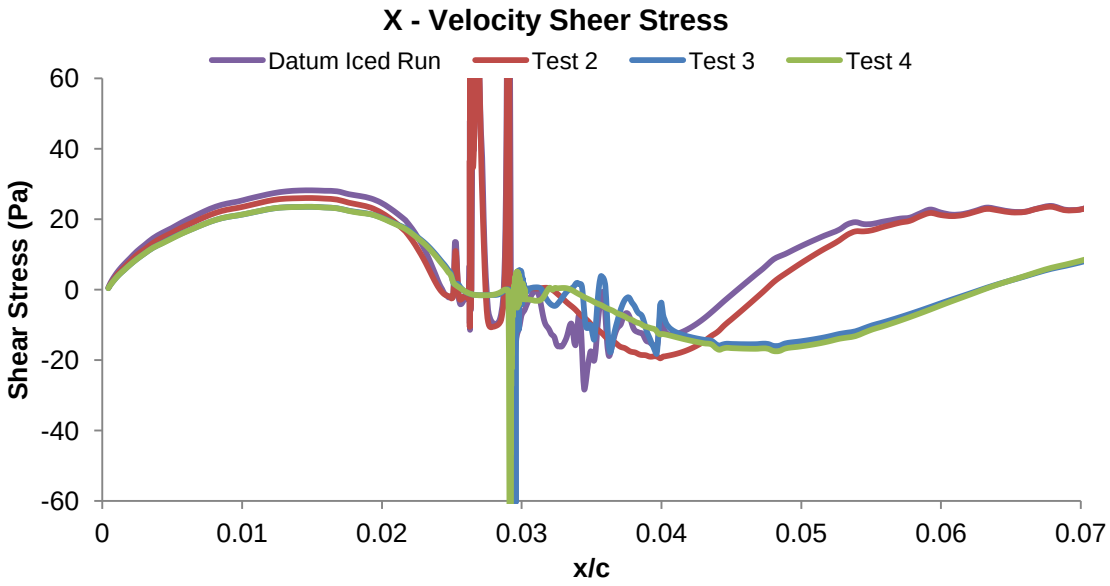

Figure 5.35: X-Wall Shear Stress Profile for Ice Structure Analysis at Runback Ice Location

Figure 5.36 provided a clearer profile of shear stress for the datum iced run and test case 2 around the wake region. A point of interest was the different reattachment points for the streamline type and ridge type ice shapes but also the variation in reattachment for both streamline types' runback ice shapes (datum iced case and test case 2). In Figure 5.36 the initial increase in shear stress up to 0.016x/c was a result of accelerated flow along the suction surface.

The observed difference in shear stress profile up to this point indicated a difference in the flow properties before the ice shape had been reached. Figure 5.37 confirms there was a variation in the flow properties at the leading edge. The minimum Cp peak for test case 2 was reduced relative to the datum iced run.

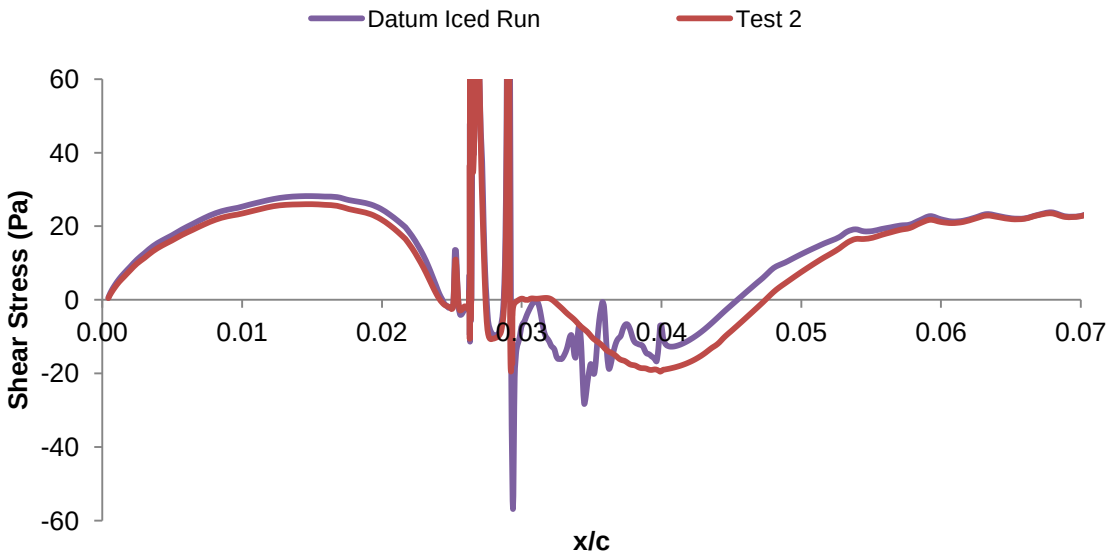

Figure 5.36: X-Velocity Shear Stress for Datum Iced Run and Test Case 2 at Runback Ice Location

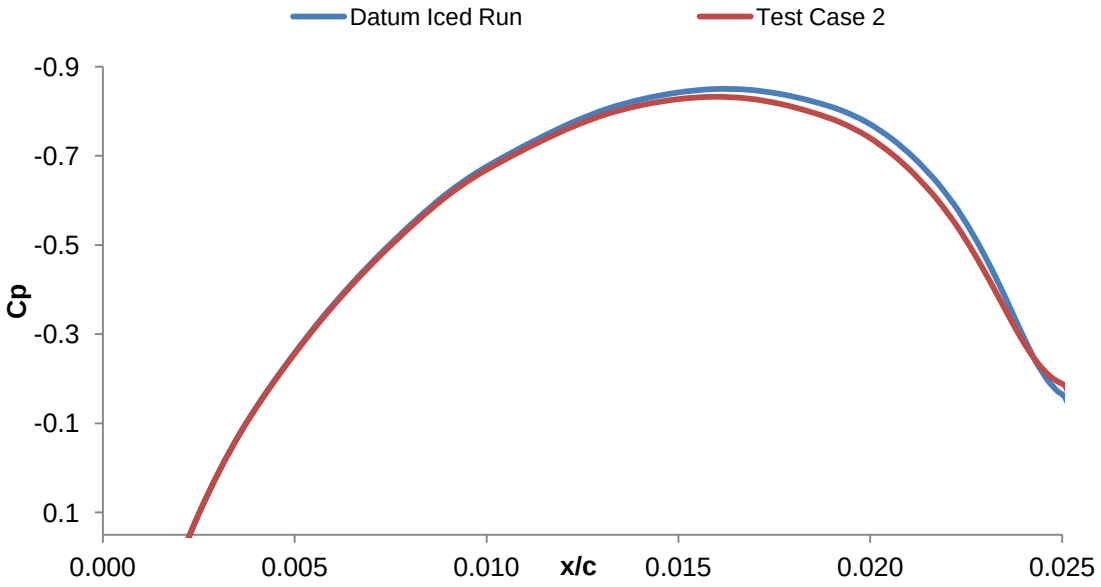

Figure 5.37: Pressure Coefficient Comparison of Suction Surface for Ice Structure Analysis at Leading Edge

The velocity contours for the datum iced run and test case 2 are shown in Figure 5.38. The contour maps were not equalised to help portray the variation in maximum velocity across the top of the ice shapes. The maximum velocities were 224ms^{-1} and 221ms^{-1} for the datum iced run and test case 2 respectively.

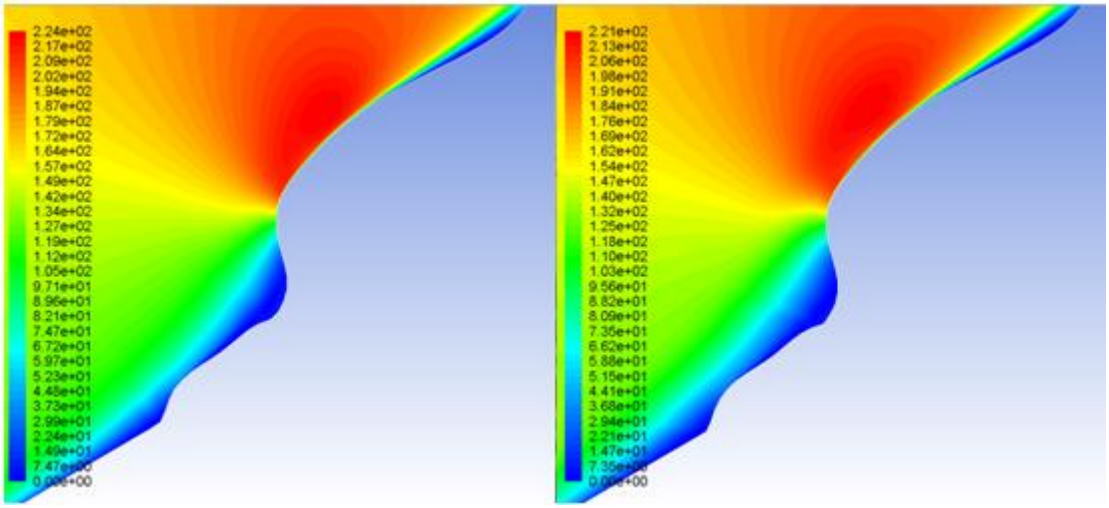

Figure 5.38: Velocity Magnitude Contour Plot Comparison for Datum Iced Run & Test Case 2

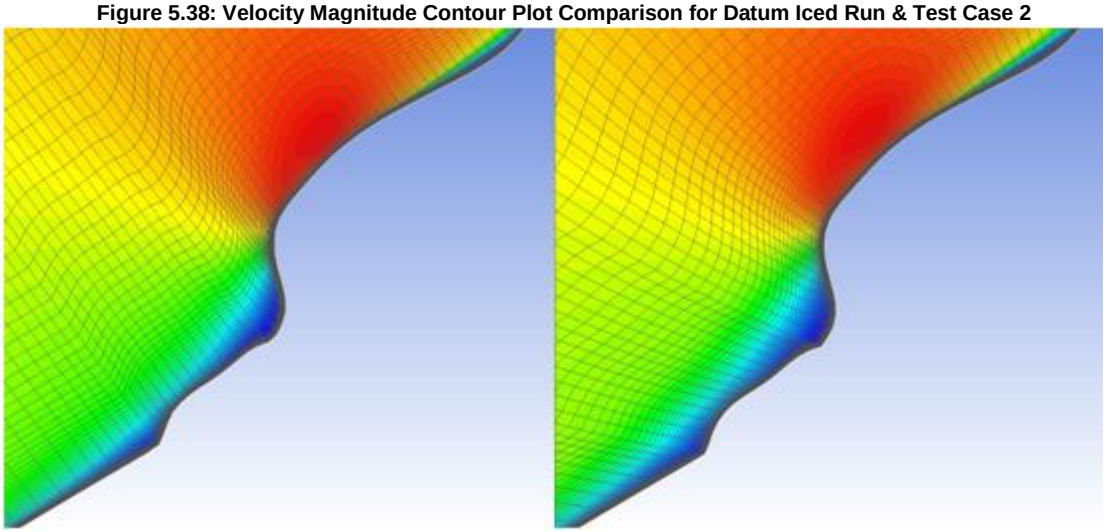

Figure 5.39: Velocity Magnitude Contour Plot Comparison for Datum Iced Run & Test Case 2 (with Mesh)

To eliminate any numerical inconsistencies, the same working mesh file was used for all four test cases. The leading edge geometry and node spacing remained unchanged throughout the ice structure study. The only variation was the skewness around the ice shape.

To verify that these observed differences for the datum iced run and test case 2 are not due mesh quality, a second mesh was created for test case 2 (test case 2a) with the skewness removed. Test case 2a grid spacing remained unchanged relative to the datum iced run.

The results are not shown as no noticeable difference in the C_p, C_f or force coefficients was observed. However there was some variation in the velocity profiles shown below. The revisions made to the mesh for test case 2 are shown in Figure 5.40. These revisions were to the orthogonality of the boundary

layer mesh. Attempts were made to align the elements with the curvature of the airfoil.

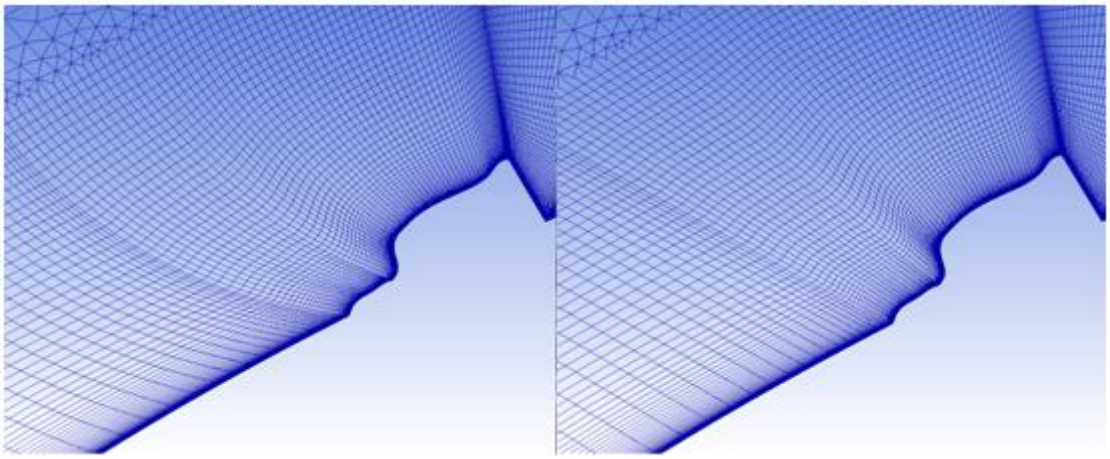

Figure 5.40: Mesh Change Comparison for Test Case 2 & 2a

Five boundary layer velocity profiles were taken for the datum iced run, test case 2 and 2a at positions progressing towards the runback ice shape depicted in Figure 5.41.

The boundary layer profiles in Figure 5.42 though to Figure 5.49 show the normalised velocity profiles for the datum iced run, test case 2 and 2a. The boundary layer profiles are similar for test case 2 and 2a. From 0.022x/c onwards some variations in the velocity distribution close to the ice shape were observed. For all locations in test case 2 and 2a the shape of the boundary layer profiles were similar. Small variations between the datum iced run and test case 2 was observed.

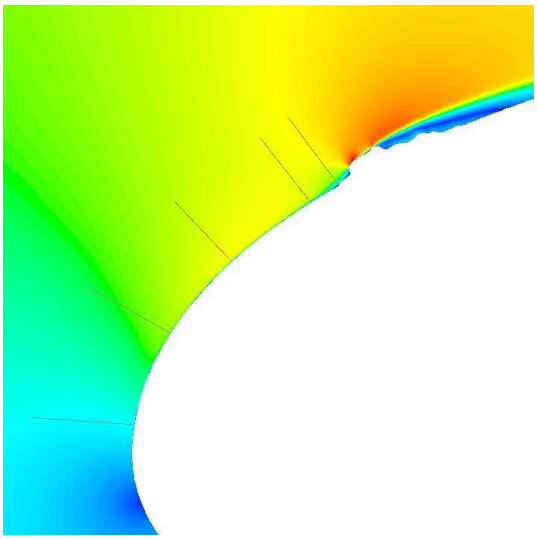

Figure 5.41: Velocity Profile Positions for Ice Structure Analysis

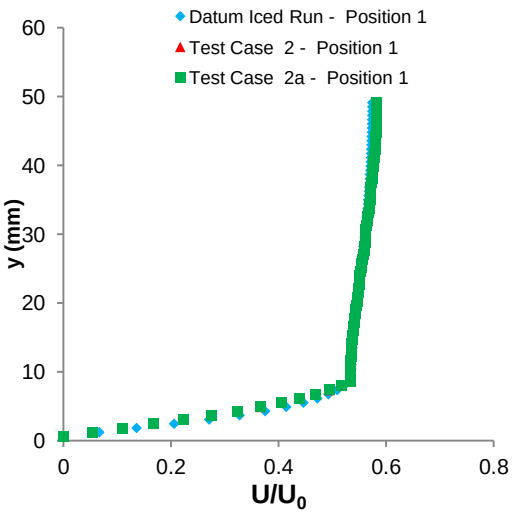

Figure 5.42: Boundary Layer Velocity Profile Plot at x/c 0.0007 for Ice Structure Analysis

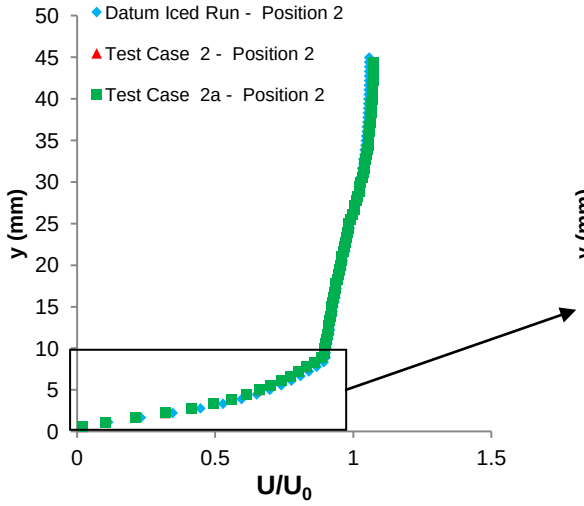

Figure 5.43: Boundary Layer Velocity Profile Plot at x/c 0.005 for Ice Structure Analysis

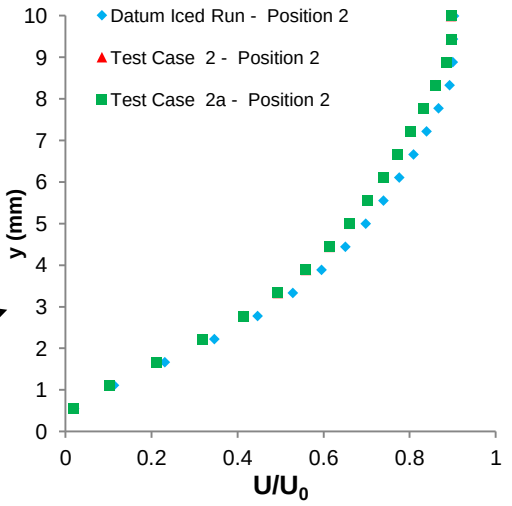

Figure 5.44: Boundary Layer Velocity Profile Plot at x/c 0.005 for Ice Structure Analysis at Boundary

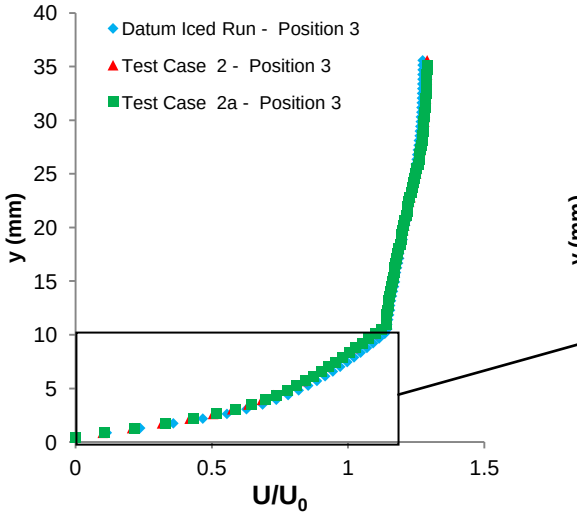

Figure 5.45: Boundary Layer Velocity Profile Plot at x/c 0.012 for Ice Structure Analysis

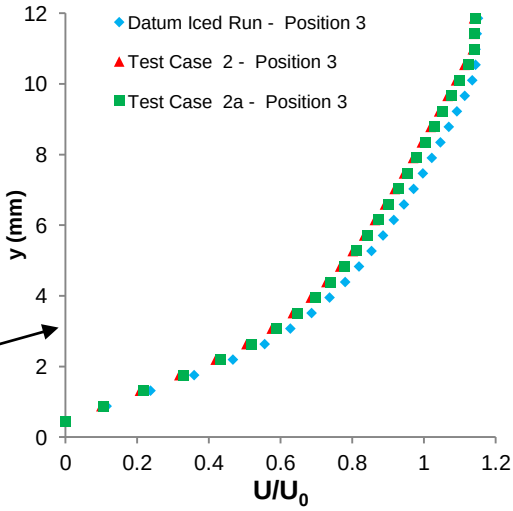

Figure 5.46: Boundary Layer Velocity Profile Plot at x/c 0.012 for Ice Structure Analysis at Boundary

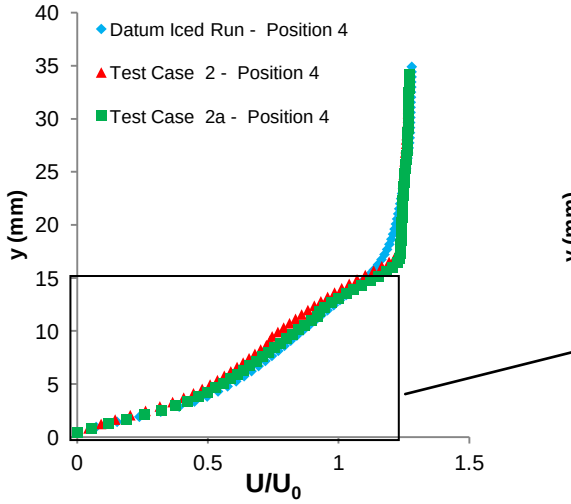

Figure 5.47: Boundary Layer Velocity Profile Plot at x/c 0.022 for Ice Structure Analysis

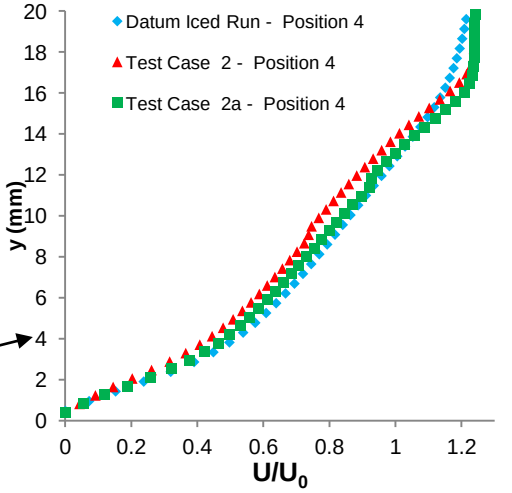

Figure 5.48: Boundary Layer Velocity Profile Plot at x/c 0.022 for Ice Structure Analysis at Boundary

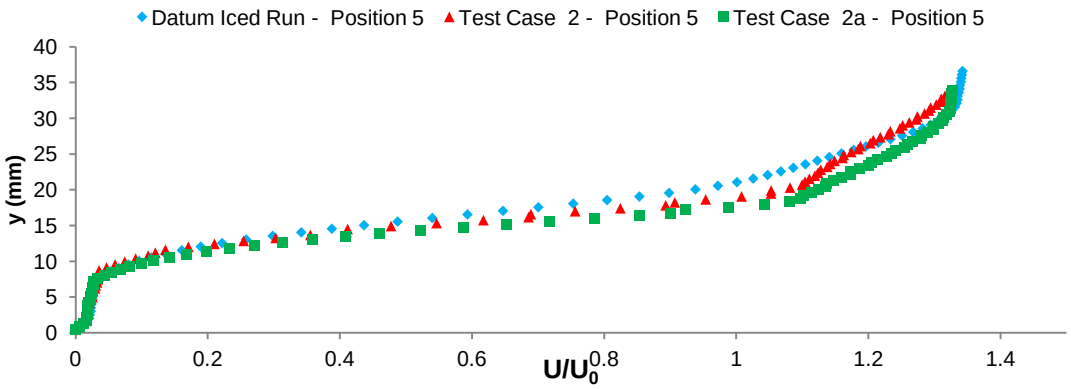

Figure 5.49: Boundary Layer Velocity Profile Plot at x/c 0.025 for Ice Structure Analysis

A clear difference in flow properties for the datum iced location and test case 2 was observed. The boundary layer profiles for the datum iced run were smoother as the flow reached free stream velocity. This feature was not observed for test case 2 or 2a.

The author concedes there were some discrepancies between the velocity profiles in test case 2 and 2a but the overall boundary layer profiles were similar. The aim here was to show the variations in the datum iced run and test case 2 are a result of physical properties and not due to numerical error or uncertainties. The variation between test case 2 and 2a was significantly smaller than the size of the variations observed for between the datum iced location and test case 2. These findings implied observed variations were due to the geometrical features of the runback ice shape affecting the flowfield.

The lack of runback ice geometry in test case 2 allowed for a larger recirculation zone and later reattachment point. Although the flow had separated there was ‘some interaction’ with the recirculating flow in the separation bubble and the runback ice geometry. It remained unclear how the change in geometry in the recirculation zone was affecting the Cp at the leading edge.

The reattachment zone for test case 3 and 4 were close to identical. In this case a reattachment position of 0.0624x/c was found. The ridge type ice shapes produced a substantially longer recirculation zone. Unlike the datum iced run and test case 2, the presence of runback ice geometry and the fluctuation seen in the shear stress did not alter the position of reattachment (Figure 5.50). Although the location of reattachment was unchanged for test case 3 and 4, there was some interaction between the geometry and the fluid in the recirculation zone which caused the fluctuations in shear stress across the wake region.

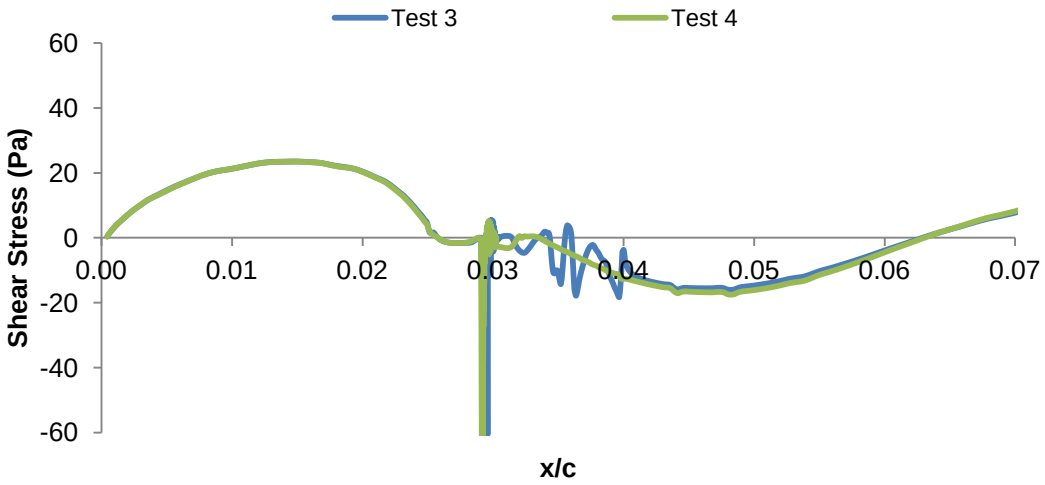

Figure 5.50: X-Velocity Shear Stress for Test Case 3 & 4 at Runback Ice Location

The runback ice structure geometrical analysis found:

- The datum iced run and test case 2 showed similarities in profile but slight variations to reattachment lengths. The presence of a disturbance after the point of detachment played a role on the size of the separation bubble and consequent point of reattachment. Test cases 3 and 4 observed very little variation due to the geometrical features on the back face of the runback ice shape. These same trends were observed by Lee, et al., [110] via experimental testing and showed high-fidelity two-dimensional simulations could capture the detailed flowfield interaction based on subtle geometrical changes.
- An abrupt change in geometry had an effect on the pressure field and minimum Cp production.
- Test case 3 and 4 showed excellent similarities with each other. The ridge ice shapes produced a longer wake region and displayed a change to the flow properties not consistent with the streamline type runback ice shapes.
- The geometry of the ridge ice after flow detachment did not produce any significant variation to flow properties.
- Datum iced run (actual runback ice profile) and test case 4 (forward facing quarter round ridge ice profile) showed poor agreement.
- Critical features of the runback ice highlighted that small geometric details played a significant role on the flow field and consequent downstream flow. Potapczuk, [112] found significant variability of ice accretion as a function of chord length. Even though the uniform icing conditions remained the same, the ice shape profile varied significantly. The ice structure studies have shown small variation to the geometry can significantly alter the flow field and reported force coefficients.

6. Wind Tunnel Validation

"To acquire knowledge, one must study; but to acquire wisdom, one must observe."

- Marilyn Vos Savant

Aerodynamic tests on three runback ice shapes were conducted using the Cranfield University Atmospheric Boundary Layer Wind Tunnel (ABLWT).

The representative runback ice shapes produced at the Cranfield Icing Tunnel (CIT) by Alègre, [104] were used to estimate the aerodynamic drag penalties associated with different runback ice shapes.

This chapter outlines the results and findings from the wind tunnel experimental data and comparison against RANS solver results.

Two methods were adopted for drag measurements within the boundary layer. A wake survey method (WSM) using a Pitot probe rake was used providing an indirect method for calculating the drag coefficient. A six component dynamic force/moment balance was used as a direct method for drag coefficient values.

Experimental velocity profiles and drag coefficient for runback ice shape 1 was compared with ANSYS FLUENT simulations using the Menter's $k-\omega$ SST and Spalart-Allmaras turbulence models.

6.1. 8' x 4' Atmospheric Boundary Layer Wind Tunnel

The ABLWT (Figure 6.1 & Figure 6.2) is an open circuit layout wind tunnel, with a closed test section; the test section dimensions are 8'x4' (2,4m x 1,2m) as shown in Figure 6.3. Maximum flow speed of 16ms^{-1} was possible over a 15m flow development section.

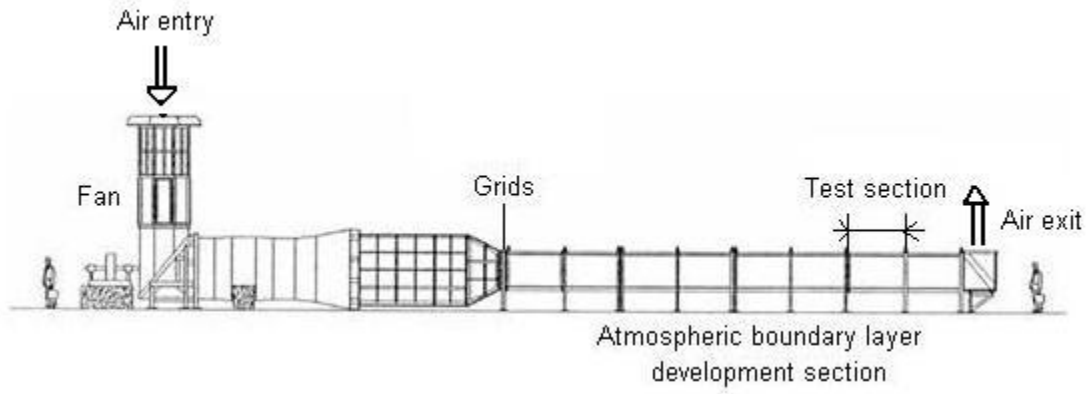

Figure 6.1: Cranfield 8' x 4' Atmospheric Boundary Layer Wind Tunnel Schematic [113]

Figure 6.2: Cranfield 8’ x 4’ Atmospheric Boundary Layer Wind Tunnel

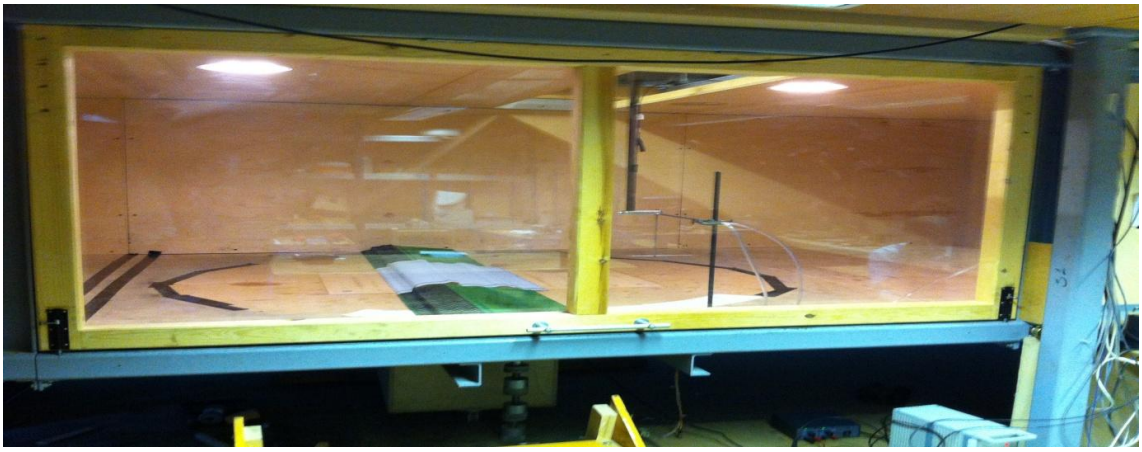

Figure 6.3: Cranfield 8’ x 4’ Atmospheric Boundary Layer Wind Tunnel Test Section

6.2. Runback Ice Selection and Creation

A number of runback ice castings were available from the CIT study by Alègre, [104] which were carefully selected for aerodynamic analysis in the ABLWT. The process of capturing the runback ice shapes was challenging and required an innovative moulding and casting technique. The issues which arose were a result of below freezing working temperatures. Finding a suitable material which could effectively cure over the runback ice was required and work done by Alègre, [114] recommended silicone among other materials as viable option for capturing runback ice. Alègre, [104] used silicone as the base material but added a number of catalysts to lower the curing time in the tunnel to 5 hours at 9°C below freezing. A wooden box was constructed to hold the silicone based moulding material in place over the runback ice shape (Figure 6.4). This meant the technique used to capture the detailed runback ice structure was executed in situ. The silicone based mounding was robust enough to create multiple casting (Figure 6.5).

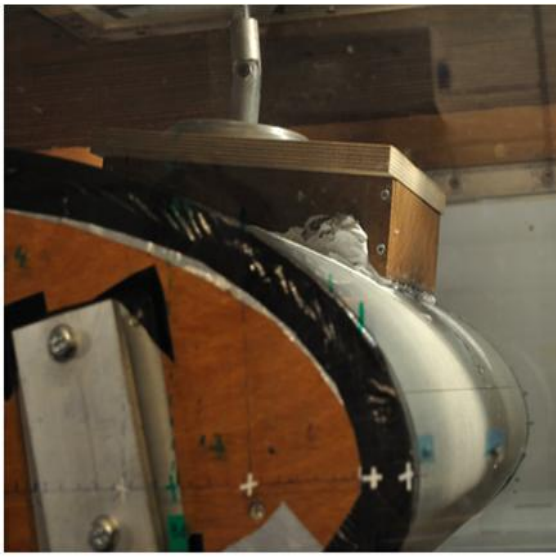

Figure 6.4: Hybrid 737 Airfoil with Wooden Moulding Box Courtesy of [104]

Figure 6.5: Typical Runback Ice Casting Courtesy of [104]

Careful tracing of the ice casting provided the vertex point used to create two dimensional runback ice profiles on selected CIT runs (Figure 6.6 & Figure 6.7).

Figure 6.6: Ice Casting used for Aerodynamic Analysis [1]

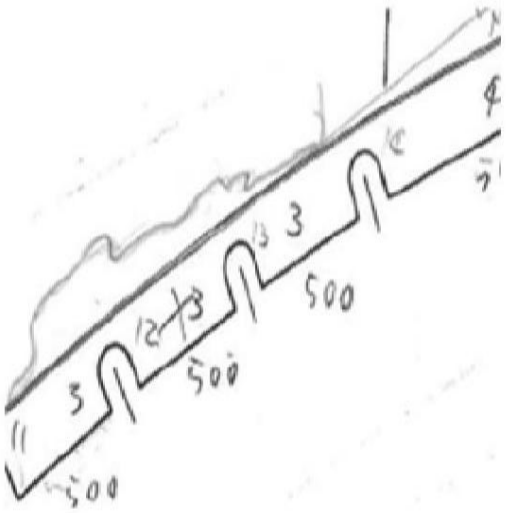

Figure 6.7: Two-Dimensional Tracing of Selected Runback Ice Casting [1]

The representative runback ice shapes formed very close to the full scale Boeing 737 leading edge. The typical thickness of the boundary layer for a full scale airfoil was between 7cm and 20cm and the leading edge was around 1 to 2mm. It was not possible to produce a boundary layer of this size. To this end the size of the runback ice shapes were significantly enlarged to ensure correct boundary layer thickness and Reynolds number regimes remained comparable.

The runback ice shapes were enlarged by scale of 700:1. The ice casting runback ice shape with a length of 0.6cm scaled up to a length of 42cm for the wind tunnel scale wood model (Figure 6.8 & Figure 6.9).

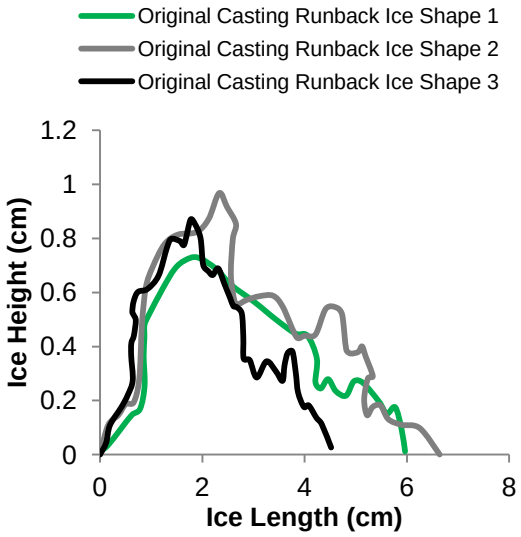

Figure 6.8: Realistic Casting Runback Ice Shape Size

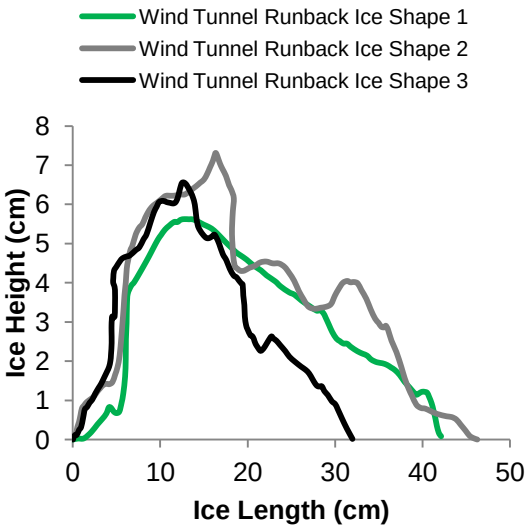

Figure 6.9: Wind Tunnel Scaled Runback Ice Shape Size

The scaled vertex data points were given to the Cranfield on-site technicians to reproduce using medium density fibreboard. Some trimming of edges was required to accommodate the tools used to cut the profile.

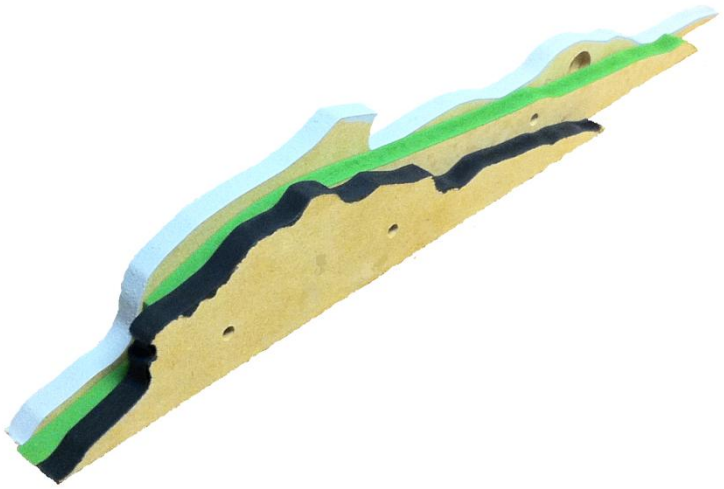

Figure 6.10: Wooden Runback Ice Shapes used in ABLWT

6.3. Test Equipment

The test arrangement and instrumentation used are shown in Figure 6.11. A pitot rake was used to measure the total pressure. The rake comprised of 40 pressure tubes spaced at 4.763mm apart. The lowest position attainable for the pressure tube was 3.5mm.

A suction device was used to reduce the size of the boundary layer thickness. The aim was to consider the drag penalty associated with the different ice shapes for the same atmospheric conditions and compare with numerical models.

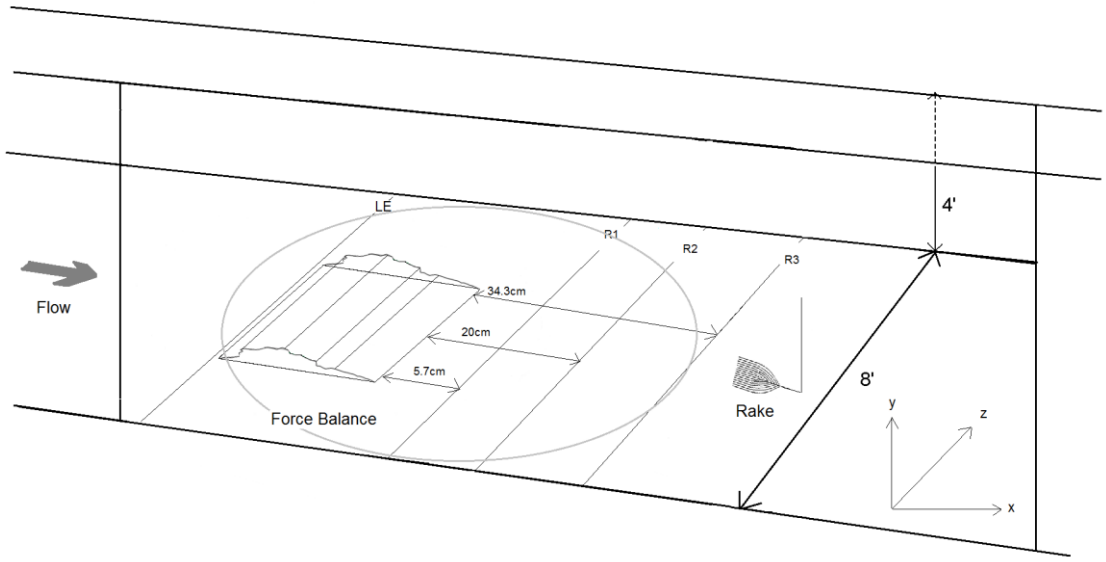

Figure 6.11: Working Section Schematic 1

6.3.1. Pitot Probe Rake

A Pitot probe rake was fixed to a three-component traverse system which mapped the flow in the stream-wise and span-wise direction. The setup consisted of a 40 Pitot probes rake. The Pressure transducers PX139 (0.3psi to 30psi) linked to the rake were calibrated by Jenny Holt (Cranfield University Wind Tunnel Technician). Accuracy estimates can be found in the

Appendix.

The probe inside and outside diameters were 0.5mm and 1.6mm respectively with a maximum rake height of 190.775mm. The frequency set for the data acquisition by the Pitot rake was 1000Hz.

The span-wise traversing mechanism mapped the boundary layer at 15 locations across a range of z=-325mm and z=325mm (Figure 6.12). The sample time at each location was 20 seconds.

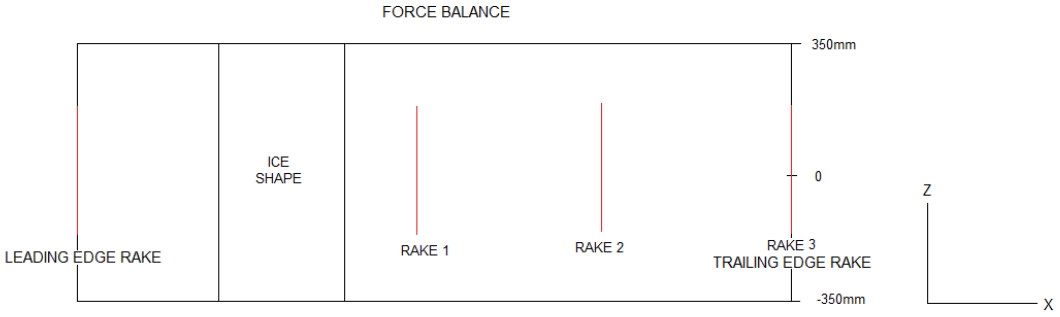

Figure 6.12: Working Section Schematic 2

6.3.2. Force Balance

A six component dynamic force/moment balance was used to attain the skin friction drag associated with the runback ice shapes. The floating element force balance was originally designed by DERA (Defence Evaluation and Research Agency) and acquired by Cranfield University. The resolution had been estimated to a maximum of 0.05N from previous studies conducted in the wind tunnel by Jenny Holt. The dimensions were 0.7m by 1.07m and were aligned to the floor of the working section. The force balance was mounted to a turntable wooden cut-out which was separated by thin air gaps (~1mm).

6.3.3. Other Instrumentation

Free stream measurements were taken approximately 1m ahead of the working section to provide the reference velocity U_∞ and dynamic pressure q_∞. Pressure P_∞ and Temperature T_∞ measurements were taken using a barometer Druck DPI 141 (±0.1Pa) and a thermometer RS Temp 261 (±0.1°C). The acquisition apparatus was setup by Jenny Holt using the National Instruments (NI PCI6036E) board.

6.4. Testing Procedure

The preliminary requirement was to accurately measure the drag production for different ice shapes using two different measurement techniques and to match the flow characteristics including drag coefficient results from the numerical solver.

Initial wind tunnel setup and calibration was conducted by Jenny Holt (Cranfield Technician). The testing phase was assisted by Cranfield University MSc student Rabaia Khawaga as part of her final project.

Following the successful calibration of the instrumentation, flat plate measurements were conducted. The force balance leading and trailing edge positions were used to measure the boundary layer using the total pressure rake. The total pressure rake measured the boundary layer at 15 locations across the span of the wind tunnel working section. This duration provided ample time for force balance data acquisition.

Three runback ice shapes were used for drag prediction tests. A final run was conducted using all three ice shapes in alternating fashion. Data from runback ice shape 2 and 3 were not included in this study. There were a number of discrepancies with the wake survey method due to flow separation. As a result only data for runback ice shape 1 and the combined runback ice shape have been provided.

The testing procedures were carried out in the following order:

- Force Balance Setup and Calibration
- Total Pressure Rake Setup and Calibration
- Flat Plate Leading Edge Measurements
- Flat Plate Trailing Edge Measurements
- Runback Ice Shape 1, 2 and 3:
    - Rake Position 1
    - Rake Position 2
    - Rake Position 3
- Alternating Runback Ice Shapes Run:
    - Rake Position 1
    - Rake Position 2
    - Rake Position 3

The results for the force balance have been removed from this study due to issues with repeatability. Since the experiments were conducted the mount for

the force balance has been modified to rectify the problem. However there was insufficient time to run the tests again re-evaluate the results.

6.5. Flat Plate Boundary Layer Analysis

An overview and insight on the characteristics of the flat plate boundary layer are shown in this section.

6.5.1. Boundary layer Characteristic

The boundary layer characteristic at the working section was evaluated against the well known Prandtl 1/nth Law:

$$u = u_1 \left(\frac{y}{\delta}\right)^{1/n}$$

Equation 6.1: Prandtl 1/nth Boundary Layer Law

The gradient of the boundary layer profile indicates whether the flow is laminar or turbulent. The 1/7th and 1/9th power corresponds to a flat plate boundary layer Reynolds number of 10^5<Re<10^7 and 10^6<Re<10^8.

The flat plate boundary layer characteristic at the leading and trailing edge of the force balance, effectively the working section is shown in Figure 6.13 and Figure 6.14 respectively. At the leading edge the experimental boundary layer velocity profile at the centre line, 0z/b through to 0.57z/b, closely followed the 1/9th Prandtl turbulent power law. Accordingly the turbulent boundary layer Reynolds number was between 10^6 and 10^8. The trailing edge profile shown in Figure 6.14 revealed a small variation relative to the leading edge boundary layer where the profile was a closer match to a 1/8th power law. The working section of the floor was cut out to accommodate the force balance and so likely to have slightly disrupted the flow due to the small gaps in the floor. However, the leading edge characteristics of the boundary layer were of interest as this provided the basis of the type of flow which would interact with the runback ice shapes.

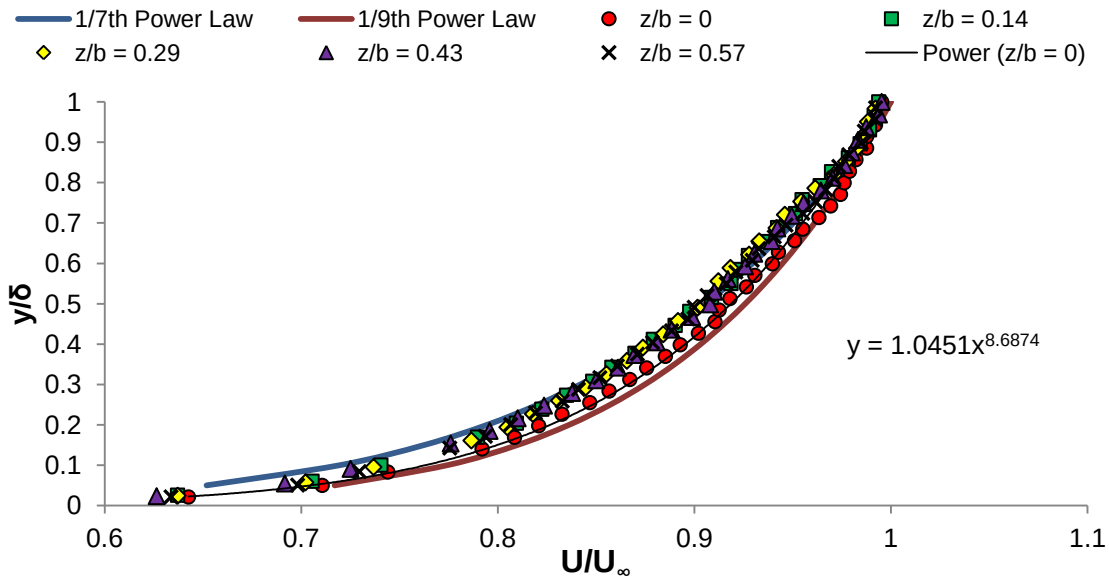

Figure 6.13: Flat Plate Boundary Layer Profile for Working Section Leading Edge

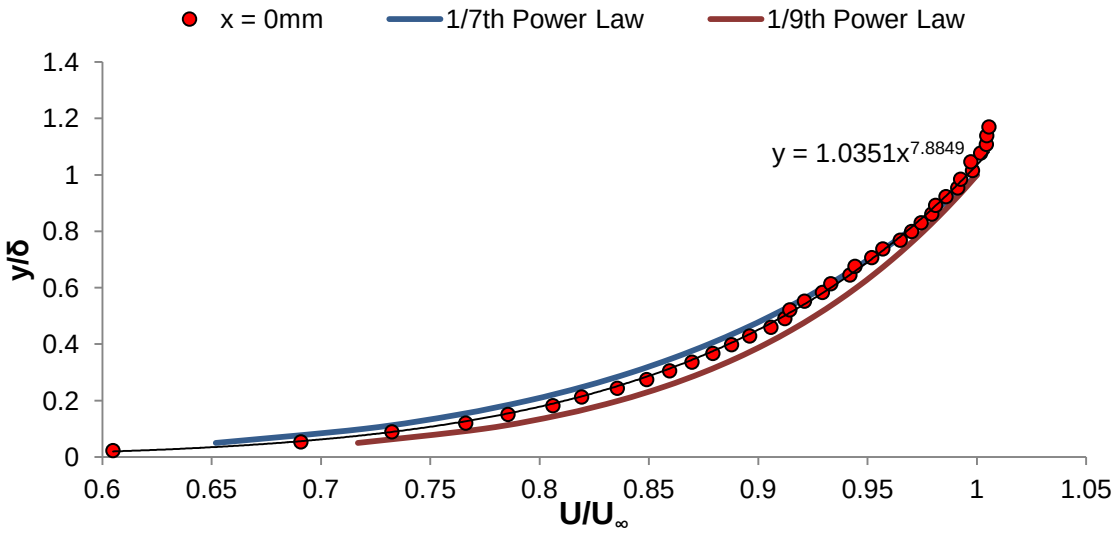

Figure 6.14: Flat Plate Boundary Layer Profile for Working Section Trailing Edge

The 1/9th power law holds for both leading and trailing edge conditions and corresponding Reynolds number regime allows the use of Equation 6.2 and Equation 6.3.

$$\delta = \frac{0.27x}{Re_x^{\frac{1}{6}}}$$

Equation 6.2: Boundary Layer Thickness

$$Re_x = \frac{\rho U_\infty x}{\mu}$$

Equation 6.3: Reynolds Number

Where x is the virtual origin of the turbulent boundary layer growth

Combining Equation 6.2 and Equation 6.3 yields:

$$x = \left(\left(\frac{\delta}{0.27} \right) \left(\frac{\rho U_\infty}{\mu} \right)^{\frac{1}{5}} \right)^{\frac{6}{5}}$$

Equation 6.4: Virtual Origin of Turbulent Boundary Layer

The virtual origin for the turbulent boundary layer at the leading and trailing edge of the force balance was 8.99m and 9.14m respectively. This related to a Reynolds number of 7.74×10^6 and 8.02×10^6 for the leading and trailing edge respectively.

A Reynolds number of 4.6×10^5 was where ice formation occurred on the B737 airfoil with atmospheric conditions matching the 45 minute EASA hold condition. Unfortunately reducing the boundary layer thickness any further was not possible. The local Reynolds number at 1.5 metre along the 4 metre airfoil was comparable to the wind tunnel Reynolds number. The core research aspect was to experimentally measure the drag losses associated with representative runback ice shapes and compare against two-dimensional numerical simulations. This allowed a level of freedom when considering the runback ice size scaling with respect to Reynolds number and satisfied the working parameters for the ABLWT.

6.5.2. Span-wise Variation

The span-wise variation was considered for the flat plate tunnel run. The span-wise dynamic pressure at four different heights on the pitot rake is shown in Figure 6.15. The dynamic pressure across the negative z-axis produced a noticeable drop at -0.5z/b. The magnitude of instrumentation error did not account for the observed variation across the span of the tunnel and was not observed with previous wind tunnel experiments with similar setup.

The boundary layer thickness (δ) across the span of the tunnel produced a significant range of 8.99cm (Figure 6.16). The normalised boundary layer thickness for the flat plate wind tunnel at the working section was calculated using $0.995U/U_\infty$. U_∞ was taken as the mean of the 5 highest (y-axis) probes from the total pressure rake. The boundary layer thickness range from all 15 rake locations was from 135 to 227mm.

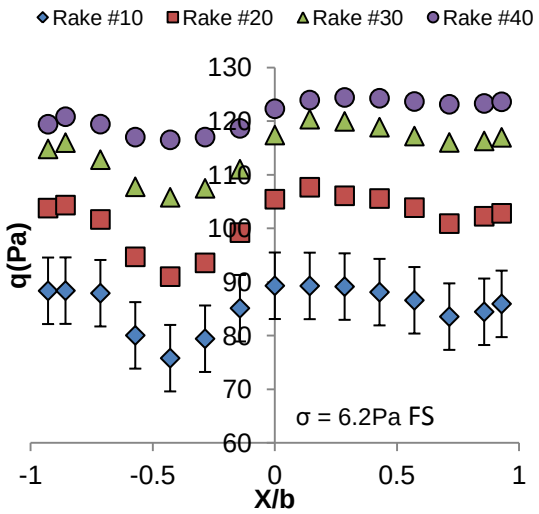

Figure 6.15: Flat Plate Wind Tunnel Span-wise Dynamic Pressure Variation

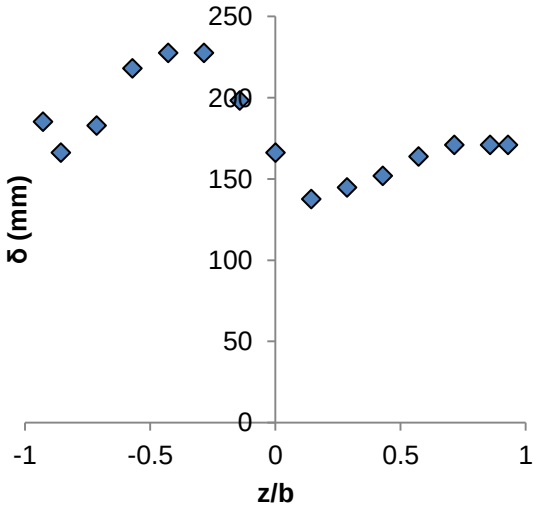

Figure 6.16: Flat Plate Wind Tunnel Span-wise Boundary Layer Thickness Variation

The average boundary layer thickness across the positive span of the tunnel was 159.61mm. Figure 6.17 shows the runback ice normalised against the boundary layer thickness.

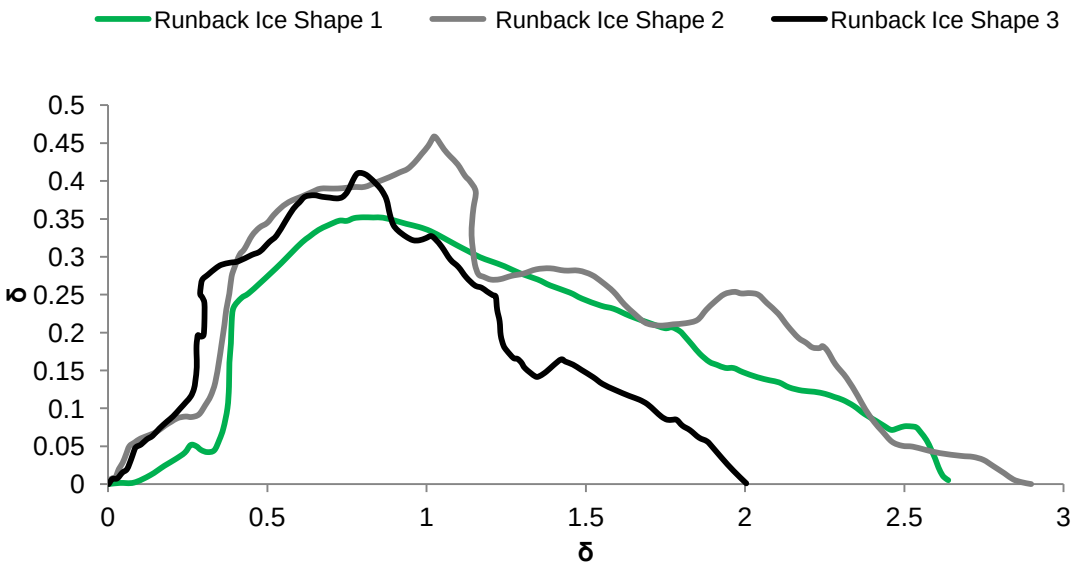

Figure 6.17: Runback Ice Normalised against Boundary Layer Thickness

The velocity variation observed for the flat plate boundary layer across the span of the working section is shown in Figure 6.18 & Figure 6.19. The profiles across the span is split into 2 graphs for clarity; the positive and negative z/b axis regions.

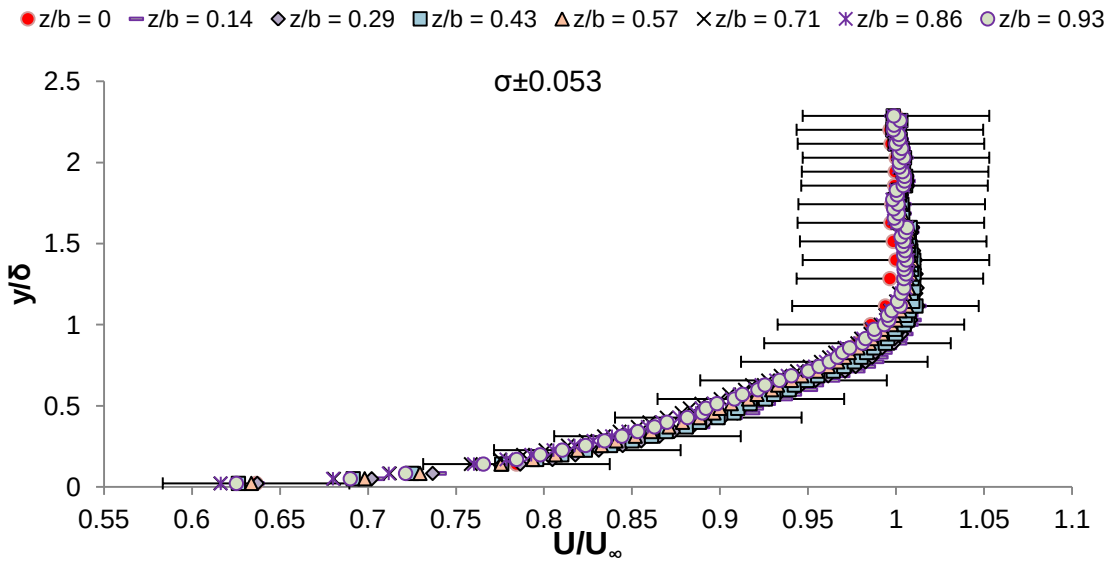

Figure 6.18: Positive z-axis Span-wise Boundary Layer Velocity Profiles for Flat plate Leading Edge

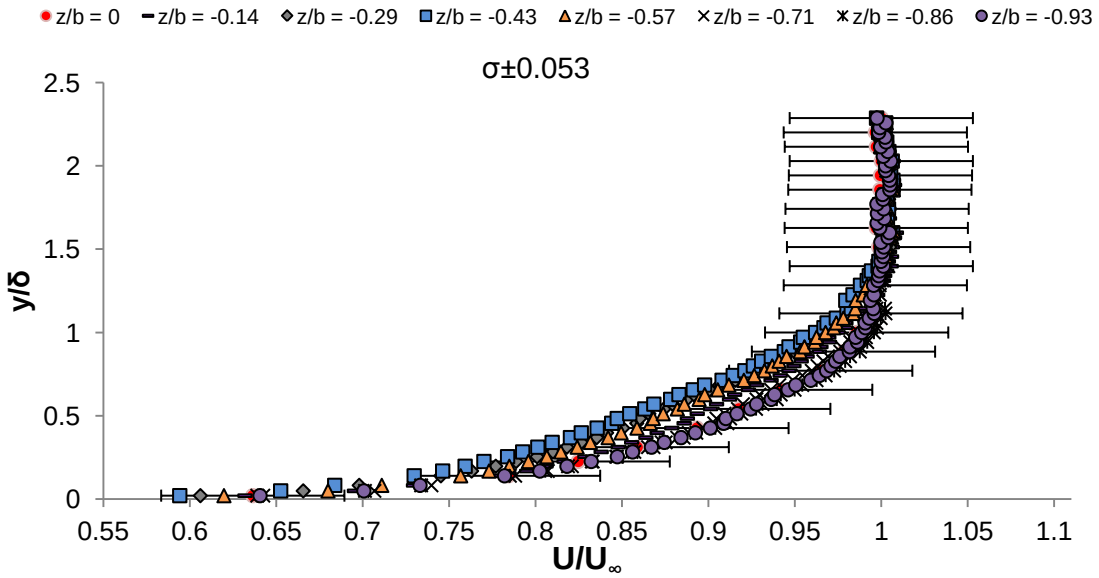

Figure 6.19: Negative z-axis Span-wise Boundary Layer Velocity Profiles for Flat plate Leading Edge

The variation across the tunnel from the centreline (0z/b) differed from positive to negative orientation. The largest variation was seen in the negative region at –0.43z/b from the centreline shown in Figure 6.19. In contrast there was very little variation across the positive z-axis (Figure 6.18).

The span-wise variation for the dynamic pressure, boundary layer thickness and boundary layer velocity profiles suggested the results from the centreline to the positive z/b axis region are close to uniform.

It was decided to only consider the data obtained from a range of five span-wise positions from 0z/b to 0.57z/b (0mm to 200mm). The boundary layer thickness variation between 0z/b and 0.57z/b was 28.6mm. Figure 6.20 shows the boundary layer profiles for this range.

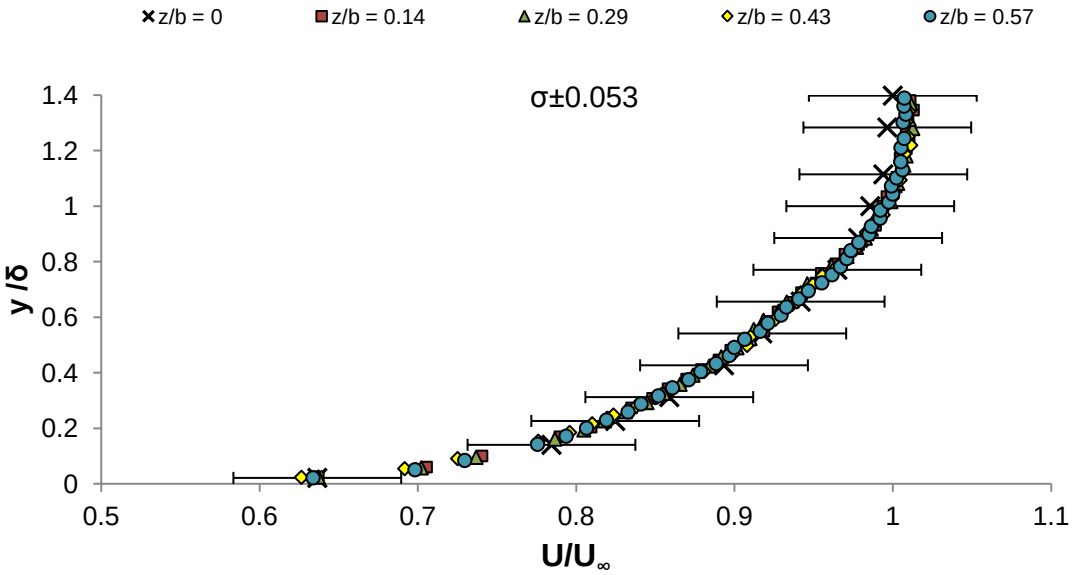

Figure 6.20: Flat Plate Boundary Layer Profile for Selected Span-wise Locations

The variation on the negative z/b axis clearly indicated some disturbance in the tunnel. The cause of the inhomogeneous behaviour across the span of the ABLWT remained unknown.

6.6. Drag Force Analysis

6.6.1. Wake Survey Method (WSM):

The wake survey method technique was developed by Jones, [115] to determine the profile drag of wings from total pressure and static pressure measurements in the wake of the airfoil close behind the trailing edge.

A pivot-traverse method was used to capture the pressure distribution in the wake produced by the airfoil or as in this case the ice shapes. By measuring the plane perpendicular to the mean flow an indirect method to calculate the drag was permissible by relating the drag to the integral of the momentum deficit.

$$C_{d,non-dimensional} = \frac{2}{scV_{\infty}^{2}} \iint_{0}^{l} V(V_{\infty} - V)dA$$

Equation 6.5: Jones, [115] Non-Dimensional Drag Coefficient

Where

s= Span of the SFB (0.7m) - Usually span of the wing
c= Length of SFB (1.07m) – Usually chord length

Considering each streamline (locations along the traverse map):

$$C_{d,non-dimensional} = \frac{2}{cV_\infty^2}\int_0^l V(V_\infty - V)dl$$

Equation 6.6: Jones, [115] Non-Dimensional Drag Coefficient at each Spanwise Location

Substituting the dynamic pressure relation $q = \frac{1}{2}\rho V^2$ Equation 6.6 was reduced to Equation 6.7 for the drag coefficient per unit span:

$$C_{d,non-dimensional} = \frac{2}{c}\int_0^l \left(\sqrt{\frac{q}{q_\infty}} - \frac{q}{q_\infty}\right)dl$$

Equation 6.7: Jones, [115] Non-Dimensional Drag Coefficient in terms of Dynamic Pressure

Where l is the height (y-axis).The trapezium rule for small increments of l was used as shown in Equation 6.8:

$$C_{d,non-dimensional} \approx \frac{2}{c}\sum_i \left(\sqrt{\frac{q}{q_\infty}} - \frac{q}{q_\infty}\right)\Delta l_i$$

Equation 6.8: Jones, [115] Non-Dimensional Drag Coefficient using Trapezium Rule

Equation 6.8 was used to calculate the drag force per unit span across the tunnel at the centreline 0 z/b.

$$DRAG_{per\ unit\ span} = C_{d,non-dimensional} * q * c$$

Equation 6.9: Jones, [115] Drag Coefficient per unit Span

Equation 6.9 essentially provided the drag coefficient per unit span at each traverse location mapped by the rake. Integration over the area across the span of the mapped locations provided the drag for the whole span (total drag). However with significant variation across the negative z-axis, it was decided to apply a small modification to the approach for deriving the total drag across the span. The original method by [115] and adopted by [116] for her MSc thesis was labelled as Wake Survey Method 1. The modified approach was labelled as Wake Survey Method 2. Both methods are shown.

6.6.2. Wake Survey Method 1:

The total drag for the entire span of the ABLWT required integrating over the length of the 15 spanwise map locations. Essentially the trapezium rule was again employed to find the area under the total drag curve (Figure 6.21).

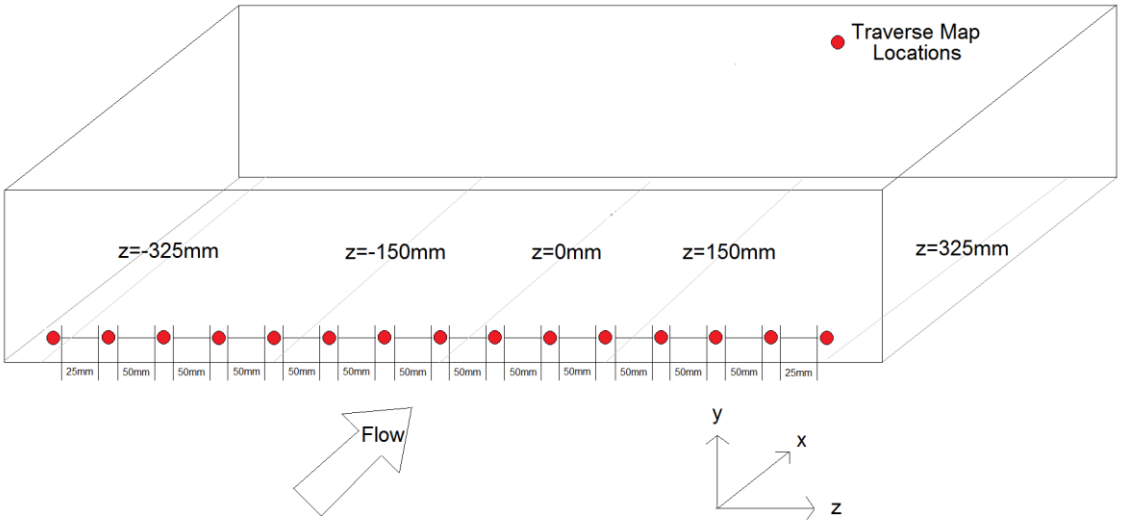

Figure 6.21: Schematic of 15 Spanwise Total Pressure Rake Locations

Integrating over the span (±z) provides the total drag force (Equation 6.10).

$$DRAG_{TOTAL} = \int_{-z}^{z} DRAG_{per\ unit\ span}\ dz$$

Equation 6.10: Total Drag Integral for Wake Survey Method 1

The trapezium rule can again be applied to approximate the integral (Equation 6.11)

$$DRAG_{TOTAL} \approx \sum_{i} DRAG_{per\ unit\ span}\ \Delta z_i$$

Equation 6.11: Total Drag for Wake Survey Method 1 using Trapezium Rule

The final results are presented as drag coefficients (Equation 6.12).

$$C_{d,Uncorrected\ 3D} = \frac{DRAG_{TOTAL}}{qS}$$

Equation 6.12: Corrected Drag Coefficient for Wake Survey Method 1

A total of 15 locations mapped the span of the working section. The distance between each map location was 50mm with the exception of the two extreme rake locations (±325mm) which were 25mm from the preceding map location.

Integration using the trapezium numerical method scheme introduced errors as the fluctuations are not captured due to large step sizes. This was the case for the spanwise integral.

Figure 6.22 shows the drag coefficient per unit span broken up into multiple trapeziums to find the area under the curve. The shaded red region indicates the variation between the actual area and approximated area. Since data values only exist at 50mm spacing's (except either extreme) the error introduced was appreciable. Although this error was not quantified, attempts have been made to demonstrate its existence.

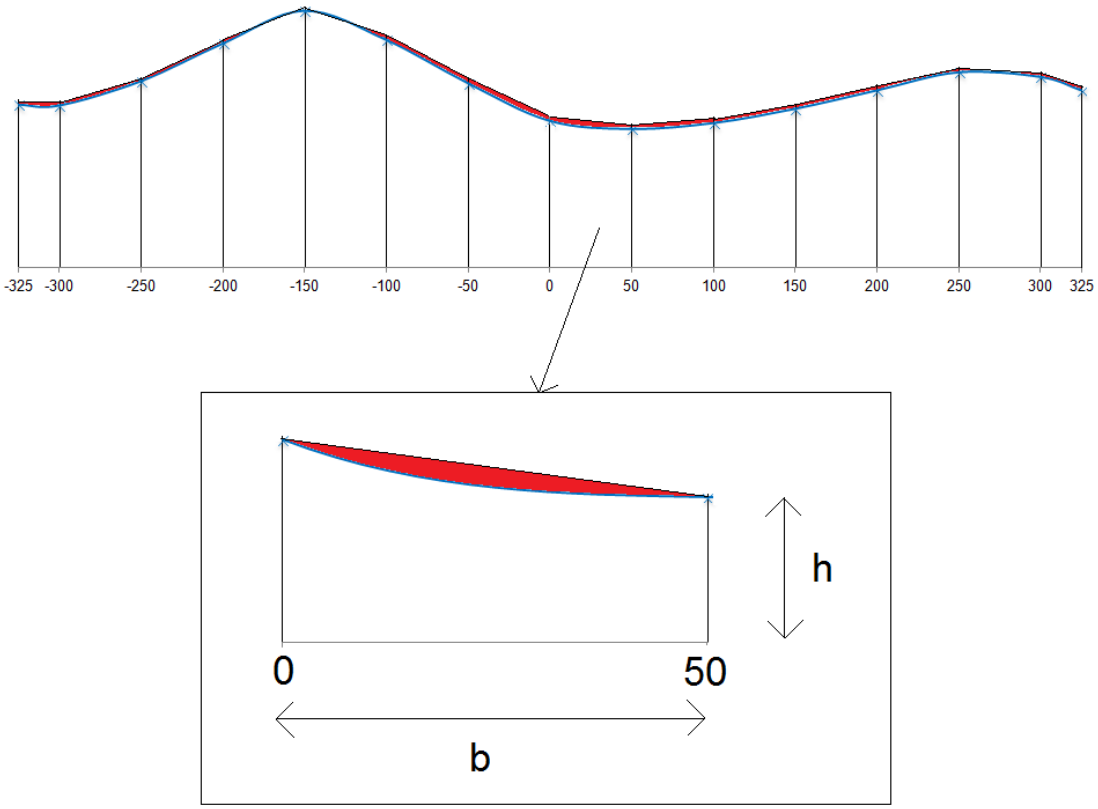

Figure 6.22: Illustration of Induced Error from Trapezium Rule Integration

6.6.3. Wake Survey Method 2 (Modified Approach):

The modified approach assumed each traverse map location drag value as the total drag. Fundamentally inferring the total drag across the wake in the spanwise direction was uniform at the individual traverse map locations. Consequently the drag coefficient per unit span shown in Equation 6.9 was used to calculate the total drag across the span of the working section (Equation 6.13).

$$DRAG_{SFB\ span} = DRAG_{per\ unit\ span} * 0.7$$

Equation 6.13: Total Drag using Wake Survey Method 2

Equation 6.13 essentially provided $3D$ drag from the $2D$ drag profile multiplied by the span (0.7m)

Uncorrected $3D$ C_d from the $3D$ Drag was given by Equation 6.14:

$$C_{d,Uncorrected\ 3D} = \frac{DRAG_{SFB\ span}}{q * S}$$

Equation 6.14: Corrected Total Drag using Wake Survey Method 2

Where S was the area of the skin friction balance (0.7*1.07)

Each map location was converted via this method and allowed the total drag to be plotted against each map location whereas in method 1, this was not an option.

The corrected three-dimensional drag coefficients for both wake survey methods were found using Equation 6.15. Please note each $C_{d,Flat\ Plate\ 3D,T.E}$ value was derived using their respective WSM. The trailing edge (T.E) values were used to correct the drag coefficient results. The rake location at which the WSM for the ice shape was calculated coincides with the T.E flat plate location; consequently these values were used to correct the ice drag coefficient values.

$$\Delta Cd_{WSM} = C_{d,Uncorrected\ 3D} - C_{d,Flat\ Plate\ 3D,T.E}$$

Equation 6.15: Drag Coefficient Correction for both Wake Survey Methods

6.7. Flat Plate Results

The results from the indirect wake survey methods are presented in this section. The drag coefficient via Jones' wake survey methods one and two are shown in Figure 6.23. As stated earlier method 1 required integrating over the 15 spanwise map locations which provided a single total drag coefficient value. Accordingly the results for wake survey method 1 are displayed for comparison purposes. This approach allows a visual inspection of total drag coefficient using both approaches and how integrating over the fluctuations still presented an acceptable result. Once again the focus of the core results for comparison purposes were confined to the positive z-axis region (Figure 6.24) and the chosen five traverse location results are shown in Figure 6.25.

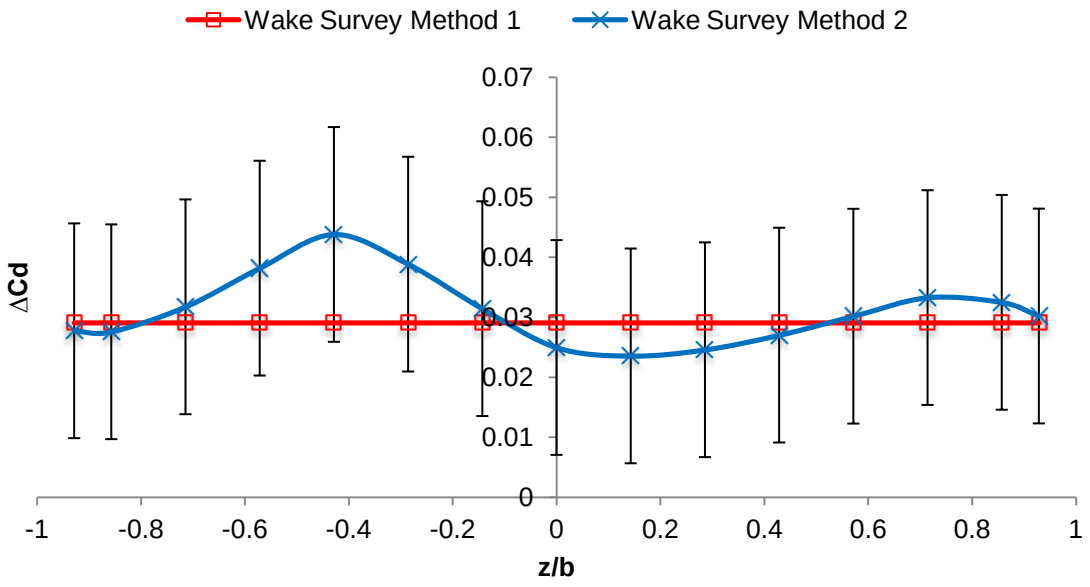

Figure 6.23: Flat Plate Trailing Edge Drag Coefficient Comparison for Wake Survey Method 1 & 2

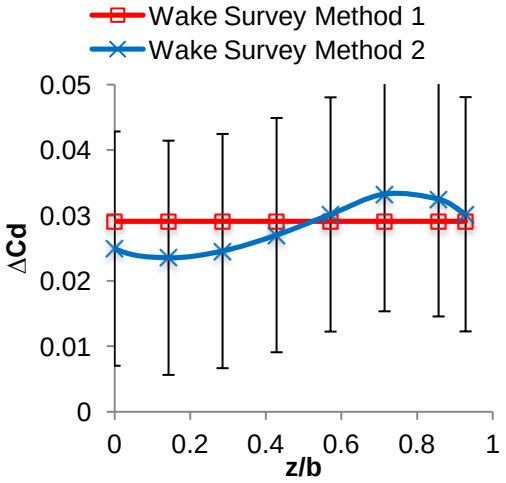

Figure 6.24: Flat Plate Trailing Edge Drag Coefficient Comparison for Wake Survey Method 1 & 2 (Positive z-axis)

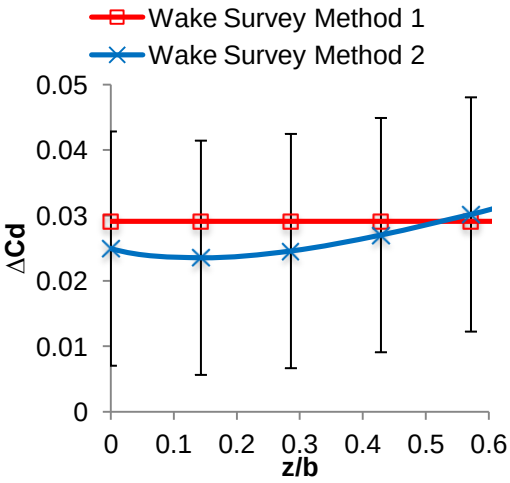

Figure 6.25: Flat Plate Trailing Edge Drag Coefficient Comparison for Wake Survey Method 1 & 2 (0-0.6z/b)

6.8. CFD Modelling

Attempts were made to capture the boundary layer characteristics using a RANS numerical solver. ANSYS FLUENT software package was used and two turbulence models were evaluated; Spalart-Allmaras one-equation model and the Menter's $k-\omega$ SST two-equation eddy-viscosity model.

ANSYS FLUENT runs for the flat plate tunnel and runback ice shape 1 were conducted for drag coefficient and wake boundary layer velocities comparisons.

The initial conditions for the solver were based on the experimental conditions for the flat plate and runback ice shape run. The initial pressure, temperature and free stream velocity are used. A schematic of the domain can be seen in Figure 6.26 and the runback ice in Figure 6.27.

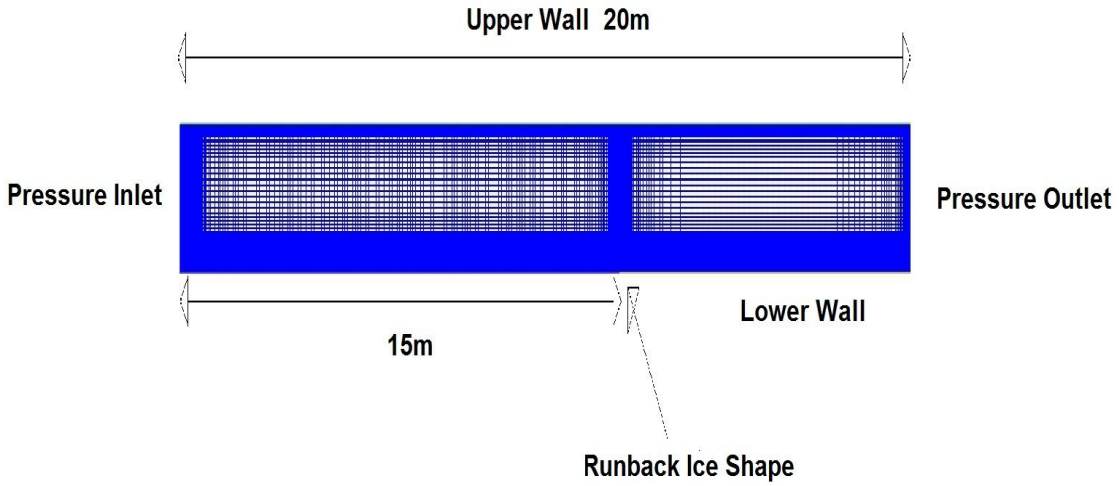

Figure 6.26: ANSYS FLUENT Wind Tunnel Domain

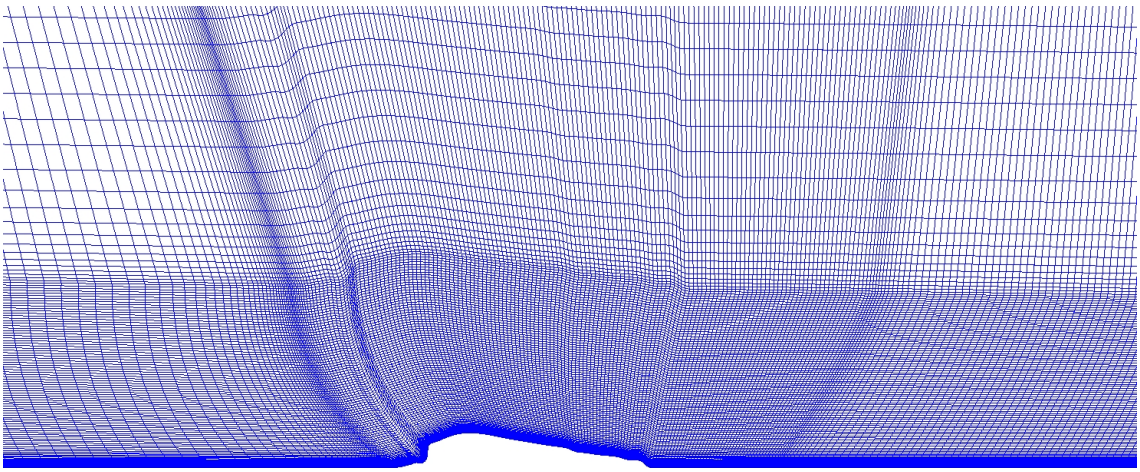

Figure 6.27: ANSYS FLUENT Wind Tunnel Runback Ice

An initial flat plate boundary layer mesh was created to allow the boundary layer to develop until the thickness was similar to the wind tunnel working section. The position where the ANSYS FLUENT model formed a boundary layer thickness comparable to the experimental boundary layer thickness was 9m from the Pressure Inlet. A structured boundary layer was implemented using ANSYS ICEMCFD. The mesh density was strategically increased around the inlet, outlet and in the region of the ice shape. The boundary layer was resolved with a y^+ of less than 1 for all simulations (Figure 6.28).

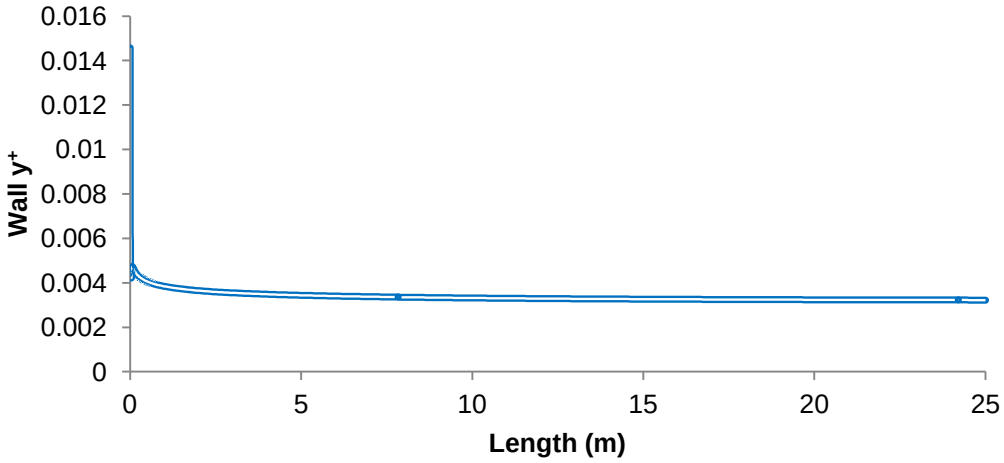

Figure 6.28: ANSYS FLUENT Flat Plate y^+ across Domain Floor

A preliminary wind tunnel study was conducted alongside Nwgu, [117]. The aim of the study was to conduct a wind tunnel run using a hotwire probe and a different force balance. The instrumentation used was:

- Hotwire Anemometer (Dantec 55P11 single-sensor hot wire anemometer)
- Pitot-static tube (Furness model FC0318)
- Force Balance

An overview of the testing procedure is outlined:

1. Setup tunnel for flat plate
2. Setup Labview software interface
3. Set Run speed (400-600rpm)
4. Hotwire Anemometer survey of wake
5. Repeat procedure for runback ice shapes.

Due to calibration issues from the force balance, the results were not conclusive and a second attempt was made with the help of Khawaja, [116] and results shown in this chapter.

The instrumentation used for this preliminary wind tunnel study by Nwgu, [117] was not used for the second study. Although a total pressure rake provided a larger data set, the rake did not provide any data on the turbulent intensity.

The hotwire probe results of Nwgu, [117] provided the turbulent intensity data required for a 600rpm run with average free stream velocity of 14.39ms^{-1}. The average turbulent intensity recorded from several 600rpm runs 3%. The data from the original preliminary study used to calculate turbulent intensity values can be found in the

Appendix. A more detailed description of the preliminary run can be found in the Cranfield MSc thesis by Nwgu, [117].

The boundary layer thickness for the flat plate run at the leading edge was 200mm. Parameters used for the CFD initial conditions can be found in Table 6.1.

Parameters	Flat Plate Run	Runback Ice Shape 1
Total Pressure (Pa)	99123	100397
Gauge Pressure (Pa)	98995	100269
Temperature (K)	294.45	296.7
Density (kgm^{-3})	1.17	1.17
Turbulent Intensity (%)	0.03	0.03
Length Scale (m)	0.05	0.05
1st Cell Size (m)	2x10^{-6}	2x10^{-6}

Table 6.1: FLUENT Solver Parameters

6.8.1. Flat Plate Boundary Layer CFD Comparison

A comparison of experimental and numerical flat plate boundary layer velocity profiles for the 5 chosen traverse map locations was undertaken. The normalised velocity U/U_∞ against the boundary layer thickness δ for the flat plate boundary layer is shown in Figure 6.29. The boundary layer thickness calculation was based on each individual spanwise position where the velocity had reached 99.5% of the free stream velocity U_∞. For all calculations the free stream velocity was taken by averaging the top 5 pressure points given by the

total pressure rake. The uncertainty and error involved with using the top 5 values was evaluated and shown in the

Appendix.

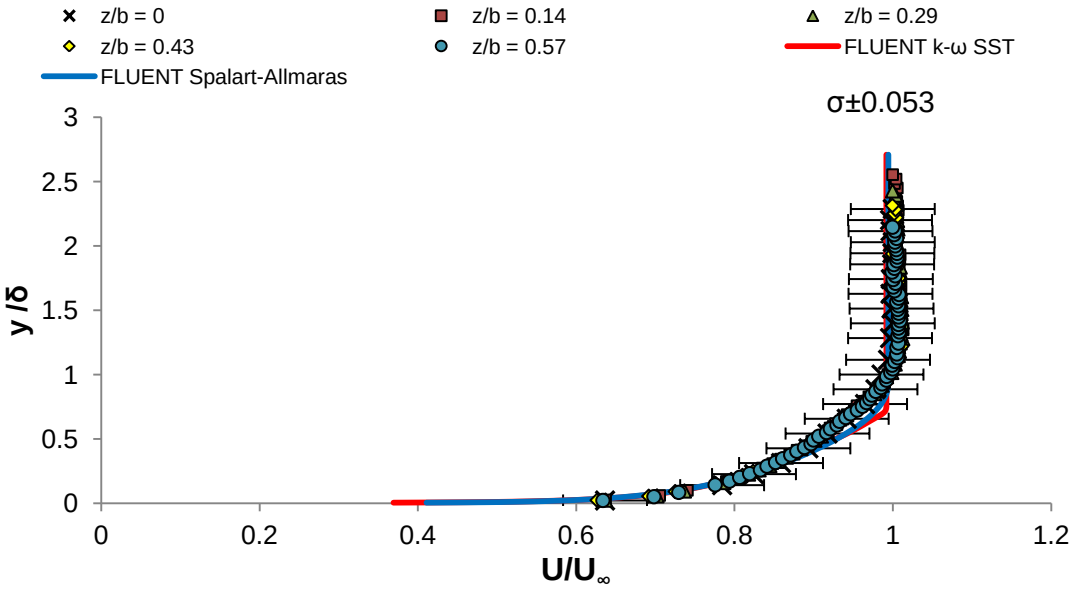

Figure 6.29: Leading Edge Flat Plate Boundary Layer Profile for Chosen Spanwise Locations against Numerical Predictions

The numerical velocity profile at the boundary layer provided an acceptable comparison against the experimental data. The only deviation from the experimental profile occurred near the boundary layer thickness value set at 99.5% of the free stream velocity. The numerical velocity profile was normalised against the average of the five selected map location from the free stream velocities.

Above the boundary layer thickness height, the extrapolated inlet velocity from the boundary condition was achieved and numerical models depict two-dimensional uniform flow. The experimental profile showed a slight increase in velocity around the boundary layer thickness value not modelled by the numerical solver. The experimental velocity beyond a height of 2δ depicted the same free stream velocity as the numerical models.

Boundary layer profile for both the experimental and numerical data in terms of their normal units, i.e. velocity in ms^{-1} and height in millimetres are available in the Appendix.

A summary of the flat plate results are:

- Leading edge boundary layer profile exhibited a turbulent profile comparable to the 1/9th power law.
- Based on the 1/9th power law; Reynolds number for flow was 7.74x10^{6} and 8.02x10^{6} for the leading and trailing edge respectively.
- The virtual origin for the turbulent boundary layer based on their relevant Reynolds number at the leading and trailing edge of the force balance was 8.99m and 9.14m respectively.
- The trailing edge rake position corresponded to rake position 3 for the iced tunnel runs. Consequently the trailing edge drag coefficient value was used as the correction value for all wake survey method drag results.

Table 6.2 below highlights the overall results found for the flat plate using the WSM. All WSM values were used to correct the drag coefficient results for the iced runs.

Flat Plate WSM Location	Wake Survey Method 1 Drag Coefficient	Wake Survey Method 2 Drag Coefficient
0 z/b	0.0249	0.0290
0.14 z/b	0.0235	
0.29 z/b	0.0245	
0.43 z/b	0.0270	
0.57 z/b	0.0301	

Table 6.2: Drag Coefficient Results for Flat Plate using Wake Survey Methods 1 & 2

6.9. Runback Ice Shape 1

Runback ice shape 1 (Figure 6.30) was the ice shape which best represented the realistic runback ice shape based on the EASA 45 minute hold configuration and was of particular interest to the sponsors; Airbus.

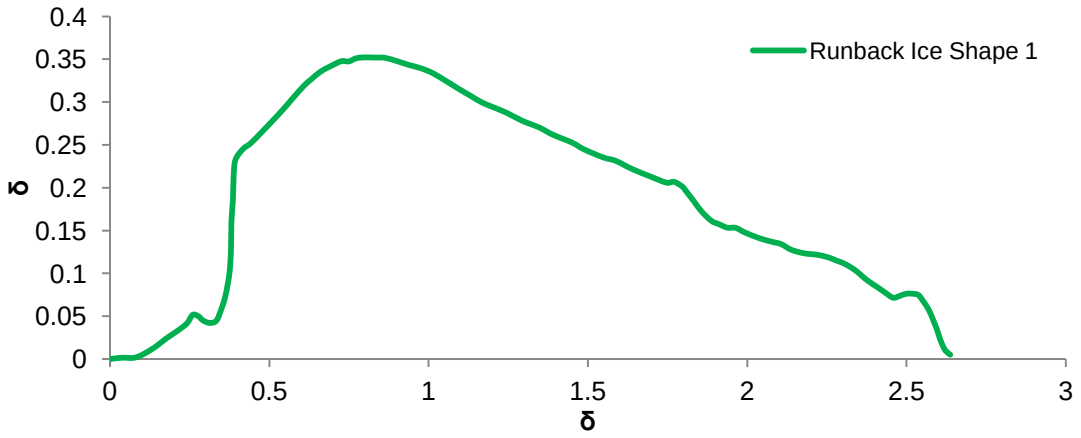

Figure 6.30: Runback Ice Shape 1 Two-Dimensional Profile

Although variations were observed across the entire ice casting, the leading edge profile seen in Figure 6.30 represented the profile observed across a significant proportion of the three-dimensional casting. The leading edge profile for this shape was of particular interest as the Runback Ice Structure Detail Analysis in Chapter 5.5 highlighted the need to accurately represent the leading edge geometry.

The results are presented in the following order:

- Wake Survey Method Results
  - Method 1
  - Method 2
- Comparison of all drag coefficient results with numerical prediction

6.9.1. Results

The two wake survey methods shown in Figure 6.31 provide a visual comparison of total drag coefficients for both methods. The straight line observed for Method 1 represented a single value obtained by integrating over the spanwise working section.

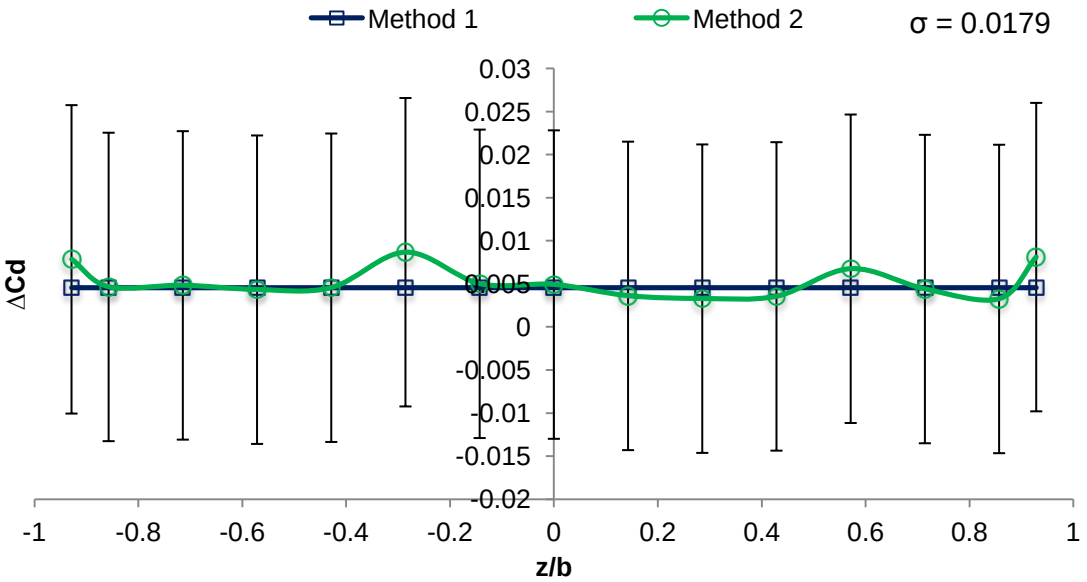

Figure 6.31: Corrected Total Drag Coefficient Comparison for both Wake Survey Methods

The error bars reduce the resolution of the variations when using method 2 (Figure 6.32).

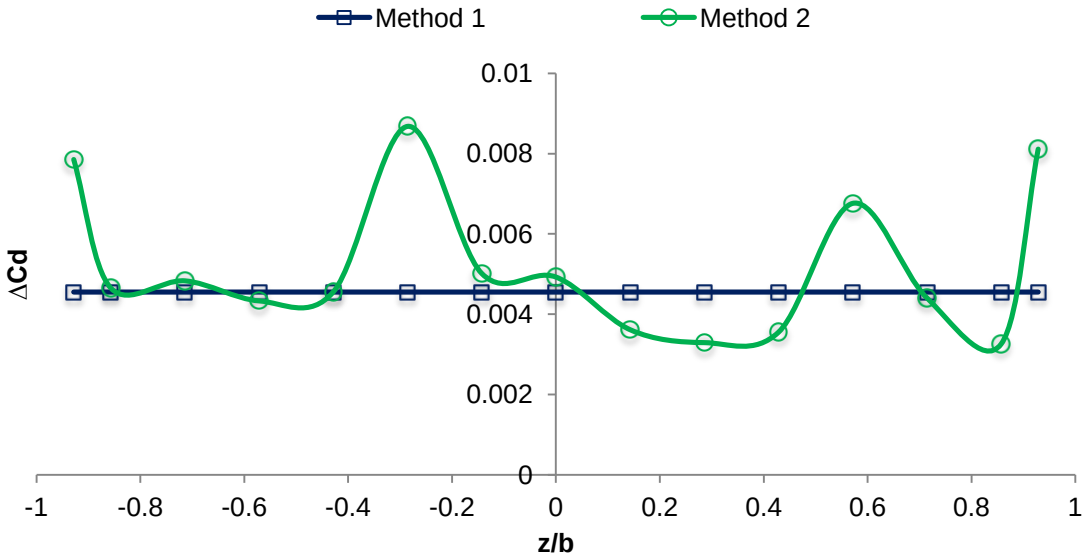

Figure 6.32: Corrected Total Drag Coefficient Comparison for both Wake Survey Methods (without Error Bars)

Although variations are observed across the spanwise section, the integration process and associated errors induced using this method still provided an acceptable result in terms of overall drag value.

A closer inspection around the chosen spanwise locations is shown with and without error bars in Figure 6.33 and Figure 6.34 respectively.

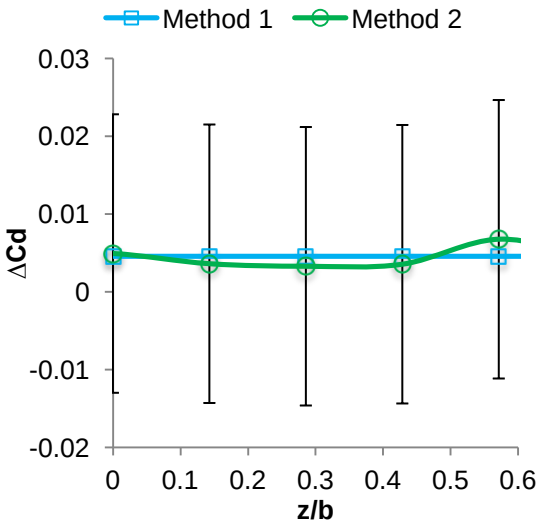

Figure 6.33: Corrected Total Drag Coefficient Comparison for both Wake Survey Methods (Selected Spanwise Locations)

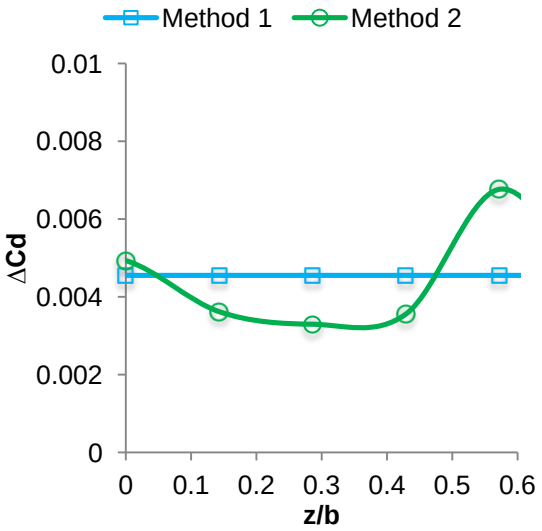

Figure 6.34: Corrected Total Drag Coefficient Comparison for both Wake Survey Methods (Selected Spanwise Locations) 2

A comparison of the drag coefficients using all methods is shown in Figure 6.35.

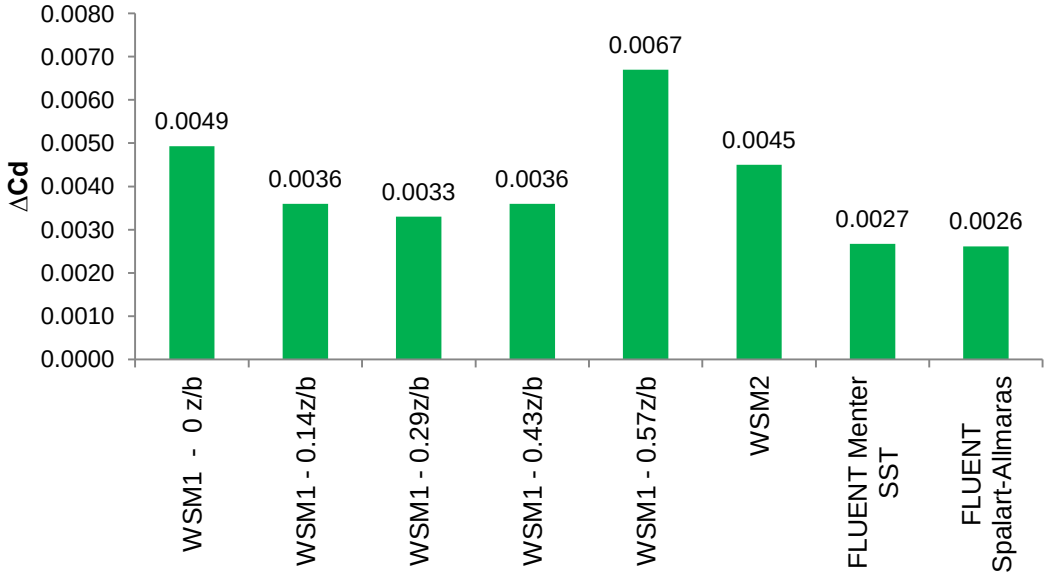

Figure 6.35: Corrected Drag Coefficient Comparison for Runback Ice Shape 1

With the exception of 0.57z/b the overall comparison of all drag coefficient profiles were comparable. The wake survey results for both methods were in good agreement. The numerical result for both turbulence models under predicts the drag relative to WSM2 by 41% and 42% for the Menter SST and Spalart-Allmaras turbulence models respectively.

6.9.2. Wake Profile Boundary Layer Thickness

The velocity profiles from the numerical solver were plotted against the selected spanwise locations; 0z/b to 0.57z/b. All boundary layer profiles are shown with both normalised axis (Figure 6.36). No variation between the $k-\omega$ SST and Spalart-Allmaras turbulence model was observed.

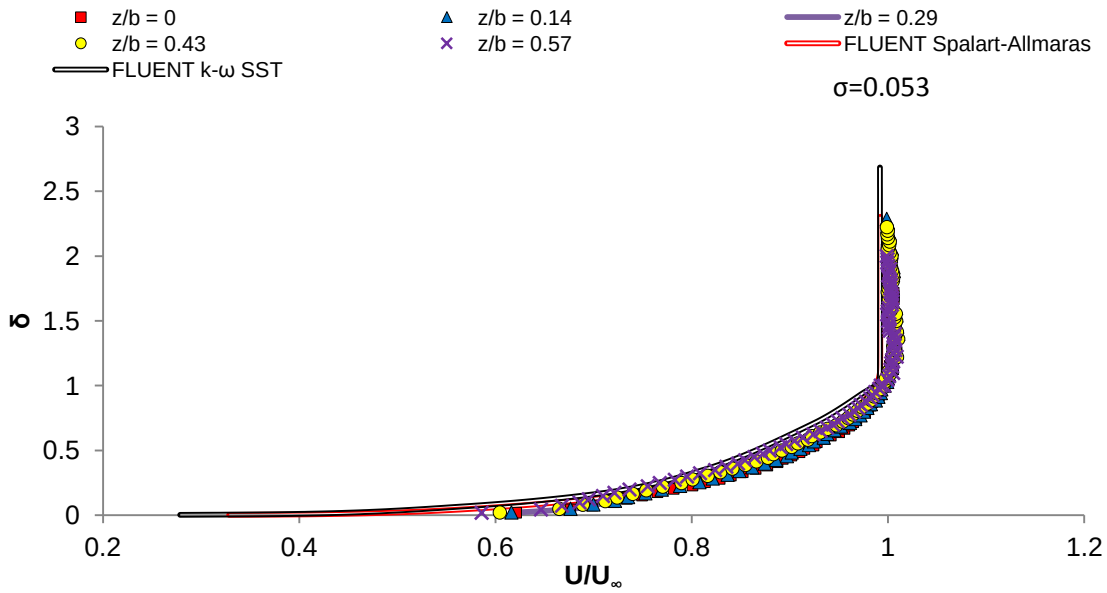

Figure 6.36: Boundary Layer Velocity Profile for Runback Ice Shape 1 at all Selected Spanwise Locations

A closer inspection of the boundary layer profiles for each spanwise location has been included in the Appendix.

The numerical data points are dependent on grid density. With a first cell size of $2x10^{-6}$m and expansion ratio of 1.2, ANSYS FLUENT provided an abundance of data points well within the viscous sublayer. This level of detail was not possible experimentally. However a comparison of the velocity at the first experimental rake position with the numerical profile indicated a slight under prediction up to 20-30mm (Figure 6.37). From this point onwards the numerical velocity profile was comparable with the experimental boundary layer. This was observed for all span wise locations.

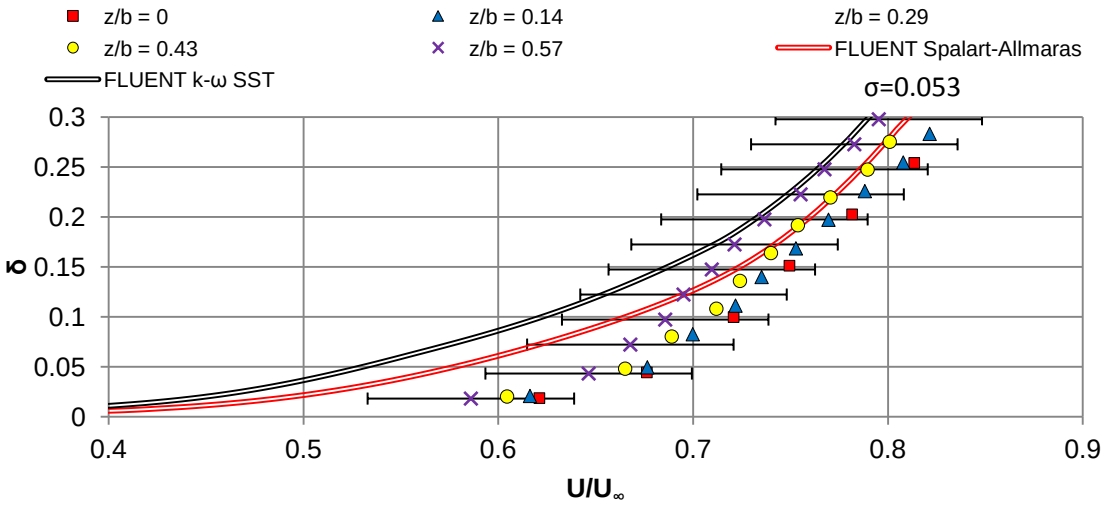

Figure 6.37: Boundary Layer Velocity Profiles for Runback Ice Shape 1 with Uncertainty

6.10. Combination Runback Ice Shape Setup

The combination runback ice shape setup was conducted to help provide a more realistic observation of the flow behaviour and ultimately the drag associated by combining all three runback ice shapes. The three shape profiles used for this setup are shown in Figure 6.38 through to Figure 6.40.

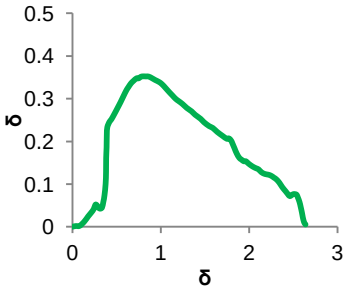

Figure 6.38: Runback Ice Shape 1

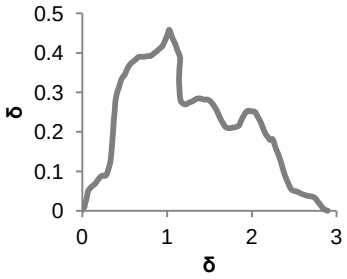

Figure 6.39: Runback Ice Shape 2

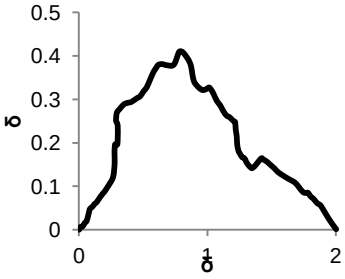

Figure 6.40: Runback Ice Shape 3

The results are presented in the following order:

- Wake Survey Method Results
  - Method 1
  - Method 2
- Comparison of all drag coefficient results

Unfortunately a two-dimensional mesh for the combination setup could not be produced and no ANSYS FLUENT simulation was performed. This setup essentially used all three runback ice shapes fixed together in alternating steps to represent the three dimensional nature of the castings.

6.10.1. Results

A comparison of the two wake survey methods is shown in Figure 6.41. In comparison to the span wise variation seen for runback ice shape 1, the combined runback ice run was surprisingly linear up to 0.7z/b.

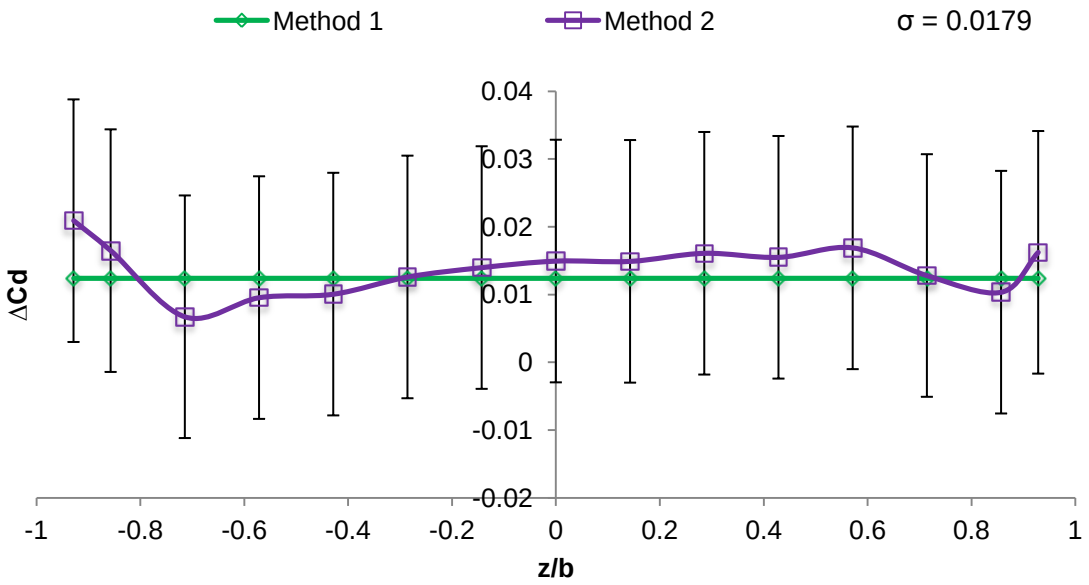

Figure 6.41: Wake survey Method Corrected Drag Coefficient Results for Combination Runback Ice Setup

The removal of the error bars again provided greater resolution of the spanwise drag variations (Figure 6.42). As seen throughout the entire experimental data, the region between 0 - 0.6z/b provided the most reliable and linear results (Figure 6.43).

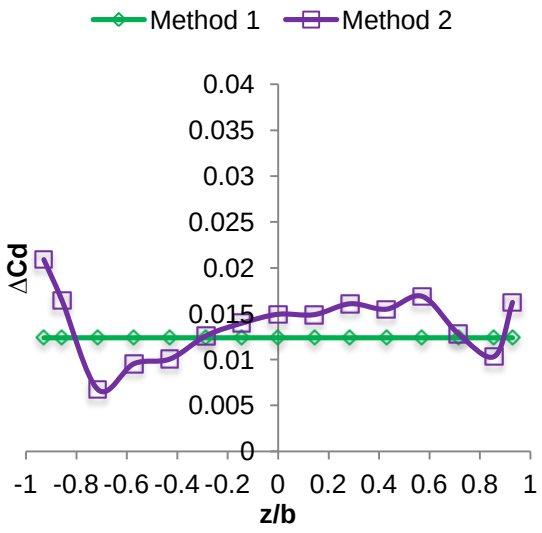

Figure 6.42: Wake survey Method Corrected Drag Coefficient Results for Combination Runback Ice Setup (Excluding Uncertainty)

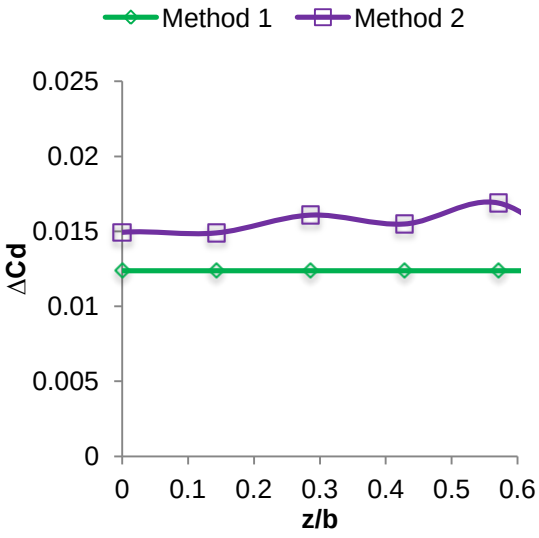

Figure 6.43: Wake survey Method Corrected Drag Coefficient Results for Combination Runback Ice Setup for Selected Spanwise Locations (Excluding Uncertainty)

An overview of all experimental results is shown in Figure 6.44. Excellent agreement was found throughout the spanwise locations using WSM1 against the integral WSM2. The maximum discrepancy of 26% was observed between the WSM2 and WSM1 at spanwise location 0.57z/b. The slight under prediction (relative to the WSM1 spanwise points) can be apportioned to the lower drag coefficient values around the location from -0.3z/b through to -0.75z/b.

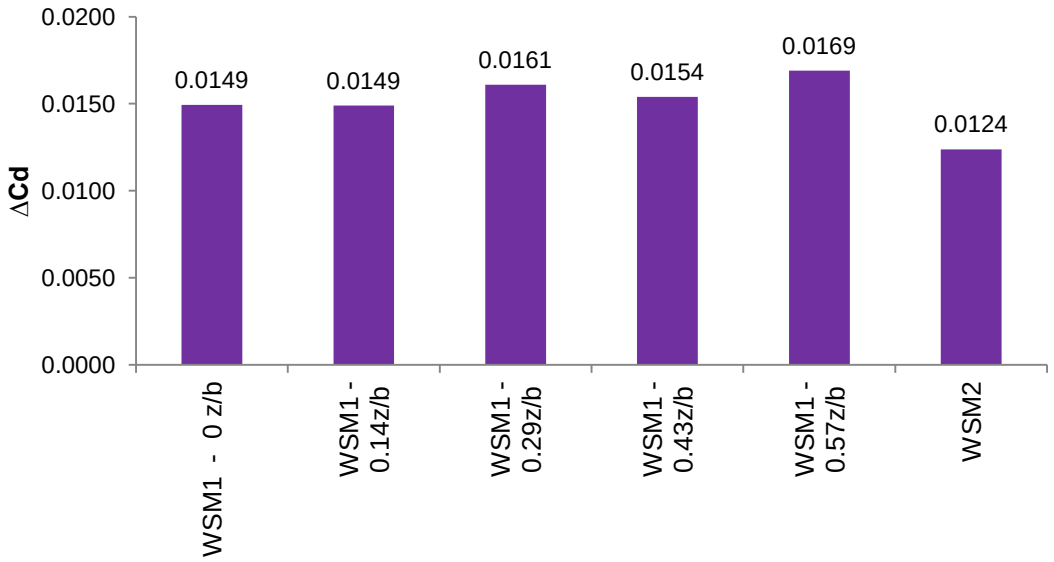

Figure 6.44: Experimental Corrected Drag Coefficient Comparison for Combination Runback Ice Setup

The WSM1 drag results varied from 0.0149 to 0.0169. The WSM1 drag coefficient value at 0.43z/b was close to the average for all WSM1 results.

6.10.2. Wake Profile Boundary Layer Thickness

The boundary layer velocity profile for the experimental spanwise location between 0z/b and 0.57z/b were evaluated. The plot in Figure 6.45 showed a small deviation at the 0z/b spanwise location. Closer inspection of both the raw data plot and normalised plot can be found in the Appendix.

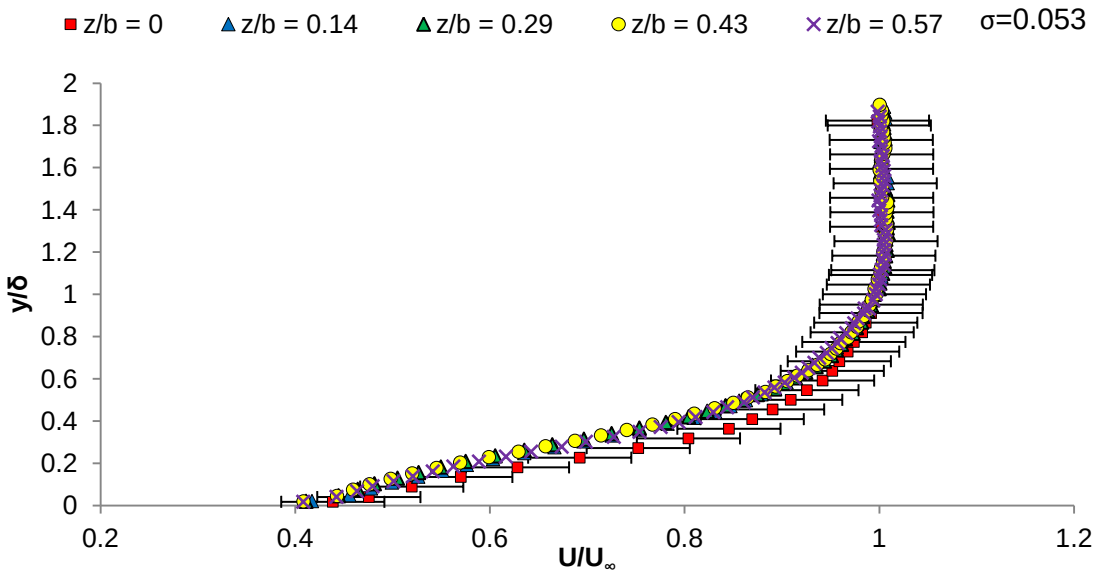

Figure 6.45: Boundary Layer Velocity Profile for Combination Runback Ice Setup at all Selected Spanwise Locations

The variation between the spanwise plots was attributed to the abrupt boundary layer thickness change shown in Figure 6.46 and is particularly noticeable in Figure 6.47.

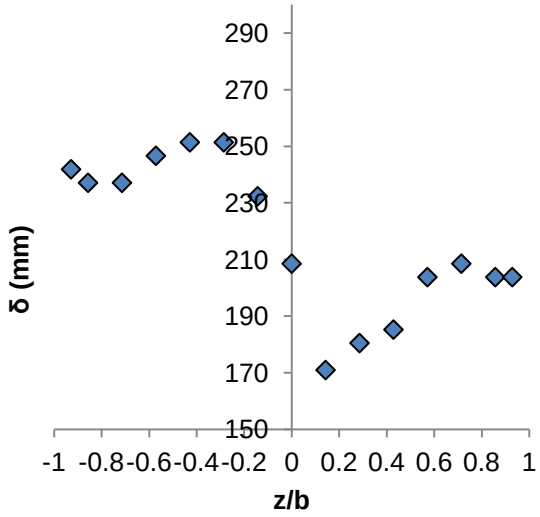

Figure 6.46: Spanwise Boundary Layer Thickness Variation for Combination Runback Ice Setup

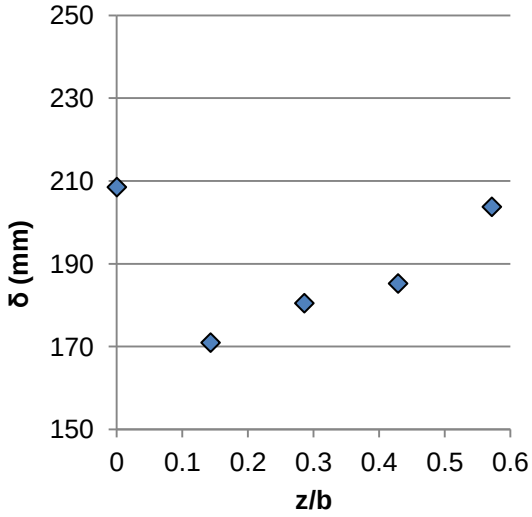

Figure 6.47: Spanwise Boundary Layer Thickness Variation for Combination Runback Ice Setup 2

After considering the entire boundary layer profile data points across the spanwise mapped locations, the velocity profiles variation over almost the entire negative z/b spanwise region, up to and including 0.2z/b, exhibited higher velocity variations relative to the selected spanwise locations. It was concluded the deviation for the 0z/b spanwise location was due to the unknown spanwise effects seen throughout the experimental study.

6.11. Conclusions

6.11.1. Experimental results

The experimental results presented the opportunity to compare two different mathematical approaches for indirect method developed by Jones, [115] that utilised a total pressure rake to survey the wake of the object concerned.

Jones, [115] wake survey method was originally developed to capture the pressure changes through the wake of an airfoil suspended in a controlled environment such as a wind tunnel. These pressure maps of the wake at various spanwise locations were converted into a total drag force using the equations detailed in Wake Survey Method section.

This wake survey technique is well established when dealing with airfoils or any object suspended providing adequate means to capture the pressure loss in the wake are available. However in this instance, the nature of the experimental setup did not allow a full survey of the wake. The runback ice shapes were attached to the force balance which was flush with the tunnel floor. The total pressure rake required a custom holder to ensure all pitot probes were secure and aligned. This restricted the total pressure rake to a minimum distance from the ground; in our case, the limit was 3.5mm. A visual representation of this error is shown in Figure 6.48.

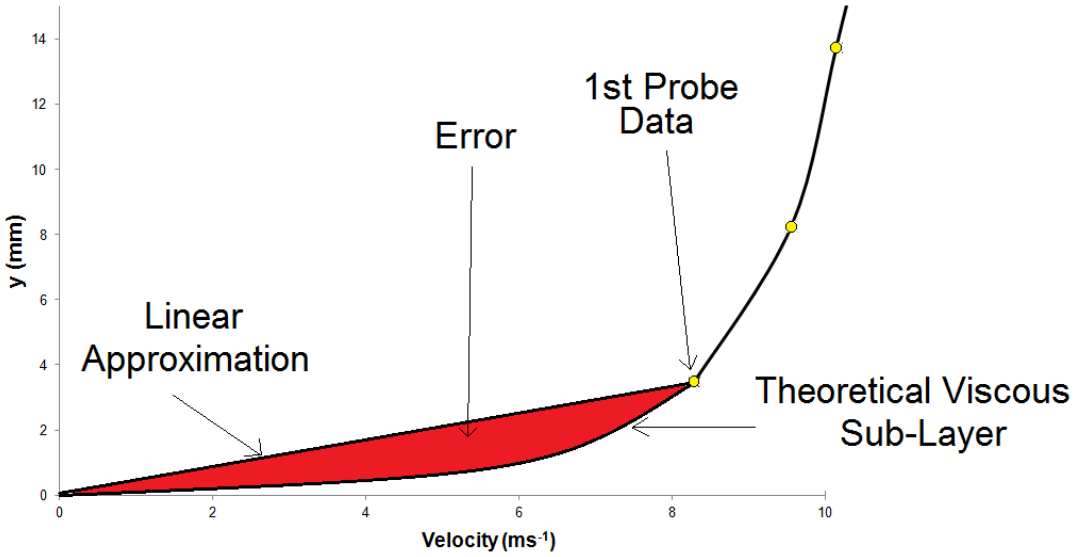

Figure 6.48: Representation of Experimental Error Associated with Total Pressure Rake

Although the results found throughout this experimental study are acceptable, a key area of considerable interest was the first 3.5mm of the boundary layer due to its complex nature and effect on force coefficients. Restrictions with the apparatus did not allow reading below 3.5mm. Unfortunately a realistic or feasible way to quantify this error was not available; however it was prudent to be aware of its existence and possible improvements for future experimental runs using this technique.

A comparison of the two wake survey method for both experimental iced runs is shown in Figure 6.49. The combined runback ice setup provided comparable results for the two wake survey methods. This was expected as the overall spanwise variation was considerably less for the combined runback ice shape run. Although the percentage values for variation seem large for the two methods, when considering the relative size of the drag coefficient, the results were considered to be similar.

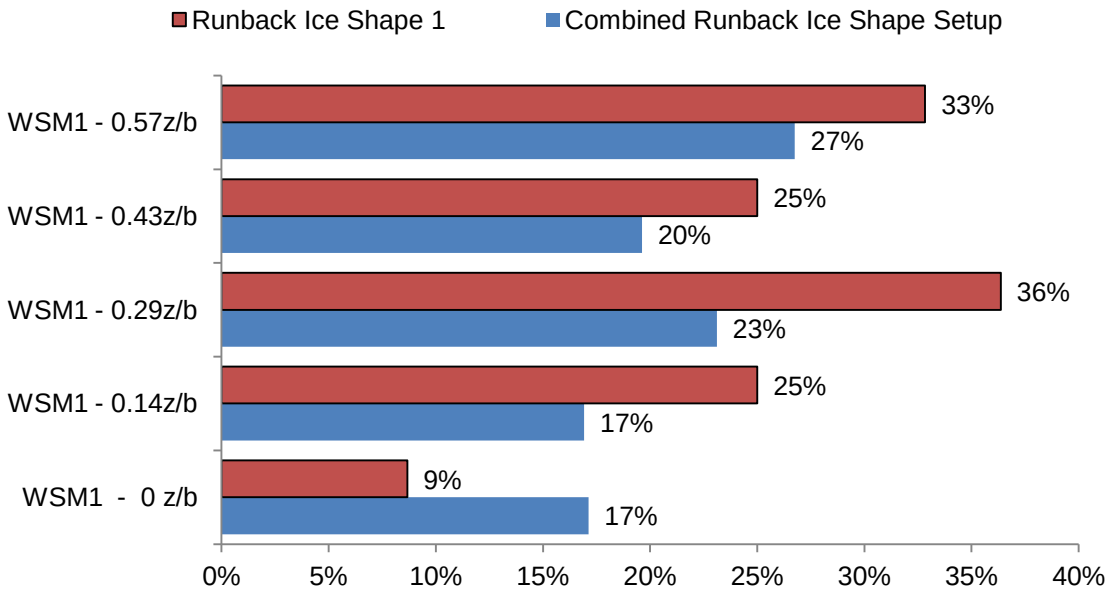

Figure 6.49: Comparison of Wake Survey Method 1 against Wake Survey Method 2 for all Experimental Runs

6.11.2. Effects of Three-Dimensionality

The Pitot tube rake traversing mechanism uses span-wise pressure measurements which allowed a survey of the flow three-dimensionality. The flat plate span-wise pressure reading was not uniform. This lack of spanwise flow regularity was seen throughout all flat plate and runback ice shape runs. Therefore analysis on the potential three-dimensionality of the flow induced by the runback ice obstruction was not possible.

6.11.3. CFD Comparison

Drag coefficient and velocity profile data for two FLUENT turbulence models were considered; Menter's $k-\omega$ SST two equation and Spalart-Allmaras one-equation model.

An initial flat plate CFD run allowed the boundary layer development to a point where the characteristic profile matched the flat plate leading edge experimental data.

ANSYS FLUENT runs were conducted for runback ice shape 1. Both Menter's $k-\omega$ SST and Spalart-Allmaras models predicted the wake profiles at the rake 3 position very well. The drag coefficient difference between Menter's $k-\omega$ SST and Spalart-Allmaras model was small; $6x10^{-5}$. A comparison of Menter's $k-\omega$ SST model against all experimental results is shown in Figure 6.50. The SST and Spalart-Allmaras models, under predicted the drag coefficient for all drag results available. The drag coefficient variation ranged from 13% to 82%. The high discrepancy with the WSM1 drag coefficient at 0.57z/b relative to the numerical values was attributed to the higher drag value predicted by the wake survey method which was a consequence of the tunnel spanwise variation.

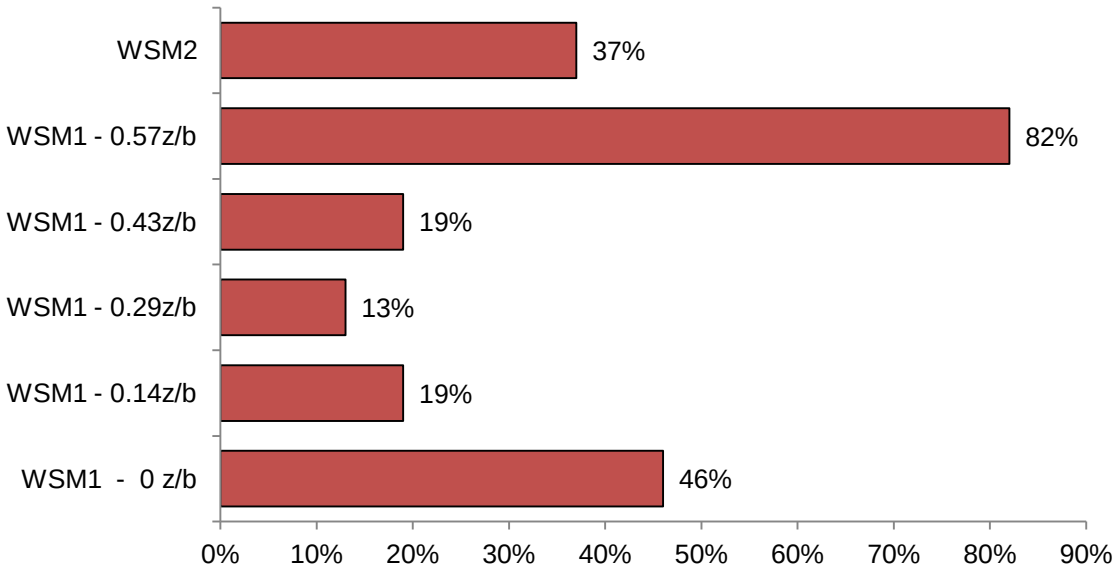

Figure 6.50: Comparison of Menter SST Turbulence Model Results against all Experimental Data for Runback Ice Shape 1

No apparent trends were found with regards to boundary layer thickness.

7. Optimisation

"Success is stumbling from failure to failure with no loss of enthusiasm."
- Winston Churchill

A four part multi-objective optimisation study is detailed in this chapter.

7.1. Ice Location Optimisation

The runback ice location optimisation study considered the movement of runback ice on the upper surface of an airfoil. For this simulation a 4m B737-700 airfoil used in Chapter 5 (Boeing 737-700 Airfoil Numerical Study
) was used.

7.1.1. Objectives

The aim of this study was to investigate relative performance degradation from runback ice with respect to chord length. For various chord positions, the runback ice produced a varied effect on the lift and drag performance. As seen in Chapter 5, the pressure distribution for the clean airfoil was the key element which dictated the performance degradation. This optimisation study provided an insight into how the runback ice disturbance affected the airfoil at different chord location.

A secondary consideration was the influence of boundary layer thickness relative to the runback ice height. Research on boundary layer and chord ratio scaling was addressed in Chapter 2 and highlighted the different results when two different runback ice scaling methods were applied. The ice location optimisation process coupled with a runback ice height size of 7.2mm provided an opportunity to consider how the boundary layer interacted with disturbances of comparable height. As the ice location was moved towards the trailing edge, the boundary layer thickness increased and lead to a point where the thickness was comparable with ice height. Further along the chord from this point the boundary layer thickness was taller than the disturbance (runback ice).

7.1.2. Datum Conditions

The datum conditions are set to match the 45 minute hold case in continuous icing condition as required by the EASA. These have been outlined in detail in Chapter 5. A calibrated speed of 118ms^{-1} at 17000ft for a static temperature of -9°C was required at an angle of attack of 3° were the boundary conditions used for the ANSYS FLUENT solver.

7.1.3. Optimisation Setup

The objective functions for this multi-objective optimiser was to maximise lift ($\bar{F}_1$) and minimise drag($\bar{F}_2$) as shown in Equation 7.1 and Equation 7.2.

$$\bar{F}_1 = -\left(\frac{Cl_{\bar{x}_1}}{Cl_{datum}}\right)$$

Equation 7.1: Lift Coefficient Objective Function for Ice Location Optimisation

$$\bar{F}_2 = \left(\frac{Cd_{\bar{x}_1}}{Cd_{datum}}\right)$$

Equation 7.2: Drag Coefficient Objective Function for Ice Location Optimisation

The design parameter for this study was the runback ice chord location with a range of variability of 0.0215x/c to 0.113x/c. The FLUENT solver convergence criterion and force coefficient variation check was used as a hard constraint.

The memory and search control features of the MOTS were initially set based on the optimiser process which was discussed in more detail in Section 3.5.2. MOTS Overview). Table 7.1 outlines these features.

Short Term Memory Allocation	15
Long Term Memory Allocation	4
Intensification Point	15
Diversification Point	25
Step Size Reduction Point	45

Table 7.1: Ice Location Optimiser Memory and Search Control Variables

The initial datum run ice location position was set to match the experimental icing tunnel run conducted by Alègre, [104]. For this particular runback ice run, the icing conditions are shown in Table 7.2 and the overall optimisation processes in Figure 7.1.

	Limit of Heated Zone (x/c)	Total Heat Input (kW)	Start of Runback Ice (x/c)	Tunnel Run Time (minutes)
Datum Run	0.0215	0.703	0.022875	20

Table 7.2: Ice Location Optimiser Datum Run Conditions

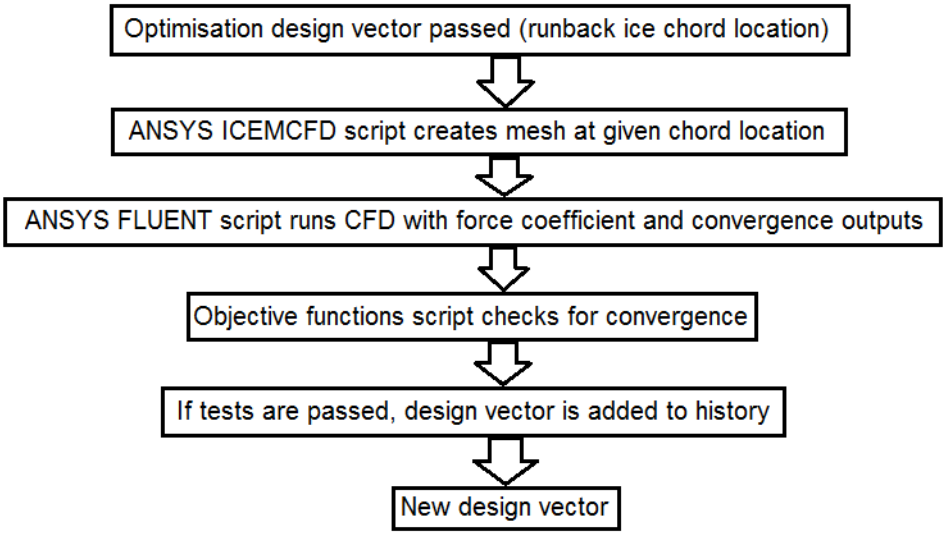

Figure 7.1: Flow Chart for Ice Location Optimiser

Discussions on transition to turbulence were held with sponsors Airbus. The conclusions of these talks were that transition would occur very early in practise due to runback water tripping the flow from laminar to turbulent. Therefore the CFD model was setup to be fully turbulent from the outset.

In practise the runback ice shape movement along the chord would impact on the runback ice shape geometrical features and height. Implementation of these geometrical ice changes was beyond the scope of this study.

7.1.4. Results

The progress of the optimiser was monitored via a number of output files. Figure 7.2 illustrates the behavioural history for the optimisation process. The i_local value specifies the number of consecutive unsuccessful optimisation iterations. Bound by the initial memory and search control variables set in Table 7.1:

1. 50 search intensification steps occurred. For the search intensification to initiate, 15 consecutive unsuccessful iterations must be tallied.
2. 50 search diversification steps occurred. For the search intensification to initiate, 25 consecutive unsuccessful iterations must be tallied.
3. 49 step size reductions occurred. For each reduction in step size, 45 consecutive unsuccessful iterations must be tallied. Every step size reduction reduces the step size by a factor of 0.7. The initial step size was set at 0.0015. The final step size was 3.8×10^{-11}.

The total number of CFD steps was 2285. 4 Pareto-optimal runback ice locations were found.

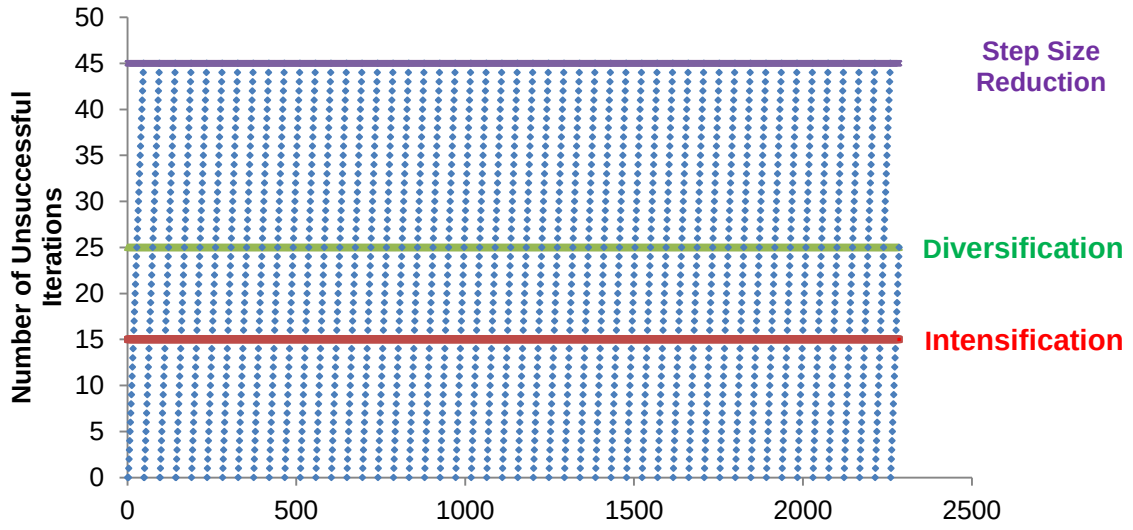

Figure 7.2: Ice Location Optimiser History

As can be seen in Figure 7.3 the optimiser search history initially focuses down in a linear fashion towards the final Pareto solutions shown in Figure 7.4.

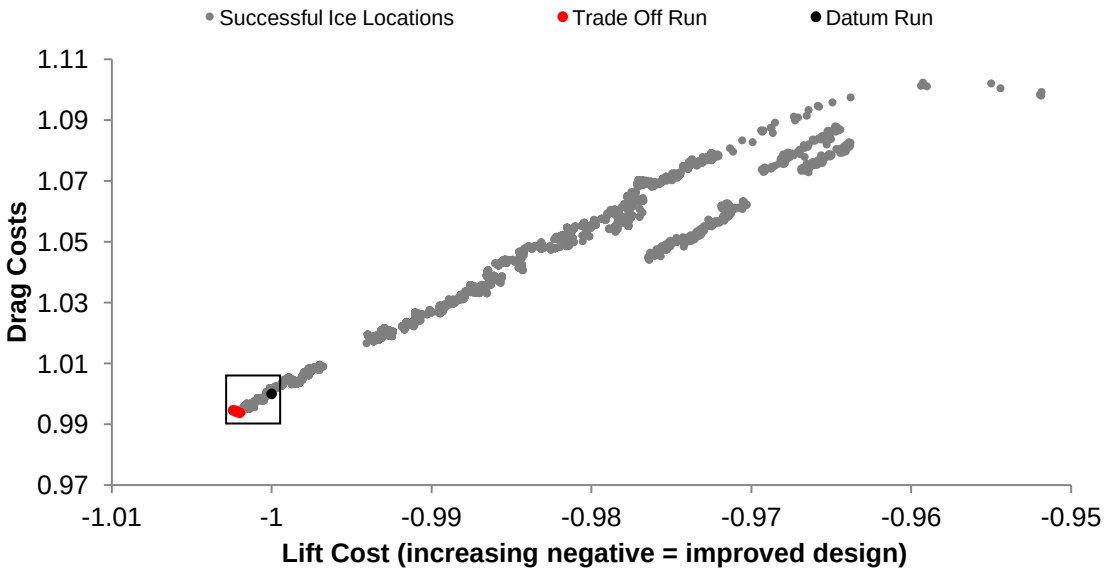

Figure 7.3: Ice Location Optimisation Costs

The optimisation runs close to the datum and optimum locations have been highlighted by the square box and this section can be seen more clearly in Figure 7.4.

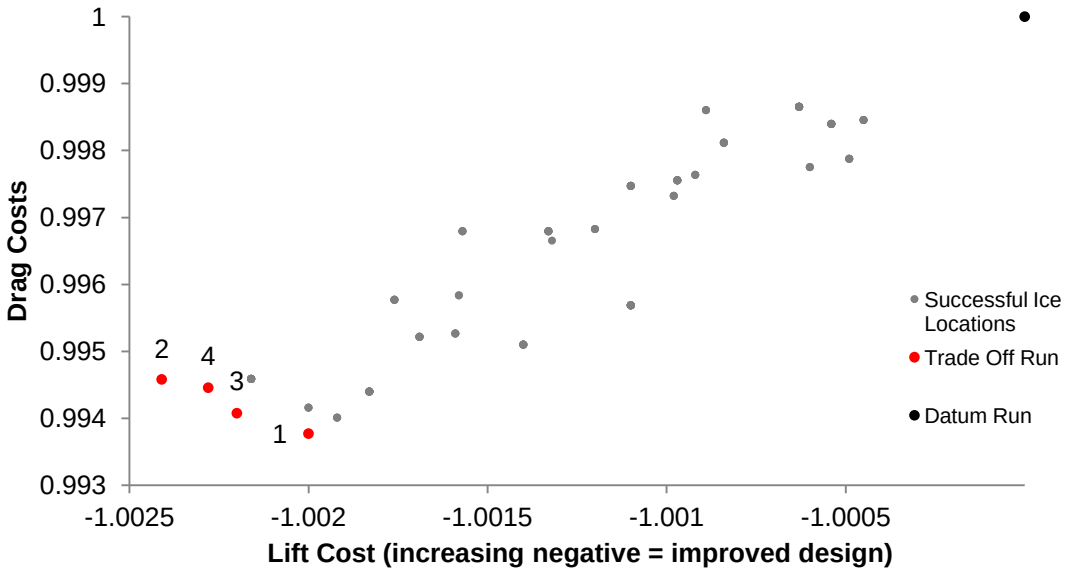

Figure 7.4: Pareto Optimum Locations

The ice location optimisation produced four optimum locations. All optimum positions were individually run to consider them in more detail. Comparison of the individually run force coefficients against the optimisation costs found a maximum delta of 0.04% and 0.16% for the lift coefficients and drag coefficients respectively (Table 7.3). This variation was deemed negligible and provided confidence that all optimum positions did offer a performance advantage over the datum position and the optimisation code was producing consistent results which could be verified.

Optimum Runs Case Number	Ice Location (x/c)	Lift Cost	Drag Cost	CFD Lift Coefficient	CFD Drag Coefficient	Lift Coefficient Delta[3]	Drag Coefficient Delta[4]
Optimum Run 1	0.0218	-1.00200	0.99377	0.4671	0.01200	0.03%	0.16%
Optimum Run 2	0.0216	-1.00241	0.99458	0.4672	0.01201	0.03%	0.16%
Optimum Run 3	0.0217	-1.00220	0.99407	0.4672	0.01200	0.03%	0.16%
Optimum Run 4	0.0216	-1.00228	0.99446	0.4672	0.01201	0.04%	0.16%
Datum	0.0229	-1.0	1.0	0.4660	0.01210		

Table 7.3: Ice Location Optimum Chord Locations

All optimum locations were located closer to the leading edge of the airfoil relative to the datum position (x/c=0.0229). All four optimum locations produced an increase in lift and reduction in drag relative to the datum chord location (Table 7.4). The maximum increase for the lift coefficient was obtained from Optimum Run 2 (0.28%). A maximum reduction for the drag coefficient of 0.78%

[3] Percentage Variation against Datum Solution
[4] Percentage Variation against Datum Solution

was found from Optimum Run 1. The improvements in both coefficients were very small.

Optimum Runs Case Number	Ice Location (x/c)	Lift Coefficient Improvement[5] (%)	Drag Coefficient Improvement[6] (%)
Optimum Run 1	0.0218	0.23	0.78
Optimum Run 2	0.0216	0.28	0.70
Optimum Run 3	0.0217	0.25	0.75
Optimum Run 4	0.0216	0.26	0.71

Table 7.4: Ice Location Optimum Ice Location Improvement

The optimum pressure coefficient profiles are shown in Figure 7.5 along with the clean and datum airfoil cases. It becomes difficult to distinguish any of the optimum runs as they were so close together. Figure 7.5 allows a closer examination of the local pressure changes due to the runback ice shape. Apart from the obvious variation due to their respective locations on the airfoil, the profile of the datum and all optimum runs were identical.

The velocity on the upper surface trailing edge for the optimum runs was found to be lower and thus improved lift and drag coefficients. The addition of the runback ice changed velocity profile on the suction surface and the stall type characteristics towards a thin-airfoil stall (trailing edge stall). These results were consistent with the findings of Pan, et al., [44] and also observed by Whalen, et al., [118] for their warm hold ice simulation. Confirmation of these findings would require a number of runs at higher angles of attack to define the lift-break characteristics relative to the clean airfoil.

[5] Against Datum CFD Solution
[6] Against Datum CFD Solution

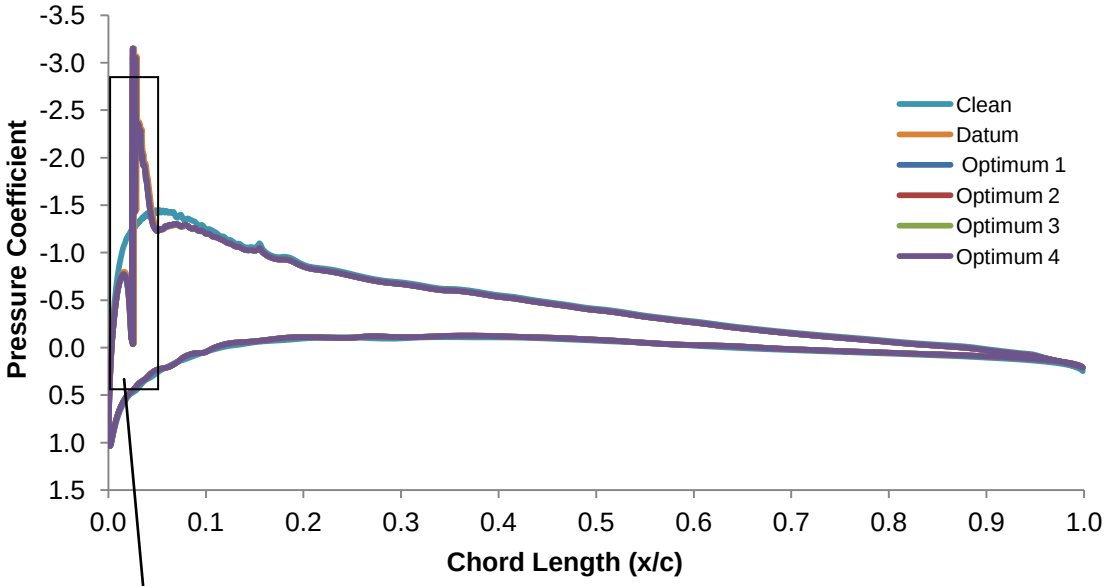

Figure 7.5: Pressure Coefficient Comparison for Ice Location Optimum Runs

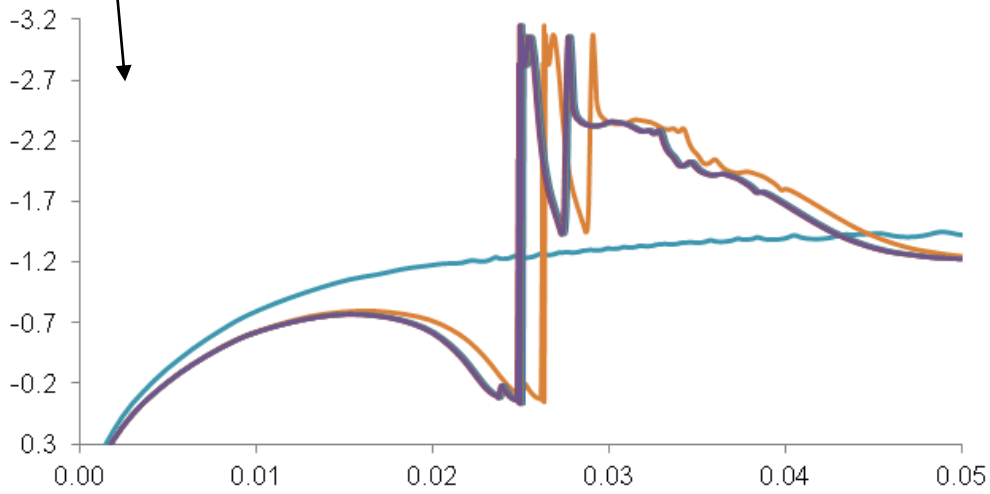

Figure 7.6: Pressure Coefficient Comparison for Ice Location Optimum Runs at Ice Region

A final inspection of the four optimum runs force coefficients against chord location was conducted (Figure 7.7 & Figure 7.8). As the runback ice locations were so close to each other and variation in lift and drag coefficients were so small, no meaningful analysis could be carried out with just these four positions.

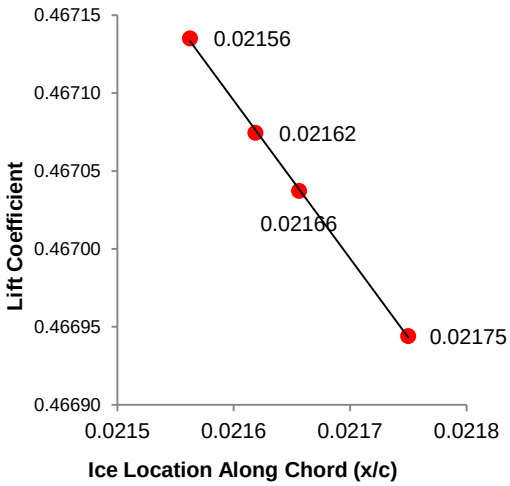

Figure 7.7: Optimum Ice Location against Lift Coefficient

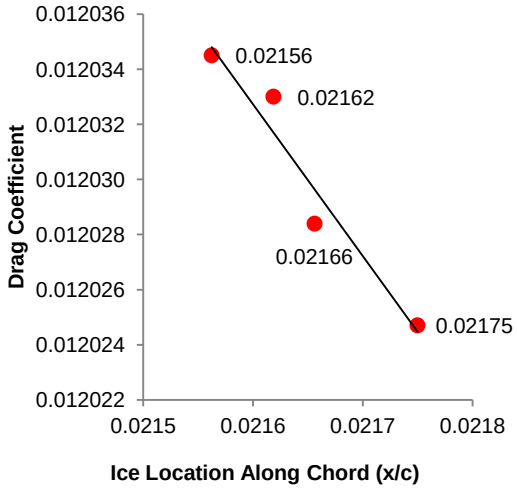

Figure 7.8: Optimum Ice Location against Drag Coefficient

All four optimum locations were within 0.75mm of each other. The maximum variation in lift and drag coefficients for all optimum positions was 0.0002 and 0.00001 respectively. The results indicated the Boeing 737-700 airfoil was very sensitive to a small build-up of runback ice at the optimum location. Since all Fluent CFD runs were conducted to second order discretisation accuracy it was deemed sensible to consider the optimum positions as a single averaged optimum location; 0.0216x/c.

The location difference between the datum and Optimum Run 2 runback ice 5.25mm. Moving the runback ice location by this amount towards the leading edge provided an improvement in lift and drag of 0.28% and 0.70% respectively. Since the locations movement and consequent variation in force coefficients are small, another CFD run was conducted with the runback ice shape moved 0.013125x/c towards the trailing edge (Datum Plus). The aim here was to corroborate these small variations with respect to runback ice location.

Moving the runback ice shape by 5.25mm towards the trailing edge reduced the performance by 0.21% and 0.53% for the lift and drag coefficients respectively. The results in Table 7.5 show the relative variation for the optimum and datum plus CFD runs against the datum run. The expected force coefficient variation with chord length illustrated the fidelity of the CFD methods implemented.

	Position Relative to Datum	Lift Coefficient Variation Relative to Datum (%)	Drag Coefficient Variation Relative to Datum (%)
Optimum	-5.25mm	0.28%	0.70%
Datum Plus	+5.25mm	0.21%	0.53%

Table 7.5: Force Coefficient Variation for Optimum & Datum Plus Ice Location Study

The rearward movement of the ice shape produced a lift and drag variation of similar magnitudes as seen when comparing the force coefficient variation between the datum and optimum chord location.

The small changes in both the location and corresponding force coefficients indicated the robustness of the multi–objective optimiser. After a significant number of diversification attempts and an exhaustive global search of the design space, the optimiser found four optimum locations which were regarded as a single location; Optimum Run 2 at 0.0216x/c.

The sensitivity study corroborated the force coefficient variation with respect to runback ice location and the fidelity of the numerical model used.

Selected Test Cases

A number of positions along the main central line of the optimiser history were selected to determine how the lift and drag costs were affected by ice location.

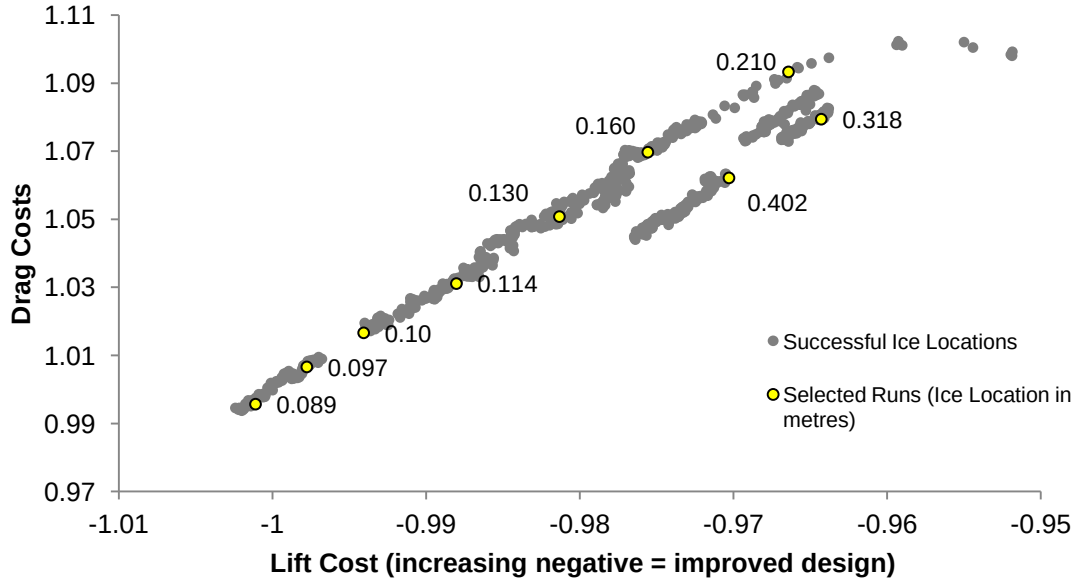

Figure 7.9: Ice Location Design Space Selected Runs

These 9 positions were chosen along the optimiser search history. For each position individual ANSYS FLUENT cases were run to validate and confirm the costs from the optimiser output (Table 7.6). The maximum variation was 0.31% and 0.86% for the lift and drag coefficient respectively.

Validation Runs Case Number	Ice Location (x/c)	MOTS Lift Cost	MOTS Drag Cost	Computed Lift Coefficient	Computed Drag Coefficient	Lift Coefficient Delta	Drag Coefficient Delta
Selected Case 1	0.022	-1.001	0.996	0.467	0.0120	0.04%	0.16%
Selected Case 2	0.024	-0.998	1.007	0.464	0.0123	0.17%	0.82%
Selected Case 3	0.025	-0.994	1.017	0.465	0.0122	0.31%	0.86%
Selected Case 4	0.029	-0.988	1.031	0.461	0.0125	0.15%	0.03%
Selected Case 5	0.033	-0.981	1.051	0.458	0.0127	0.13%	0.10%
Selected Case 6	0.040	-0.976	1.070	0.454	0.0130	0.17%	0.10%
Selected Case 7	0.052	-0.966	1.093	0.450	0.0132	0.13%	0.10%
Selected Case 8	0.079	-0.964	1.079	0.450	0.0130	0.05%	0.13%
Selected Case 9	0.100	-0.970	1.062	0.452	0.0129	0.01%	0.69%

Table 7.6: Selected Runs Force Coefficient Variation for Ice Location Optimisation Study

The maximum lift and drag coefficient variation across all 9 selected runs against the datum was 3.52% & 9.22% for the lift and drag coefficient respectively (Table 7.7).

Selected Run	Lift Delta From Datum Run	Drag Delta From Datum Run
1	0.15%	0.44%
2	0.39%	0.51%
3	0.28%	1.51%
4	1.05%	3.14%
5	1.74%	4.98%
6	2.61%	7.08%
7	3.48%	9.22%
8	3.52%	7.80%
9	2.98%	6.96%

Table 7.7: Lift and Drag Coefficient Variation from Datum Runback Ice Location

Select Run 1 of 9 (highlighted in red) was the only chord location where an improved lift and drag coefficient was found. This was also the only selected run where the runback ice was located closer to the leading edge relative to the datum because the four optimum solutions in this region were very close together. A review of the pressure coefficient profiles at the runback ice locations and trailing edge revealed relationships with ice location and airfoil performance.

As the air accelerated over the ice shape, the local Cp minimum peak observed was reduced with increasing chord length (Figure 7.11). The maximum velocity observed over the runback ice shape against chord length for the selected runs is shown in Figure 7.12.

Small disturbances of the runback ice size of 0.0018k/c (runback ice height, k, to chord ratio, c) allowed the airfoil to produce a significant proportion of its

upper surface suction pressure regardless of ice location. However subtle differences in the maximum velocities over the airfoil and consequent suction peaks altered its pressure profile characteristics. There was a clear relationship with ice location and reduced velocity at the trailing edge. At higher angles of attack this feature could have a more profound effect on the airfoils ability to create peak lift coefficient values. However without performing a study with varying angle of attack, this could not be confirmed.

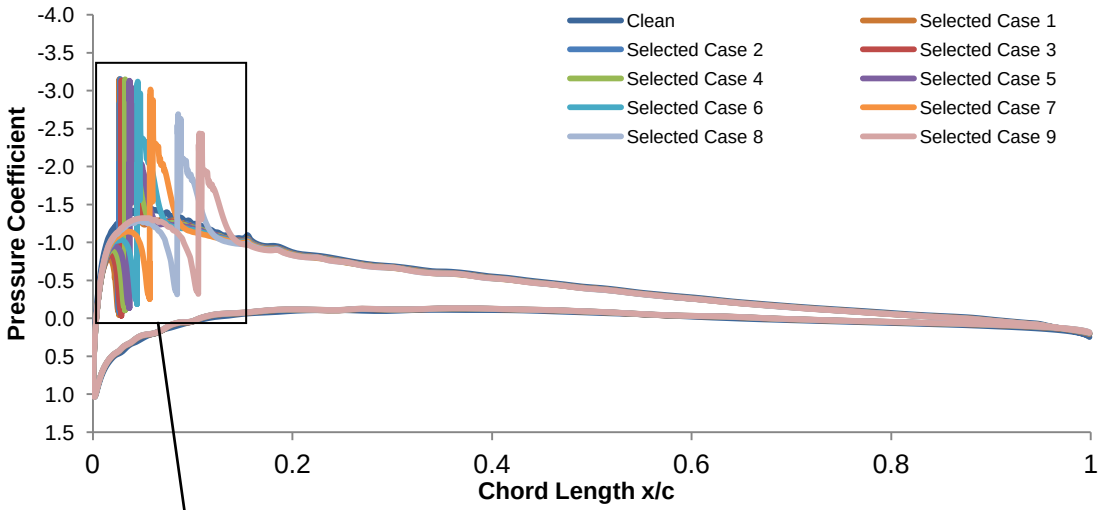

Figure 7.10: Selected Cases Pressure Coefficient Comparison for Ice Location Optimisation

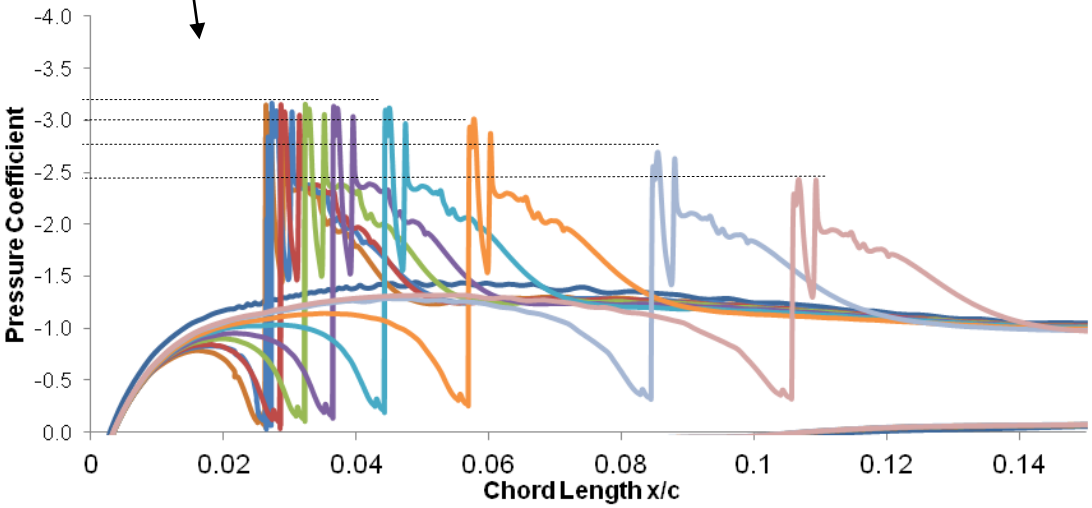

Figure 7.11: Selected Cases Pressure Coefficient Comparison at Ice Location

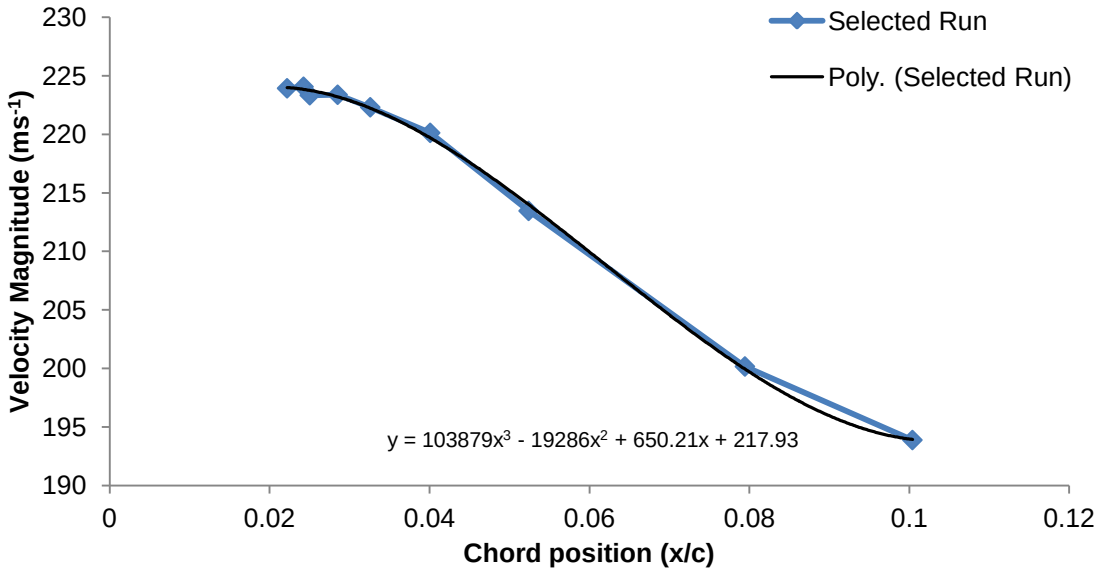

Figure 7.12: Selected Cases Maximum Velocity Magnitude Comparison against Ice Location

The runback ice location relative to peak suction was considered. Previous work on critical runback ice locations highlighted the region around peak suction produced the highest lift coefficient losses [10]. However these finding were based on large ridge ice shapes which significantly reduced the velocity in these locations relative to the clean airfoil. As a consequence this did not allow a noticeable suction peak to be produced. For this study the runback ice shape was significantly shorter in height and thus did not replicate the condition observed in published literature. Peak suction for this case occurred at 0.04x/c. Runback ice shape located at peak suction showed no variation between runback ice shape pressure profiles.

Figure 7.13 and Figure 7.14 indicates the selected runs (shown with data labels of the ice location normalised against the chord) where a clear relationship was revealed. The lift and drag deteriorate as the runback ice shape moves towards the trailing edge.

The lift coefficient variation with respect to runback ice location is shown in Figure 7.13. A clear trend was observed where the lift coefficient performance deteriorated as the ice location moved along the chord from 0.022x/c to 0.06875x/c. From this point onwards the lift coefficient began to improve. The optimiser was limited in its movement up to 0.1125 x/c hence further data was not shown. Most of the points follow a second order polynomial apart from the region around a chord location of 0.08x/c.

The drag coefficient variation with respect to ice location is shown in Figure 7.14. Again a second order polynomial followed the trend with the exception of

the region around 0.08x/c. The drag coefficient increased as the runback ice moves along the chord up to 0.06875x/c. From this point onwards (up to 0.1125x/c) the drag coefficient began to reduce.

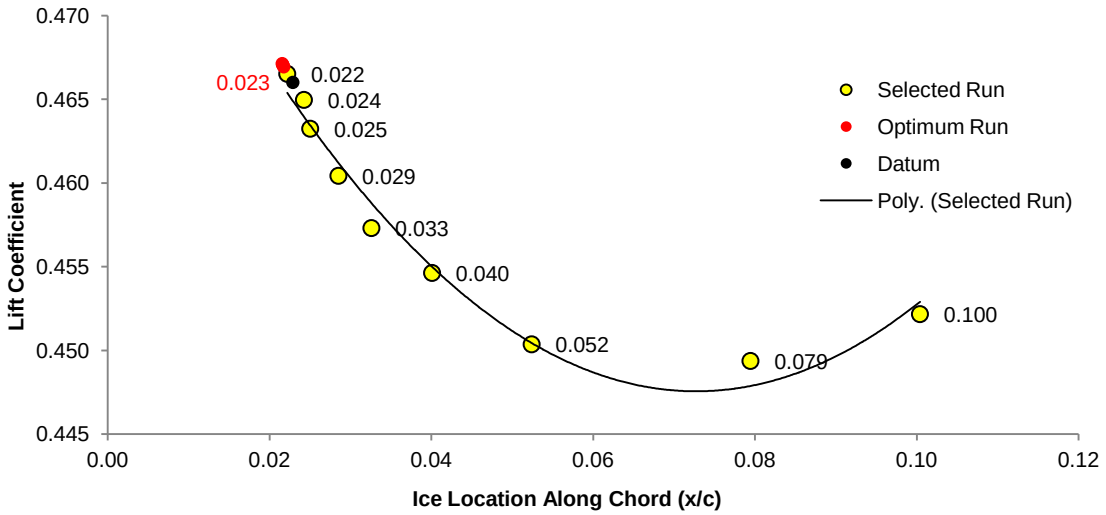

Figure 7.13: Ice Location against Lift Coefficient for Selected Runs

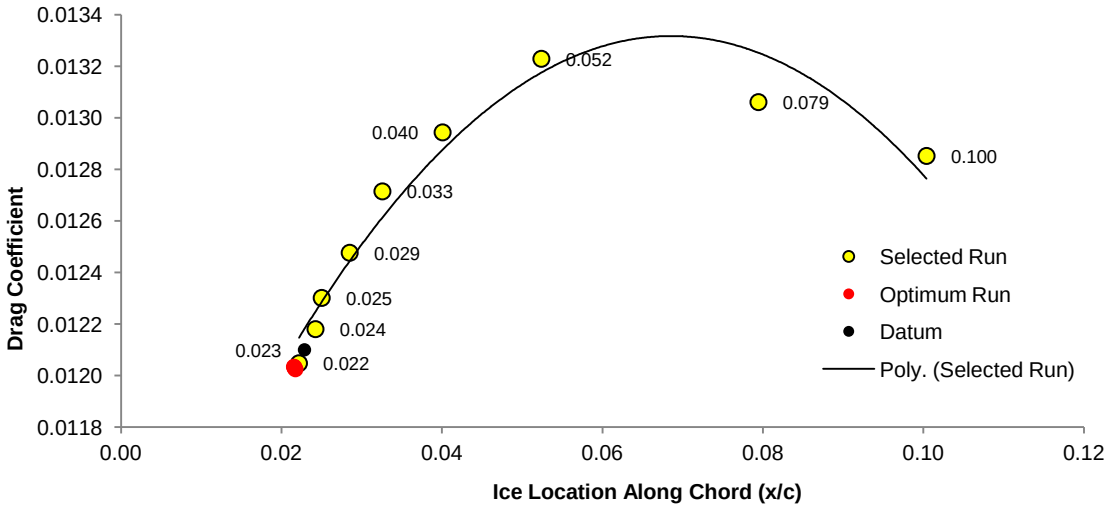

Figure 7.14: Ice Location against Drag Coefficient for Selected Runs

The optimum performance with runback ice on a Boeing 737-700 airfoil for the hold condition occurred close to the leading edge (0.02-0.0225x/c). The performance then fell as the ice moved along the chord until a position of 0.06875x/c was reached. From this point onwards the lift and drag coefficient began to improve.

Recent studies by Papadakis, et al., [32] on step ice and roughness for a range of chord lengths of 1%, 3%, 5% and 8% found that the 2mm and 4mm forward-facing quarter round ice shapes produced the largest performance losses at 1% chord location. These results were conducted using a laminar flow wing with full span control surface. The angle of attack was set to 7°. At this angle of attack the flow separation was significantly higher than at 3° AOA. As a result, the conflicting results were not comparable. The same issue occurred for larger runback ice shapes. The correlation between runback ice height and shape discussed in the literature review (Chapter 2) highlighted these problems in more detail.

The selected runs highlighted an offset of force coefficient results from the observed trend at 7.9% chord length position. The objective functions script within the optimiser outputs the history for each successful optimisation run. The lift and drag coefficients against their relative ice locations can be seen in Figure 7.15 through to Figure 7.18. Three test cases were investigated to find the reason for this offset; T1, T2 and T3.

The force coefficients for test cases 1 to 3 are shown in Table 7.8.

Case	Ice Location (x/c)	Lift Coefficient	Drag Coefficient
Test 1	0.0707	0.445	0.01332
Test 2	0.0795	0.449	0.01306
Test3	0.0943	0.451	0.01302

Table 7.8: Ice Location Optimisation Force Coefficient for Test Cases

To ensure there were no errors within the mesh creation, CFD solver and output scripts, all three test were conducted again. A visual inspection and grid quality check was performed and no errors were found.

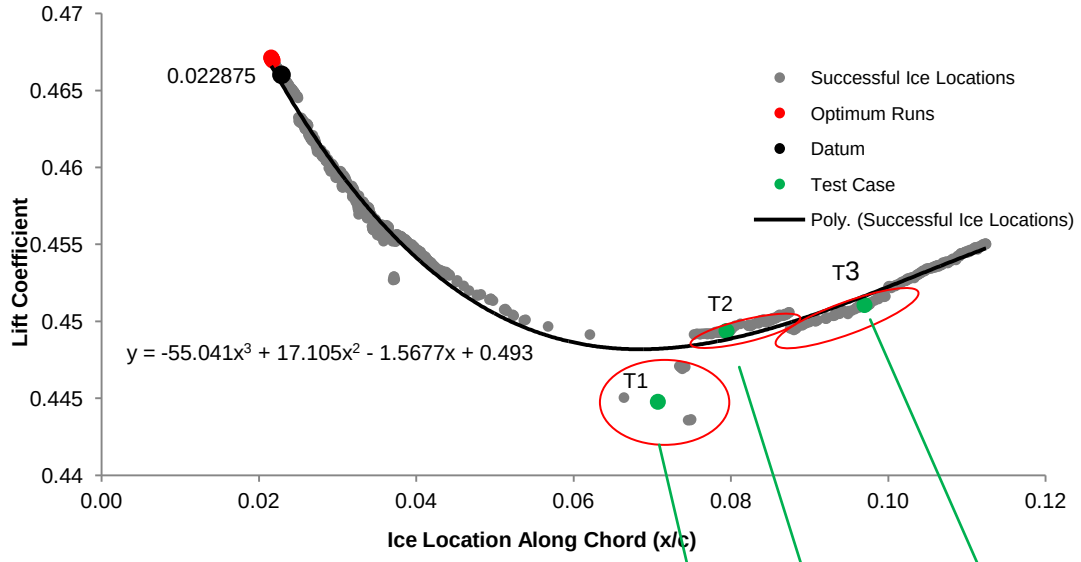

Figure 7.15: Ice Location against Lift Coefficient Feasible Runs

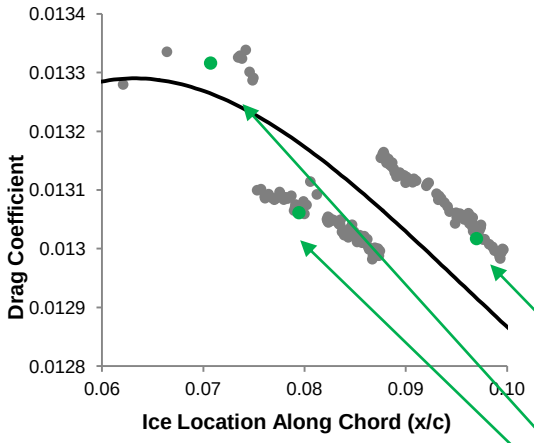

Figure 7.16: Test Point for Ice Location against Drag Coefficient

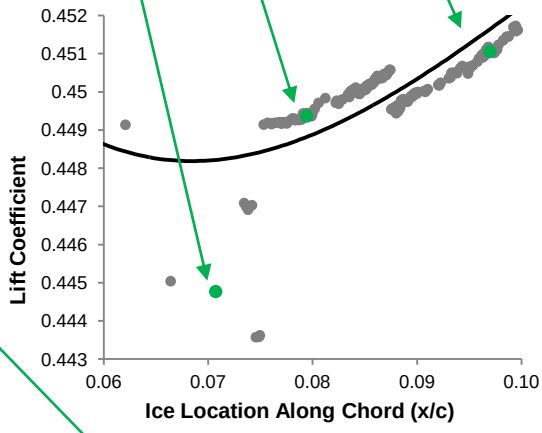

Figure 7.17: Test Points for Ice Location against Lift Coefficient

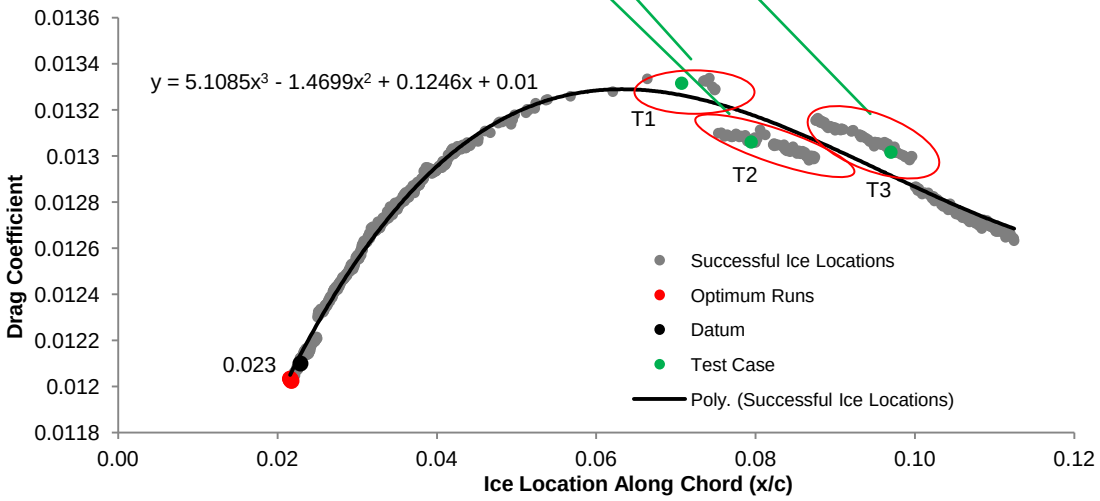

Figure 7.18: Ice Location against Drag Coefficient Feasible Runs

Selected Cases 4, 5, 6 and 7 are chosen as their location, with respect to test case 1,2 and 3, helped analyse the changes that occurred to the flow field in the area shown in Figure 7.15 through to Figure 7.18. Selected case 8 was the same run as test case 2 and was omitted.

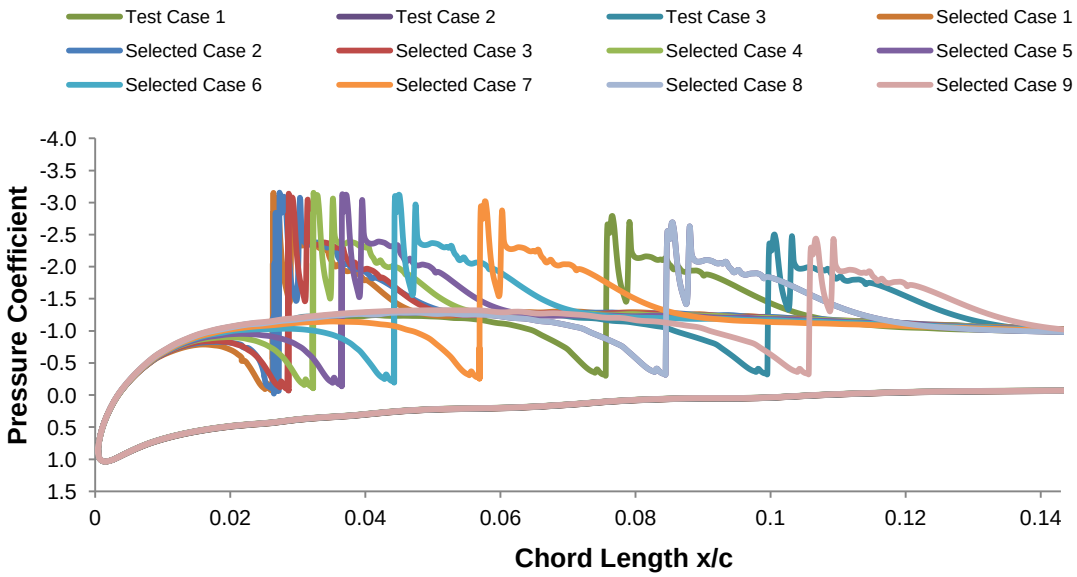

Figure 7.19: Pressure Coefficient Comparison for a range of Selected and Test Cases at Runback Ice Location

Another parameter considered was the size of the separated region with respect to runback ice chord location. Up to selected case 7, an increase in the length of the separated zone resulted in an increase in drag (Figure 7.20).

Test cases 1 to 3 and select run 9 were excluded in Figure 7.20. Figure 7.21 includes these positions and the correlation was no longer observed for all ice location positions above 0.0795x/c.

Pan, et al., [44] found that their biggest performance degradation for ridge ice (0.0139k/c) occurred at 0.1x/c which produced a smaller separation bubble than that seen at 0.2x/c for the same ice shape. They concluded the separation bubble length may not be a robust predictor of critical ice shape locations. However, as highlighted in Chapter 5.5, a comparison between runback ice shapes and ridge ice did not allow for direct comparison of these relationships.

Velocity contour plots depicting the size of the separation bubbles are shown in Figure 7.22 through to Figure 7.25.

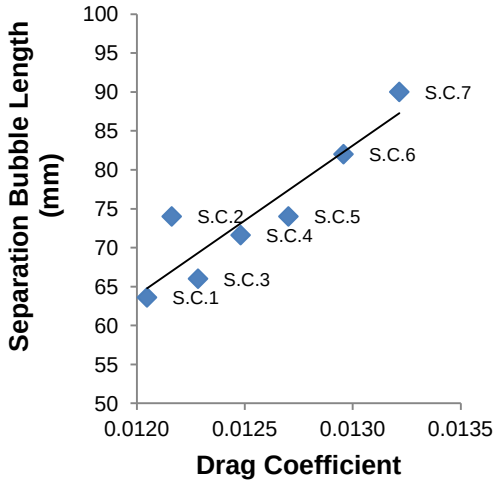

Figure 7.20: Drag Coefficient against Length of Separated Region for Selected Runs 1 - 7

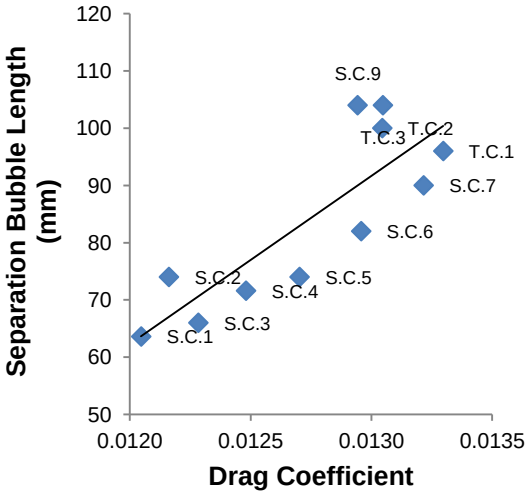

Figure 7.21: Drag Coefficient against Length of Separated Region for all Test and Selected Runs

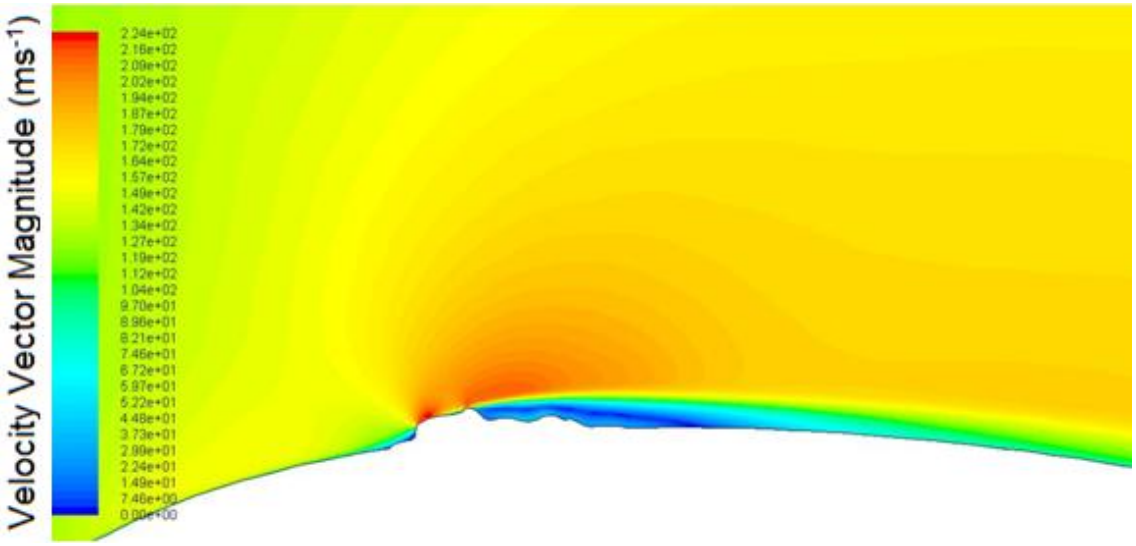

Figure 7.22: Velocity Contour Plot for Selected case 1

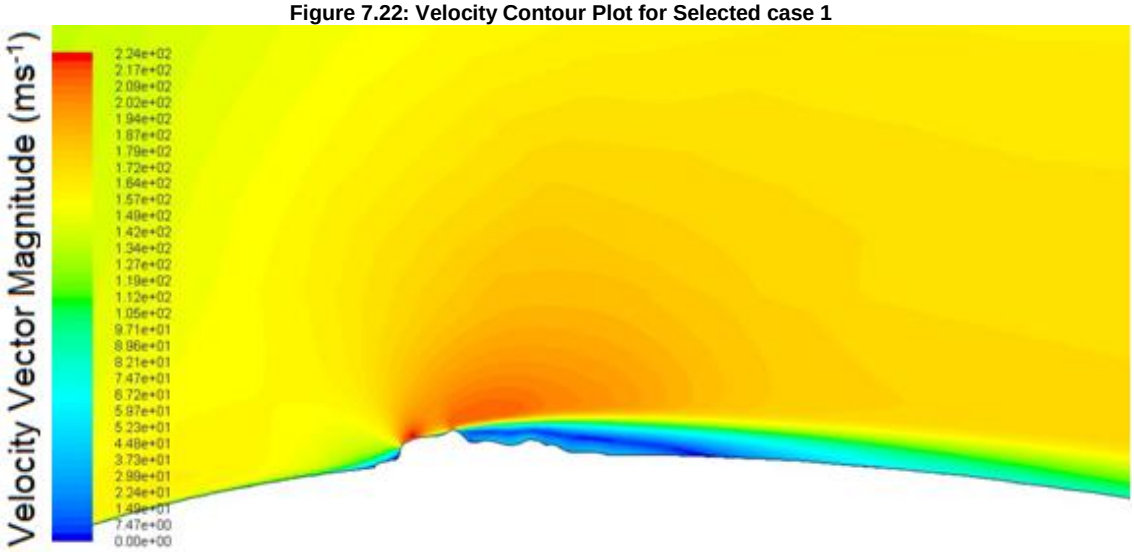

Figure 7.23: Velocity Contour Plot for Selected case 5

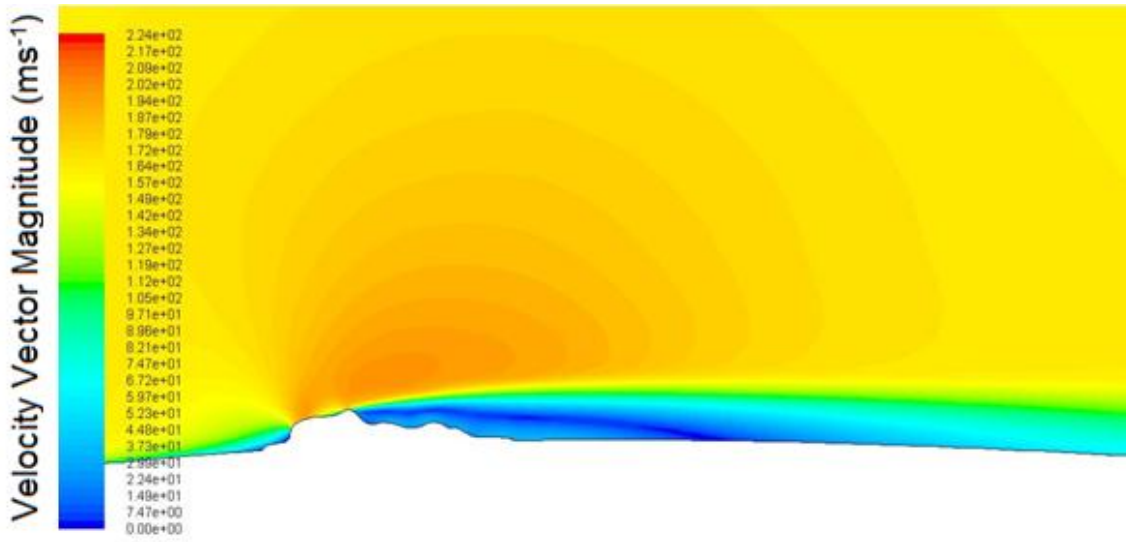

Figure 7.24: Velocity Contour Plot for Selected Case 9

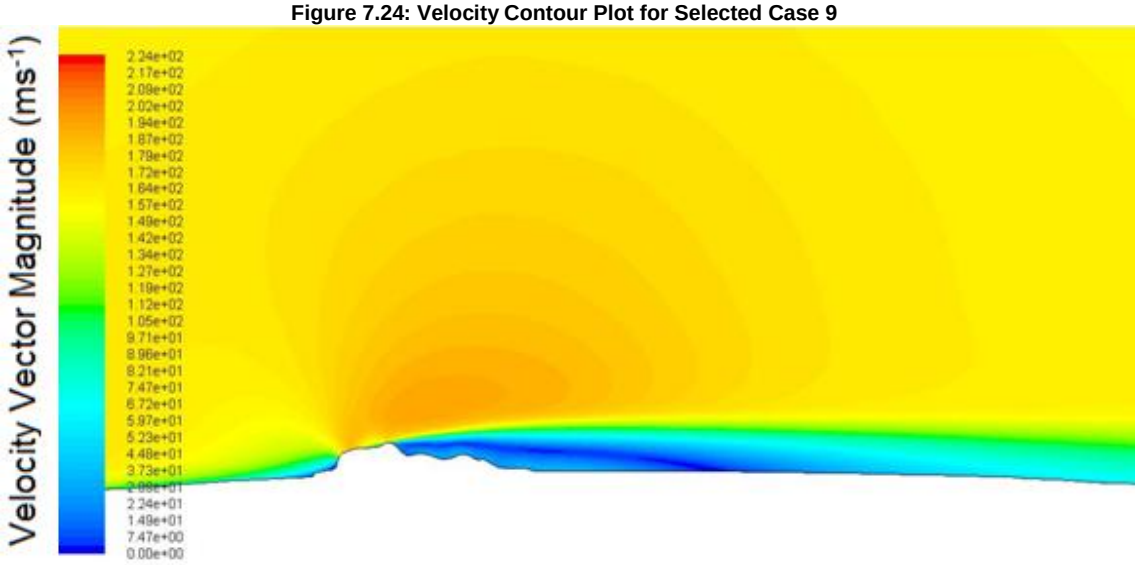

Figure 7.25: Velocity Contour Plot for Test Case 2

The contour plots for runback ice locations further along the chord (selected case 9 and test case 2) show visibly larger regions of separated flow.

Boundary layer scaling insight

Work on runback ice scaling for a warm hold case was conducted by Whalen, et al., [118]. They compared two scaled runback ice shape based on boundary layer and geometrical chord scaling methods. The two cases were in significant disagreement where the maximum lift was increased by 14.7% for the geometrical scaled runback ice but decreased by 34.5% for the boundary layer scaled runback ice. Flowfield analysis showed the separation bubble created by the geometrically scaled shape was significantly smaller relative to the boundary layer scaled runback ice shape.

There was some interaction with the size of the boundary layer and height of the ice shape that remained unknown. Whalen, et al., [118] eluded to this stating that at some height between the two scaled runback ice heights (0.0044k/c and 0.0052k/c) the iced airfoil went from improving to degrading the performance at high angles of attack.

For this study the boundary layer thickness around the 6.5% to 10% chord region was compared to the height of the runback ice shape. The results found the region where the discrepancies with test cases 1,2 and 3 occur were also where the runback ice height was comparable with the boundary layer thickness (Figure 7.26). The circled region highlights where the force coefficients deviate from the trends observed.

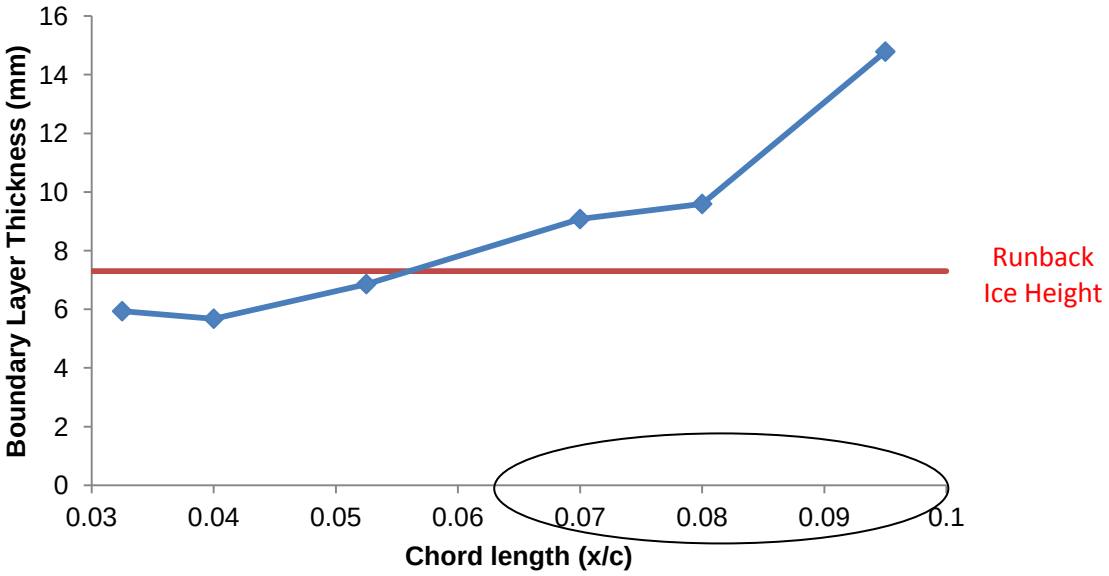

Figure 7.26: Boundary Layer Thickness and Runback Ice Height Comparison

Whalen, et al., [118] found the separation bubble for the boundary layer runback ice was much larger than the geometrically scaled runback ice. In this case the size of the separation bubble for the test cases was slightly larger than the expected trends highlighted in Figure 7.20. When the size of the boundary layer is larger than the runback ice height, these apparent trends fail to hold.

7.2. Airfoil Shape Optimisation for Fixed Ice Formation Location

The shape optimisation study modified the shape of a B737-700 airfoil with runback ice fixed at 0.023x/c. This was the original datum position used for the Ice Location Optimisation study in Chapter 7.1.

7.2.1. Objectives

This study implemented a multi-objective tabu search optimiser to modify the datum airfoil profile using a free-form deformation (FFD) geometry modeller to improve the lift and drag characteristics. The chord profile modification changed the clean pressure profile. Previous studies by Broeren, et al., [109] and Pan, et al., [44] showed that the effects of runback ice were highly dependent on the pressure profile of a specific airfoil. Modification to the shape of the airfoil and consequent pressure profile provided insight on the interaction between the runback ice and a particular airfoil profile.

The objective was to find an iced airfoil profile which performed better than the datum design in terms of lift and drag performance.

7.2.2. Datum Conditions

The datum conditions were set to match the 45 minute hold case in continuous icing condition as required by the EASA. These have been outlined in detail in Chapter 5. However the calibrated speed of 118ms^{-1} at 17000ft for a static temperature of -9°C at an angle of attack of 3°C.

The optimisation code was performed at 3° AOA in line with the hold condition which was of particular interest for sponsors Airbus. As a result it remained unknown how these new optimised airfoil designs would perform across a flight envelope.

7.2.3. Optimisation Setup

This was a multi-objective optimisation code to maximise lift $(\bar{F}_1)$ and minimise drag $(\bar{F}_2)$ for airfoil profiles $(\bar{x}_1)$ using the Boeing 737-700 airfoil as the datum geometry. The objective functions for this multi-objective optimisation study are given in Equation 7.3 & Equation 7.4:

$$\bar{F}_1 = -\left(\frac{Cl_{\bar{x}_1}}{Cl_{datum}}\right)$$

Equation 7.3: Objective Function for Lift Costs

$$\bar{F}_2 = \left(\frac{Cd_{\bar{x}_1}}{Cd_{datum}}\right)$$

Equation 7.4: Objective Function for Drag Costs

The design parameter for this study was the airfoil shape change via FFD. A numerical criterion was also implemented to ensure CFD solver converged and was utilised as a hard constraint.

The memory and search control features of the MOTS for this study remains unchanged from the Ice Location Optimisation study.

The modification to the airfoil shape was achieved using a FFD tool. The FFD development was founded from imaging software where manipulation of a solid object was achieved using a number of control points. Numerous FFD tools were available. For this study a tried and tested FFD tool previously incorporated into the MOTS code was used as the geometry modelling tool. Sederberg, et al., [119] produced an algorithm which deformed solid geometric models in a free-form manner. Any type or degree of freedom could be deformed including:

- Planes
- Quadrics
- Parametric surface patches
- Implicitly defined surfaces

This technique is based on trivariate Bernstein polynomials (Equation 7.5). This technique enables deformation of objects by manipulating the control points.

$$X_{FFD} = \left(\sum_{i=0}^{l} \binom{l}{i} (1-s)^{l-i} s^{i}\right)\left(\sum_{j=0}^{m} \binom{m}{j} (1-t)^{m-j} t^{j}\right)\left(\sum_{k=0}^{n} \binom{n}{k} (1-u)^{n-k} u^{k}\right) P_{ijk}$$

Equation 7.5: Trivariate Bernstein Polynomial

X_{FFD} is a vector containing the Cartesian coordinates of the displaced point
P_{ijk} is a vector containing the Cartesian coordinates of the control point.

The code was implemented using FORTRAN as the source code with a C++ interface script. This optimisation study used 16 control points with a level of freedom dictated by the parameters set in the mots_master file. The 16 control points did not cover the leading and trailing edge. These were kept fixed to the original datum design. Both the thickness and trailing edge profile allowed for improved designs and provided chord profiles that were considered feasible.

7.2.4. Results

The progress of the optimiser was monitored via a number of output files. Figure 7.27 illustrates the behavioural history for this optimisation process. The i_local value specified the number of consecutive unsuccessful optimisation iterations. Four search intensification steps occurred; for the search intensification to initiate, 15 consecutive unsuccessful iterations were tallied. 0 diversification steps and step size reductions were made.

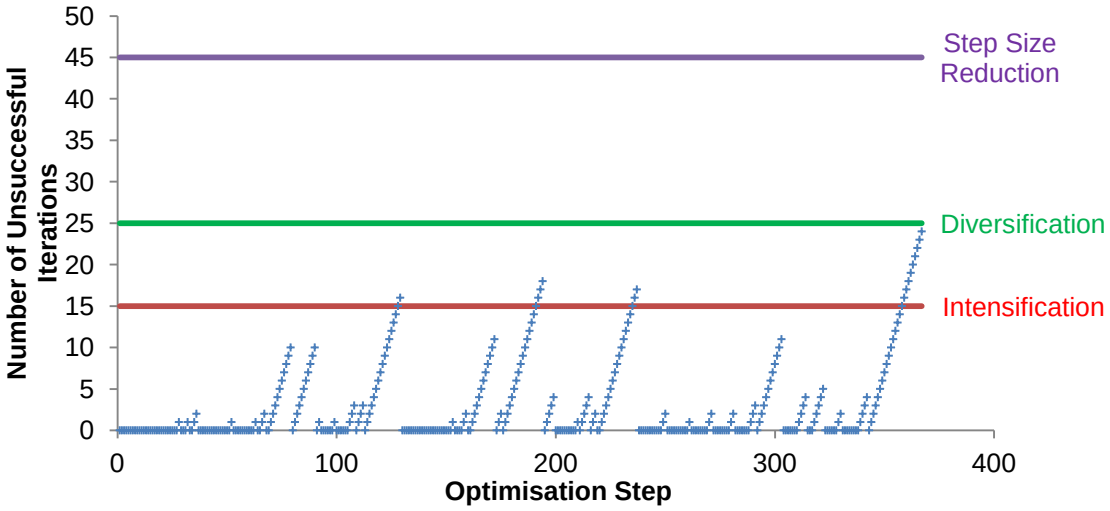

Figure 7.27: Airfoil Shape Optimisation for Fixed Ice Formation Location Optimiser History

This optimisation study was executed to accomplish two tasks; Shape optimisation validation and test execution of the geometry modeller. Both of these tasks were fulfilled and the findings are presented.

3209 airfoil profiles were evaluated out of which 1276 were not feasible. The number of feasible airfoil profiles was 1933. 76 optimum chord profiles were found forming the Pareto front shown in Figure 7.28.

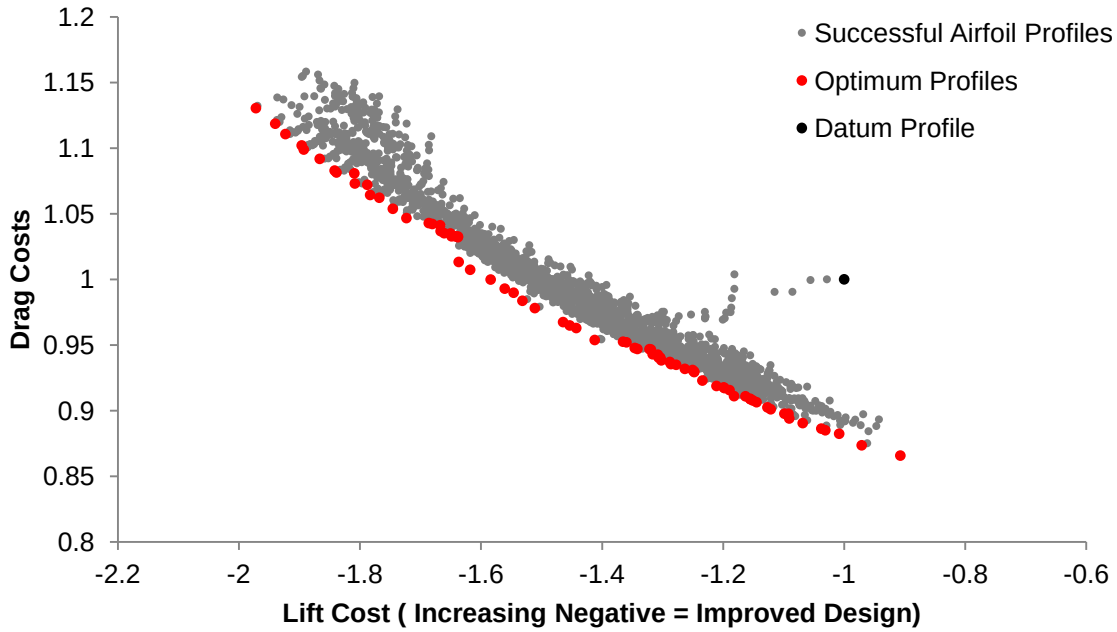

Figure 7.28: Airfoil Shape Optimiser Costs

7.2.5. Optimiser Check and Validation

Five selected profiles shown in Figure 7.29 were used to analyse the accuracy of the individual CFD solutions. All profile force coefficients from the CFD solution and extrapolated lift and drag force coefficients from the optimiser cost output were compared in the final two columns in Table 7.9.

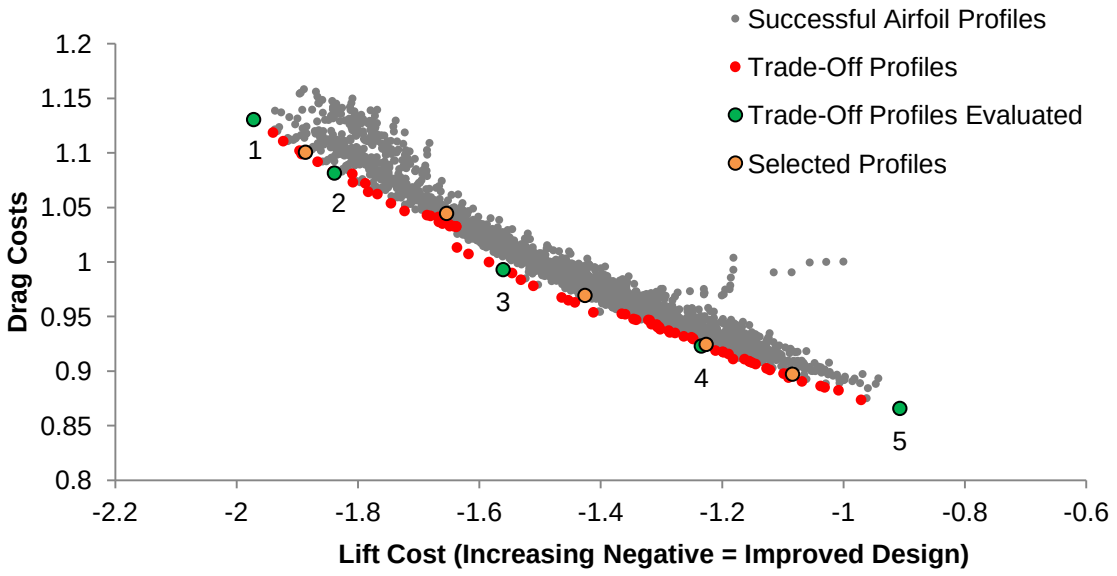

Figure 7.29: Airfoil Shape Optimiser Costs with Selected Profiles

Selected Runs	Optimiser Lift Cost	Optimiser Drag Costs	Coefficient of Lift	Coefficient of Drag	Variation in Lift Coefficient (%)	Variation in Drag Coefficient (%)
1	-1.89	1.10	0.899	0.014	4.53%	2.72%
2	-1.65	1.04	0.788	0.013	0.00018%	0.00031%
3	-1.43	0.97	0.679	0.012	0.00007%	0.00004%
4	-1.08	0.90	0.516	0.011	0.00002%	0.00003%
5	-1.23	0.92	0.584	0.011	0.00025%	0.00002%

Table 7.9: Shape Optimisation Selected Runs Verification

The selected (and optimum run) checks were successful. The variation in the lift and drag coefficients were well below 0.01% except for selected run 1 which produced a variation of 4.53% and 2.72% for lift and drag coefficients respectively.

7.2.6. Pareto-Optimum Analysis

Analysis of the optimal Pareto front offered a range of profiles to consider. A parametric study of all 76 profiles was not feasible. However many profiles shared similar profiles with only small variations between them. Five profiles were selected which represented a majority of the Pareto front (Figure 7.29). The selected profiles highlighted in Figure 7.29 are used later in the study for validation purposes. The 5 Pareto-optimal profile shapes are shown in Figure 7.30 through to Figure 7.34 and are named trade-off profiles. Trade off profiles 1 and 2 are similar and trade-off profiles 3, 4 and 5 share a similar kink in the trailing edge profile.

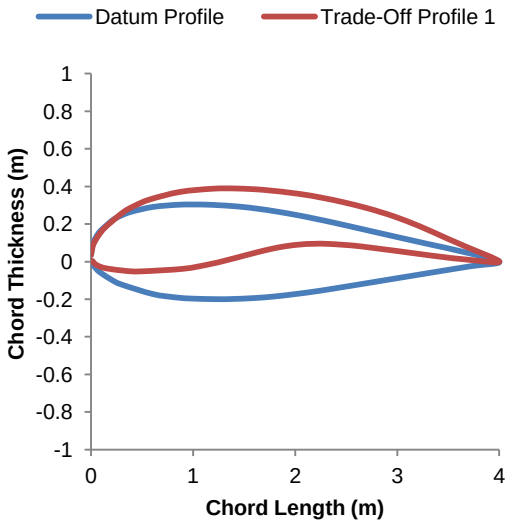

Figure 7.30: Trade-Off Profile 1 Comparison

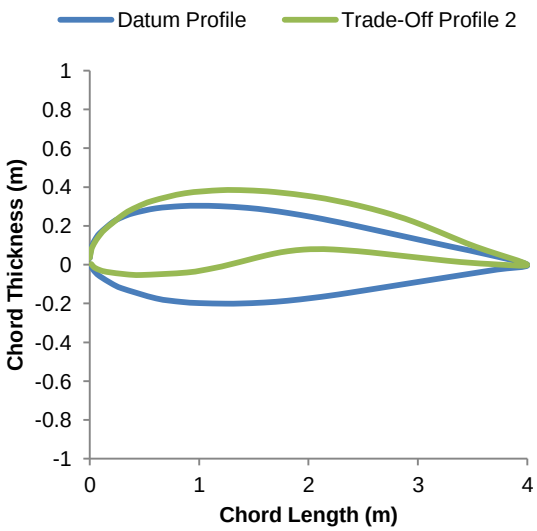

Figure 7.31: Trade-Off Profile 2 Comparison

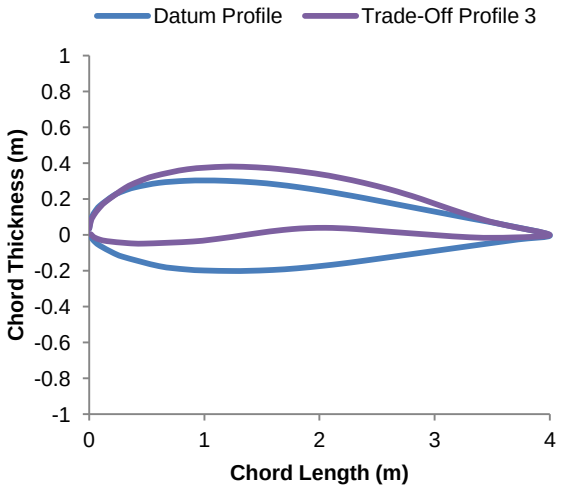

Figure 7.32: Trade-Off Profile 3 Comparison

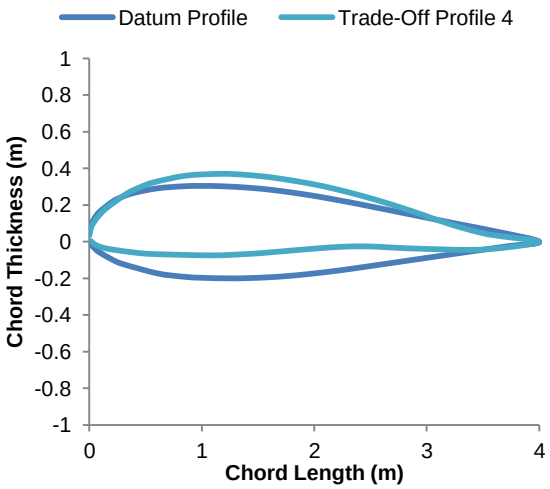

Figure 7.33: Trade-Off Profile 4 Comparison

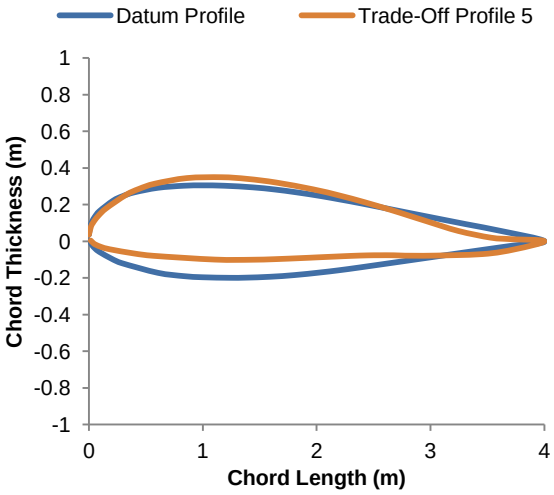

Figure 7.34: Trade-Off Profile 5 Comparison

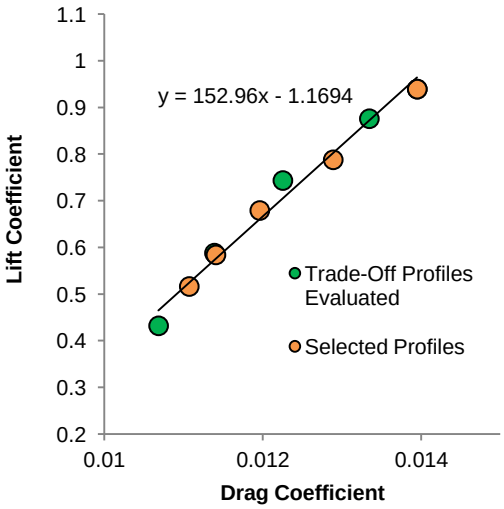

Figure 7.35: Lift to Drag Ratio for Selected Runs and Trade-Off Profiles

Figure 7.35 shows the lift to drag ratio for all selected and trade-off profiles. The expected linear profile for increasing lift with increasing drag was found. Table 7.10 outlines the clean and iced configuration coefficients for all trade-off runs.

Trade-Off Runs	Clean Configuration Lift Coefficient	Clean Configuration Drag Coefficient	Iced Configuration Lift Coefficient	Iced Configuration Drag Coefficient
Datum	0.494	0.0100	0.476	0.0123
1	0.958	0.0126	0.939	0.0139
2	0.891	0.0120	0.875	0.0133
3	0.754	0.0111	0.743	0.0122
4	0.596	0.0105	0.587	0.0113
5	0.437	0.0099	0.432	0.0106

Table 7.10: Clean and Iced Force Coefficient Results for Trade-Off Pareto-Optimal Runs

The performance of the trade-off profiles in clean conditions was not explored within the optimisation code. As a result, individual CFD runs in clean configuration were run for the trade-off runs. The trade-off runs produced an improvement in lift and drag when run in clean conditions. Trade-off profile 1 produced the largest improvement in lift relative to the datum by 90% but also increased the drag coefficient by 38.76%. Moving through the trade-off profiles one to five, a gradual reduction in lift and increasing drag was observed (Figure 7.36 & Figure 7.37). Figure 7.38 and Figure 7.39 show the iced trade-off profile results along with the datum B737 airfoil results. The profiles with better lift characteristics also carried higher drag penalties for the clean configuration runs. All trade-off profiles exhibited poorer drag performance relative to the datum. However the maximum improvement in lift for the iced configuration relative to the datum was a considerable 97.19%.

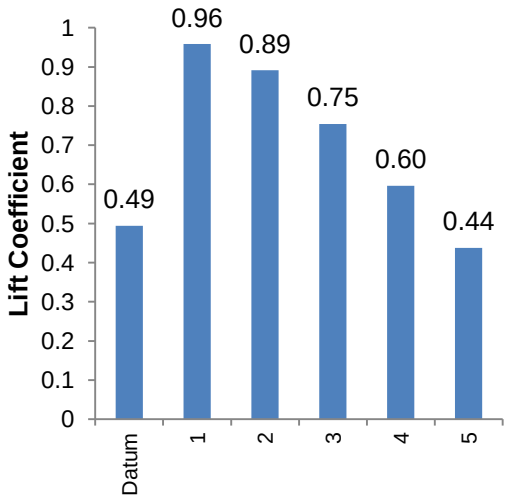

Figure 7.36: Lift Coefficient Comparison for Trade-Off Profiles in Clean Configuration

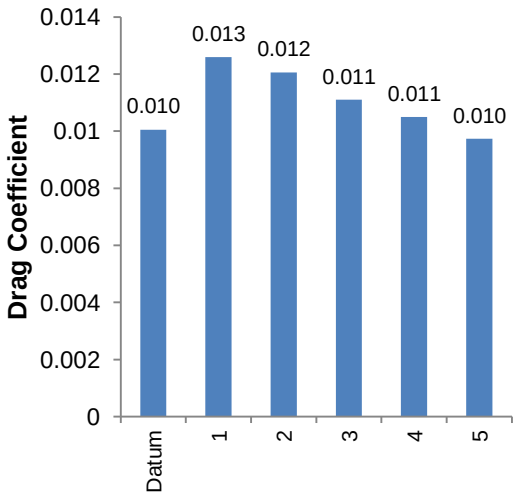

Figure 7.37: Drag Coefficient Comparison for Trade-Off Profiles in Clean Configuration

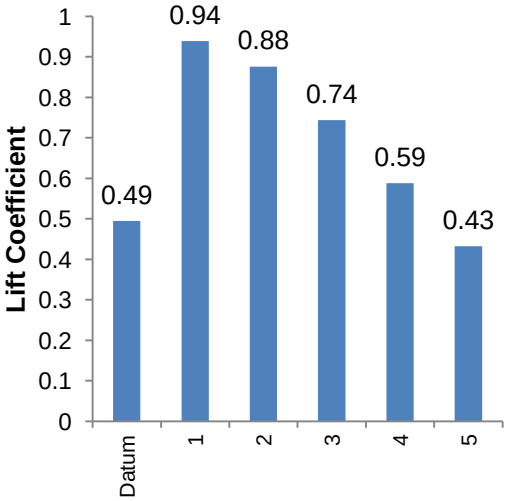

Figure 7.38 Lift Coefficient Comparison for Trade-Off Profiles in Iced Configuration

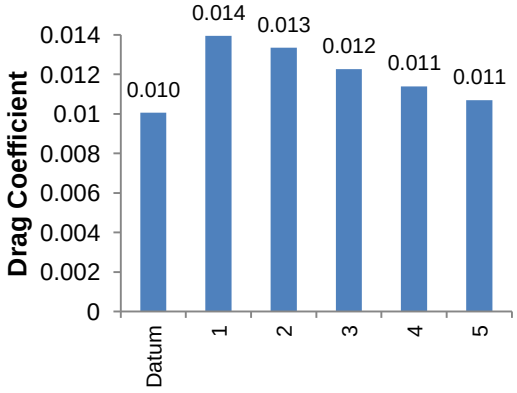

Figure 7.39: Drag Coefficient Comparison for Trade-Off Profiles in Iced Configuration

The adverse effects of runback ice formation for the trade-off profiles were considered. The datum profile produced the largest loss due to the runback ice. Trade-off profiles 1 and 2 produced the smallest losses due to runback ice formation (Figure 7.40 & Figure 7.41).

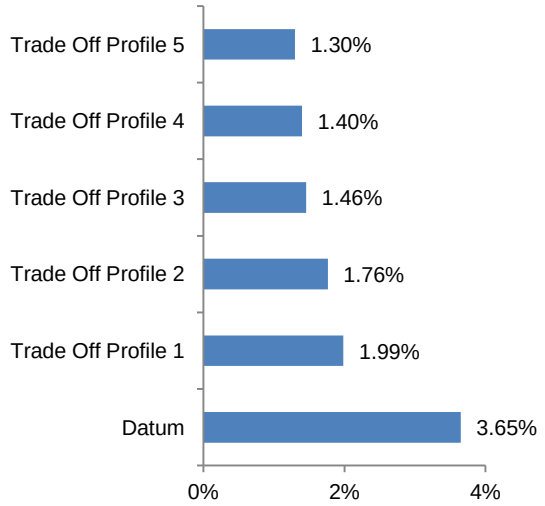

Figure 7.40: Lift Coefficient Performance Loss in Iced Configuration

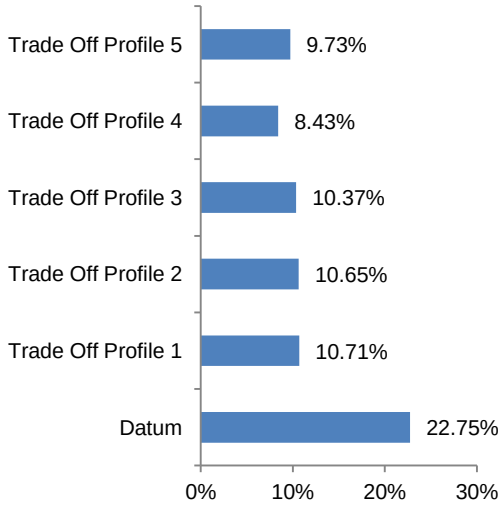

Figure 7.41: Drag Coefficient Performance Loss in Iced Configuration

To minimise the performance loss due to runback ice formation whilst trying to maintain respectable clean condition characteristics provided a challenge.

The trade-off airfoils all provided smaller performance losses due to runback ice formation for EASA 45 minute hold condition relative to the datum B737 airfoil.

The trade-off airfoils which achieved the higher lift & drag coefficient values suffered to a greater extent.

Trade-off Profile 1 performance losses were 1.99% and 10.71% for lift and drag coefficients respectively.

The drag coefficients provided similar results for trade-off profiles 3, 4 and 5. Trade-off profile 2 produced the smallest amount of loss for the drag coefficient at 8.43%.

Trade-off profiles 1 and 2 produced the highest lift coefficient values. The pressure profile for the clean configuration produced a significantly larger pressure differential across the upper and lower surfaces (Figure 7.42). The curvature of the lower surface, particularly the 50% chord region where the profile drastically reduced in thickness, decelerated the flow which in turn produced a higher local static pressure and enhanced its lift capabilities further. Another interesting feature was the suction peak moved further downstream

and was less prominent. The pressure recovery region was less aggressive and remained sustained further along the chord relative to the datum B737 airfoil.

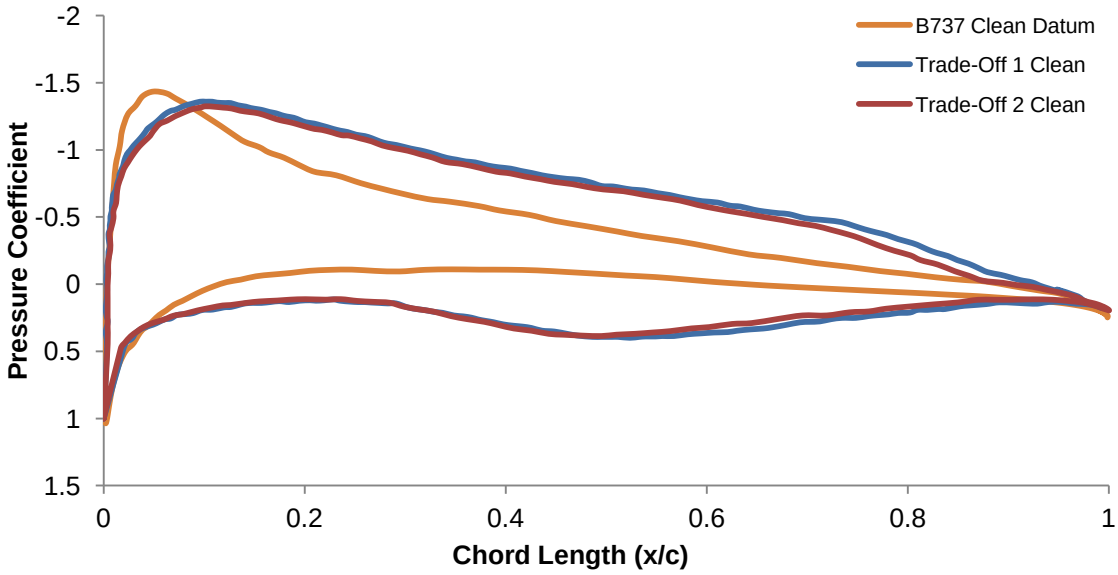

Figure 7.42: Pressure Coefficient Comparison for Clean Trade-Off Profiles 1 & 2

Trade-off profile 3 performed better than trade-off profile 4 and 5. The 'kink' in the lower surface again provided a greater differential for the upper and lower surface pressures and allowed a greater lift production. The datum B737 airfoil produced a larger suction peak relative to all other profiles shown in Figure 7.43. Trade-off profile 3 also produced a larger suction peak relative to trade-off profiles 4 and 5.

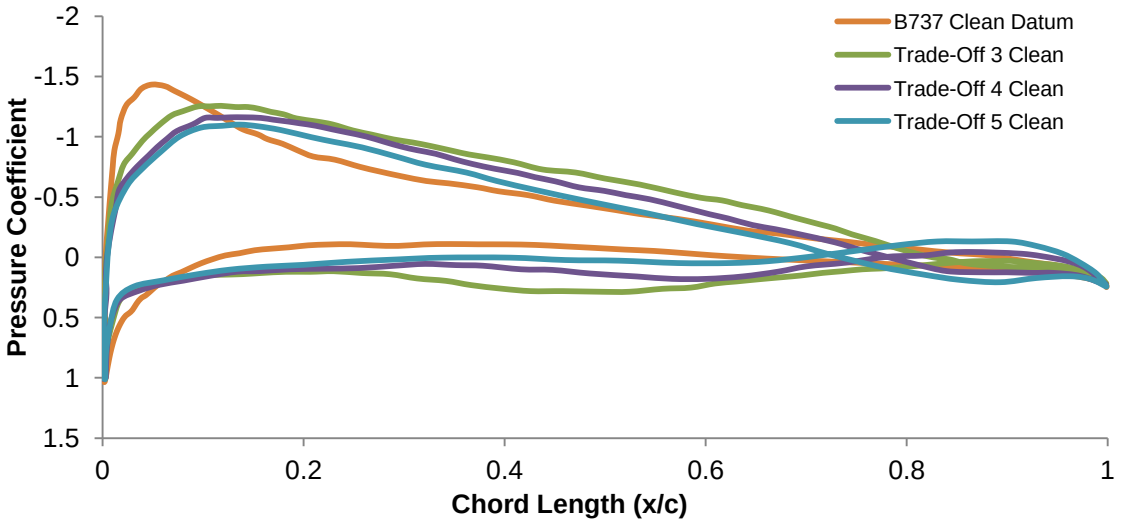

Figure 7.43: Pressure Coefficient Comparison for Clean Trade-Off Profiles 3, 4 & 5

Figure 7.44 highlights the consequence of the trailing edge lower surface profile found in trade-off profiles 3, 4 and 5 alongside the velocity magnitude contour plot in Figure 7.45.

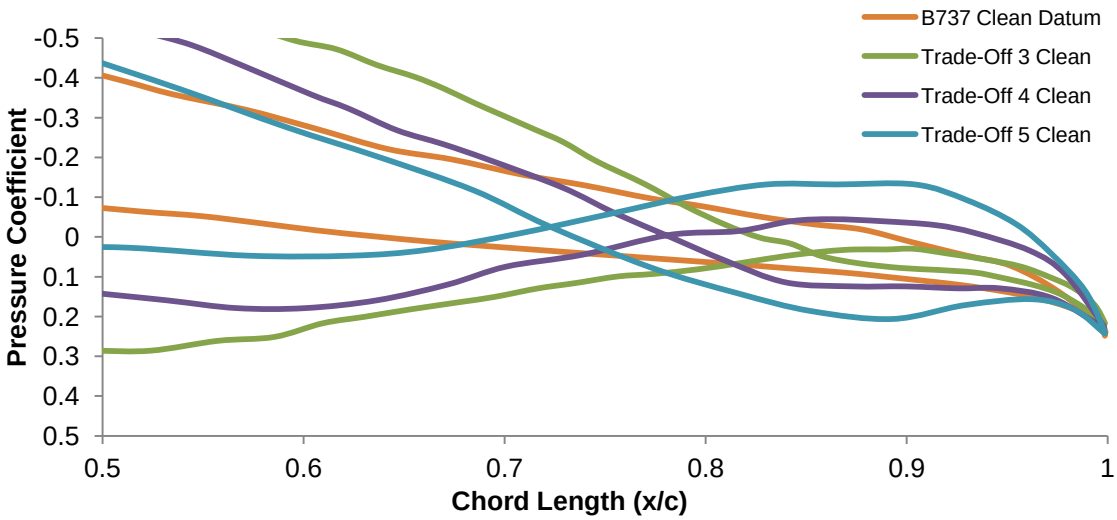

Figure 7.44: Pressure Coefficient Comparison for Clean Trade-Off Profiles 3, 4 & 5 at Trailing Edge

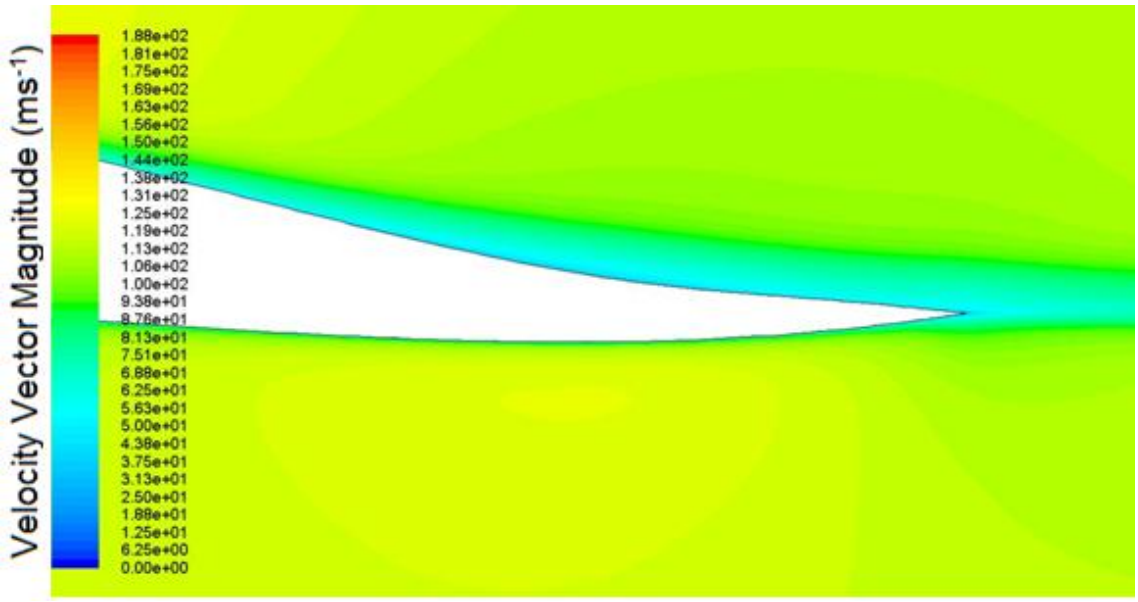

Figure 7.45: Velocity Magnitude Contour Plot at Trailing Edge for Trade-off Run 5

Figure 7.46 and Figure 7.47 show the iced pressure coefficient profiles for all trade-off runs. Similar to the datum B737 airfoil, the runback ice did not disrupt the initial pressure drop. The adverse pressure gradient region remained sustained along the chord as seen in the clean configuration.

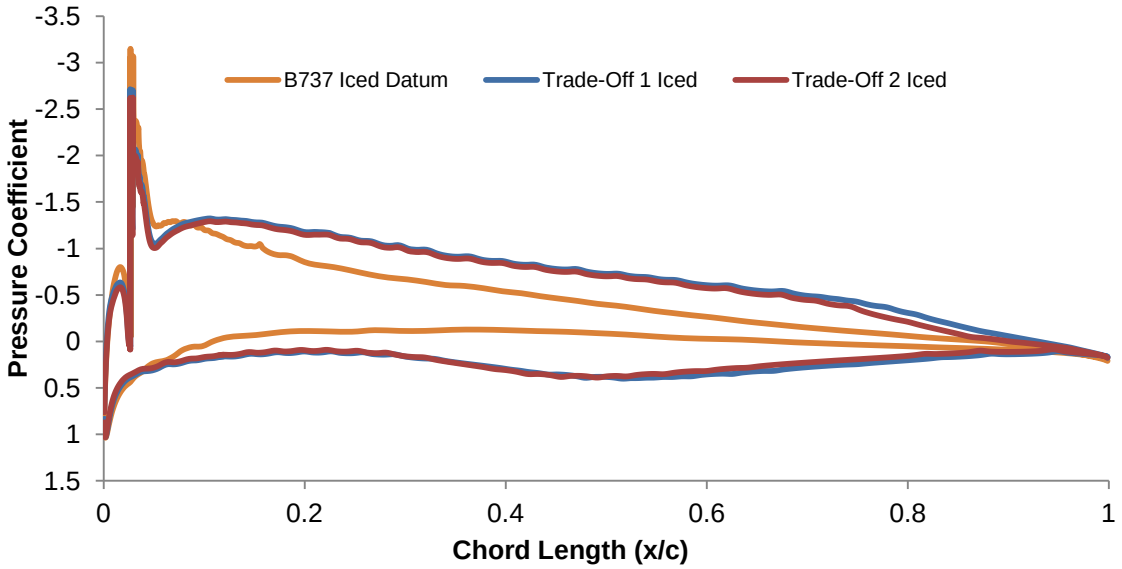

Figure 7.46: Pressure Coefficient Comparison for Iced Trade-Off Profiles 1 & 2

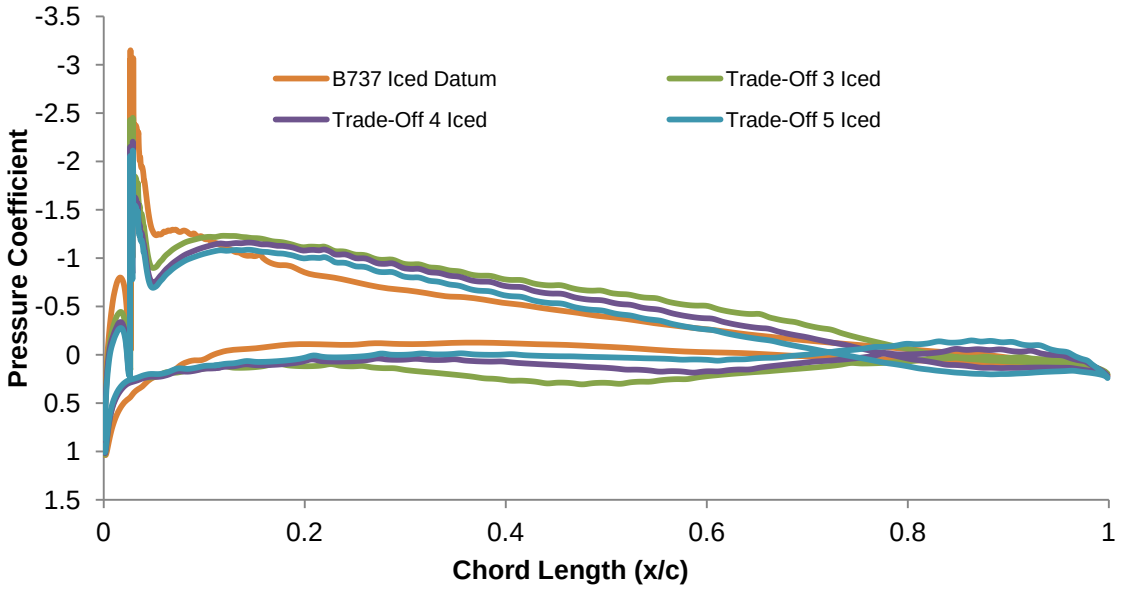

Figure 7.47: Pressure Coefficient Comparison for Iced Trade-Off Profiles 3, 4 & 5

7.2.7. Ice Location Analysis

The trends found in the ice location optimisation study (Chapter 7.1) were extended to this study. The aim was to try and reaffirm the lift and drag coefficient behaviour with respect to ice location up to 0.125x/c.

Trade-off profiles 1, 3 and 5 were used for this ice location study. 7 chord locations were chosen ranging from the limit of the heated zone for this experimental ice profile (0.088m) to 0.5m. The ice location optimisation study design space ranged from 0.088m to 0.45m (0.022 – 0.125x/c) as shown in Table 7.11.

Location (m)	0.088	0.0915	0.15	0.2	0.3	0.4	0.5
Location (x/c)	0.022	0.02288	0.0375	0.05	0.075	0.1	0.125

Table 7.11: Ice Location Position Chosen for Shape Optimisation Study

The lift and drag coefficients plotted against the ice location matched a forth and third order polynomial respectively for the ice location optimisation study. Figure 7.48 to Figure 7.53 show the lift and drag coefficient relationship with respect to ice location for trade-off profile 1, 3 and 5.

The best fit polynomial for trade-off profiles 1 and 3 lift coefficient graphs was a third order polynomial. For trade-off profile 5, the best fit was a straight line.

As the runback ice shape was placed further along the chord, the lift coefficient reduced. For trade-off profiles 1 and 2 the gradient decreased after 0.7x/c. This was similar to the ice location optimisation run albeit the transition occurred closer to the leading edge (0.5x/c). Trade-off profiles 1 and 3 exhibited the lift degradation plateau but did not show any signs of improvement as seen in the ice location optimisation study.

The drag coefficient relationship with ice location for trade-off profile 1 and 3 display the plateau around 0.7x/c. Once again no sign of improvement to the drag force was seen.

To corroborate the relationship seen in the ice location optimisation study, it was necessary to assess where the boundary layer thickness was equal to the runback ice height. A number of CFD runs before and after this location would be required to confirm these findings. With limitations to the amount of time for this study, a comprehensive ice location study using the trade-off profiles 1, 3 and 5 was not made.

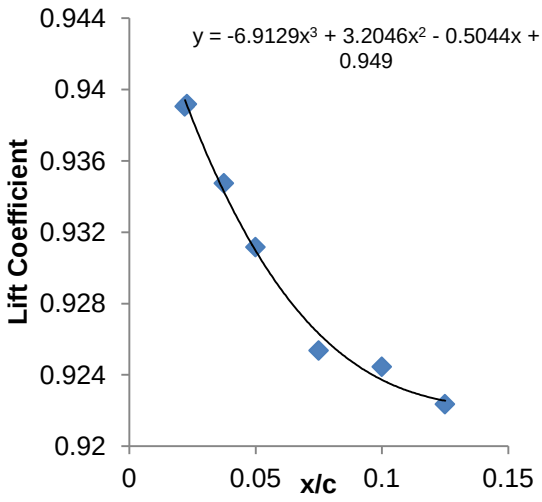

Figure 7.48: Ice Location & Lift Coefficient Comparison for Trade-Off Profile 1

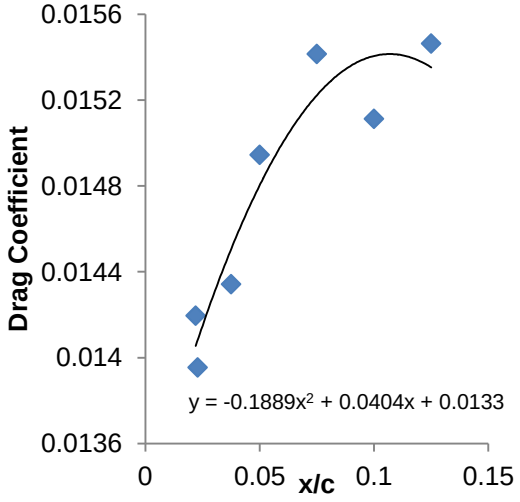

Figure 7.49: Ice Location & Drag Coefficient Comparison for Trade-Off Profile 1

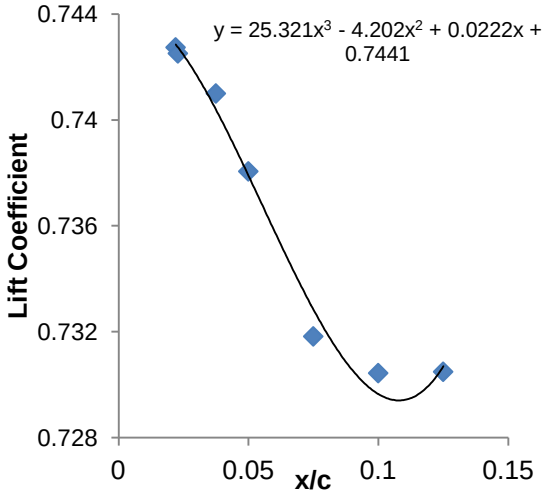

Figure 7.50: Ice Location & Lift Coefficient Comparison for Trade-Off Profile 3

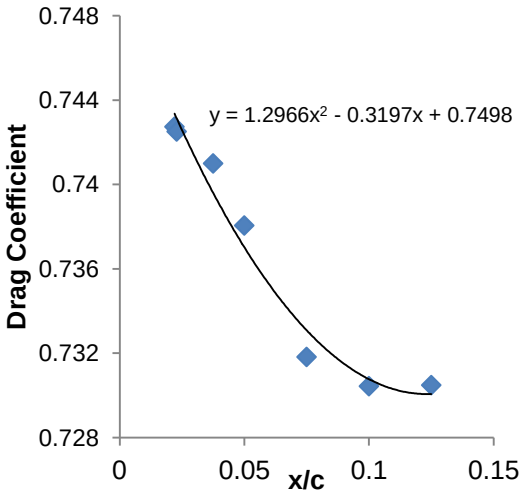

Figure 7.51: Ice Location & Drag Coefficient Comparison for Trade-Off Profile 3

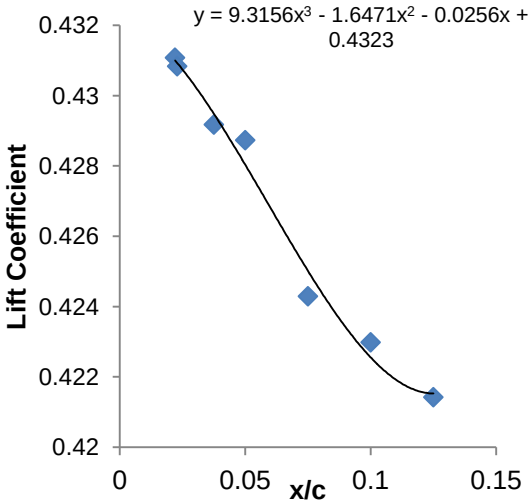

Figure 7.52: Ice Location & Lift Coefficient Comparison for Trade-Off Profile 5

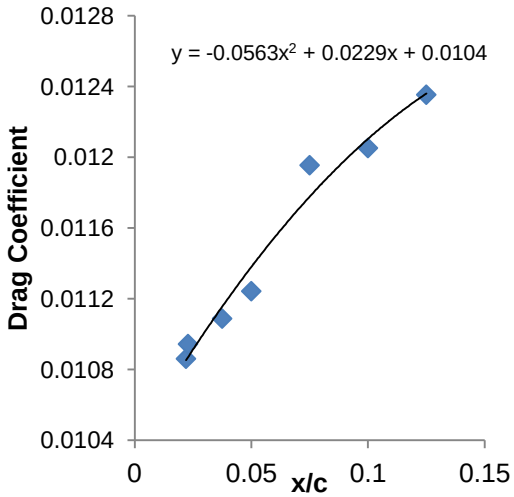

Figure 7.53: Ice Location & Drag Coefficient Comparison for Trade-Off Profile 5

The ice location optimisation study conducted for optimum runs 1, 3 and 5 revealed trends which can be considered similar to those seen in Chapter 7.1 in terms of overall drag and lift coefficient performance with respect to ice location. To provide more conclusive analysis on the trends seen, a larger number of ice locations would be needed at the upper end of the ice formation chord location as well as smaller ice location steps.

7.2.8. Summary

Optimising aerodynamic performance of an airplane main wing requires significant research and design. Different flight regimes require different airfoil characteristics and combined with the challenges of propulsion integration the process becomes extremely complex. It is not practical to then compromise the aerodynamic performance by changing the airfoil shape to ensure greater robustness in possible iced conditions. In this regard this optimisation study was somewhat artificial and was undertaken to compare shape optimisation using FFD by Ghisu, et al., [43], as well as to assess real runback ice shapes on a real wing profile. Airbus had expressed interest to investigate possible optimal changes for tail fin profile where greater aerodynamic flexibility could be accommodated; see Chapter 7.3 - Representative Tail Plane Profile Optimisation.

Ghisu, et al., [43] performed a profile shape optimisation with idealised ridge ice on a reference NACA 23012 profile. Comparisons of best lift and drag profiles are shown in Figure 7.54. The profiles on the left hand side of the page are the optimum lift and drag designs based on the NACA 23012 datum airfoil by Ghisu, et al., [43]. The right hand side shows the best lift and drag airfoil profiles for the B737-700 datum airfoil used in this study.

The variations observed can be attributed to the lack of clean profile consideration. The trailing edge of both sets of profiles displayed more aggressive changes. The best delta lift profile from Ghisu, et al., [43] showed a much larger variation relative to the best lift coefficient profile found in this study.

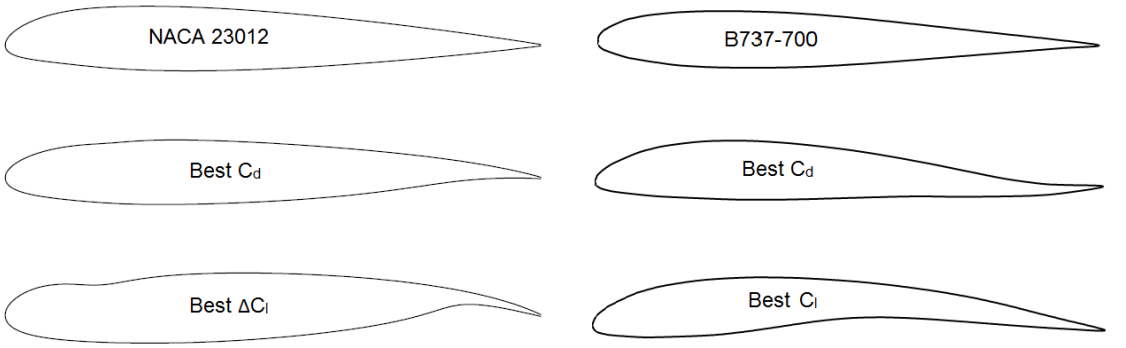

Ghisu, T., Jarrett, J. & Parks, G., 2011. Robust Design Optimization with Respect to Ice Accretion. *Journal of Aircraft,* 48(1), pp. 287-304

Airfoil Shape Optimisation for Fixed Ice Formation Location

Figure 7.54: Optimal Lift and Drag Coefficient Airfoil Profile Comparison against [43]

One of the goals for this study was to implement a geometry modelling tool for aerodynamic optimisation and consider what constraint handling modifications would be required for feasible designs without significantly reducing the design space.

A number of observations were made:

- The aggressive curvature at the trailing edge of trade-off profiles 3, 4 and 5 intuitively suggest the pitching moment produced by the airfoil would render its design unfeasible. A modification to the MOTS code to constrain the moment using a weighted penalty (soft constraint) would ensure unfeasible airfoil designs were not considered.
- A hard constraint applied to the lift and drag coefficient of new airfoil profiles (design vector) in clean (cruise) configuration.

The FFD geometry handler worked efficiently with this optimisation setup. This optimisation study provided useful insight on the constraint handling measures required for practical shape optimisation problems implemented in Section 7.3.

7.3. Representative Tail Plane Profile Optimisation

7.3.1. Tail Plane Airfoil Theory and Design

The vertical plane, also known as the fin or vertical stabiliser differs from the key function of the horizontal airfoil. The primary functions of a vertical plane are to provide stability and trim.

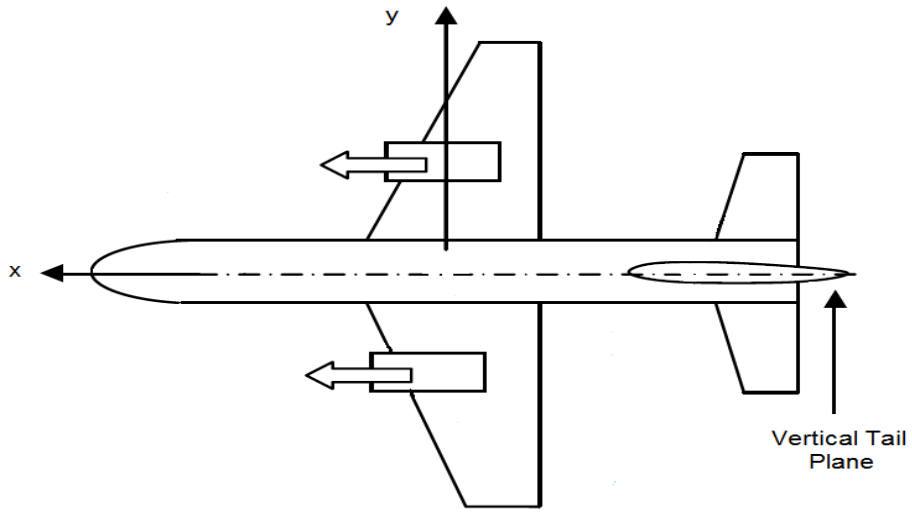

Figure 7.55: Typical General Transport Airplane Tail Plane Setup

In general aviation airplanes one of the fundamental design parameters of the vertical plane is that it must remain symmetrical along the x-z plane as shown in Figure 7.55. For modern airplanes directional stability is introduced as part of the design process with the symmetrical placement of main wings, engines and horizontal tail plane. Thus the placement of the vertical tail plane must lie along the symmetry line of the airplane to maintain a symmetrical profile [120]. To this end, a number of airplanes sport a variation of the NACA 0009 and the NACA 0012 airfoil. Another factor to consider when designing a vertical plane airfoil is the compressibility effect. The maximum velocity around the tail plane must not exceed that of the main wing. A number of methods are used to achieve this but the most common is to introduce a thinner airfoil section. However in real applications this may not always be possible and thickness constraints for structural integrity are readily applied.

The datum airfoil for this optimisation study was the NACA 0012 airfoil.

7.3.2. Objectives

The ice accretion phenomenon affects all critical aerodynamic structures including the main wing and tail plane. To consider modifying the shape of an airfoil requires a great deal of research and design. There are numerous challenges which affect the performance of an airfoil/wing when considering the airplane as a whole.

To consider a shape change for the main airplane wing to compensate for a small build-up of runback ice was deemed impractical. However a modification to the tail plane could be considered due to the lack of anti-icing system and the resulting consistent formation of ice.

To this end, shape optimisation of the Airbus fleet tail wing warranted a more detailed analysis of the potential benefits of a shape change on the tail plane.

The aim of this optimiser was to provide Airbus with a new airfoil design which reduced the iced drag coefficient penalties without sacrificing the performance when running in a clean (datum) configuration.

7.3.3. Datum Conditions

The datum clean and iced environmental conditions were set to match the 45 minute hold case in continuous icing condition as required by the EASA. As this was a vertical plane, the angle of attack was set to zero with the assumption of no crosswinds. In line with the EASA hold condition, a speed of 118 ms^{-1} and ambient temperature of -9° C was used throughout this optimisation study. The chord length of the NACA 0012 was 1 metre which corresponded to a Reynolds Number of $5x10^6$.

The ice formation differed from previous optimisation studies. As the angle of attack was set to zero, combined with symmetrical placement and shape of the tail plane, ice formation was accreted on both surfaces. The placement and scale of the runback ice was reduced by a factor of 4 in line with geometrical scaling.

The scaling method used was a decision based on the literature available at the time. Without experimental data for full-scale and quarter-scale aerodynamic data to compare, no conclusive direction on scaling methods was available. The original runback ice shapes were formed on a full-scale four metre Boeing 737-700 airfoil whereas this study used a one metre NACA 0012 airfoil. Unfortunately due to time constraints running two separate optimisation processes considering both types of scaling methods was not an option. An

optimisation code based on boundary layer scaling would be academic as no experimental data was available to make any conclusive remarks.

7.3.4. Optimisation Setup

This was a single objective optimisation study utilising the multi-objective Tabu Search optimiser used throughout this thesis and developed by Jaeggi, et al., [86]. The objective function was to minimise the average drag coefficient for an iced and clean NACA 0012 airfoil case.

$$Objective\ Function = \Delta\, Cd + f_1$$

$$\Delta\, Cd = \frac{\left(\frac{(Cd_{ice} + Cd_{clean})}{2}\right)}{\left(\frac{Cd_{datum_{ice}} + Cd_{datum_{clean}}}{2}\right)}$$

Equation 7.6: Normalised Drag Cost Calculations for Representative Tail Plane Profile Optimisation

Although the optimiser used was designed as a multi objective optimiser, the code was adapted by Dr Timoleon Kipouros for single objective use; to minimise drag.

The design parameter for this study was the airfoil shape change via FFD.
The optimisation run was subject to a number of hard constraints and the inclusion of a soft constraint penalty for the moment coefficient. The hard constraints for the clean case run are:

Clean Flow Solver Test	Inequality	Criteria
Clean Drag Coefficient	<=	Clean Datum Drag Coefficient
Clean Drag Coefficient	>	0
Clean Drag Coefficient Variation	<	0.00001
Clean Lift Coefficient Variation	<	0.00001
Clean Moment Coefficient Variation	<	0.00001

Table 7.12: Clean Case Hard Constraints for Representative Tail Plane Profile Optimisation

The clean lift/drag coefficient variation was used as the FLUENT solver convergence test. For the clean case coefficients, the fluctuations must remain smaller than 0.00001 for the last 100 CFD iterations to satisfy the convergence criteria set for this optimisation process.

The constraints shown in Table 7.12 were required to be satisfied before the iced case flow solver was executed. Along with the clean case hard constraints, the iced case also had a set of hard constraints and a soft constraint penalty.

Iced Flow Solver Test	Inequality	Criteria
Iced Drag Coefficient	>	0
Iced Lift Coefficient	<	0.01
Iced Drag Coefficient Variation	<	0.00001
Iced Lift Coefficient Variation	<	0.00001
Iced Lift Coefficient Variation	<	0.00001
Iced Moment Coefficient Variation	<	0.00001

Table 7.13: Iced Case Hard Constraints for Representative Tail Plane Profile Optimisation

The soft constraint penalty was applied if:

$$Cm_{clean} > (Cm_{datumclean} * 1.1).$$

Equation 7.7: Soft Constraint Penalty Criteria for Representative Tail Plane Profile Optimisation

The additional 10% margin was added to the datum moment coefficient in Equation 7.7 to compensate for the tiny variations in the moment coefficient for new profile designs. Initial testing of the optimisation process revealed a tendency for new profile designs with promising drag coefficients to fall prey to the soft constraint penalty. These improved designs had a moment coefficient greater than the datum but well within 10%. The datum moment coefficient was 0.001261 and the new value with the added 10% was 0.00139. The penalty was calculated using a weighted function shown in Equation 7.8.

$$f_1 = 0.4\left(1 - \frac{Cm_{clean}}{Cm_{datumclean}}\right)^2$$

Equation 7.8: Soft Constraint Penalty Function for Representative Tail Plane Profile Optimisation

The constant applied to the function in Equation 7.8 was calculated by considering relative changes in the moment coefficient for a range of profile designs. The penalty of 40% was applied.

As discussed in Chapter 3.5.2. MOTS Overview) the memory and search control features of the MOTS were initially set based on the optimiser process. Table 7.14 outlines these features. The one of the changes from previous MOTS studies was the initial step size; reduced to 0.05 from 0.07. From initial testing it became apparent the initial step size for the FFD code was too large.

Figure 7.56 provides a flow diagram of the overall optimisation processes. This was not intended to be an exhaustive overview of the optimiser process, merely a visual aid to best portray how this optimisation code differed from the other optimisation case studies.

Short Term Memory Allocation	15
Long Term Memory Allocation	4
Intensification Point	15
Diversification Point	25
Initial Step Size	0.05
Step Size Reduction Point	35

Table 7.14: Representative Tail Plane Profile Optimiser Memory and Search Control Variables

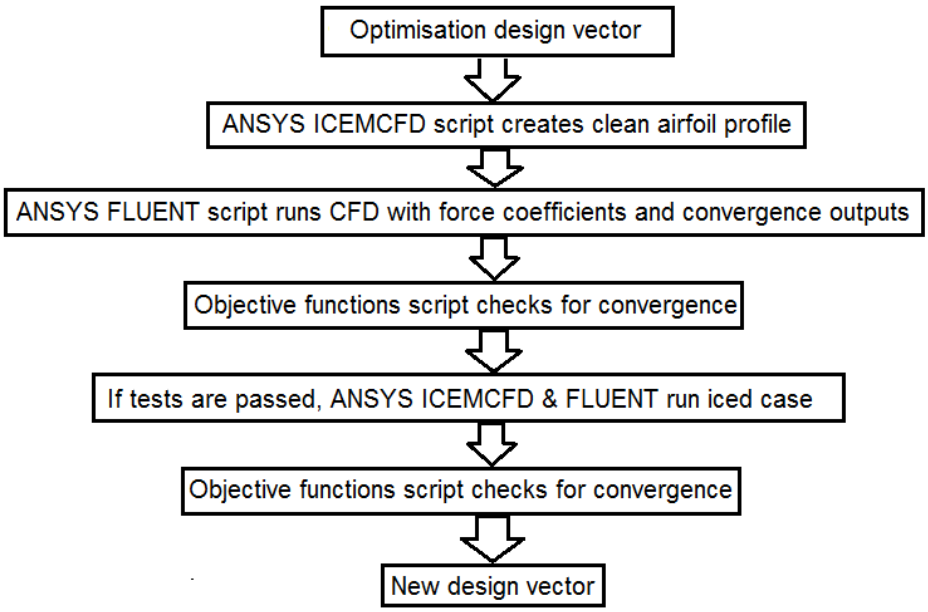

Figure 7.56: Flow Chart for Representative Tail Plane Profile Optimiser

7.3.5. Validation

The tail plane profile optimisation study the NACA 0012 airfoil was chosen due to its numerous uses in airplanes such as the Cessna 152, B-17 Flying Fortress and the helicopter Sikorsky S-61 SH-3 Sea King. In terms of computation validation, the NACA 0012 airfoil offered a number of resources to quickly identify any inconsistencies in preliminary numerical results. A small grid dependency study was conducted to ensure the force coefficient was not grid dependent. Details of the study are not covered here since a detailed mesh dependency study was discussed in the Boeing 737-700 Airfoil Numerical Study The force coefficients in

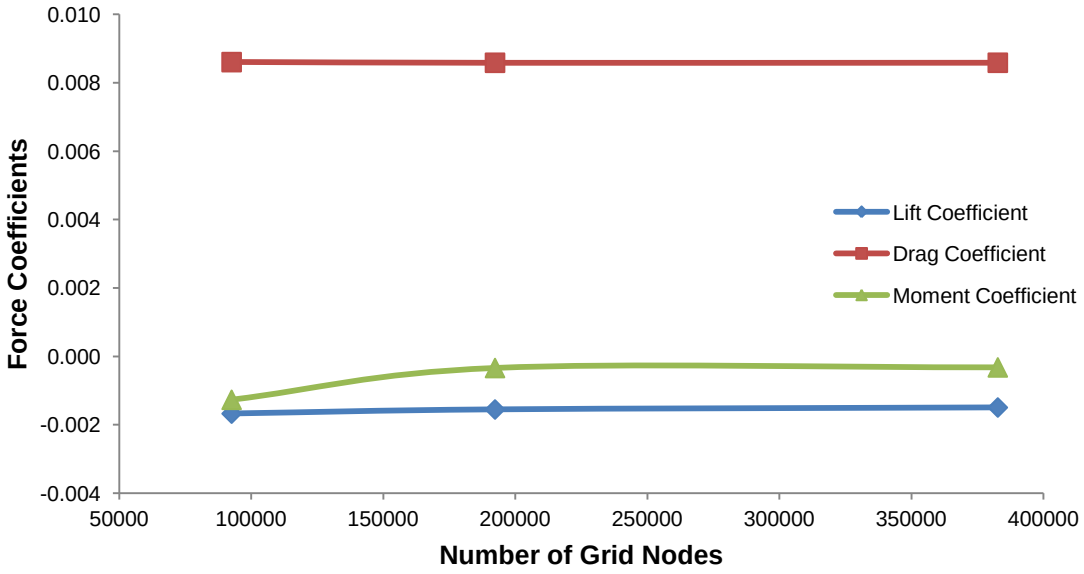

Figure 7.57 display the variation in lift, drag and moment coefficients for a varying number of mesh densities and were found to show very small variations with respect to mesh density for mesh sizes over 150,000 cells.

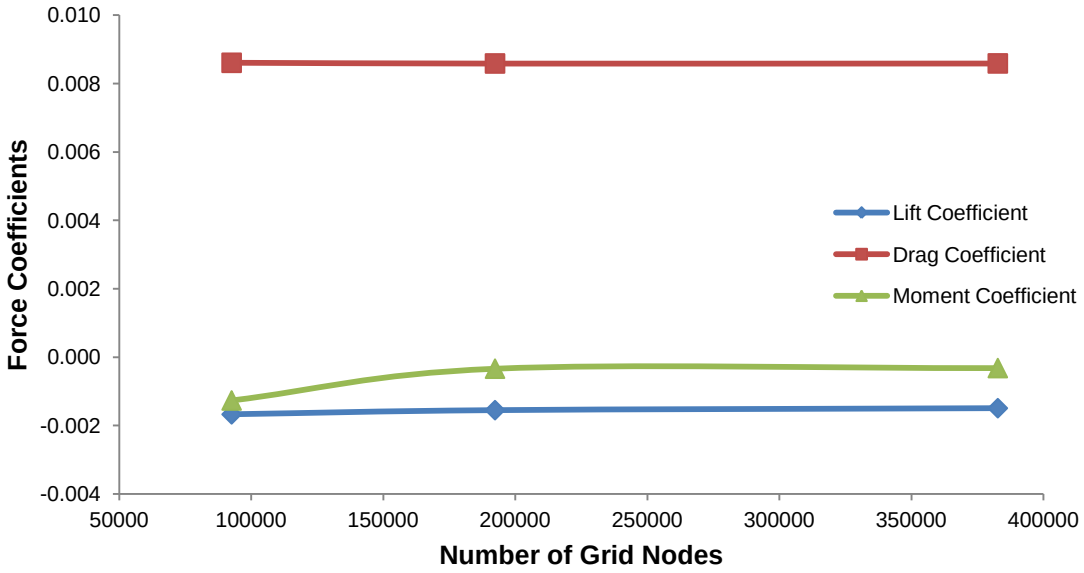

Figure 7.57: Grid Dependency Study for Representative Tail Plane Profile Optimisation Validation

Eleni, et al., [83] published work on turbulence model evaluations using the NACA 0012 and was used to validate the clean (datum) configuration for this optimisation procedure. The Reynolds number throughout the reference evaluations was $3x10^6$ for a chord length of 1 metre. Abbot & Doenhoff, [121] produced a large amount of theoretical and experimental data on various NACA airfoils including the NACA 0012. The aim of this publication was to supply a source of validation for airfoils at subcritical speeds.

The force coefficients for the datum condition compared to Eleni, et al., [83] show good agreement as shown in Table 7.15. The variation in the lift and drag coefficients were 10.52% and 1.16% respectively. The core consideration for this optimisation process was the drag coefficient which showed excellent agreement with published literature. The mesh utilised throughout this optimisation study was not perfectly symmetrical. Due to this non-uniformity the lift coefficient, a non-zero lift coefficient result, was observed.

Model	Lift Coefficient	Drag Coefficient	Moment Coefficient
[83]	-0.0019	0.0084	no data from this source
$k-\omega$ SST	-0.0016	0.0086	-0.0012

Table 7.15: Force Coefficient Comparison for Representative Tail Plane Profile Optimisation Validation

Garrick, [122] provided an insightful report with theoretical pressure distributions for twenty airfoils at different angles of attack. Figure 7.58 shows a comparison of the theoretical pressure profile for a NACA 0012 at zero angle of attack against the numerical results for the datum NACA 0012 airfoil in clean configuration. For a symmetrical airfoil at zero angle of attack, the pressure

profiles across the airfoil showed no signs of any non-physical attributes and compared well against reference comparison. Only the upper surface profiles have been shown since the angle of attack was zero and the airfoil was not cambered; therefore lower surface plots were identical.

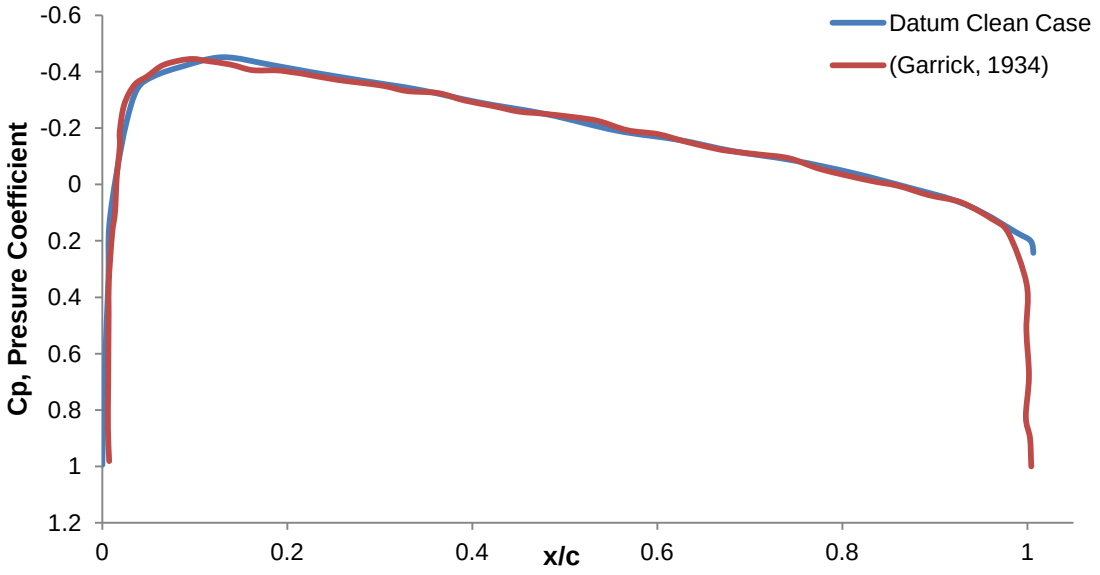

Figure 7.58: Surface Pressure Coefficient Validation for Representative Tail Plane Profile Optimisation Datum Clean Case at 0 AOA

Successful validation for the clean NACA 0012 airfoil in clean configuration provided the basis for the optimisation setup. Figure 7.59 illustrates the performance cost for the NACA 0012 airfoil with runback ice on both surfaces.

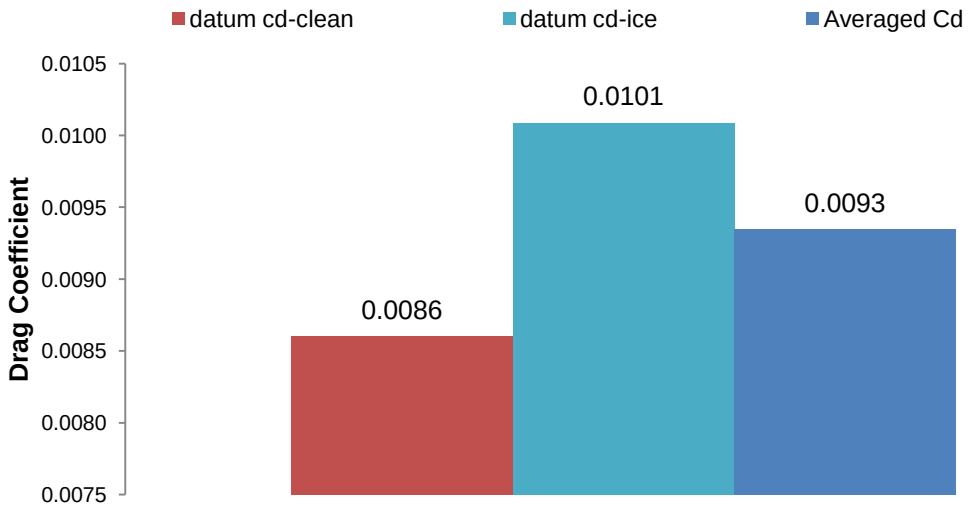

Figure 7.59: Datum Case Drag Coefficient Comparison for Representative Tail Plane Profile Optimisation

The key force coefficient for this optimisation study was the drag force. The aim was to minimise drag without compromising the stability of the airplane by keeping both lift and moment coefficients as close to zero as possible.

The drag coefficient increased by 17.3% for the datum iced case compared with the clean airfoil run. The averaged drag coefficient for both the clean and iced datum run was 0.0093. This was the base value the optimiser used to normalise the average force coefficients for each new airfoil profile evaluated. The lift and moment coefficients for each new design were not used for any cost calculations. The optimiser was set up to check that the values for lift and moment for clean and iced runs were not above a set value. This ensured the airfoil did not produce any unwanted lift or moment force. These set values can be found in Table 7.12 and Table 7.13 for the clean and iced cases respectively.

Velocity contour and vector plots for the datum airfoil in iced configuration can be found from Figure 7.60 through to Figure 7.63. The maximum velocity occurred at the leading edge of the ice shape. As the flow approached the runback ice a stagnation point at the initial point of blockage was seen followed by a rapid increase in speed over the runback ice shape. The maximum velocity difference for the NACA 0012 airfoil in clean and iced configuration highlighted a speed differential of 26ms^{-1}.

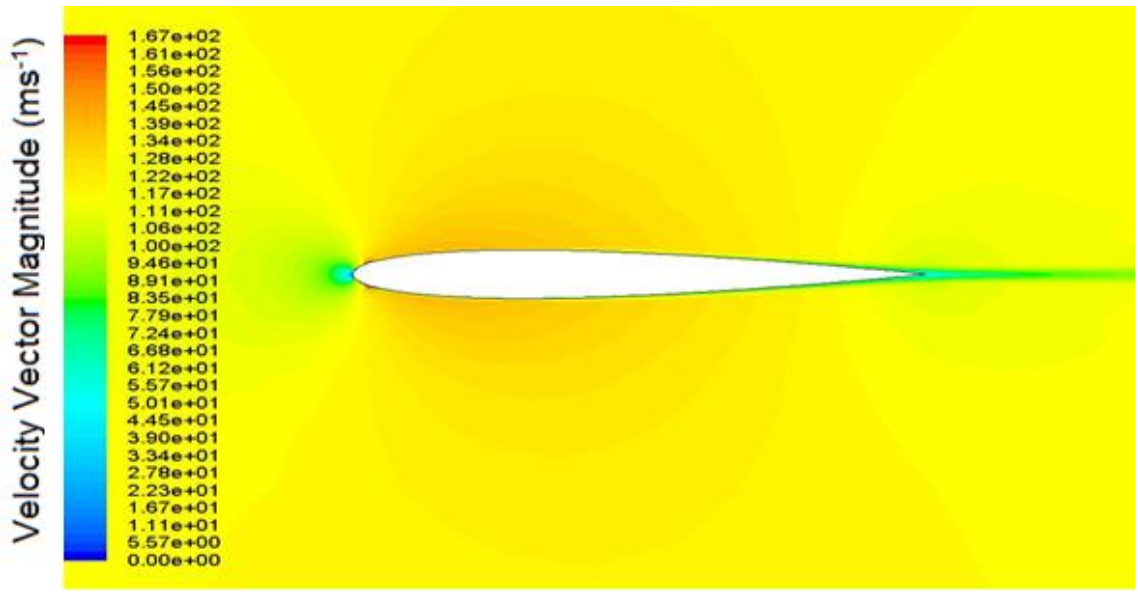

Figure 7.60: Contours of Velocity Magnitude for Representative Tail Plane Profile Optimisation Datum Iced Case

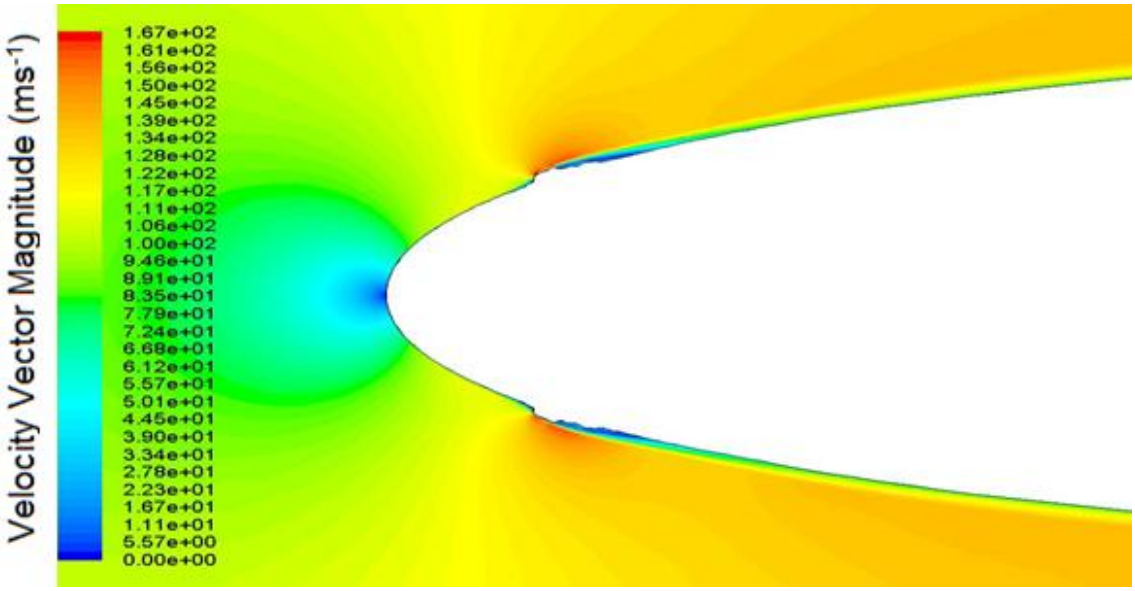

Figure 7.61: Contours of Velocity Magnitude Close to Ice Location for Representative Tail Plane Profile Optimisation Datum Iced Case

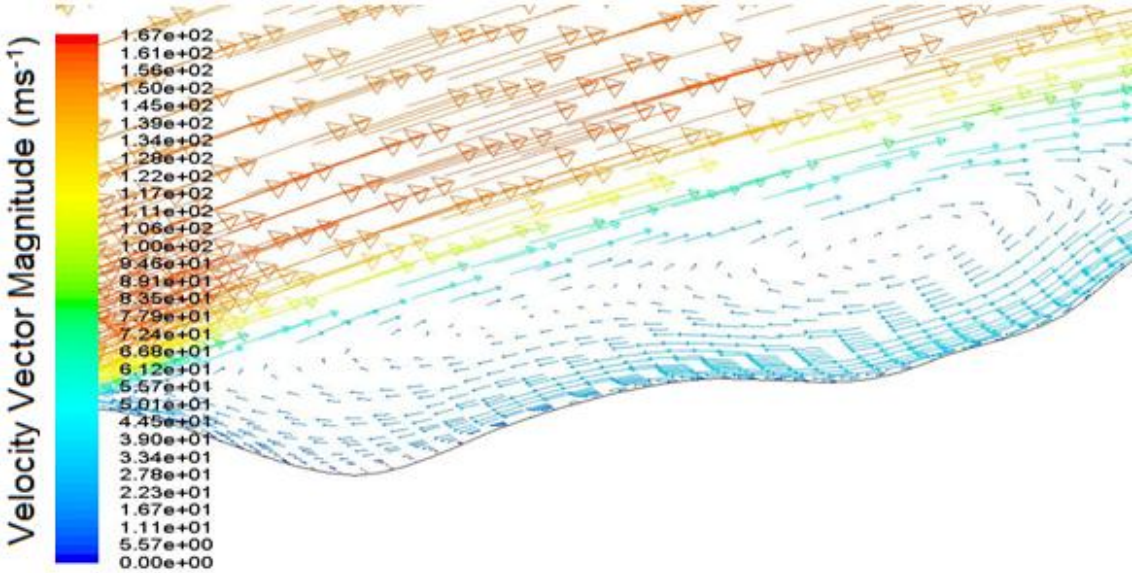

Figure 7.62: Optimum Design Velocity Vector Plot around Runback Ice Shape for Representative Tail Plane Profile Optimisation

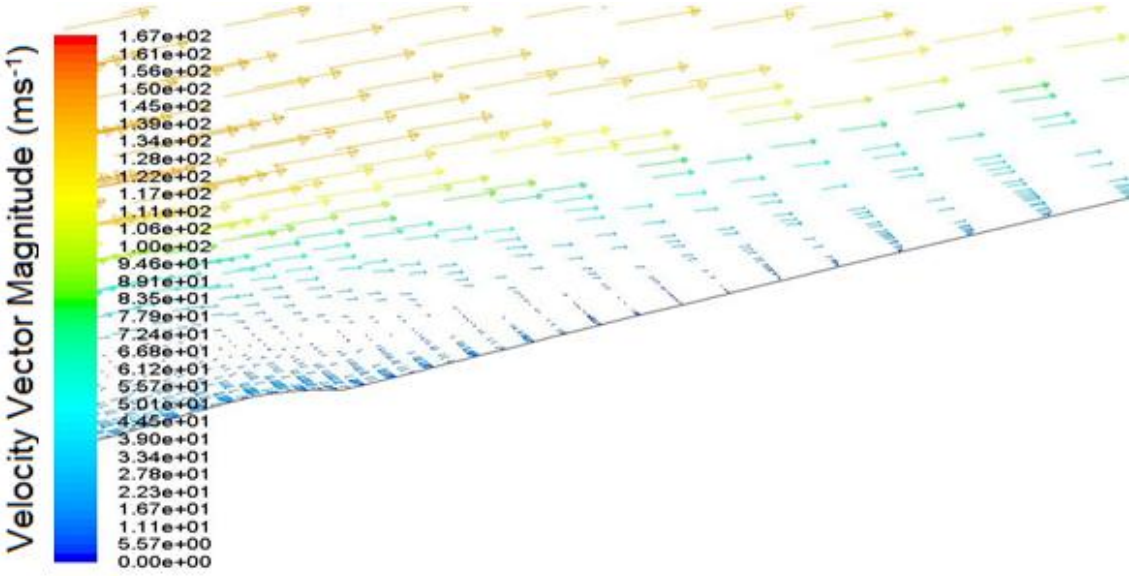

Figure 7.63: Optimum Design Velocity Vector Plot Aft of Runback Ice Shape for Representative Tail Plane Profile Optimisation

The surface pressure coefficient plot in Figure 7.64 provided some insight into the unexpected lift coefficient for the datum iced case. The pressure spike that occurred in the iced datum run was the stagnation point created just in front of the runback ice shape. As the minimum pressure spike began to recover, a larger recovery in pressure just aft of the ice shape was observed. This was where the flow separation occurred. This recovery helped provide some explanation for the small variation in the lift coefficient for both cases. For both cases the pressure almost immediately stabilised and consequently the lift coefficient remained very similar.

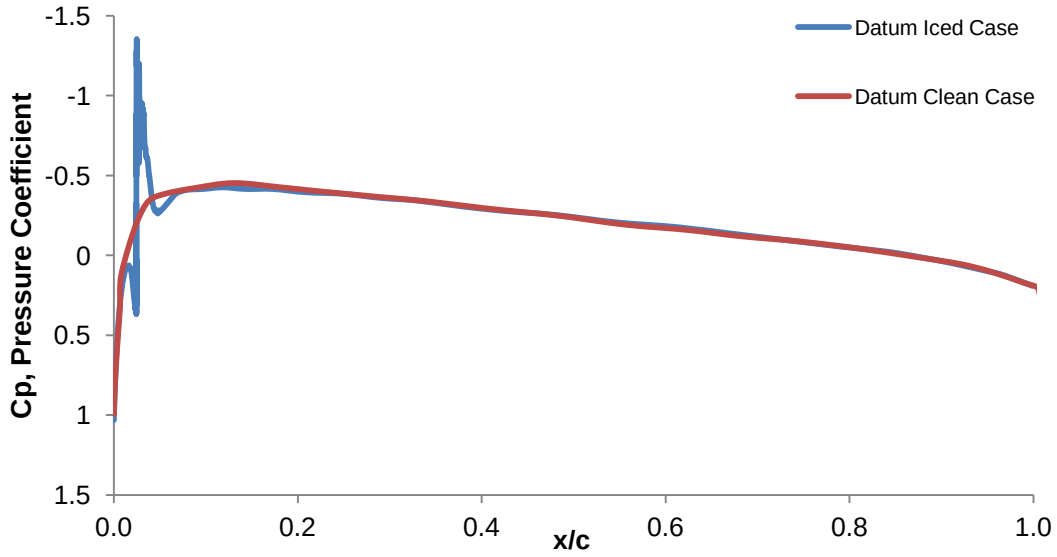

Figure 7.64: Surface Pressure Coefficient for Representative Tail Plane Profile Optimisation Datum Clean and Iced Case Comparison

A drag coefficient increase of 17.3% was accounted for by the wake produced from the runback ice shape. The skin friction drag remained close to equal for the clean and iced datum case since no changes were made to the material or its roughness properties. The total increase in drag was attributed to form drag which was inferred as a cost due to the increased velocity over the ice shape. A clear aim for the optimisation process was to reduce this velocity, thus the wake region via airfoil shape modifications.

7.3.6. Results

The progress of the optimiser was monitored via a number of output files. Figure 7.65 illustrated the behavioural history for this optimisation process. The i_local value specified the number of consecutive unsuccessful optimisation iterations.

Bound by the initial memory and search control variables set in Table 7.14:

1. 12 search intensification steps occurred. For the search intensification to initiate, 15 consecutive unsuccessful iterations were tallied.
2. 12 search diversification steps occurred. For the search intensification to initiate, 25 consecutive unsuccessful iterations were tallied.
3. 9 step size reductions occurred. For each reduction in step size, 35 consecutive unsuccessful iterations were tallied. Every step size reduction reduces the step size by a factor of 0.7. The final step size was 0.002018.

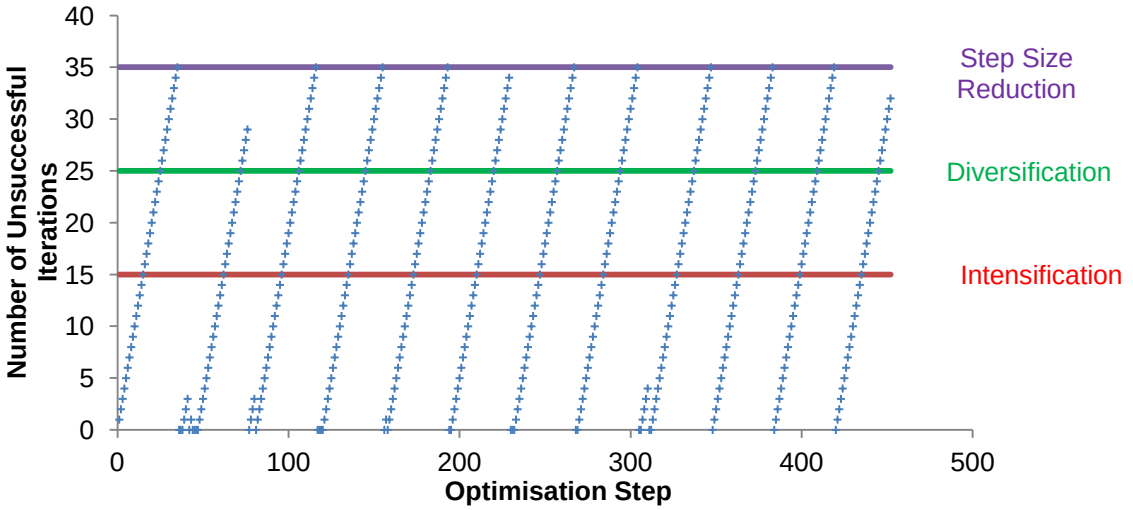

Figure 7.65: Representative Tail Plane Profile Optimiser Monitoring Data

The total of 4669 airfoil profiles was evaluated and 701 feasible profiles were found. All 701 feasible designs are shown in Figure 7.66. The notable features were the soft penalty designs. One soft penalty profiles was selected for analysis.

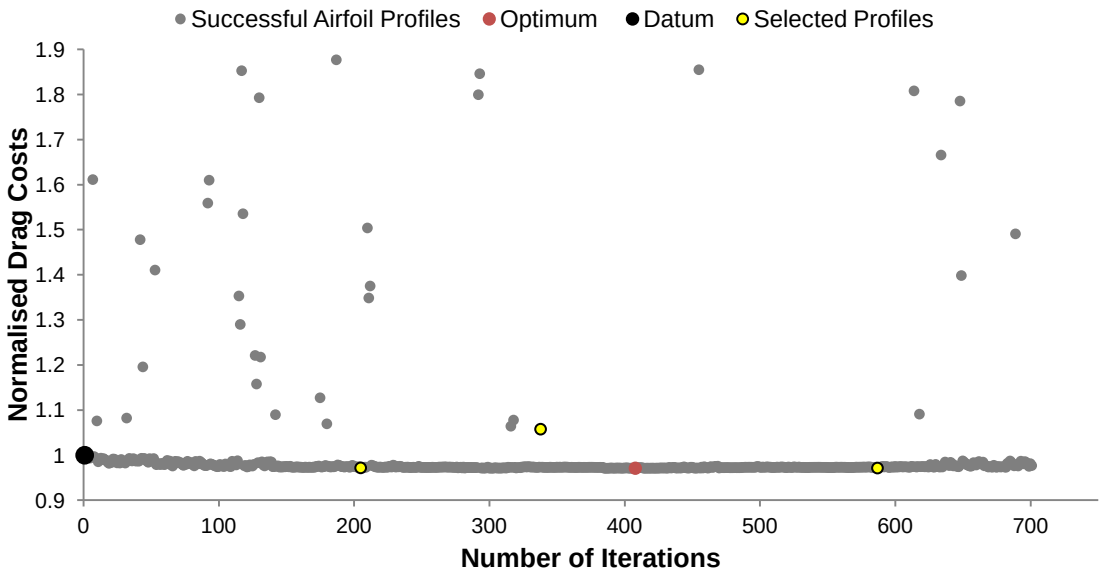

Figure 7.66: Representative Tail Plane Profile Optimiser Search Pattern

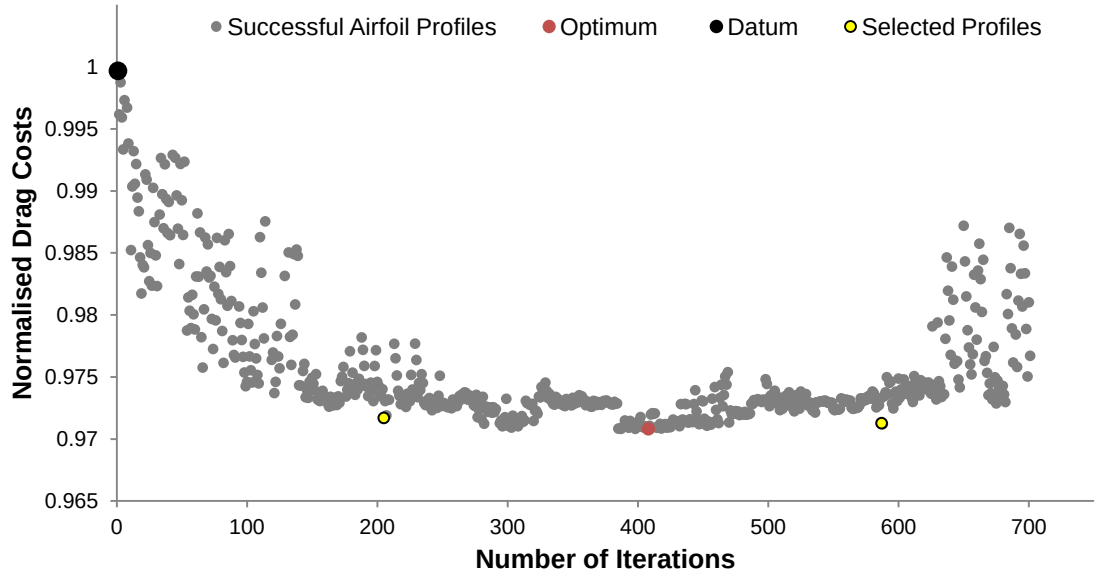

Figure 7.67: Representative Tail Plane Profile Optimiser Search Pattern 2

Figure 7.67 provided a clearer picture of the optimiser search pattern. Since this was a single objective optimisation problem there was one optimum design. The optimum design was found after 409 optimiser iterations.

7.3.7. Analysis

A number of airfoil profiles were chosen based on their low drag costs. The optimum design, two selected cases and a third case with a soft penalty constraint added (Case 3) were used for analysis.

Optimiser Airfoil Profiles	Optimiser Drag Costs
Case1	0.9717
Case 2	0.9713
Case 3	1.0574
Optimum	0.9708

Table 7.16: Representative Tail Plane Profile Optimiser Selected and Optimum Run Costs

Figure 7.68 through to Figure 7.71 present the selected and optimum shape profiles relative to the datum profile. Although the shapes differed from the original NACA 0012 profile, all the new design profiles were very similar relative to each other. An overlay of all four profiles can be seen in Figure 7.72.

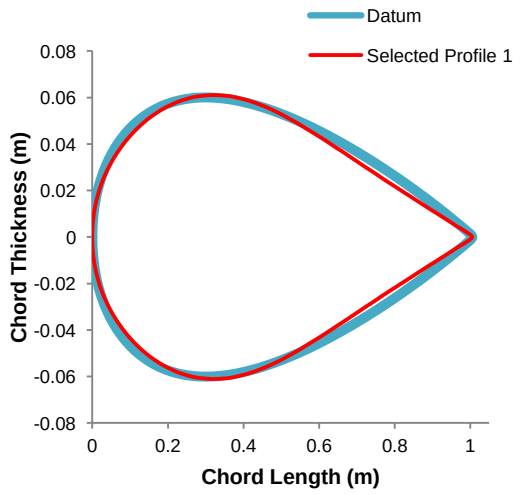

Figure 7.68: Representative Tail Plane Selected Profile 1

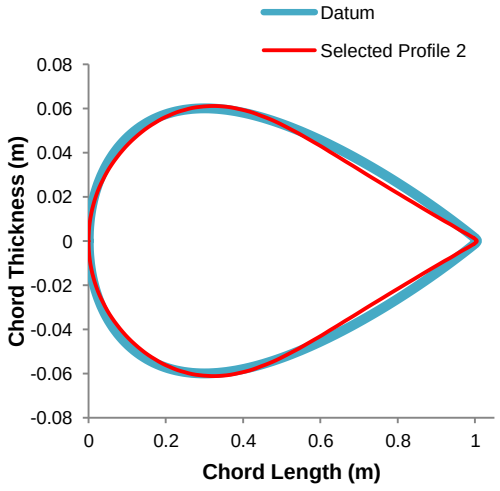

Figure 7.69: Representative Tail Plane Selected Profile 2

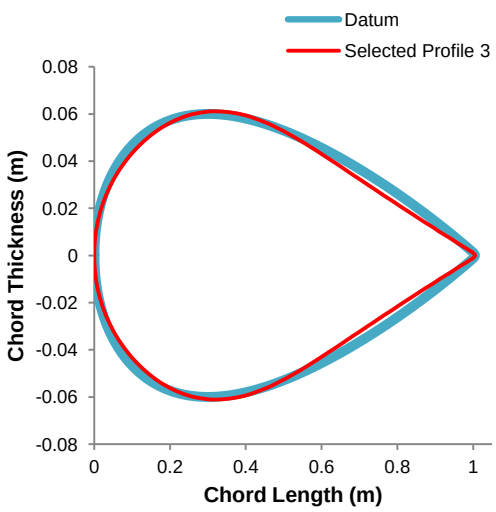

Figure 7.70: Representative Tail Plane Selected Profile 3

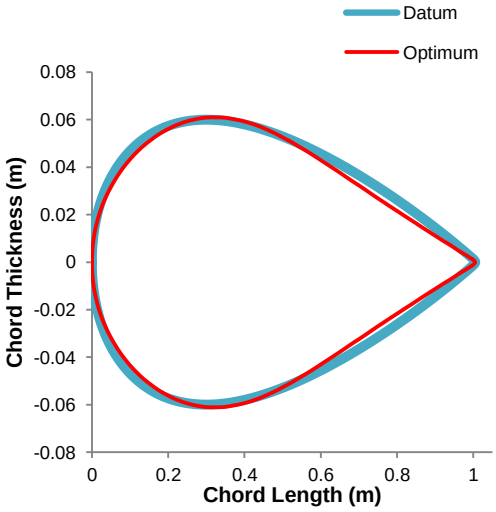

Figure 7.71: Representative Tail Plane Optimum Profile

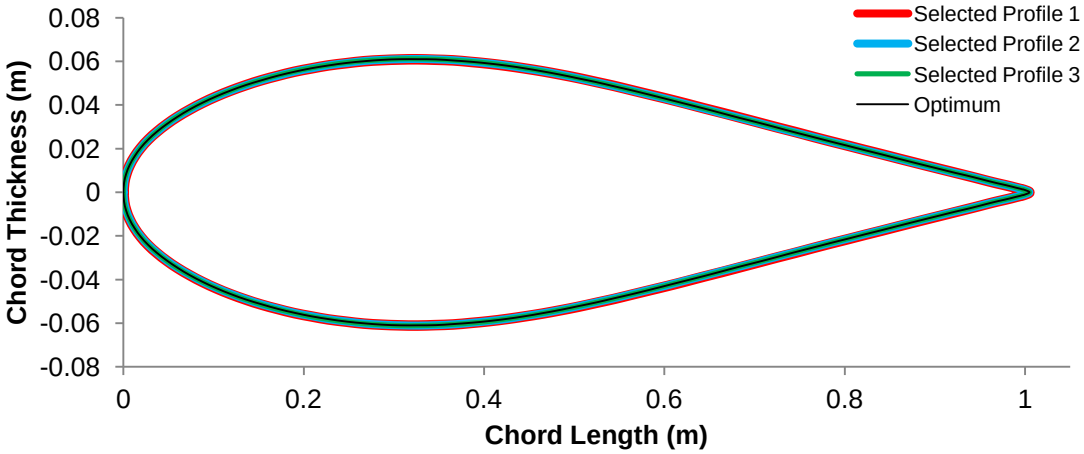

Figure 7.72: Overlay of Airfoil Profiles for Representative Tail Plane Optimiser

133 vertex points created each airfoil profile. For each selected profile the maximum variation out of all the vertex points relative to the optimum airfoil vertex point can be seen in Table 7.17. The maximum variation across all three selected profiles was 1.43%. With such a small variation from all four profiles, only the optimum design was analysed.

Optimiser Airfoil Profiles	Maximum x-coordinate Variation	Maximum y-coordinate Variation
Case 1	0.80%	1.12%
Case 2	1.43%	0.34%
Case 3	0.11%	0.83%

Table 7.17: Vertex Point Variation for the Representative Tail Plane Profile Optimiser

The optimum airfoil profile produced a drag reduction of 1.84% and 3.1% for the clean (Figure 7.73) and iced (Figure 7.74) runs respectively. The averaged

reduction in drag for both cases was 2.6% (Figure 7.75). Table 7.18 highlights the force coefficients for datum and optimum airfoil design. The selected case data was added for reference only.

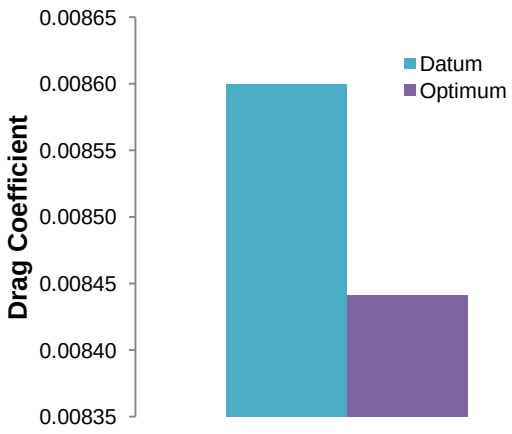

Figure 7.73: Clean Drag Coefficient Comparison for Representative Tail Plane Profile Optimisation

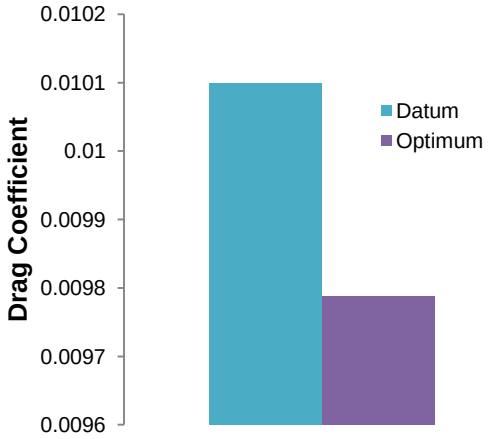

Figure 7.74: Iced Drag Coefficient Comparison for Representative Tail Plane Profile Optimisation

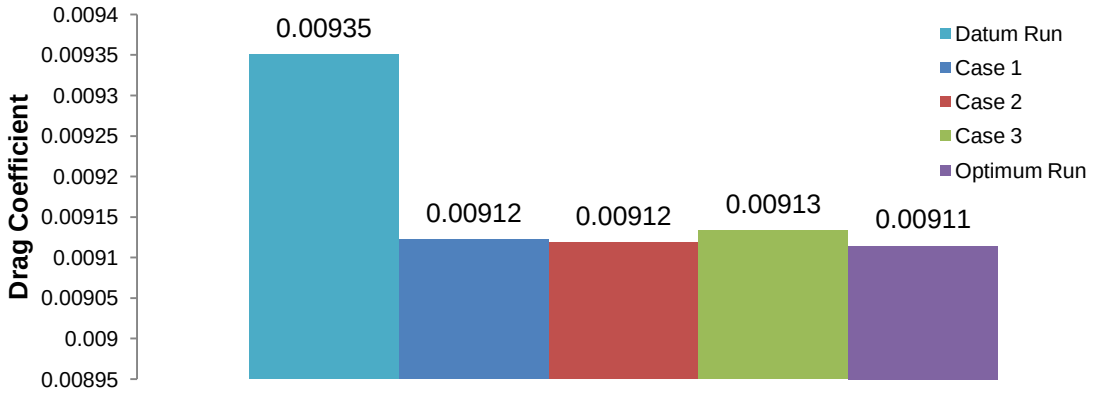

Figure 7.75: Averaged Drag Coefficient Comparison for Representative Tail Plane Profile Optimisation

Optimiser Output Airfoil Profiles	Clean Lift Coefficient	Clean Drag Coefficient	Clean Moment Coefficient	Iced Lift Coefficient	Iced Drag Coefficient	Iced Moment Coefficient
Datum	0.0016	0.0086	0.0012	0.0021	0.0101	0.0002
Optimum	0.0055	0.008442	0.00122	0.00077	0.00979	0.0003
Case 1	0.0049	0.008447	0.00108	0.00096	0.00980	0.0004
Case 2	0.0052	0.008440	0.00114	0.00044	0.00980	0.0002
Case 3	0.0062	0.008444	0.00140	0.00082	0.00982	0.0004

Table 7.18: Force Coefficients for Representative Tail Plane Profile Optimiser Airfoil Designs

Surface pressure coefficient plots for the datum and optimum profiles are shown in Figure 7.76 & Figure 7.77. Both the clean and iced optimum runs did not peak as low for Cp in the initial pressure gradient phase. This variation from the datum was a direct result of the lower peak velocity over the leading edge of the

optimum airfoil (Table 7.19). Following this initial pressure gradient phase, the optimum design exhibited a longer region of pressure recovery.

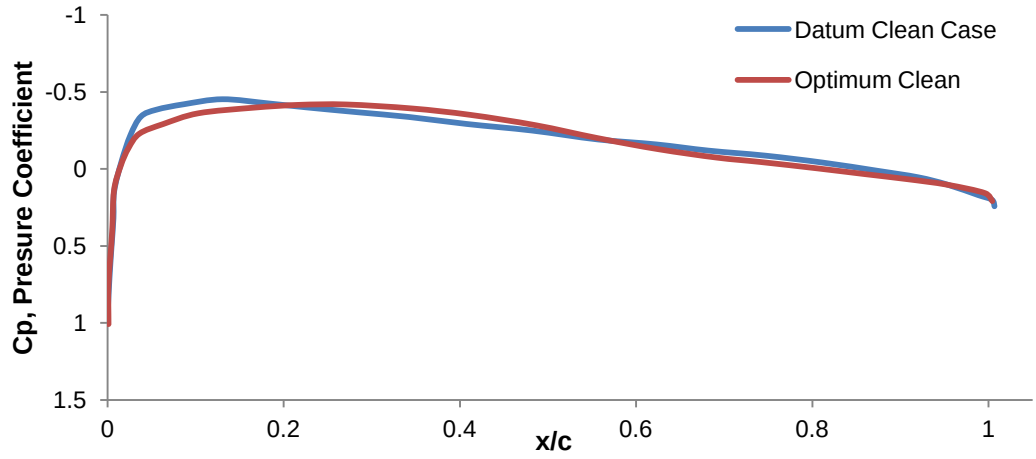

Figure 7.76: Clean Surface Pressure Coefficient Comparison for Representative Tail Plane Profile Optimiser

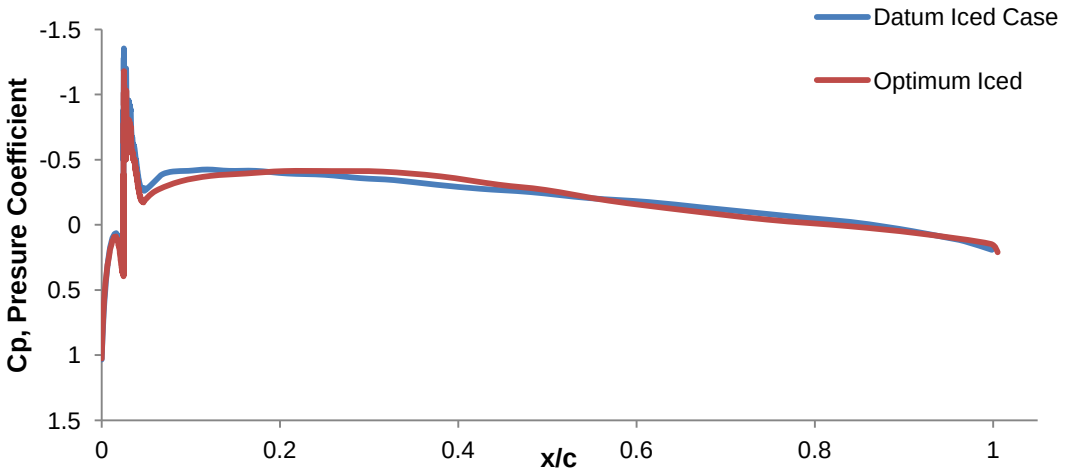

Figure 7.77: Iced Surface Pressure Coefficient Comparison for Representative Tail Plane Profile Optimiser

Case	Maximum Velocity (ms^{-1})
Datum Clean	139.93
Optimum Clean	138.9
Datum Iced	166.04
Optimum Iced	159.72

Table 7.19: Maximum Velocity Comparison for Representative Tail Plane Profile Optimiser

During the initial pressure gradient phase, the initial step increase for Cp in Figure 7.77 was due to a high pressure region created by the stagnation point from the runback ice as shown in Figure 7.78. This was followed by a low pressure zone over the ice shape. In Figure 7.80 the low pressure zone was attributed to the high velocity at the leading edge of the ice shape.

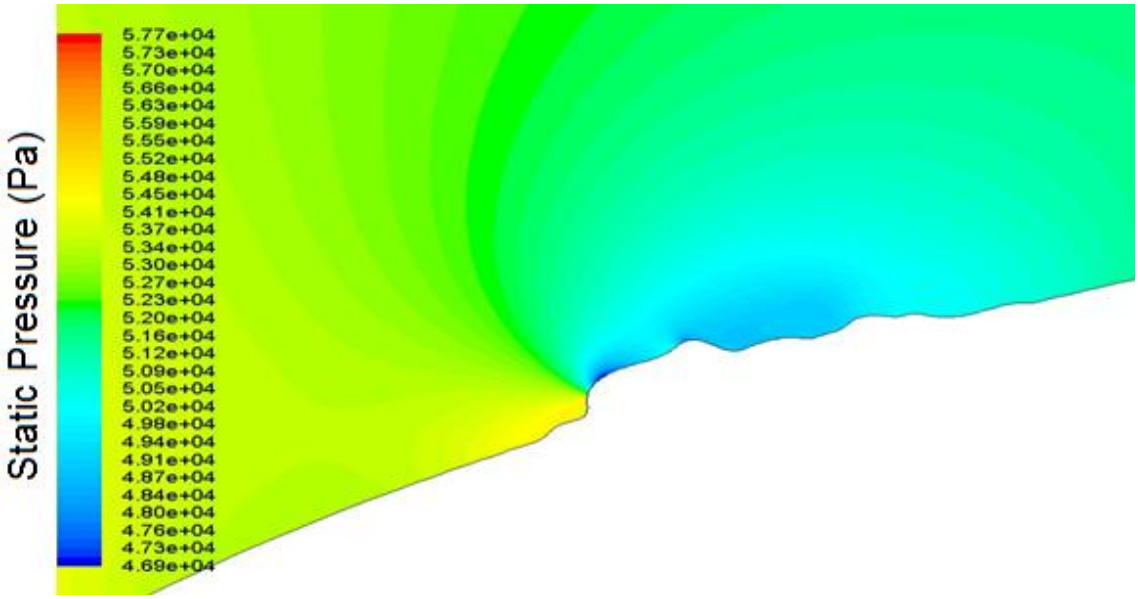

Figure 7.78: Optimum Iced Profile Static Pressure Contour Plot for Representative Tail Plane Profile Optimiser

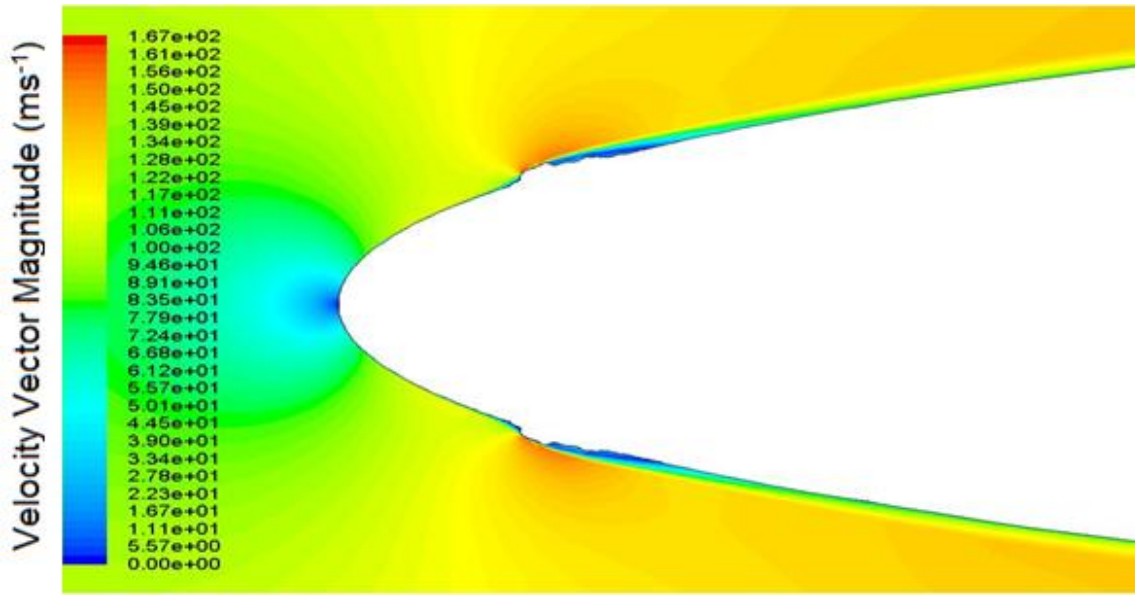

Figure 7.79: Optimum Iced Profile Velocity Magnitude Contour Plot for Representative Tail Plane Profile Optimiser

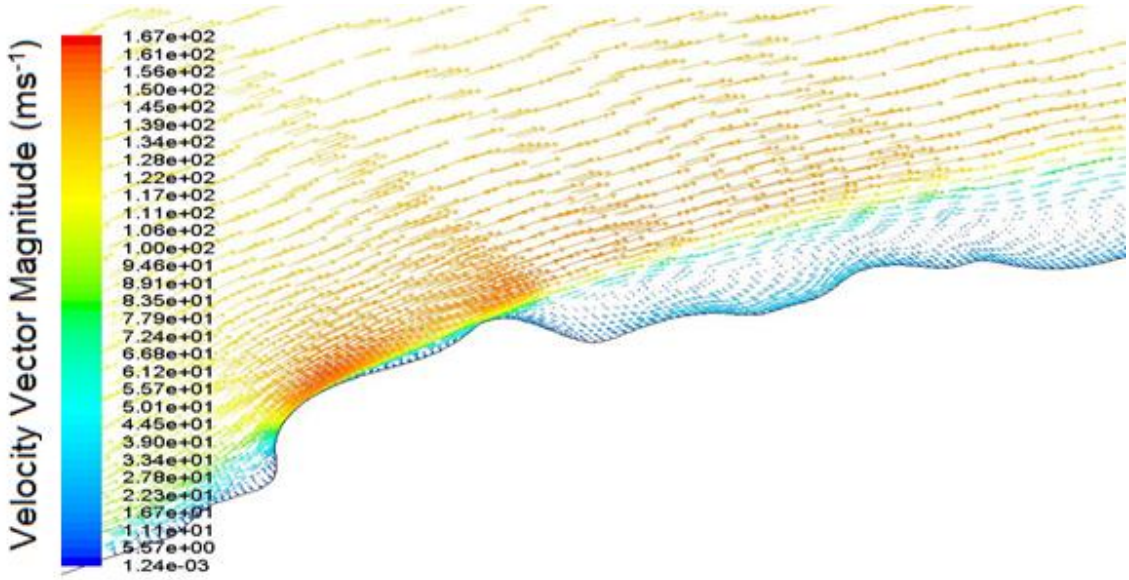

Figure 7.80: Optimum Iced Profile Velocity Vectors for Representative Tail Plane Profile Optimiser

To conclude this optimisation study provided an improved airfoil design which exhibited a lower drag value in both clean and iced configuration. The average reduction in lift for both configurations was 2.6%. A number of other profiles were considered and found each airfoil shape to be very similar to the optimum profile highlighting the robustness of the optimiser and that the subtle changes made to the leading edge resulted in a lower peak velocity, which in turn provided a reduction in drag. The iced configuration optimum profile boasted a drop in peak velocity over the runback ice shape of 6.32ms^{-1} which in turn resulted in a drag coefficient drop of 3.1%.

7.4. Anti Icing Optimisation

7.4.1. Objectives

This was a multi-point (all three runback ice shapes considered) optimisation process. The aim of this study was to minimise the leading edge surface temperature. For a variable temperature input the position where the temperature of the airfoil surface reached freezing point varied along the chord.

The objective functions for this multi-objective optimiser was to minimise heat input, maximise lift and minimise drag. Three runback ice shapes were evaluated for each design vector. The mean of the three runback ice shape force coefficients (objective functions) was used to evaluate the costs:

$$F_1 = \left(\frac{\overline{Cl_{x_1}}}{\overline{Cl_{datum}}} \right)$$

Equation 7.9: Objective Function 1

$$F_2 = \left(\frac{\overline{Cd_{x_1}}}{\overline{Cd_{datum}}} \right)$$

Equation 7.10: Objective Function 2

The design parameter for this study was the heat input with a range of variability of 1°C to 110°C. The FLUENT solver convergence criterion was used as a hard constraint.

The optimisation process used the Boeing 737-700 airfoil in clean configuration with a leading edge temperature provided by the design vector. The leading edge temperature was extrapolated and mesh files were created with the runback ice placed at the location where surface temperature reached zero Celsius. At this point a loop ran three FLUENT iced simulations for the three different runback ice shapes (Figure 7.81). The average for all three runback ice configurations was used to calculate the optimisation costs for a given design vector. Experimental setup for datum run heat input was 703W which equated to a surface temperature of 5.7°C.

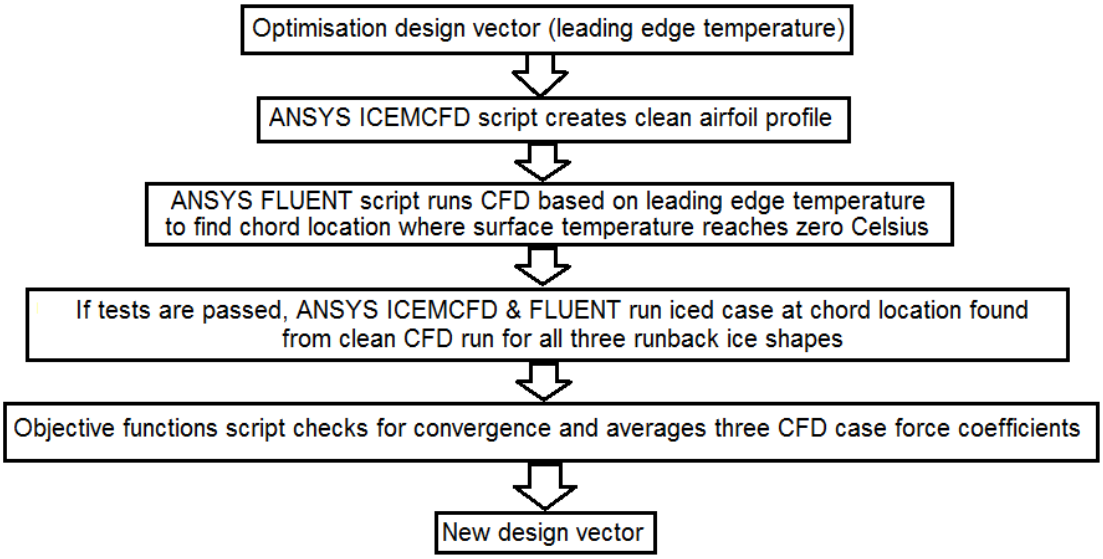

Figure 7.81: Anti Icing Optimisation Setup

7.4.2. Heat Transfer Computational Setup

The hybrid airfoil used at the CIT was attached with heaters to an aluminium inner skin (Figure 7.82). The skin was a 1cm thick aluminium sheet. The experimental hybrid airfoil used in the CIT was equipped with 37 k-type thermocouples with an accuracy of ±1° [104].

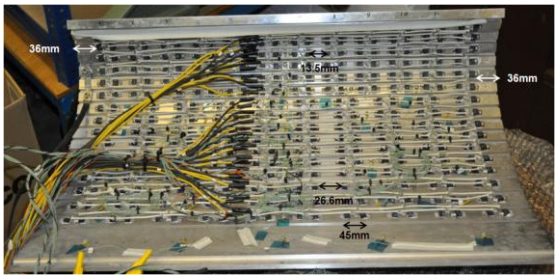

Figure 7.82: Leading Edge Inner Skin Wiring [104]

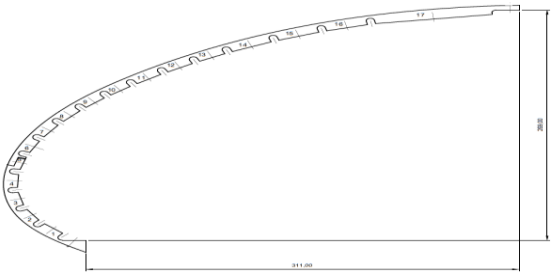

Figure 7.83: Sketch of Leading Edge Skin [104]

Modelling heat transfer properties using ANSYS FLUENT was accomplished using conjugate heat transfer (shell conduction not available for two-dimensional problems). To appropriately model the heater setup seen in Figure 7.83 both the leading edge heat input and aluminium thickness was created (Figure 7.84). The domain setup and treatment of the thin aluminium skin was similar to the approach used by Domingos, [123] for their two-dimensional thermodynamic model.

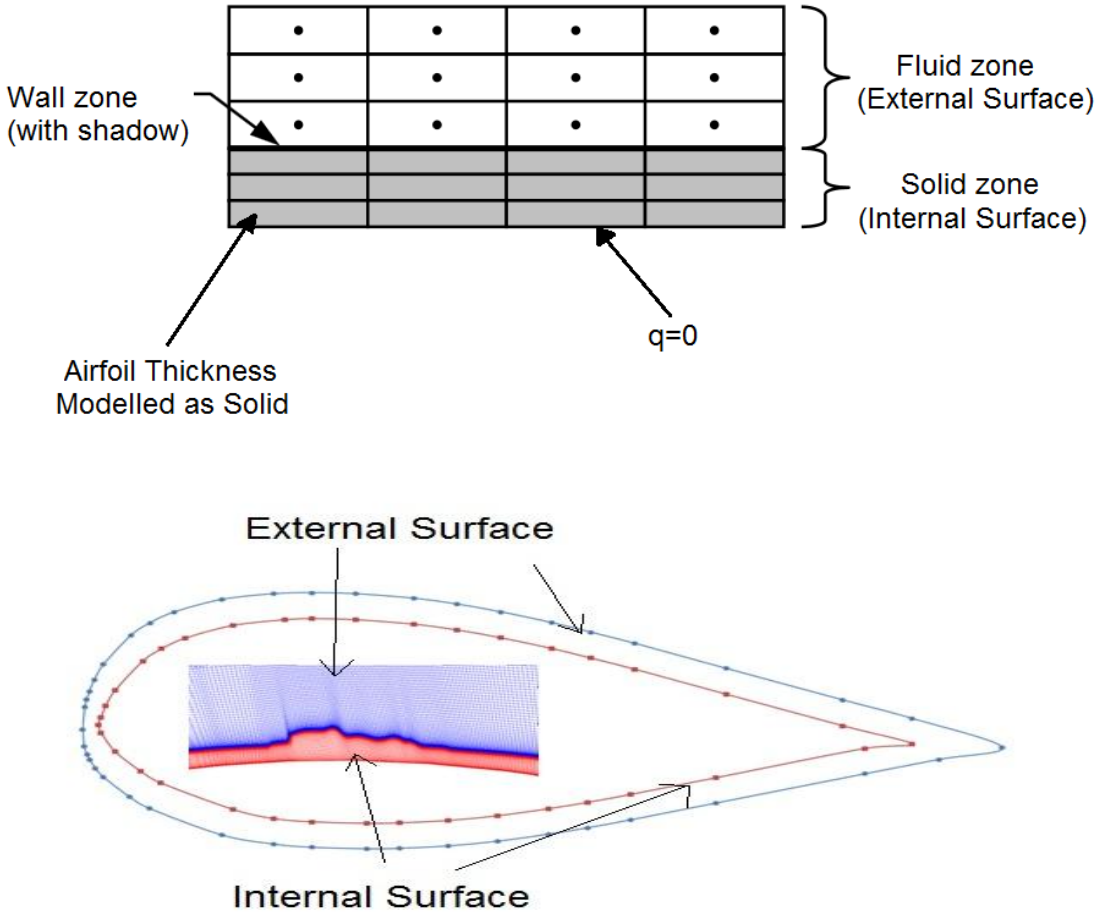

Figure 7.84: Numerical Model Surface Illustration

The solid zone modelled the aluminium thickness and also incorporated the runback ice shape. The fluid zone modelled the air around the airfoil and both domains were connected using ANSYS FLUENT shadow wall feature. Within the airfoil, the walls were treated as adiabatic and conduction only occurred along the aluminium airfoil frame.

7.4.3. Experimental Heat Transfer Correlation

The atmospheric conditions set by Alègre, [104] at the CIT to create the ice shape profiles in Figure 7.85 are given in Table 7.20. Due to CIT limitations, the free stream velocity specified by the EASA 45 minute hold condition of 118ms-1 was not possible. FLUENT simulations conducted by Alègre, [104] investigated the local upper surface velocity variation for the different tunnel velocities and found only a small variation. Consequently it was reasonable to assume that the runback ice shapes created at the CIT at a speed of 85ms^{-1} was a realistic representation of the typical ice shape formation that may occur for the EASA hold condition.

	Angle of Attack (AOA)	Free Stream Velocity (ms^{-1})	Free Stream Temperature (°Celsius)	CIT Run time (minutes)	Total Heat Input (kW)	Limit of Heated zone (m)	Surface Temperature (°Celsius)
Experimental Atmospheric Conditions [104]	8	85	-9	20	0.703	0.086	5.7

Table 7.20: CIT Atmospheric Conditions for Datum Runback Ice Profiles set by [104]

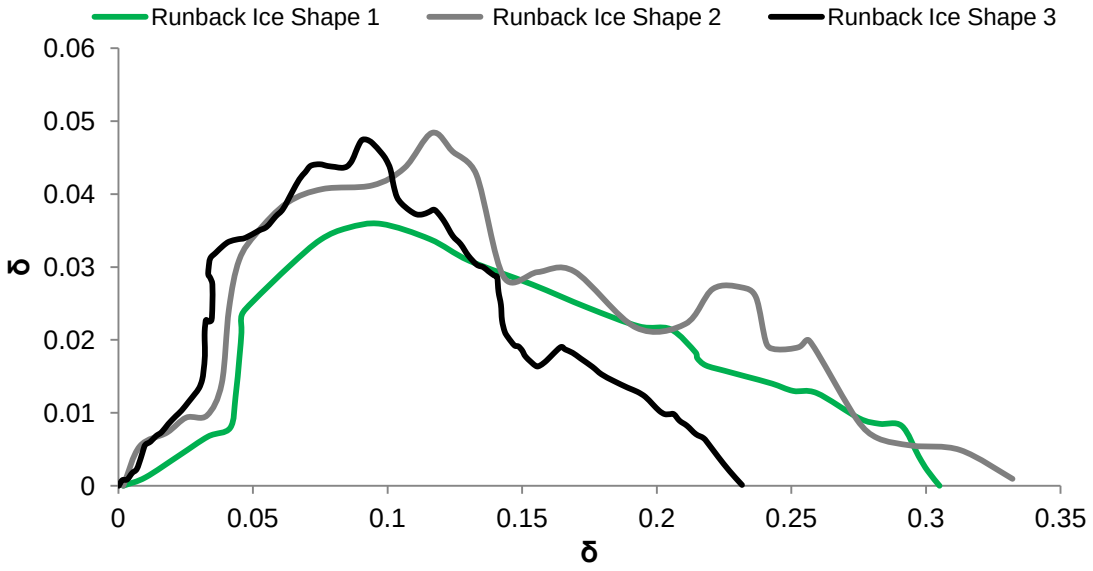

Figure 7.85: Datum Runback Ice Profiles for Anti-Icing Optimisation

Aerodynamic validation of the B737 airfoil using adiabatic walls was conducted in Chapter 5. Since the objective of this optimisation study was to reduce the leading edge surface temperature, validation of the numerical heat transfer was conducted against experimental data. Although no experimental data on the heat transfer coefficient was available, thermocouples within the leading edge B737 hybrid airfoil provided a temperature profile along the chord. A comparison of the experimental temperature profile against FLUENT datum setup is shown in Figure 7.86.

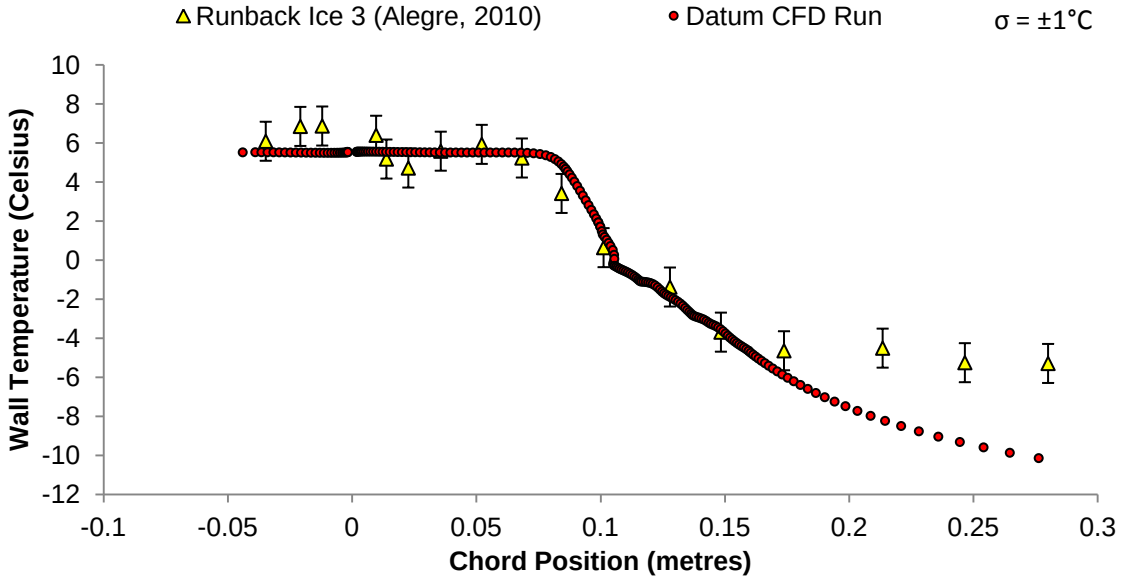

Figure 7.86: Comparison of Numerical and Experimental Leading Edge Surface Temperature

Good agreement was found from the leading edge up to 0.17m. The heated region ended at 0.086m. Conductive and convective heat transfer was consistent with experimental data over a range 84mm. Since the optimisation setup placed the ice shape where the surface temperature reached zero, the need to accurately resolve the thermal conduction further along the airfoil would have increased the computational costs and was considered unnecessary. Laccarino's, [124] work on two-dimensional heat transfer prediction suggested the need to validate combined convection and conduction. Since the numerical results for leading edge temperature variation matched closely to the experimental data, this was viewed as a combined heat transfer validation. Conduction across the 1cm thick aluminium surface was modelled. The velocity was set to match the CIT velocity at 85ms^{-1} which allowed for convective heat transfer modelling. A contour plot of the temperature drop from the limit of the heated zone to below freezing and consequent ice formation location is shown in Figure 7.87.

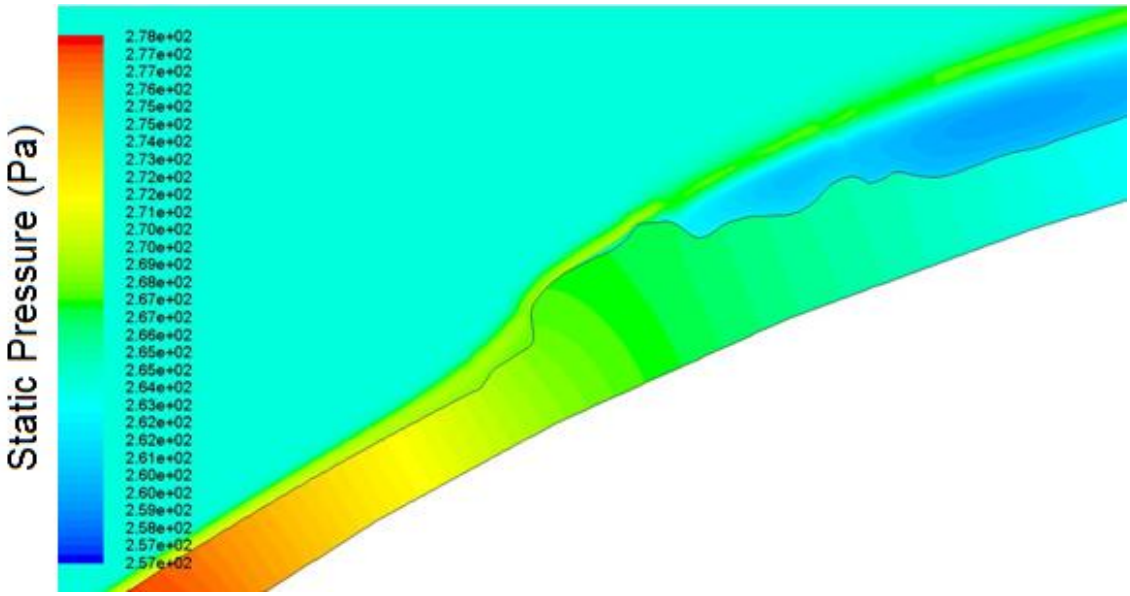

Figure 7.87: Contour Plot of Static Temperature for Datum Runback Ice 2

Heat input data from Alègre, [104] was used to investigate the relationship between the leading edge surface temperatures and heat input in Watts for the resistors within the heating element. A linear relationship was found (Figure 7.88). A temperature range of 10-40°C was observed for a power input ranging from 700-2300 Watts.

The range of variability applied to the heat input for this study was chosen based on the freedom of ice movement set by the author. The Ice Location Optimisation study had a range of variability from 0.023 – 0.113x/c along the chord. To this end a number of FLUENT CFD runs were conducted to find the upper limit for the range of variability heat input. A range of 1 to 110°C leading edge temperatures were tested to allow a range similar to that set for Ice Location Optimisation study. The linear relationship in Figure 7.89 showed the chord position where the upper surface wall temperature reached zero for a given leading edge heat input. With a range of variability for the heat input found at 1 - 110°C the corresponding ice formation chord position range was 0.022 - 0.125x/c.

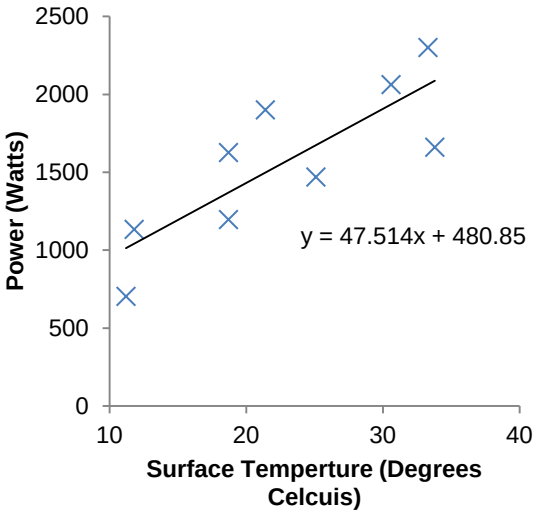

Figure 7.88: Heating Element Power Usage and Surface Temperature Correlation

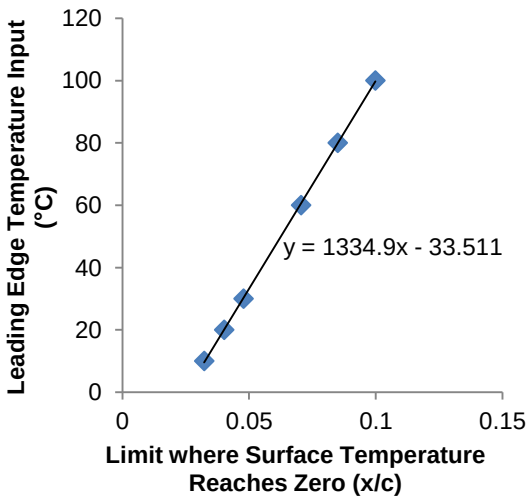

Figure 7.89: Leading Edge Temperature and Point of Freezing Correlation

Table 7.21 shows the calculated dimensionless temperature based on the wall and fluid temperature. Using the relevant dimensionless temperature value input for ANSYS FLUENT, a second order polynomial relationship was found with the leading edge temperature and area-weighted average heat transfer coefficient (Figure 7.90).

Wall Temperature (K)	Fluid Temperature (K)	Reference Temperature (K)
283.15	264.15	31.89932873
293.15	264.15	48.68844912
303.15	264.15	65.47756951
333.15	264.15	115.8449307
353.15	264.15	149.4231714
373.15	264.15	183.0014122

Table 7.21: Anti-Icing Optimisation Reference Temperature for ANSYS FLUENT

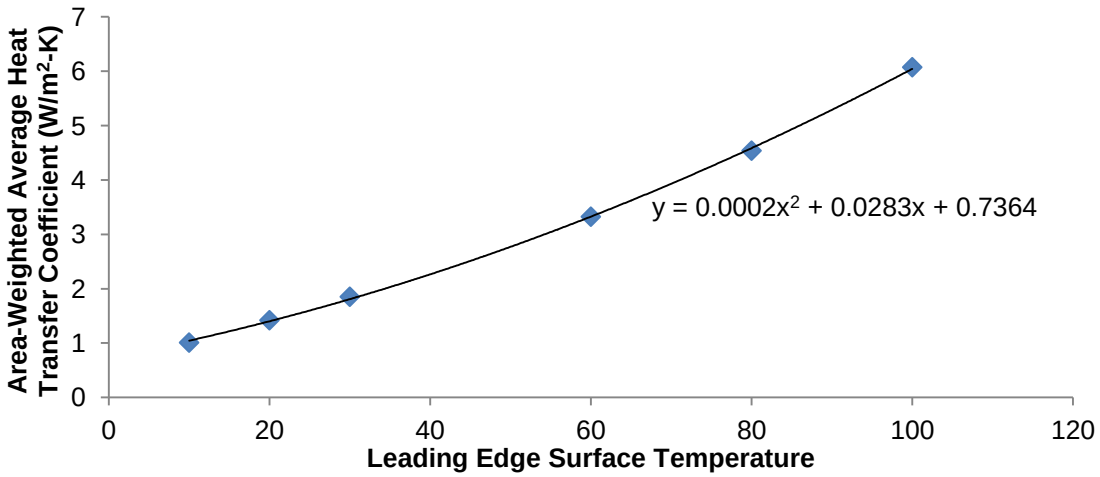

Figure 7.90: Heat Transfer Coefficient against Leading Edge Surface Temperature

7.4.4. Datum Validation & Results

The numerical solver setting used for this optimisation study matched the 45 minute hold case outlined by the EASA. The datum temperature input and heated region was set to 5 °C and 0.023x/c which was in line with the experimental setup by Alègre, [104].

The initial datum CFD runs for all three ice shapes was evaluated. The lift and drag coefficient performance is shown in Figure 7.91 & Figure 7.92. The lift coefficient loss relative to the clean B737 airfoil was 1.6%, 5.4% and 5.8% for runback ice shape 1, 2 and 3 respectively. The increase in drag relative to the clean B737 airfoil was 8.7%, 28.4% and 32.1% for runback ice shapes 1, 2 and 3 respectively. The performance loss increased with increasing ice shape number. The results agreed with wind tunnel ice shape performance losses. The minimum and maximum losses for individual ice shapes based on their geometry were ice shape 1 and 3 respectively. The results also showed the performance losses for ice shape 2 and 3 are very similar.

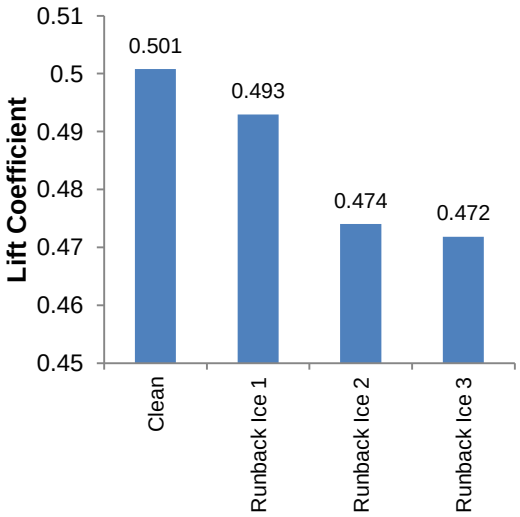

Figure 7.91: Lift Coefficient Comparison for Anti-Icing Optimisation Datum Runback Ice Shapes

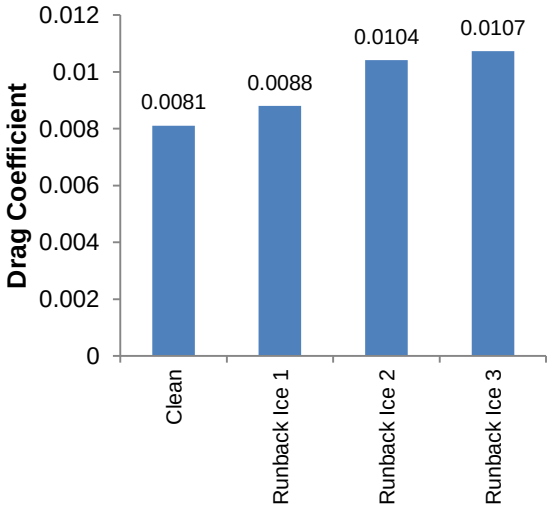

Figure 7.92: Drag Coefficient Comparison for Anti-Icing Optimisation Datum Runback Ice Shapes

The pressure coefficient profiles for the clean configuration B737 airfoil and three iced configuration airfoils are shown in Figure 7.93. The x-axis chord location was only considered where the runback ice shape formed. The suction peak observed for ice shape 1 was larger than that seen for ice shape 2 and 3. The velocity magnitude difference observed for runback ice shape 1 and 3 was 28ms^{-1} (Figure 7.94 - Figure 7.96). The increased accelerated velocity over runback ice shape 1 allowed for a larger suction peak. The geometry characteristics for runback ice shape 1 allowed for the flow to remain separated for a very short length. The position of reattachment from the separation point of the ice shape was only 2mm. The reason for the short length of detached flow

was due to the ice profile after the point of maximum height. This position where detachment occurred was followed by a smooth gradient which reduced in height. This behaviour was not observed for runback ice shape 2 and 3 which displayed larger separated regions due to more aggressive height changes to the ice shape profile. The point of reattachment for runback ice shape 2 and 3 was 27.5mm and 24.3mm respectively. The velocity difference between runback ice shape 2 and 3 was only 1.63ms^{-1}; ice shapes 2 and 3 appeared to share many similarities.

The observed variation in pressure recovery for runback ice shape 1 relative to runback ice shape 2 and 3 was attributed to length of the recirculation zone.

The flow was considered turbulent close to the point of separation; at the maximum height of each runback ice shape. This turbulence allowed further entrainment of the boundary layer which helped the flow to reattach. The geometric features of runback ice 1 shape were more streamline and lacked the aggressive step in height. The consequence was a smaller wake region. These small variations observed for runback ice shape 1 facilitated a smaller aerodynamic penalty relative to runback ice shape 2 and 3.

The leading edge temperature variation for all runback ice shapes was minimal. A small variation for runback ice shape 1 was observed at 0.034x/c accounted for by the different separated zone lengths. The heat transfer coefficient (HTC) profile around the runback ice shape is shown in Figure 7.98.

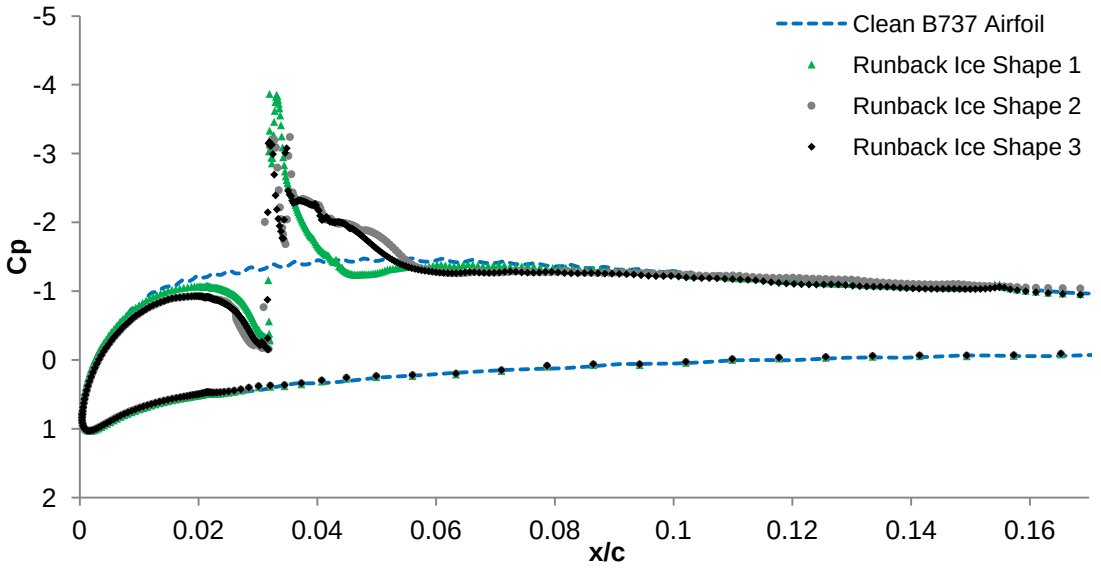

Figure 7.93: Pressure Coefficient Profile for Anti-Icing Optimisation Datum Runback Ice Shapes

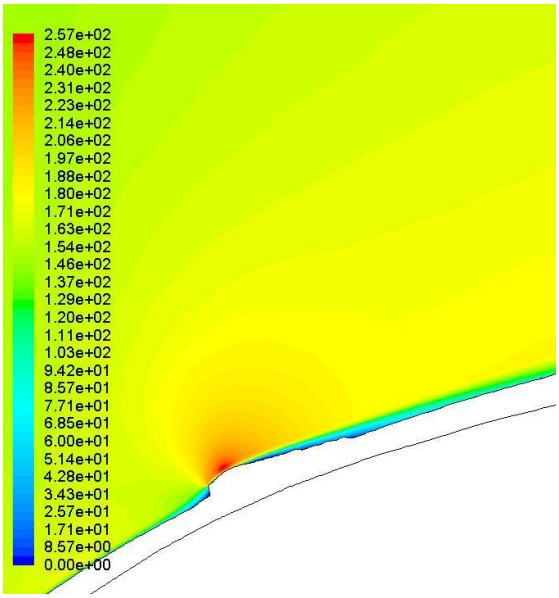

Figure 7.94: Velocity Magnitude Contour Plot for Anti Icing Optimisation Runback Ice Shape 1

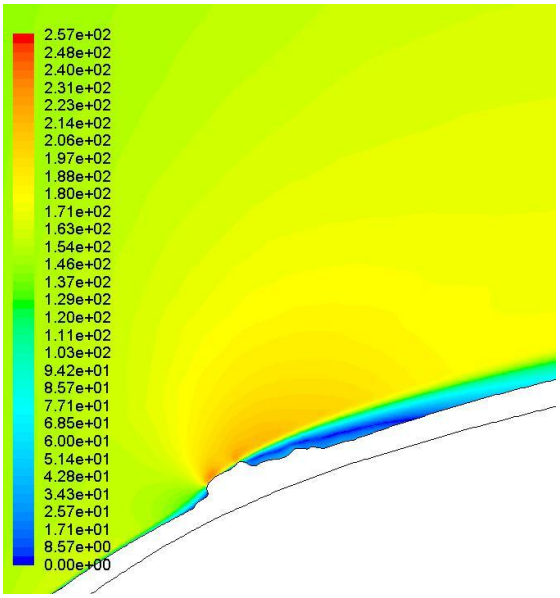

Figure 7.95: Velocity Magnitude Contour Plot for Anti Icing Optimisation Runback Ice Shape 2

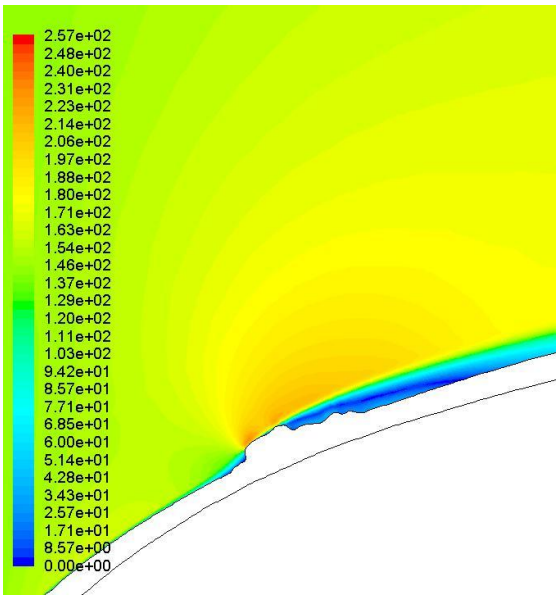

Figure 7.96: Velocity Magnitude Contour Plot for Anti Icing Optimisation Runback Ice Shape 3

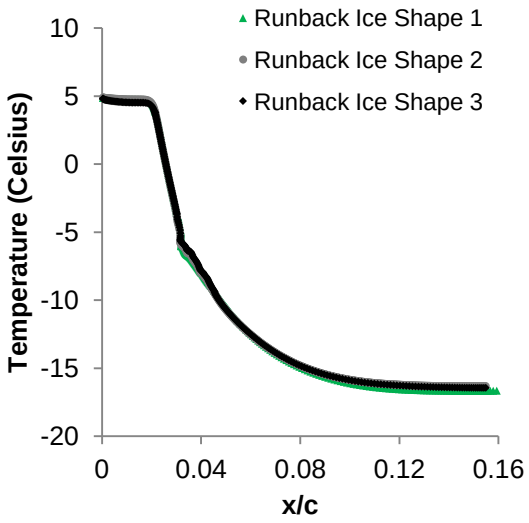

Figure 7.97: Leading Edge Temperature Profile for Anti-Icing Optimisation Datum Runback Ice Shapes

The dimensionless temperature (T^+) used for the datum runs was 23.5.

The HTC around the leading edge (heated zone up to 0.0215x/c) was most prominent. This was expected as the total heat flux across the leading edge produced the largest temperature differential. The local velocity variations for all three runback ice shapes up to the ice shape allowed for a variation in the heat transfer coefficient profile. The point of separated flow showed a large increase in heat transfer followed by significant reduction in the heat transfer coefficient where flow reattachment occurs. At this point the temperature difference

between the airfoil surface and fluid temperature was minimal and thus heat flux was significantly reduced. By 0.1x/c the heat transfer coefficient was zero. The leading edge temperature and consequently the dimensionless reference temperature were fixed for all three datum ice shape runs, the variation in area-weighted average surface heat transfer coefficient shown in Table 7.22 were very similar.

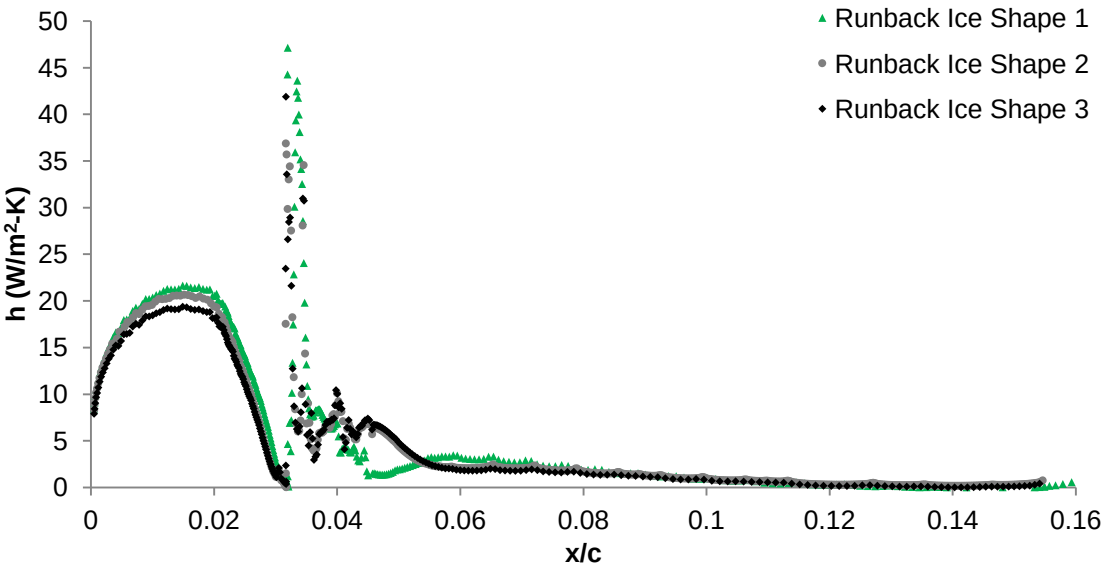

Figure 7.98: Heat Transfer Coefficient Profile for Anti-Icing Optimisation Datum Runback Ice Shapes

	Area-Weighted Average Surface Heat Transfer Coefficient (W/m^2-K)
Ice Shape 1	0.766
Ice Shape 2	0.733
Ice Shape 3	0.706

Table 7.22: Area-Weighted Average Surface Heat Transfer Coefficient for Datum Runback Ice Shapes

The Nusselt Number is the ratio of convective to conductive heat transfer.

$$Nu = \frac{convective\ heat\ transfer}{conductive\ heat\ transfer} = \frac{hL}{k_f}$$

Equation 7.11: Nusselt Number

Where

L =Chord Length (m)

k_f = thermal conductivity of the fluid (W.m^{-1}.K^{-1})

h = heat transfer coefficient (W.m^{-2}.K^{-1})

Comparison of the Nusselt Number profile in Figure 7.99 highlights the dominant local heat transfer process. High values indicated the convective heat transfer process was dominant. The variations observed from the heat transfer coefficient profile graph in Figure 7.98 was again seen for the Nusselt number profile as the thermal conductivity and chord length were fixed.

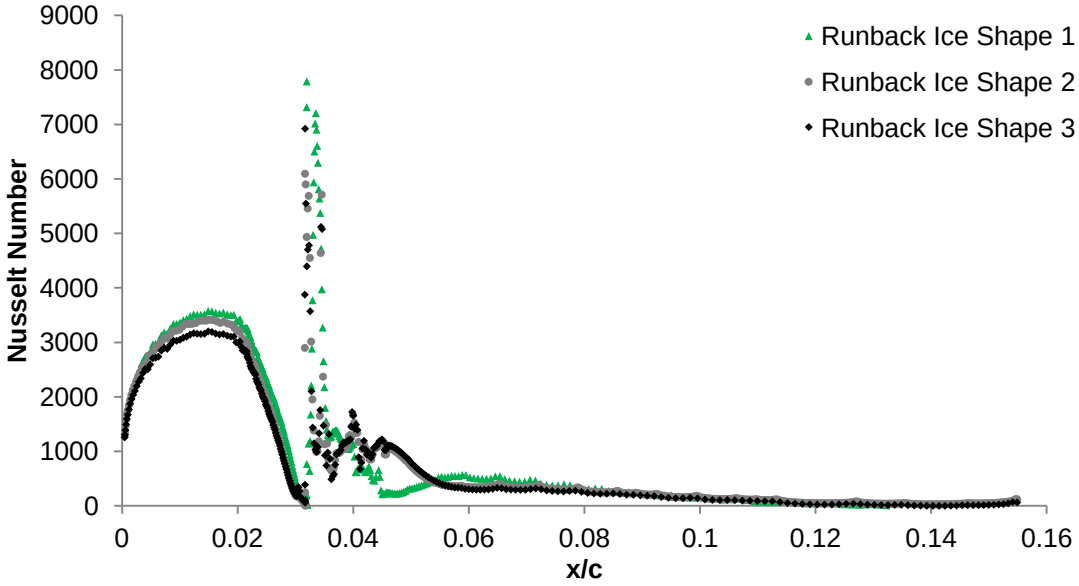

Figure 7.99: Nusselt Number Profile for Anti-Icing Optimisation Datum Runback Ice Shapes

7.4.5. Optimiser Results

The total number of CFD steps was 1259. Four Pareto-optimum leading temperature values were found.

The optimiser progress output data is shown in Figure 7.100. The number of intensification, diversification and step size reduction steps after 1259 CFD steps were 18, 16 and 13 respectively.

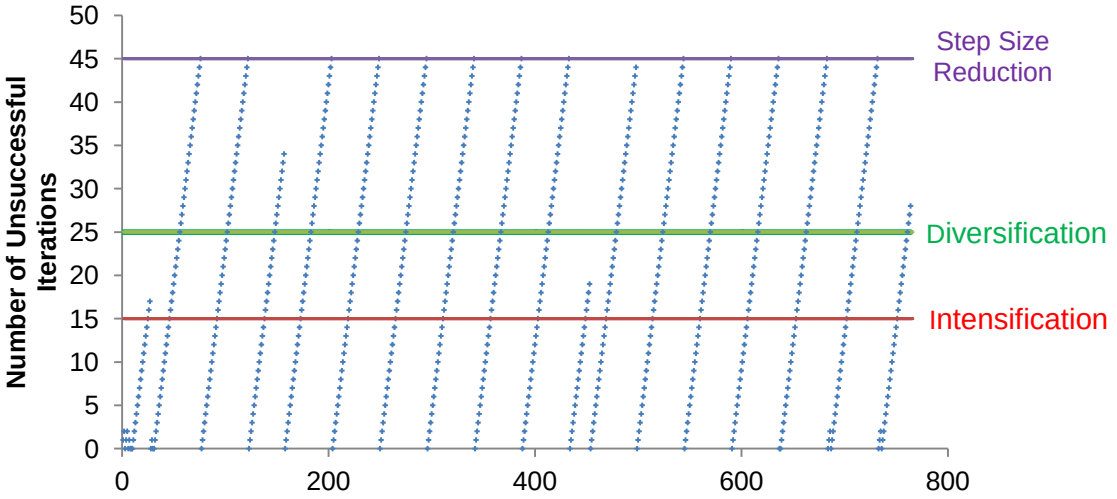

Figure 7.100: Anti Icing Optimisation History

The three-dimensional scatter plot in Figure 7.101 shows the optimiser progress for all three objectives.

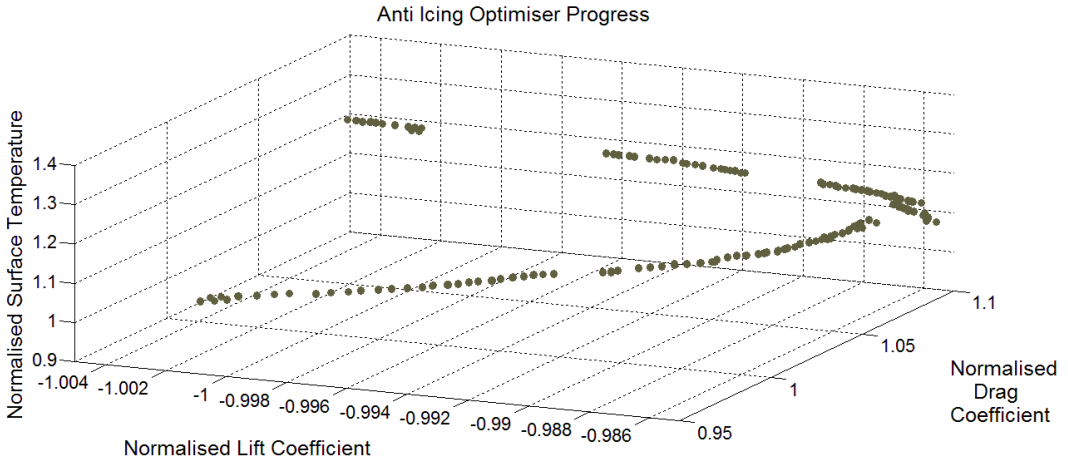

Figure 7.101: Three-Dimensional Representation for Optimiser Results

Similar to the ice location optimisation study in Chapter 7.1 improved lift coefficient designs vectors were accompanied with the improved drag coefficient. The same results are found for this optimisation study.

Figure 7.102 shows the drag coefficient against leading edge temperature. The feasible design vectors, Pareto-optimum and selected test cases are shown. The test cases were selected based on a sensitivity analysis in which the sudden variations in lift and drag were observed. Increasing leading edge surface temperature did not produce significant variations from the observed trend.

A similar relationship was observed between lift and drag coefficients as seen in the Ice Location Optimisation Study (Figure 7.103). The optimiser history did not portray a single optimisation path but a number of paths. The observed step changes highlighted with sensitivity test cases 2, 3, 4, 5 and 8 did not follow the main lift and drag trend.

In Figure 7.104 the leading edge temperature beyond 8.2° Celsius showed significant step variations which deviated from the expected trend. Since the leading edge temperature dictated the ice location formation, the improved design vectors all produced a lower leading edge temperature. However with increasing ice location along the chord (increasing heat input) these abrupt changes in the lift coefficient were observed for the highlighted test cases. Once again test cases 2, 3, 4, 5 and 8 did not fit the observed trend.

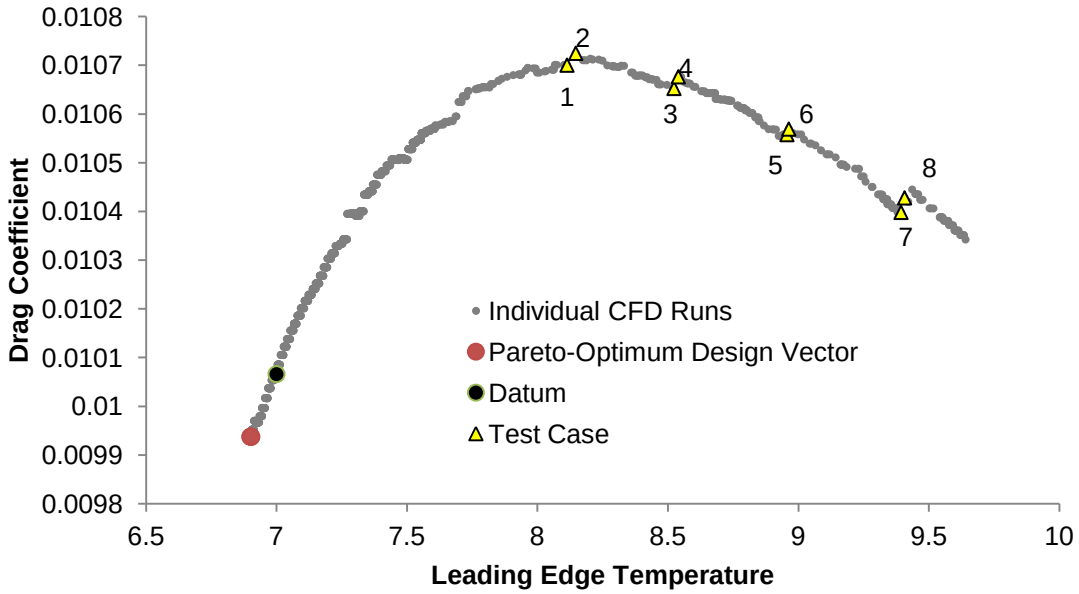

Figure 7.102: Drag Coefficient against Leading Edge Temperature for Anti-Icing Optimisation Study

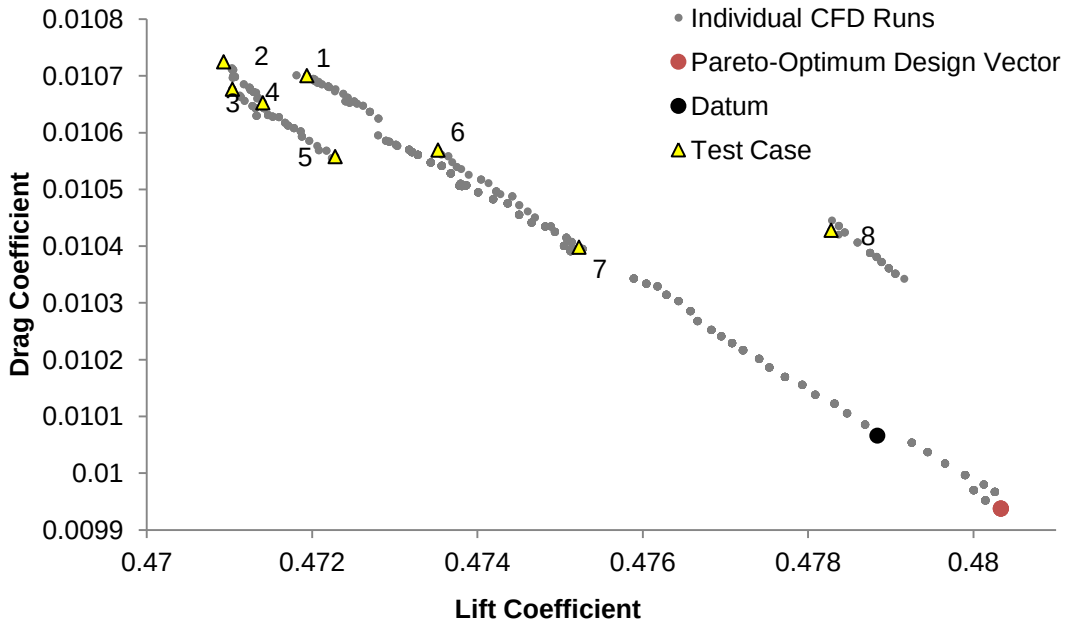

Figure 7.103: Drag Coefficient against Lift Coefficient for Anti-Icing Optimisation Study

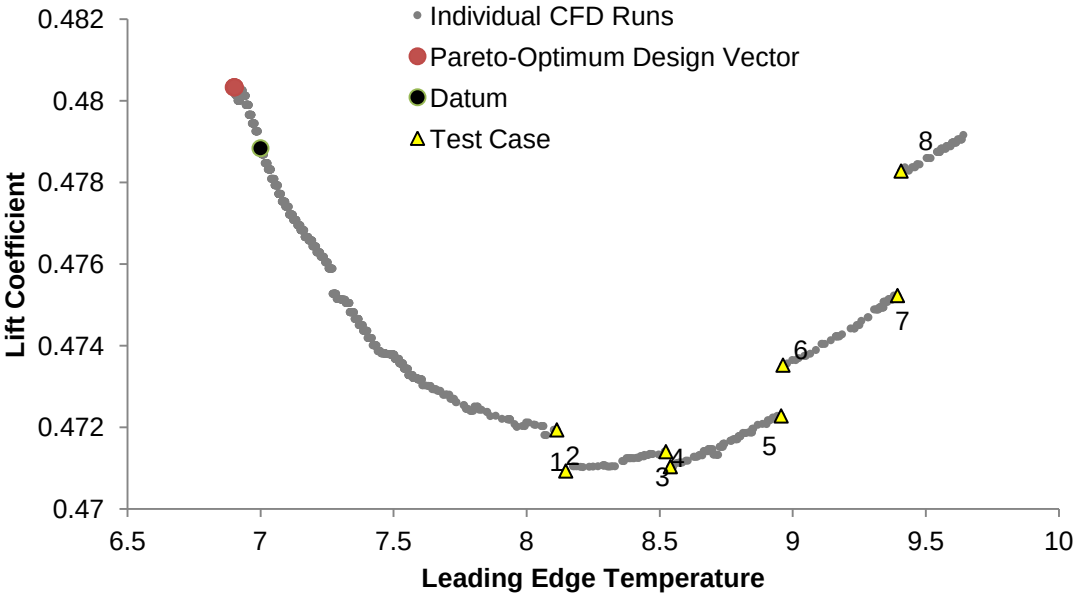

Figure 7.104: Lift Coefficient against Leading Edge Temperature for Anti-Icing Optimisation Study

The Pareto-optimum design vectors are shown in Table 7.23. The range in leading edge temperature for the four Pareto-optimum design vectors was 0.165°C. The number of step size reductions was thirteen which allowed for small steps for each design vector (leading edge temperature). As a result the small variation between the Pareto-optimum designs was expected. Variation in lift and drag coefficients was of the order of 10^{-5} and 10^{-4} respectively. As observed in Chapter 7.1, the Pareto-optimum location can be considered as a

single design vector since the variation was very small. The average leading edge temperature from the four Pareto-optimum design vectors was 1.095°C. The extensive search by the optimiser of the design space provided Pareto-optimum designs in close proximity which indicated the robustness of the MOTS algorithm.

Pareto-Optimum Case	Lift Costs	Drag Costs	Heat Costs	Lift Coefficient	Drag Coefficient	Leading Edge Temperature (°C)
1	-1.00312	0.987236	0.985632	0.48	0.010	1.004
2	-1.00312	0.987233	0.985861	0.48	0.010	1.067
3	-1.00312	0.98723	0.98612	0.48	0.010	1.139
4	-1.00312	0.987227	0.986227	0.48	0.010	1.169

Table 7.23: Pareto-Optimal Results for Anti-Icing Optimisation Study

The average lift and drag coefficient values for the three runback ice shapes was used to calculate the improvements found in lift and drag coefficients. The averaged lift and drag coefficient improvements over the datum leading edge temperature input was 0.15% and 0.45% respectively. The individual lift and drag coefficients for the datum and optimum runs are shown in Figure 7.105 and Figure 7.106. Runback ice shapes 1 and 3 for the optimum run produced improvements for lift and drag coefficient. Optimum runback ice shape 2 produced slightly higher performance costs relative to the datum.

The force coefficient performance for each runback ice shape showed slight variations. All three runback ice shapes were considered realistic in size and shape formation for the conditions stated in Table 7.20. By considering the mean of all three ice shapes when normalising the costs provided a more accurate estimate on the performance gains and losses.

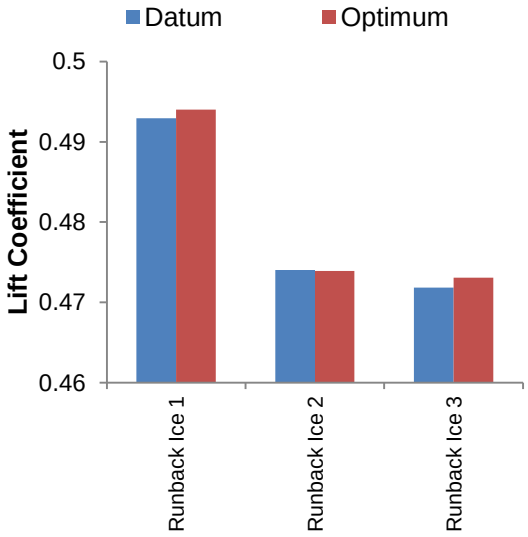

Figure 7.105: Lift Coefficient Comparison for Anti-Icing Optimiser Datum and Optimum Runs

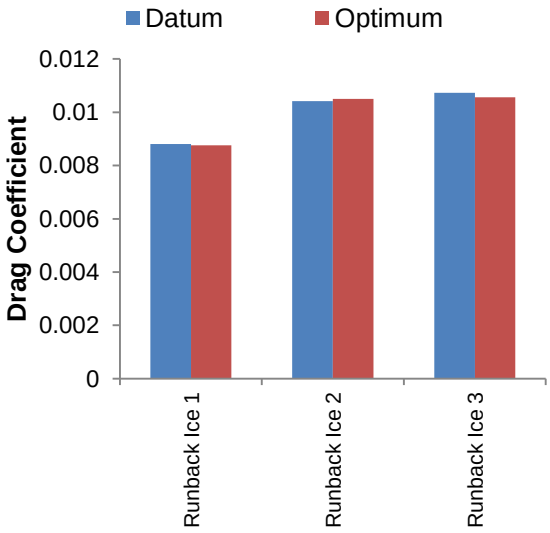

Figure 7.106: Drag Coefficient Comparison for Anti-Icing Optimiser Datum and Optimum Runs

The heat transfer and pressure coefficient comparison for the datum and optimum runs for runback ice shape 1 are shown in Figure 7.107 and Figure 7.108. The leading edge temperature for the optimum and datum runback ice shape was 1.095°C and 5.0°C respectively. Consequently the heat flux across the leading edge surface for the optimum run was lower. As a result, the chord location at which the surface temperature reached zero was reduced and ice formations occurred closer to the airfoil leading edge. This variation can be seen in Figure 7.108 where the suction peak (local maximum velocity over the ice shape) was shifted towards the leading edge. The optimum runback ice chord location was 17.4mm closer to the leading edge relative to the datum ice chord location. Figure 7.109 through to Figure 7.112 compare the datum and optimum heat transfer coefficient profiles as well as the pressure coefficient profiles for runback ice shape 2 and 3. The heat transfer coefficient characteristics for runback ice shape 2 and 3 were similar to runback ice shape 1; lower heat transfer observed at the leading edge due to lower leading edge temperature input. Apart from the location difference, the pressure coefficient profiles showed no significant variation.

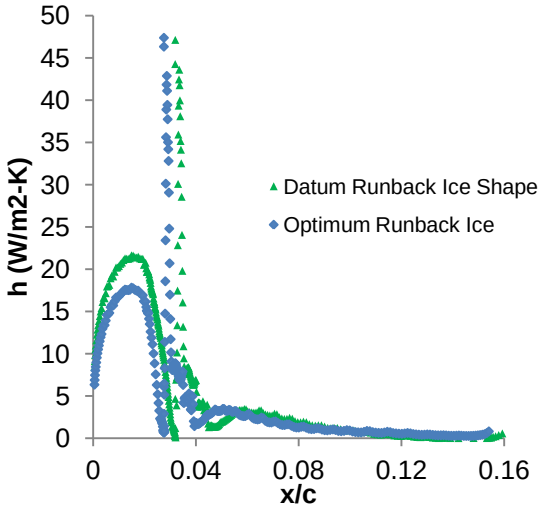

Figure 7.107: Heat Transfer Coefficient Profile Comparison for Runback Ice Shape 1

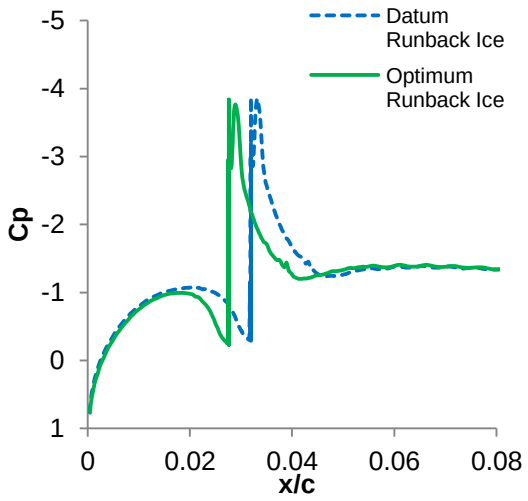

Figure 7.108: Pressure Coefficient Profile Comparison for Runback Ice Shape 1

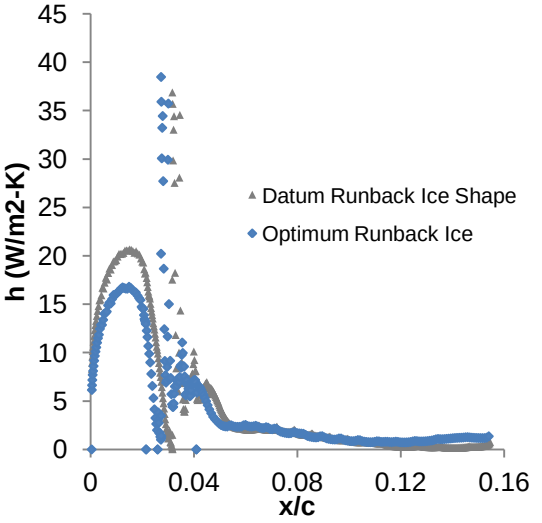

Figure 7.109: Heat Transfer Coefficient Profile Comparison for Runback Ice Shape 2

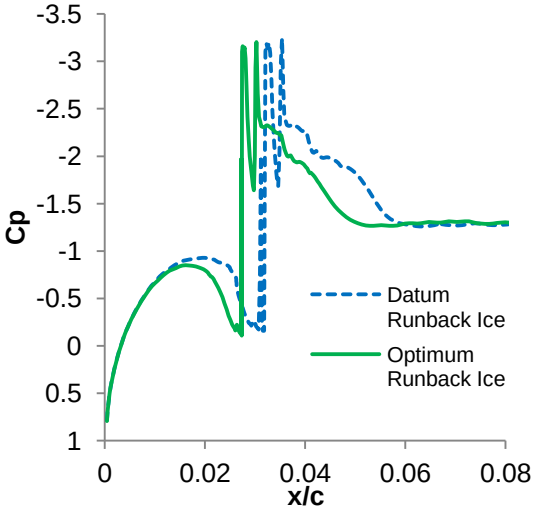

Figure 7.110: Pressure Coefficient Profile Comparison for Runback Ice Shape 2

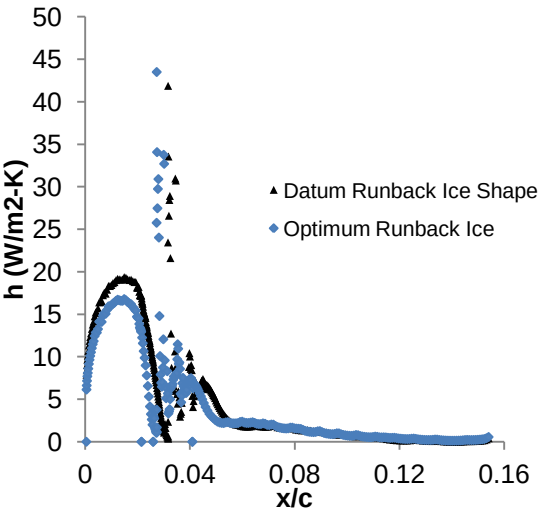

Figure 7.111: Heat Transfer Coefficient Profile Comparison for Runback Ice Shape 3

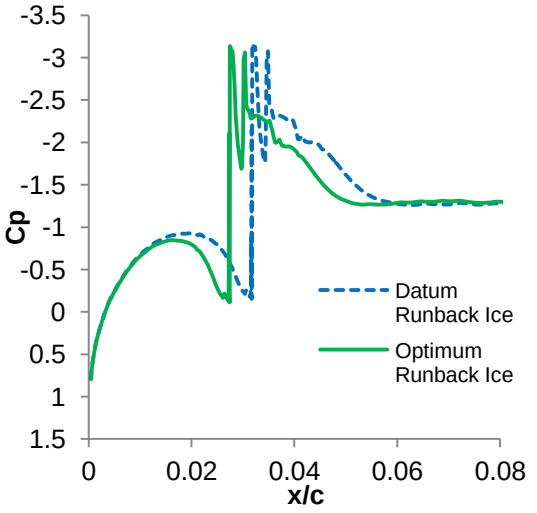

Figure 7.112: Pressure Coefficient Profile Comparison for Runback Ice Shape 3

7.4.6. Test Case Analysis

The four abrupt changes highlighted in Figure 7.103 were analysed. Eight CFD runs were conducted (Test Case 1-8) to investigate the lift coefficient step changes.

The largest lift coefficient variation was observed between test cases 7 and 8. For a 0.534°C leading edge temperature change, the lift coefficient varied by 0.64%. The actual lift coefficient variation with respect to the step change for normalised costs was small. The largest lift coefficient variation was not proportional to leading edge temperature variation. Test case 1 and 2 had the largest leading edge temperature variation at 1.33°C. For the 8 selected cases, no relationship between leading edge temperature variation and force coefficient was found.

No conclusive trends were found for the lift coefficient sensitivity. However the lift coefficient was found to be sensitive between the normalised surface temperatures of 1.15 and 1.35. The initial step observed at test case 1 and 2 was attributed to the runback ice height comparable to the size of the boundary layer thickness. The step observed at test case 3 and 4 was considered very small.

7.4.7. Summary

Successful multi-point optimisation for three objectives and one variable was accomplished. The optimiser global search of the design space found optimum leading edge temperatures where lift was maximised and drag minimised.

The overall trends found for the normalised lift and drag history were similar to the ice location optimisation study. The heat input dictated the ice formation chord location and found the locations closer to the leading edge to be aerodynamically favourable.

Four Pareto-optimum runs were found. All four runs were effectively considered as a single heat input with a range of 0.165°C. The average heat input value for the Pareto-optimum runs was 1.095°C. This was 3.905°C lower than the datum run.
The improvements found for averaged lift and drag coefficients relative to the datum were 0.15% and 0.45% respectively. Rising leading edge temperature did not provide improvements for lift or drag coefficients.

The abrupt variation for lift and drag in Ice Location Optimisation study was also observed for this optimisation study. However this trend was subject to

increasing heat input which in turn was directly related to increasing chord location for ice formation. Overall lower leading edge surface temperature yields improved lift and drag coefficients.

A second sensitivity study was conducted using 8 test cases to further understand the mechanism for the abrupt variation with leading edge temperature and thus chord location for ice formation. No conclusive difference was observed when comparing test case 1 and 2, 3 and 4, 5 and 6 or 7 and 8.

Alègre, [104] performed experimental investigations on the limit of the heated zone in combination with leading edge surface temperature increases. This provided an excellent basis on which to consider the Pareto-optimum results relative to the datum position and its influence in realistic icing conditions. The geometrical variations observed were parameterised as shown in Figure 7.113.

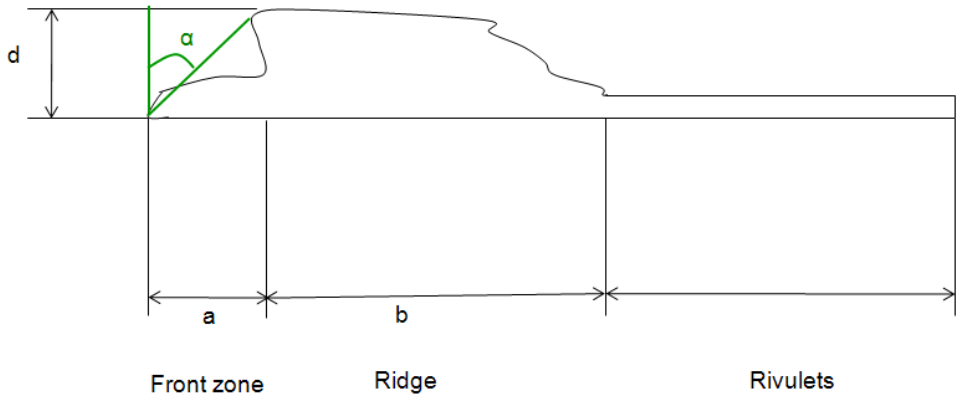

Figure 7.113: Ice Tracing Technique Courtesy of [104]

The influence on the reduced limits (position where leading edge heating element is stopped) of the heated zone and lower leading edge temperature combined lead to the following observation:

- The mass of ice was increased
- The length between the end of the heated zone and the ice shape was decreased
- The geometric features for length between the front of the ice shape and ridge section (a) and angle between surface normal and front of ice shape (α) decreased.

The key geometrical change to the ice shapes with decreasing heat input and limit of heated zone was the reduction of angle α. Another interesting finding

was the peak height, d, does not vary with changing heat input. This feature was more extensively observed when the limit of the heated zone was set to 0.086m, which was also the datum condition used throughout this study.

To change the shape of the runback ice with increasing heat input to better represent a shape typical of the runback ice shape at a given chord location was beyond the scope of this study. However it was appropriate to consider how this may have affected the overall results.

The Runback Ice Structure Detail Analysis in Chapter 5.5 found that the steep ridge ice shapes (large angle α) had a more profound effect on performance relative to the realistic runback ice shape which had a much lower angle α. This relationship was also observed for runback ice investigations from Lee & Bragg, [110] & Lee, et al., [125] where they considered different simplistic ice shapes for their aerodynamic effects. Four ice shapes were considered as shown in Figure 7.114.

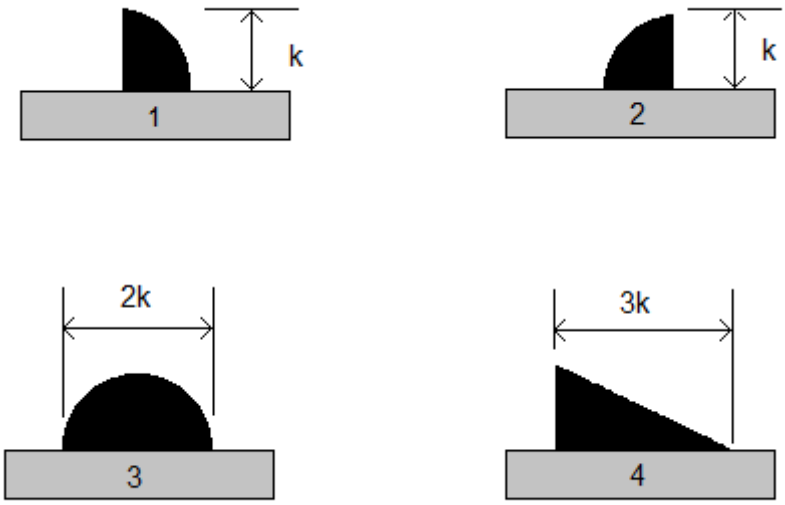

Figure 7.114: Simplistic Ice Shapes [110]

They found shape 3 allowed for greater C_{lmax}. Blunt shapes 1 and 4 produced a lower C_{lmax}. However it was noted the performance variation between the two blunt shapes was very small. These same trends were observed for the Runback Ice Structure Detail Analysis in Chapter 5.5.

With increasing heat input the experimental data suggested the runback ice shape geometric features were more akin to the ridge ice shapes where the angle (α) between the surface and peak height increased. Numerical analysis on the performance effects of ridge ice had shown larger performance losses.

Experimental studies by Lee & Bragg, [110] also agreed with these geometrical performance trends.

This anti-icing optimisation study found Pareto-optimum locations at lower leading edge surface temperatures. Experimental results suggest ice formation closer to the leading edge form ice profiles which were aerodynamically more favourable. Therefore it was reasonable to assume that general tends observed for this study, and by extension the ice location optimisation study, may become more pronounced if the suggestions on geometrical profile of ice formation from Alègre, [104] with changing heat inputs was applied.

However caution must be applied when considering runback ice formation close to the leading edge. The experimental studies by Alègre [104] also found that a combination of lower leading edge temperatures and lower limit heated zones were more susceptible to the development of horns more typically seen with leading edge ice formation. It was observed that the lower heat input runs were very sensitive to the level of Liquid Water Content (LWC) where small increases lead to large features forming into the direction of the flow (circled in Figure 7.115). This in turn led to a number of these features joining up to form a significant ridge-like feature (Figure 7.116).

Figure 7.115: Experimental Runback Ice Feature Formation Courtesy of [104]

Figure 7.116: Experimental Ridge Ice Formation Courtesy of [1]

8. Conclusions and Future Work

"What we find changes who we become."

- Peter Morville

8.1. Conclusions

The objectives of this PhD were to provide an aerodynamic study on full-scale runback ice performance effects. The sponsors, Airbus and Cranfield University collaboratively identified these aims as a result of the successful creation and capture of full-scale runback ice by [1] at the Cranfield Icing Tunnel. The new focus was therefore proposed, namely an evaluation of the aerodynamic impact using computational fluid dynamics and multi-objective Tabu Search optimisation.

In this research a single hex-core hybrid mesh was created from an ANSYS ICEMCFD script. This mesh script served a dual purpose of assisting the process of optimisation and validation.

The intial CFD process analysed three separate studies with differing airfoils. The three studies examined were for a B737-700 [1], B737-200ADV [102] and NACA 23012 [30]. The first two studies were in cruise configuration and the third simulated forward-facing quarter-round ridge ice.

Following code validation, the B737-700 airfoil was considered for a clean configuration and one with ridge ice. The aerodynamic effects due to realistic runback ice at the experimental chord location were also assessed. Although a full comparison with published data was not possible, the general losses in lift and increase of drag were reasonable based on factors such as the angle of attack, height of the runback ice with respect to chord length and the streamline nature of leading edge relative to forward-facing quarter-round simple blunt shapes.

Analysis of geometrical features based on high-fidelity two-dimensional runback ice profiles was performed. Findings revealed a significant variation in force coefficient and flowfield properties between the realistic runback ice and forward-facing quarter-round ridge ice. These findings supported the trends identified by [10] on blunt and streamline ridge ice.

In the Cranfield University atmospheric boundary layer wind tunnel, experimental testing was conducted on realistic runback ice shapes via indirect

methods and comparisons were made against the numerical results for the Shear Stress Transport $k-\omega$ and Spalart-Allmaras turbulence models.

Good agreement with experimental measurements was found despite systematic spanwise variation. The boundary layer profile comparison showed good agreement. The drag coefficient was slightly under predicted by the numerical solver and this was possibly due to lack of roughness parameters.

In summary the following results have been achieved:

a) Setup a CFD optimisation framework for multi-objective optimisation.
b) Carried out an initial set of CFD evaluations for NACA series airfoils with and without ridge ice which proved in good agreement with previous experimental and computational findings using other turbulence models.
c) Compared CFD with new experimental data for real runback ice shapes in a flat plate boundary layer which showed that CFD could capture details of the flow velocity profile development and overall drag changes.
d) Performed a first series of CFD capabilities for runback ice shapes found on a B737 wing profile.
e) Setup and ran four optimisation cases using MOTS which all demonstrated good results for highly constrained aerodynamic problems as discussed next.

Ice Location Optimisation

The first goal of this investigation was to provide useful information to Airbus on aerodynamic penalties associated with subtle changes to chord location of ice formation. These findings allowed refinement of the anti-icing system. The second objective was to considered interactions between boundary layer thickness and ice accretion heights; a phenomenon that has yet to be fully explained. Findings from numerous studies consider generic shapes ten to twenty times taller than the boundary layer thickness and do not observe these intricate interactions with boundary layer. Later studies on boundary layer scaling techniques showed the difference between the two scaling methods was significant. The four primary findings of the ice location optimisation are outlined below:

- All optimum locations were located in close proximity to the leading edge of the airfoil relative to the datum position and at the limit of the optimisation design space. This was not the observed trend from the surveyed literature. However comparison with literature for study was not available. Published results compare the loss in C_{lmax} and reduction in stall angle. Since this was an ice location optimisation study with

sponsors keen to investigate the EASA 45 minute hold case, C_{lmax} and stall conditions were not investigated.

- All Pareto-optimal locations were in very close proximity. These optimum locations were all located before the suction peak. This highlighted the robustness of the MOTS code and its ability to effectively search the design space.
- Suction surface maximum velocities reduced with increasing chord ice location reducing lift and possible promotion of early trailing edge separation at higher angles of attack.
- Lift and Drag trends were not observed after chord location reached 6% although some relationships were found to still hold up to 12% chord location. These observed discrepancies were due to boundary layer thickness becoming larger than ice height. The flowfield changes due to the transition of boundary layer height and ice height require further investigation.

Shape Optimisation for Fixed Ice Location

The focus here was to consider robust implementation of shape optimisation using FFD and best practises for constraint handling. The two core considerations for the shape optimisation at a fixed ice location are:

- Successful integration of the free-form deformation geometry modeller was accomplished. The results highlighted that some more stringent requirements for geometry constraints handling was required for shape optimisation
- Lower surface modification for optimum lift coefficient profile showed similar trends in design space to published data [43]

Representative Tail Plane Optimisation

The Sponsors were the main force behind the examination of vertical tail plane shape optimisation. A crucial assessment in this examination was whether the clean airfoil performance remained unaffected and the iced airfoil performed better compared to the datum design. The moment force was additionally considered. This was a single objective shape optimisation on NACA 0012 symmetrical airfoil with ice accretion on both surfaces. The five outcomes of representative tail plane optimisation are:

- Drag coefficient improvements for both clean and iced configurations of 1.64 and 3.1% respectively were achieved.
- Leading edge suction peak moved aft relative to datum NACA 0012 airfoil.

- Less aggressive pressure recover region was observed for optimum airfoil profile
- Maximum local velocity drop over iced optimum airfoil configuration was 6.32ms^{-1}
- Clean performance was not compromised

Anti Icing Optimisation

The primary objective for the sponsors was to reduce dependence on heat input and consider the strategic placement of more modern anti-icing systems such as heated mats. In order to meet that objective, a more complete runback ice optimisation was required. This more complete design comprised a multipoint optimisation code with 3 objectives and 1 variable; Minimise leading edge temperature output, maximise lift and minimise drag with a variable heat input.

The four key findings of the anti icing optimisation showed:

- Lift and drag costs optimiser results against heat input show trends observed in ice location optimisation.
- Heat input dictated runback ice chord location
- Favourable locations again found closer to the leading edge
- Increasing leading edge temperature did not yield improvements for lift or drag coefficients.

8.2. Recommendations and Future Work

1. Modification to the range of variability for ice location study to consider how observed trends with ice location may develop.
2. Align work more closely with known literature by increasing runback ice height and considering the worst case scenario runback ice shapes observed by Alègre, [1].
3. Turbulence model evaluation using LES/RANS hybrid for accurate prediction of separated region and reattachment positions associated with icing.
4. Further investigation using CFD on the stall characteristics of optimised airfoils
5. The anti icing study was set up to work in a segregated fashion. The design variable (leading edge heat input) allowed for an initial simulation to determine the location where surface temperatures reached freezing which defined the location for runback ice formation. This allowed a second CFD run to consider the aerodynamic penalties with runback ice. A more complete study would incorporate an icing code to dictate the

runback ice location and shape formation. Aerodynamic testing could then be conducted. Incorporation of the icing code would not be an issue with the current MOTS setup.

6. Experimental data on roughness parameters could provide some additional data for numerical comparison. The method available in ANSYS FLUENT for roughness modelling requires the cell adjacent to the wall to be larger than the roughness modelled. This would reduce the number of cells within the critical boundary layer and subsequent separated region for runback ice. Although it should be noted that the correct treatment for real roughness maybe very different to the sand grain model usually employed.
7. Two-dimensional optimum results compared with flowfield results based on a three-dimensional swept wing. Literature survey suggested the unsteady three-dimensional nature of the vortex due to flow separation is a flaw in two-dimensional RANS modelling. This was apparent at high angles of attack with large regions of separated flow. Comparison of datum and optimum results using high-fidelity three-dimensional simulations would be ideal.
8. Consider extension from cruise configuration airfoil to deployed high-lift profiles.
9. Boundary layer scaling method for optimisation of NACA tail optimisation. A second optimisation run using runback ice shapes scaled based on boundary layer thickness would provide additional information on how the two scaling method interact with the boundary layer, changing flowfield characteristics, and their effect on force coefficients.
10. The need for more accurate experimental data using the Boeing 747 airfoil with realistic runback ice.
11. Aerodynamic wind tunnel testing of representative full-scale runback ice shapes on a sectioned full-scale swept wing. This would complete the years of commitment by Cranfield University on the issue for ice accretion, particularly runback ice.

Bibliography

1. Alègre, N.: Full-scale runback ice: accretion and aerodynamic study. PhD Thesis, Cranfield (2009)
2. Lankford, T. T.: The Physics of Icing. In : Aircraft Icing: A Pilot's Guide to Supercooled Drizzle Droplets, Icing Accident Case Studies and Cold Weather Techniques. MCGraw-Hill Companies, New York, USA (2000) 1-48
3. Papadikas, M., Yeong, H., Wong, S.: Aerodynamic Performance of a Swept Wing with Simulated Ice Shapes., Reno, Nevada (2004)
4. Almendaroglu, N., Feo, A., Gent, W., Golia, C., Guffond, D., Hammond, D. W., Van Hengest, J., Kind, R., Meyer, S.: Ice Accretion Simulations. AGARD Paper AR 1997 (1997)
5. Jacobs, E.: Airfoil Section Characteristics as Affected by Protuberances. National Advisory Committee for Aeronautics Paper Report 446 (1934)
6. Thoren, R.: Icing Flight Tests on the Lockheed P2V. ASME Paper No. 48-SA-41 (1948)
7. Bowden, J.: Preliminary Investigation of Cyclic De-Icing of an Airfoil Using an External Electric Heater. National Advisory Committee for Aeronautics Paper RM E51J30 (1952)
8. Gray, V. H., von Glahn, U. H.: Effects of Ice and Frost Formations on Drag of NACA 65B1B-212 Airfoil for Various Modes of Thermal Ice Protection. National Advisory Committee for Aeronautics Paper TN-2962 (1953)
9. Calay, R. K., Holdo, A. E., Mayman, P.: Experimental Simulation of Runback Ice. Journal of Aircraft 34(2), 206-212 (1997)
10. Lee, S., Bragg, M. B.: Effects of Simulated-Spanwise-Ice Shapes on Airfoils: Experimental Investigation., Reno, Navada (1999a)
11. Broeren, A., Bragg, M.: Effects of Airfoil Geometry on Performance with Simulated Intercycle Ice Accretions. AIAA Paper 2003-728 (2003)
12. Broeren, A. P., Addy, H. E. ., Bragg, M. B.: Effects of Intercycle Ice Accretions on Airfoil Performance. AIAA Paper 2002-0240 (2002)
13. Morgan, H. L., Ferris, J. C., McGhee, R. J.: A Study of High-Lift Airfoils in the Langley Low-Turbulence Pressure Tunnel. NACA Paper TM 89125 (1987)
14. Andy, H. E., Chung, J. J.: A Wind Tunnel Study of Icing Effects on a Natural Laminar FLow Airfoil. AIAA Paper 2000-0095 (2000)
15. Lyncha, F. T., Khodadoust, A.: Effects of Ice Accretions on Aircraft Aerodynamics. Progress in Aerospace Sciences 37(8), 669-767 (2001)
16. Whalen, E. A., Broeren, A. P., Bragg, M. B., Lee, S.: Characteristics of

Runback Ice Accretions on Airfoils and Their Aerodynamic Effects. AIAA Paper 2005-1065 43rd Aerospace Science Meeting and Exhibit (2005)

17. Lee, S., Bragg, M. B.: Experimental Investigation of Simulated Large-Droplet Ice Shapes on Airfoil Aerodynamics. Journal of Aircraft 36(5), 844-850 (1999b)
18. Bragg, M. B., Broeren, A., Addy, H., Potapczuk, M., Guffond, D., Montreuil, E.: Airfoil Ice Accretion Aerodynamics Simulations. AIAA 45th Aerospace Sciences Meeting and Exhibit 2 (2007)
19. Bragg, M. B., Broeren, A. P., Blumenthal, L. A.: Iced Airfoil Aerodynamics. Progress in Aerospace Sciences 41, 323-362 (2005)
20. Diebold, J. M., Monastero, M. C., Bragg, M. B.: Aerodynamics of a Swept-Wing with Ice Accretion at Low Reynolds Number. AIAA Paper 2012-2795 (2012)
21. Broeren, A., Whalen, E. A., Busch, G. T., Bragg, M. B.: Aerodynamic Simulation of Runback Ice Accretion. Journal of Aircraft 47(3), 924-939 (2010)
22. Broeren, A. P., Bragg, M. B., Addy, H. E., Lee, S., Moens, F., Guffond, D. : Effect of High-Fidelity Ice Accretion Simulations on the Performance of a Full-Scale Airfoil Model. AIAA Paper 2008-0434 (2008)
23. Whalen, E. A., Broeren, A. P., Bragg, M. B.: Aerodynamics of Scaled Runback Ice Accretions. Journal of Aircraft 45(2), 591-603 (2008)
24. Lee, S., Bragg, M. B.: Investigation of Factors that Influence Iced Airfoil Aerodynamics. Journal of Aircraft 40(3), 499-508 (2003)
25. Potapczuk, M. G., Gerhart, P. M.: Prediction of Aerodynamic Penalties caused by Ice Formation on Various Airfoils., Reno, Nevada, USA (1985)
26. Dunn, T. A., Loth, E., Bragg, M. B.: Computational Investigation of Simulated Large-Droplet Ice Shapes on Airfoil Aerodynamics. Journal of Aircraft 33(5), 863-843 (1999)
27. Lee, S., Dunn, T., Gurbacki, H., Bragg, M. B.: An Experimental and Computational Investigation of Spanwise-Step-Ice Shapes on Airfoil Aerodynamics. AIAA Paper 98-0490 (1998)
28. Pan, J., Loth, E., Bragg, M.: RANS Simulation of Airfoils with Ice Shapes. AIAA Paper 2003-729 (2003)
29. Pan, J., Loth, E.: Detached Eddy Simulations for Iced Airfoils. Journal of Aircraft 42(6), 1452-1461 (2005)
30. Marques, S., Badcock, K. J.: Validation Study for Prediction of Iced Aerofoil Aerodynamics. The Aeronautical Journal: Royal Aeronautical Society 114(1152) (2010)
31. Gedebusch, J. A.: Computational 3-D Icing Results for Scaled DLW-F6

Geometry. AIAA Paper 2012-4653 (2012)

32. Papadakis, M., Strong, P. R., Wong, S. E., Wong, S. H.: Simulation of Residual and Intercycle Ice Shapes using Step Ice and Roughness. AIAA Paper 2012-2796 (2012)
33. Wong, S.-H., Papadakis, M., Wong, S.-C.: CFD Analysis of a Wing with a Bleed Air Ice Protection System. AIAA Paper 2013-2935 (2013)
34. Broeren, A. P., Potapczuk, M. G.: Swept-Wing Ice Accretion Characterization and Aerodynamics. AIAA Paper 2013-2824 (2013)
35. Deibold, J. M., Broeren, A. P., Bragg, M. B.: Aerodynamic Classification of Swept-Wings Ice Accretions. AIAA Paper 2013-2825 (2013)
36. Vassberg, J. C., DeHann, M. A., Rivers, S. M., Wahls, R. A.: Development of a Common Research Model for Applied CFD Validation Studies. AIAA Paper 2008-6919 (2008)
37. Lee, S., Broeren, A. P., Addy, H. E., Sills, R., Pifer, E. M.: Development of 3-D Ice Accretion Measurement Method. AIAA Paper 2012-2938 (2012)
38. Sclafani, A. J., Slotnick, J. P., Vassberg, J. C., Pulliam, T. H.: Extended OVERFLOW Analysis of the NASA Trap Wing Wind Tunnel Model. AIAA Paper 2012-2919 (2012)
39. Saeed, F., Selig, M. S., Bragg, M. B.: Hybrid Airfoil Design Procedure Validation for Full-Scale Ice Accretion Simulations. Journal of Aircraft 36(5), 769-776 (1999)
40. Fujiwara, G. E. C., Woodard, B. S., Wiberg, B. D., Mortonson, A. J., Bragg, M. B.: A Hybrid Airfoil Design Method for Icing Wind Tunnels Tests. AIAA Paper 2013-2826 (2013)
41. Jaeggi, D. M., Parks, G. T., Kipouros, T., Clarkson, P. J.: The Development of a Multi-Objective Tabu Search Algorithm for Continous Optimisation Problems. European Journal of Operational Research 185, 1192-1212 (2008)
42. T. Ghisu, J. P.: Robust Design Optimization with Respect to Ice Accretion. (2010)
43. Ghisu, T., Jarrett, J. P., Parks, G. T.: Robust Design Optimization with Respect to Ice Accretion. Journal of Aircraft 48(1), 287-304 (2011)
44. Pan, J., Loth, E., Bragg, M.: RANS Simulation of Airfoils with Ice Shapes., Reno, Navada, vol. 41st Aerospace Sciences Meeting and Exhibit (2003)
45. Shaw, J.: Handbook of Grid Generation. CRC Press, New York, Washington USA
46. Wetherill, N. P.: Mixed Structured and Unstructured Meshes for Aerodynamic Flow Simulations. The Aeronautical Journal 94(934), 111-123 (1990)

47. CFDOnline: CFD Online. (Accessed 2013) Available at: http://www.cfd-online.com/Wiki/Main_Page
48. Menter, F. R.: Two-Equation Eddy-Viscosity Models For Engineering Applications. AIAA 32, 1598-1605 (1991)
49. FLUENT, A.: 12.0/12.1 User's Guide. ANSYS Inc, Canonsburg, USA (2009)
50. Rubesin, M. W., Johnson, H. A.: A Critical Review of Skin-Friction and Heat Transfer Solutions of the Laminar Boundary Layer of a Flat Plate. Trans. ASME 71(4), 383-388 (1949)
51. Anderson Jr, J.: Fundamentals of Aerodynamics 3rd edn. McGraw-Hill, New York (2001)
52. Spalart, P. R.: Trends in Turbulence Treatments. AIAA 2003-2306 (2000)
53. Roache, P.: Perspective: A Method for Uniform Reporting of Grid Refinement Studies. Journal of Fluid Dynamics 116(3), 405-414 (1994)
54. White, F.: Chapter 9: Compressible Flow. In : Fluid Mechanics Seventh Addition. McGraw-Hill, New York (2011) 624
55. Versteeg, H. K., Malalasekera, W.: Introduction. In : An Introduction to Computational Fluid Dynamics, The Finite Volume Method. Pearson Education Limited, Essex, England (1995) 4
56. Bakker, A.: Computational Fluid Dynamics (ENGS 150): Lecture 5 - Solution Methods.
57. Barth, T. J., Jesperson, D.: The Design and Application of Upwind Schemes on Unstructured Meshes., Reno, Nevada (1989)
58. FLUENT, A.: 12.0/12.1 Theory Guide. ANSYS Inc, Canonsburg, USA (2009)
59. Neale, A., Derome, D., Bloscken, B., Carmeliet, J.: Neale, Adam, etCFD Calculation of Convective Heat Transfer Coefficients and Validation – Part 2: Turbulent Flow., Banff, Alberta (2007)
60. Meakin, C., Arnett, D.: Turbulent Convection in Stellar Interiors. 1. Hydrodynamic Simulations. The Astrophysical Journal 667(1), 448-475 (2007)
61. Sinobar, A. T.: An Informal Introduction to Turbulence 1st edn. Kluwer Acedemic Publishers, Dordrecht (2001)
62. Schlichting, H.: Boundary-Layer Theory 1st edn. McGraw-Hill Inc, Ney York (1979)
63. Gad-el-Hak, M.: Flow Control: Passive, Active, and reactive Flow Management 1st edn. Cambridge University Press, Cambridge (2000)
64. Versteeg, H., Malalasekera, W.: Tuebulence Modelling. In : An Introduction

to Computational Fluid Dynamics, The Finite Volume Method. Pearsons Education Limited, Essex, England (1995) 44-49

65. Oakley, T., Loth, E., Adrian, R.: Cinematic Particle image Verlocitmetry of a Turbulent Free Shear Layer. AIAA Journal 34(2), 299-308 (1996)
66. Reynolds, O.: On the Dynamical Theory of Incompressible Viscous Fluids and the Determination of the Criterion. A Philosophical Transactions of the Royal Society of London (1887-1895) 186, 123-164 (1895)
67. Hinze, J. O.: Turbulence. McGraw-Hill Publishing Co., New York (1975)
68. Spalart, P. R., Almaras, S. R.: A One-Equation Turbulence Model For Aerodynamic Flows. The American Institute of Aeronautics and Astronautics (1992)
69. Wilcox, D. C.: Multiscale Model for Turbulent Flows. AIAA 26(11), 1311-1320 (1998)
70. Launder, B. B., Spalding, D. B.: The Numerical Computation of Turbulent Flows. Computer Methods in Applied Mechanics and Engineering 3(2), 269-289 (1974)
71. Pettersson, K., Rizzi, A.: Comparing Different CFD Methods Accuracy in Computing Local Boundary Layer Properties. Engineering Applications of Computation FLuid Dynamics 3(1), 98-108 (2009)
72. Pan, J., Loth, E.: Reynolds-Averaged Navier-Stokes Simulations of Airfoils and Wings with Ice Shapes. AIAA Journal of Aircraft 41(4), 879-891 (2004)
73. Morongin, C., Vitagliano, P. L., Zanazzi, G., Narducci, R.: Aerodynamic Analysis of an Iced Airfoil at Medium/High Reynolds number. AIAA 46(10), 2469-2478 (2008)
74. Badcock, S.: Validation study for prediction of iced aerofoil. (2010)
75. Johansen, J.: Prediction in Laminar/Turbulent Transition in Airfoil Flows. Journal of Aircraft 36(4), 731-734 (1999)
76. Rahimi, H., Medroubi, W., Peinke, J.: 2D and 3D Numerical Investigation of the Laminar and Turbulent Flow Over Different Airfoils using OpenFOAM., Oldenburg, Germany (2013)
77. Nichols, R. H.: Turbulence Models and Their Application to Complex Flows. Version 4.01.
78. Tulapurka, E. G.: Turbulence Models for the Computation of Flow Past Airplanes. Prog. Aerospace Sciences 33, 71-165 (1997)
79. Kline, S. J., Cantwell, B. J., Lilley, G. M.: AFOSR-HTTM Stanford Conference on Complex Turbulent Comparison of Computer and Experiment., Stanford, CA (1981)
80. Young, M. E., Ooi, A.: Turbulence Models and Boundary Conditions for Bluff Body Flow., Sydney, Australia (2004)

81. Menter, F. R.: Zonal Two-Equation k-ω Turbulence Model for Aerodynamic Flows. AIAA Paper 1993-2906 (1993)
82. Menter, F., Kuntz, M., Langtry, R.: Ten Years of Industrial Experience with the SST Turbulence Model. Turbulence, Heat and Mass Transfer 4 4(1), 625-632 (2003)
83. Eleni, D., Athanasios, T., Dionissios, M.: Evaluation of the turbulence models for the simulation of the flow over a National Advisory Committee for Aeronautics (NACA) 0012 airfoil. Journal of Mechanical Engineering Research 4(3), 100-111 (2012)
84. Trapani, G., Kipouros, T., Savill, A. M.: The Design of Multi-Element Airfoils through Multi-Objective Optimization Techniques. Computer Modelling in Engineering Sciences 88(2), 107-140 (2012)
85. Shur, M., Strelets, M., Zaikov, L., Gulyaev, A., Koslov, V., Scundov, A.: Comparative Numerical Testing of the One and Two Equation Turbulence Models for Flows with Separation and Reattachment. AIAA Paper 95-0863 (1995)
86. Jaeggi, D. M., Parks, G. T., Kipouros, T., Clarkson, P. J.: A Multi-Objective Tabu Search Algorithm for Constrained Optimisation Problems. Evolutionary Multi-Criterion Optimization, LNCS 3410, 490-504 (2005)
87. Kroo, I.: Innovations in Aeronautics. AIAA Paper 2004-0001 (2004)
88. Vanderplaats, G. N., Hicks, R.: Numerical airfoil optimization using a reduced number of design coordinates. National Aeronautics and Space Administration (NASA), Washington (1976)
89. Thévenin, D., Janiga, G.: Optimization and Computational FLuid Dynamics. Springer-Verlag, Heidelberg, Berlin (2008)
90. Chelouah, R., Siarry, P.: Tabu Search Applied to Global Optimization. European Journal of Operational Research 123, 256-270 (2000)
91. Glover, F.: Tabu Search: Part 1. OSRA Journal on Computing 1(3), 190-206 (1989)
92. Glover, F.: Tabu Search: Part 2. OSRA Journal on Computing 2(1), 4-32 (1990)
93. Jones, D. F., Mirrazavi, S. K. .: Multi-Objective Meta-Heuristics: An Overview of the Current State-of-the-Art. European Journal of Operational Research 137, 1-9 (2002)
94. Harvey, S. S.: The Design Optimisation of Turbomachinery Blader Rows, PhD. Thesis. University of Cambridge, Cambridge, England (2002)
95. Kipouros, T., Jaeggi, D. M., Dawes, W. N., Parks, G. T., Savill, A. M., Clarkson, P. S.: Insight into High-Quality Aerodynamic Design Spaces through Multi-Objective Optimisation. Computer Modelling in Engineering

and Sciences 1-23, 37 (2008)

96. Yang, X. S.: Engineering Optimization: An Introduction with Metaheuristic Applications. Wiley, Hoboken, NJ (2010)
97. Kipouros, T.: Multi-Objective Aerodynamic Design Optimisation, PhD. Thesis. University of Cambridge , Cambridge, England (2006)
98. Connor, A. M., Tilley, D. G.: A Tabu Search Method for the Optimisation of Fluid Power Circuits. IMechE Journal of Systems and Control 212, 373-381 (1998)
99. Hooke, R., Jeeves, T. A.: Direct Search Solutions of Numerical and Statistical Problems. Jpurnal of ACM 8, 212-229 (1961)
100. Glover, F., Laguna, M.: Tabu Search. Kluwer Acedemic Publishers, Boston, MA (1997)
101. Saddawi, S.: Multi-Objective Computational Engineering Design Optimisation for Micro-Combustor Devices, PhD. Thesis. Cranfield University, Cranfield (2013)
102. Potapczuk, M. G.: An Experimental Investigation of Multi-Element Airfoil Ice Accretion and Resulting Performance Degredation., Reno, Nevada (1989)
103. UIUC, A.: UIUC Airfoil Coordinates Database. (Accessed 2009) Available at: http://www.ae.illinois.edu/m-selig/ads/coord_database.html#B
104. Alègre, N.: Modelisation and Simulation of Intercycle/Runback Ice., Cranfield (2009)
105. AIAA: AIAA Guide for the Verification and Validation of Computational Fluid Dynamics Simulations. (G-077-1998)
106. ANSYS: ANSYS ICEMCFD User Manual 12.0/12.1. ANSYS Inc., Canonsburg, USA (2009)
107. Richardson, L.: The Approximate Arithmetical Solution by Finite Differences of Physical Problems Involving Differential Equations, with an Application to the Stresses in a Masonry Dam., 307-357 (1911)
108. Pan, J., Loth, E., Bragg, M.: Rans Simulation of Airfoils with Ice Shapes., Reno, Navada, vol. 41st Aerospace Sciences Meeting and Exhibit (2003)
109. Broeren, A., Bragg, M.: Effects of Airfoil Geometry on Performance with Simulated Intercycle Ice Accretions., Reno, Navada (2003)
110. Lee, S., Bragg, M.: Effects of Simulated-Spanwise Ice Shapes on Airfoils: Experimental Investigation., Reno, Navada (1999)
111. Jovic, S.: An Experimental Study of a Separated/Reattached Flow Behind a Backward-Facing Step. Reh= 37,000., Moffett Field, California (1996)
112. Potapczuk, M.: An Experimental Investigation of Multi-Element Airfoil Ice

Accretion and Resulting Performance Degredation., Reno, Nevada (1989)
113. Garry, P.: Lecture Notes. Cranfield University (2010)
114. Reehorst, A., Richter, G.: New methods and materials for molding and casting ice formation., Washington (1987)
115. Jones, B.: Measurment of Profile Drag by the Pitot-Traverse Method., Cambridge (1936)
116. Khawaja, R.: Aerodnamic Drag Penalties Due to Runback Ice. Cranfield University MSc Thesis, Cranfield (2012)
117. Nwgu, V.: An Experimental Investigation of Simulated Runback Ice Shapes Within a Boundary Layer. Cranfield University MSc Thesis, Cranfield (2011)
118. Whalen, E., Bragg, A.: Aerodynamics of Scaled Runback Ice Accretions. Journal of Aircraft 45(2), 591-603 (2008)
119. Sederberg, T. W., Perry, S.: Free-form deformation of solid geometric models. Journal of ACM 20(4), 151-160 (1986)
120. Sadraey, M.: Aircraft Design: A Systems Engineering Approach. John Wiley & Sons, Ltd, Nashua, New Hampshire (2012)
121. Abbott, I., Doenhoff, A.: Theory of Wing Sections. Dover Publishing Ltd, New York (1959)
122. Garrick, I. E.: Determination of the Theoretical Pressure Distribution for Twenty Airfoils., California (1934)
123. Domingos, R.: MSc Computational Methodology for Bleed Air Ice Protection System Parametric Analysis. Wichita Stae University, Wichita (2010)
124. Iaccarino, G., Ooi, A., Durbin, P. A., Behnia, M.: Conjugate Heat Transfer Predictions in Two-Dimensional Ribbed Passages. International Jounral of Heat and Fluid Flow 23(3), 340-345 (2002)
125. Lee, S., Bragg, M. B., Kin, S.: Investigation of factors that influence iced airfoil aerodynamics., 38rd Aerospace Sciences Meeting & Exhibit (2000)
126. White, F. M.: Chapter 6: Viscous Flow in Ducts. In : Fluid Mechanics Seventh Edition. McGraw-Hill, New York (2011) 374
127. Desktop Aeronautics, I.: Desktop Aeronautics: Online Digital Textbook.

Appendix

Wind Tunnel Error Estimation

The instrumentation error given by the manufacturer:

Instrument	Accuracy
Pressure Transducer (PX139)	±0.3% of 0.3Psi
Pressure Transducer (Kimo XP300)	±0.5% of 1Pa
Barometric Pressure	±0.1Pa
Temperature	±0.1°C

Density Error Derivation

The density of air was found from the ideal gas law.

$$\rho = \frac{P}{RT} = PR^{-1}T^{-1}$$

$$\partial\rho = \sqrt{\left(\frac{\partial\rho}{\partial P}\partial P\right)^2 + \left(\frac{\partial\rho}{\partial T}\partial T\right)^2}$$

$$\partial\rho = \sqrt{\left(\frac{1}{RT}\partial P\right)^2 + \left(\frac{P}{RT}\partial T\right)^2}$$

This is the error associated with the experimental density measurement.

Constant	Symbol	Value
Gas Constant	R	287.058 J kg^{-1} K^{-1}
Temperature	T	21.3°C
Pressure	P	98995 Pa
Temperature Accuracy	∂T	±0.1°C
Pressure Accuracy	∂P	±0.1Pa

$$\partial\rho = \pm 0.076 \; or \; 6.3\%$$

Velocity Error Derivation

The uncertainty in the velocity measurement is found using the equation shown below:

$$v = \sqrt{\frac{2q}{\rho}} = 2q^{1/2}\rho^{-1/2}$$

Where

v = Wind Tunnel Velocity
ρ = Free Stream Density
q = Dynamic Pressure

Using the chain rule to take the partial derivative gives:

$$\partial v = \sqrt{\left(\frac{\partial v}{\partial q}\partial q\right)^2 + \left(\frac{\partial v}{\partial \rho}\partial \rho\right)^2}$$

$$\partial v = \sqrt{\frac{1}{q\rho}\partial q^2 + \frac{q}{\rho^2}\partial \rho^2}$$

The table below gives the error associated with the experimental velocity measurement.

Constant	Symbol	Value
Dynamic Pressure	q	122.726Pa
Density	ρ	1.192 kg m^{-3}
Pressure Accuracy	∂q	±3.68178Pa
Density Accuracy	$\partial \rho$	±0.076 kg m^{-3}

$$\partial v = \pm 0.76913 \; or \; \pm 5.3\%$$

Drag Coefficient Error Propagation using Wake Survey Method

$$F = \sqrt{\frac{q}{q_\infty}} - \frac{q}{q_\infty}$$

Using the chain rule to take the partial derivative gives:

$$\partial F = \sqrt{\left(\frac{\partial F}{\partial q}\partial q\right)^2 + \left(\frac{\partial F}{\partial q_\infty}\partial \rho\right)^2} - \sqrt{\left(\frac{\partial F}{\partial q}\partial q\right)^2 + \left(\frac{\partial F}{\partial q_\infty}\partial \rho\right)^2}$$

$$\partial F = \sqrt{\left(\frac{1}{2\sqrt{q q_\infty}}\partial q\right)^2 + \left(\frac{q}{{q_\infty}^2}\partial q_\infty\right)^2 + \left(\frac{1}{q_\infty}\partial q\right)^2 + \left(\frac{q}{{q_\infty}^2}\partial q_\infty\right)^2}$$

The error associated with the experimental velocity measurement is given in the table below:

Constant	Symbol	Value
Dynamic Pressure	q	37.57Pa
Free stream Dynamic Pressure	q_∞	112.726Pa
Dynamic Pressure Accuracy	∂q	±1.127Pa
Free stream Dynamic Pressure Accuracy	∂q_∞	±3.68178Pa

$$\partial F = \pm 0.0179$$

Other Uncertainties

- Rake Traverse Positioning (±0.1mm)
- Pitot tubes alignments (±1°)
- Uncertainty associated with average free stream velocity
  The wake survey momentum deficit method uses the dynamic pressure measurements to calculate the drag coefficient. Unfortunately, this means the span-wise pressure variation propagates to the drag across the span of the wind tunnel working section. However q_∞ values were not

averaged and instead were calculated using each span-wise location value. This variation at the uppermost pressure reading was accounted for by averaging the final 5 q_∞values.

To compare the impact of using the average of all 5, a numerical comparison was attempted. The aim was to compare the non-dimensional drag values when averaging two, five and ten of the uppermost pressure readings.

Spanwise Location (z/b)	2 Point Average Drag Coefficient	5 Point Average Drag Coefficient	10 Point Average Drag Coefficient
0.00	0.02495	0.02494	0.02600
0.14	0.02358	0.02354	0.02449
0.29	0.02458	0.02457	0.02543
0.43	0.02691	0.02700	0.02770
0.57	0.03012	0.03016	0.03087

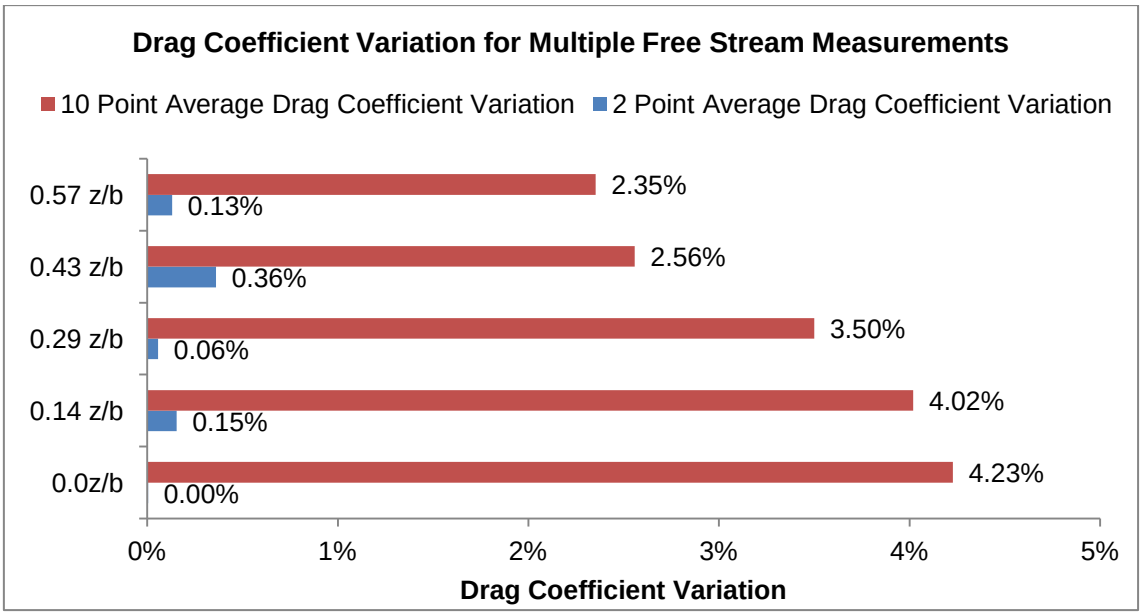

Experimental Data Used for Turbulent Intensity Calculation

Flat Plate Run [117]						
X mm	Y mm	Z mm	U Mean m/s	U RMS	U Turb	Vpitot m/s
0	0	11.5	6.165	1.569	0.254	14.562
0	0	15	6.317	1.636	0.259	14.589
0	0	20	6.518	1.771	0.272	14.571
0	0	25	6.747	1.807	0.268	14.572
0	0	30	6.862	1.892	0.276	14.563
0	0	35	7.346	1.941	0.264	14.55
0	0	40	7.633	2.015	0.264	14.557
0	0	45	8.106	2.098	0.259	14.551
0	0	50	8.205	2.143	0.261	14.557
0	0	55	8.595	2.13	0.248	14.548
0	0	60	8.916	2.075	0.233	14.562
0	0	65	9.362	2.062	0.22	14.551
0	0	70	9.897	1.935	0.195	14.529
0	0	75	10.229	1.874	0.183	14.523
0	0	80	10.262	1.91	0.186	14.532
0	0	90	11.068	1.626	0.147	14.528
0	0	100	11.524	1.346	0.117	14.538
0	0	110	11.826	1.132	0.096	14.548
0	0	120	12.15	0.895	0.074	14.54
0	0	130	12.38	0.717	0.058	14.546
0	0	140	12.556	0.635	0.051	14.53
0	0	150	12.746	0.565	0.044	14.539
0	0	160	12.797	0.559	0.044	14.517
0	0	170	12.936	0.501	0.039	14.514
0	0	180	12.975	0.483	0.037	14.507
0	0	190	13.128	0.374	0.029	14.503
0	0	200	13.163	0.345	0.026	14.514
0	0	210	13.209	0.32	0.024	14.502
0	0	220	13.261	0.253	0.019	14.494
0	0	230	13.273	0.227	0.017	14.497
0	0	240	13.301	0.179	0.013	14.481
0	0	250	13.297	0.179	0.013	14.458
0	0	270	13.316	0.143	0.011	14.493
0	0	290	13.35	0.113	0.008	14.525
0	0	310	13.351	0.107	0.008	14.52
260	0	11.5	9.844	1.103	0.112	14.338
260	0	15	10.133	1.143	0.113	14.302
260	0	20	10.601	1.083	0.102	14.351

260	0	25	10.881	1.052	0.097	14.342
260	0	30	11.067	1.04	0.094	14.357
260	0	35	11.241	1.002	0.089	14.337
260	0	40	11.551	0.967	0.084	14.337
260	0	45	11.594	0.973	0.084	14.333
260	0	50	11.746	0.956	0.081	14.297
260	0	55	11.911	0.949	0.08	14.337
260	0	60	12.141	0.893	0.074	14.352
260	0	65	12.228	0.858	0.07	14.336
260	0	70	12.325	0.843	0.068	14.334
260	0	75	12.399	0.849	0.068	14.327
260	0	80	12.493	0.795	0.064	14.342
260	0	90	12.55	0.768	0.061	14.334
260	0	100	12.928	0.708	0.055	14.306
260	0	110	13.02	0.667	0.051	14.294
260	0	120	13.132	0.627	0.048	14.255
260	0	130	13.386	0.524	0.039	14.256
260	0	140	13.497	0.476	0.035	14.297
260	0	150	13.597	0.398	0.029	14.243
260	0	160	13.633	0.357	0.026	14.254
260	0	170	13.656	0.329	0.024	14.251
260	0	180	13.697	0.32	0.023	14.252
260	0	190	13.722	0.288	0.021	14.254
260	0	200	13.741	0.298	0.022	14.325
260	0	210	13.757	0.265	0.019	14.288
260	0	220	13.753	0.243	0.018	14.251
260	0	230	13.77	0.236	0.017	14.282
260	0	240	13.756	0.245	0.018	14.309
260	0	250	13.765	0.228	0.017	14.296
260	0	270	13.782	0.229	0.017	14.335
260	0	290	13.781	0.227	0.016	14.323
260	0	310	13.787	0.226	0.016	14.313
-260	0	11.5	8.855	1.12	0.126	14.325
-260	0	15	9.097	1.103	0.121	14.343
-260	0	20	9.535	1.041	0.109	14.278
-260	0	25	9.737	1.075	0.11	14.347
-260	0	30	9.898	1.031	0.104	14.343
-260	0	35	10.006	1.025	0.102	14.301
-260	0	40	10.284	1.031	0.1	14.334
-260	0	45	10.408	0.981	0.094	14.352
-260	0	50	10.539	0.997	0.095	14.311
-260	0	55	10.602	0.962	0.091	14.324
-260	0	60	10.778	0.953	0.088	14.351
-260	0	65	10.775	0.909	0.084	14.334

-260	0	70	10.794	0.921	0.085	14.321
-260	0	75	10.881	0.867	0.08	14.349
-260	0	80	10.975	0.887	0.081	14.347
-260	0	90	11.13	0.838	0.075	14.31
-260	0	100	11.344	0.822	0.072	14.333
-260	0	110	11.431	0.823	0.072	14.344
-260	0	120	11.573	0.765	0.066	14.339
-260	0	130	11.75	0.738	0.063	14.34
-260	0	140	11.863	0.714	0.06	14.324
-260	0	150	11.925	0.695	0.058	14.329
-260	0	160	12.026	0.693	0.058	14.267
-260	0	170	12.183	0.656	0.054	14.316
-260	0	180	12.246	0.653	0.053	14.337
-260	0	190	12.352	0.648	0.052	14.343
-260	0	200	12.402	0.626	0.051	14.305
-260	0	210	12.479	0.584	0.047	14.286
-260	0	220	12.548	0.565	0.045	14.331
-260	0	230	12.614	0.581	0.046	14.28
-260	0	240	12.633	0.543	0.043	14.283
-260	0	250	12.716	0.527	0.041	14.292
-260	0	270	12.808	0.517	0.04	14.302
-260	0	290	12.881	0.495	0.038	14.278
-260	0	310	12.973	0.48	0.037	14.27

Leading Edge Flat Plate Boundary Layer Profile for Chosen Spanwise Locations against Numerical Predictions

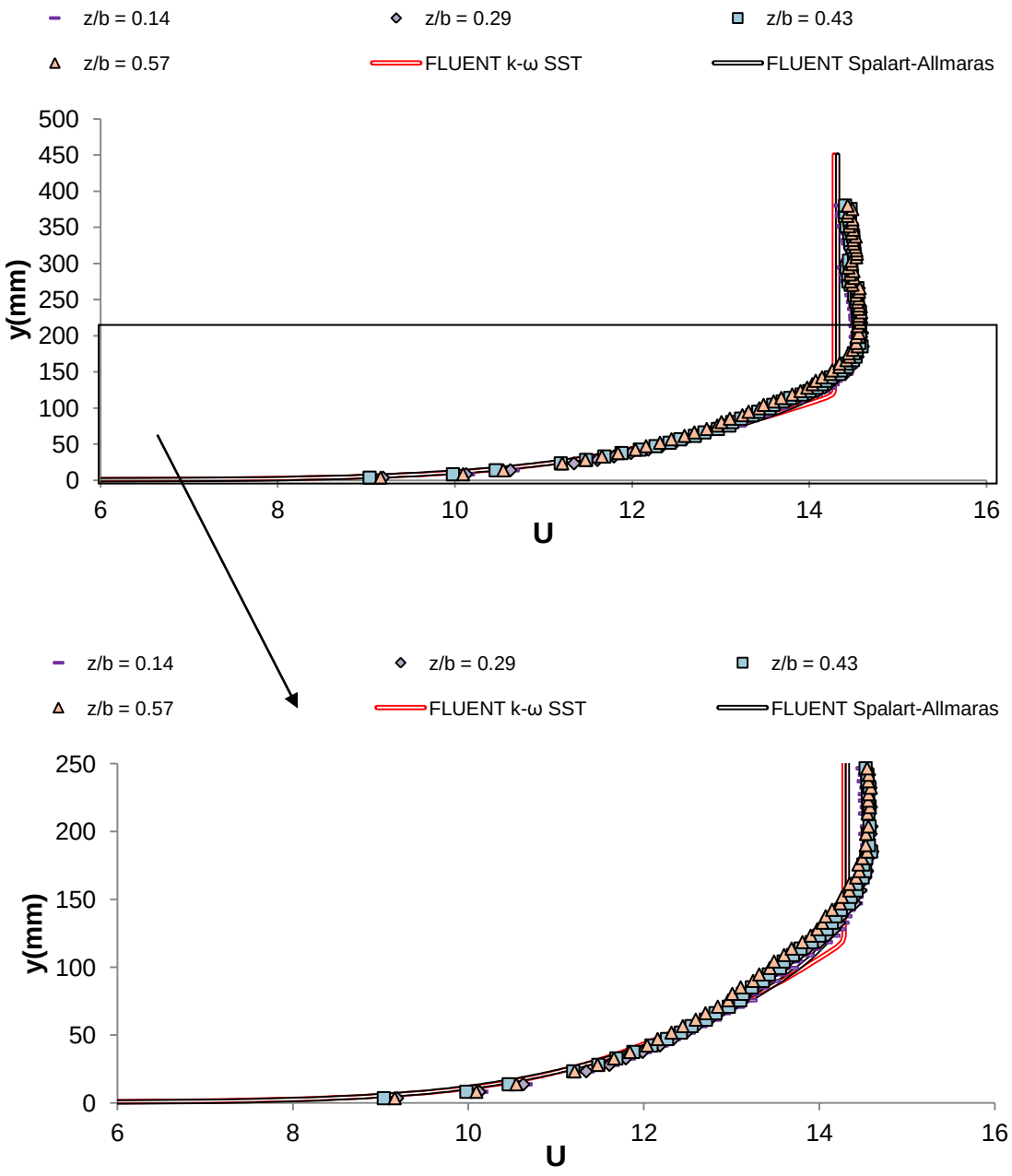

Boundary Layer Velocity Profile for Runback Ice Shape 1 for all Selected Spanwise Location

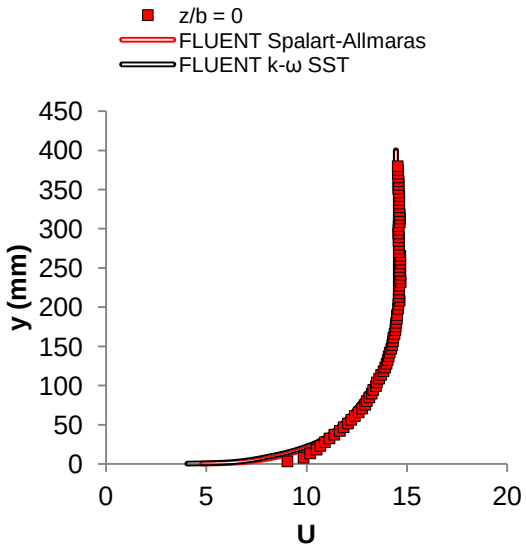

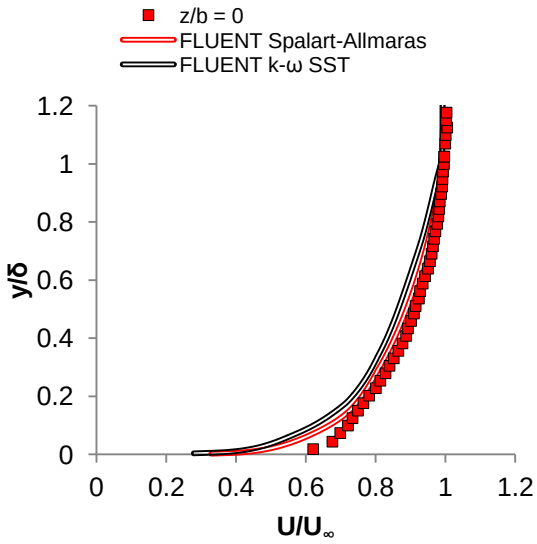

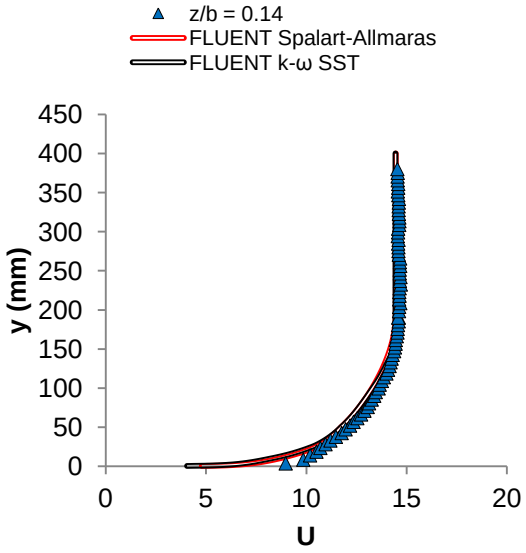

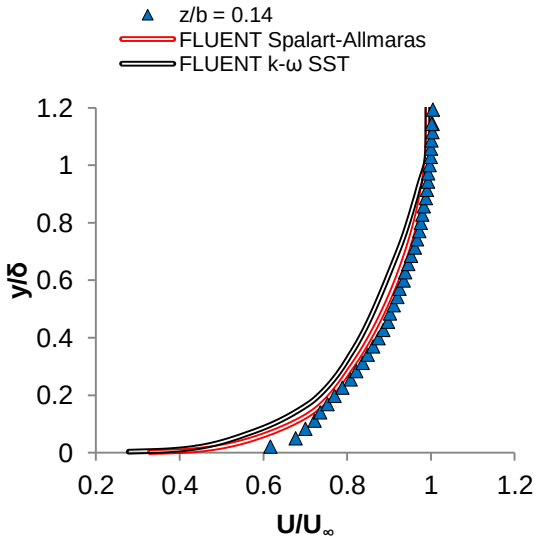

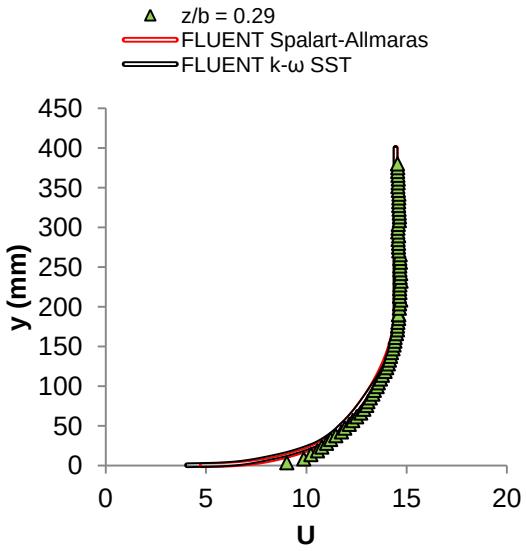
z/b = 0.29
FLUENT Spalart-Allmaras
FLUENT k-ω SST
y (mm)
U

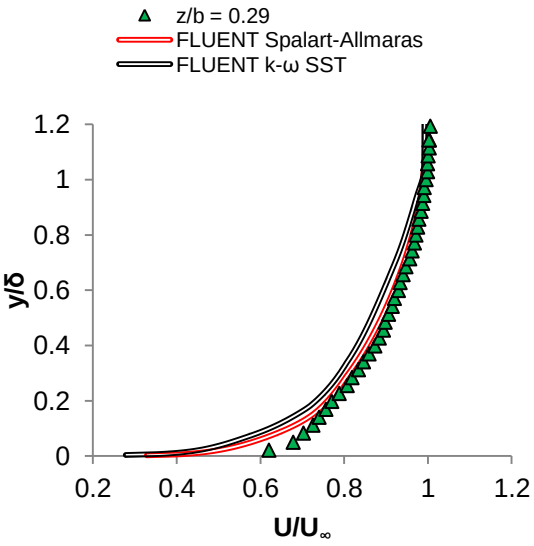
z/b = 0.29
FLUENT Spalart-Allmaras
FLUENT k-ω SST
y/δ
U/U∞

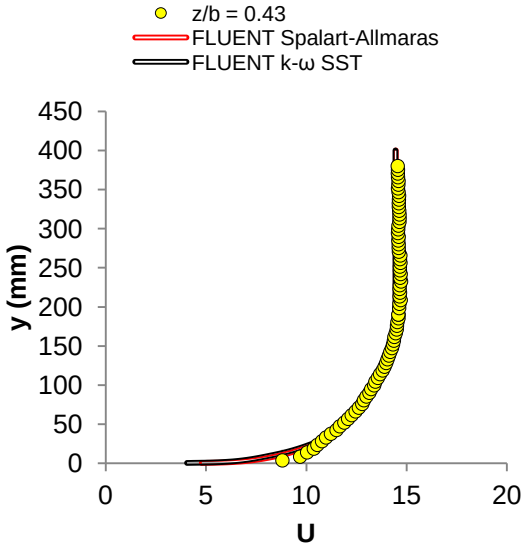
z/b = 0.43
FLUENT Spalart-Allmaras
FLUENT k-ω SST
y (mm)
U

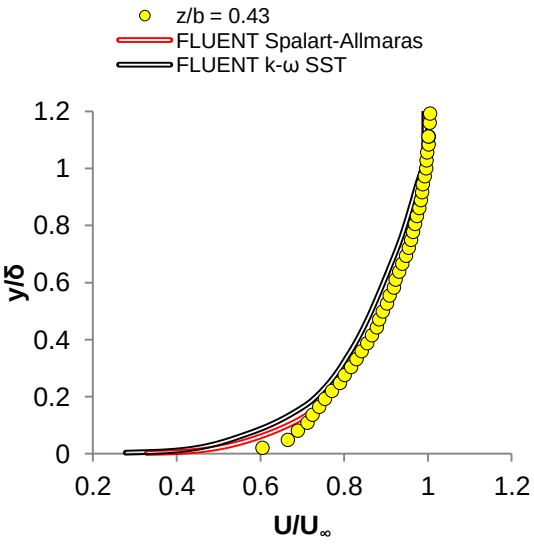
z/b = 0.43
FLUENT Spalart-Allmaras
FLUENT k-ω SST
y/δ
U/U∞

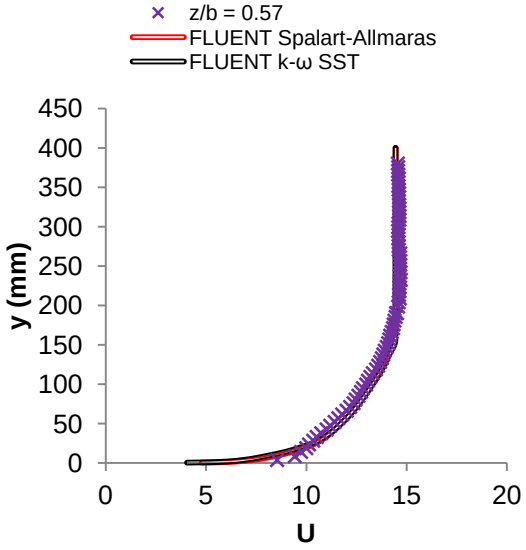
z/b = 0.57
FLUENT Spalart-Allmaras
FLUENT k-ω SST
y (mm)
U

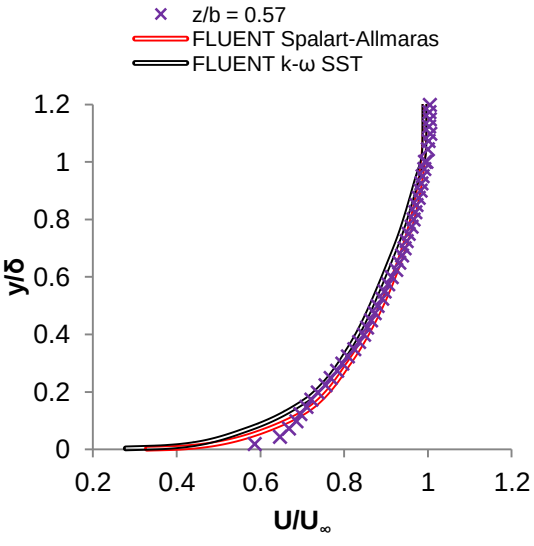
z/b = 0.57
FLUENT Spalart-Allmaras
FLUENT k-ω SST
y/δ
U/U∞

Boundary Layer Velocity Profile for Alternating Runback Ice Setup at all Selected Spanwise Locations

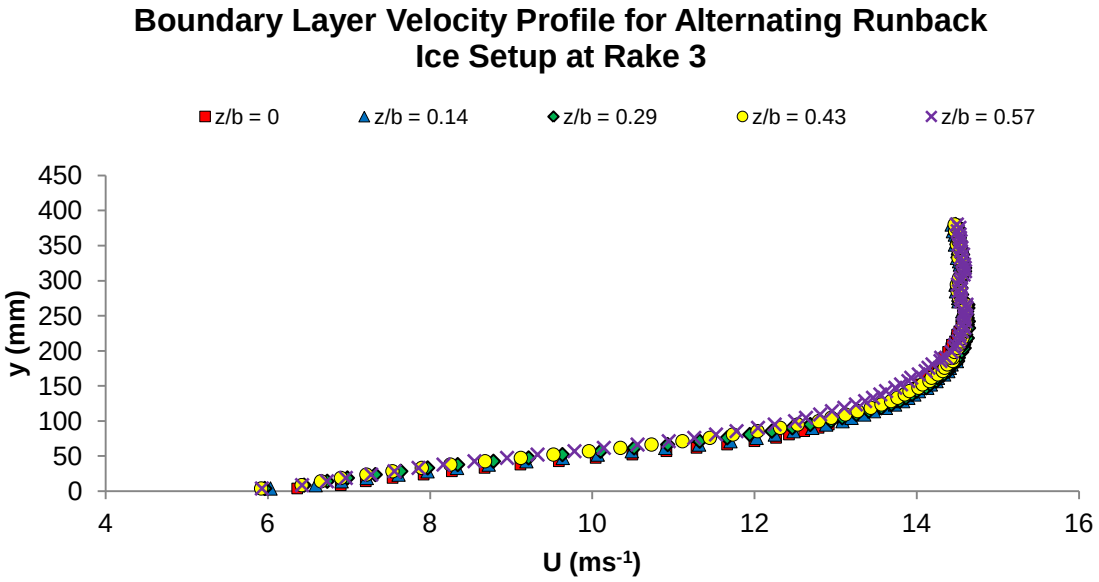

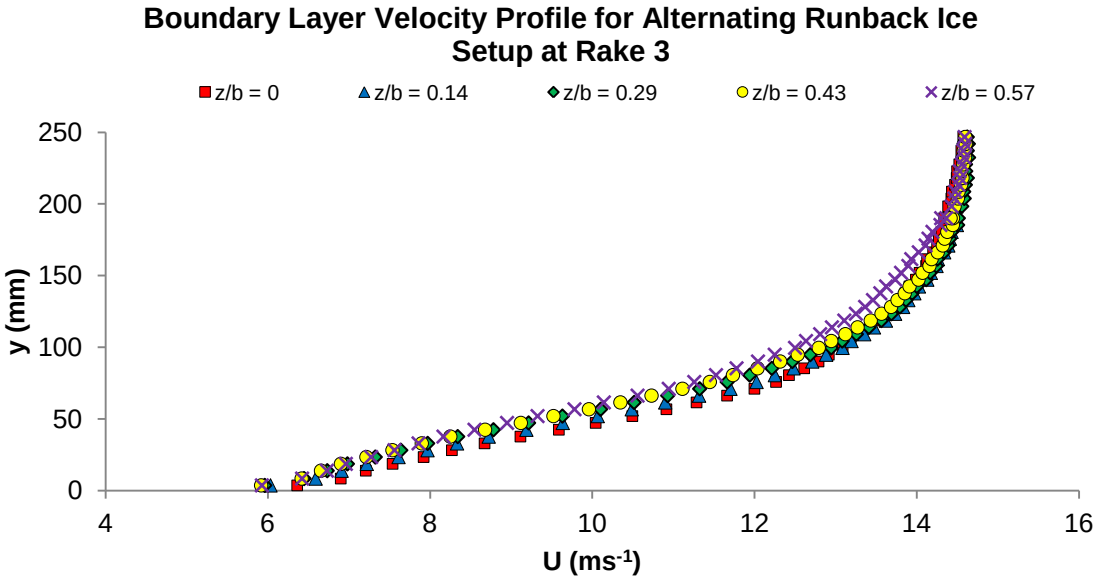

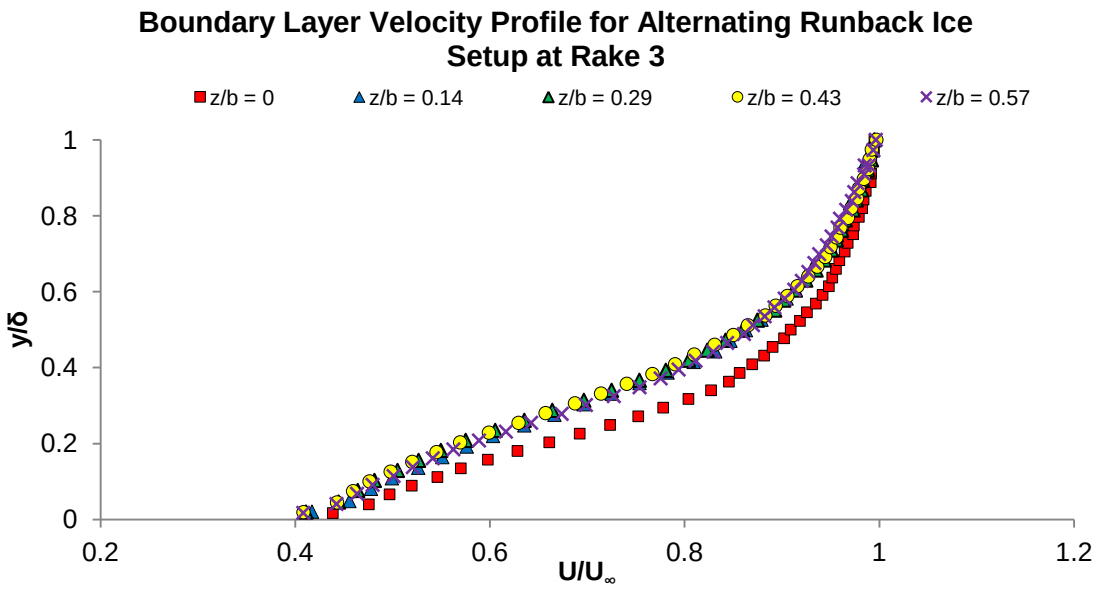

Ice Location Optimisation Flow Chart:

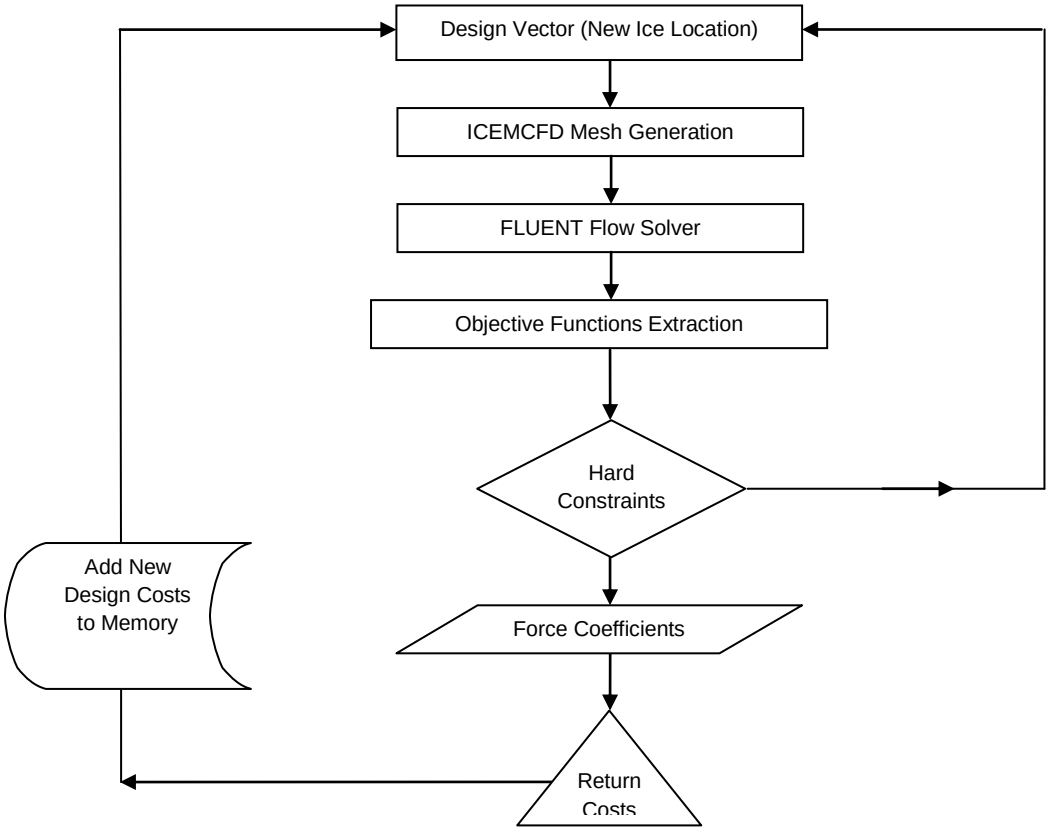

Airfoil Shape Optimisation for Fixed Ice Formation Location Flow Chart

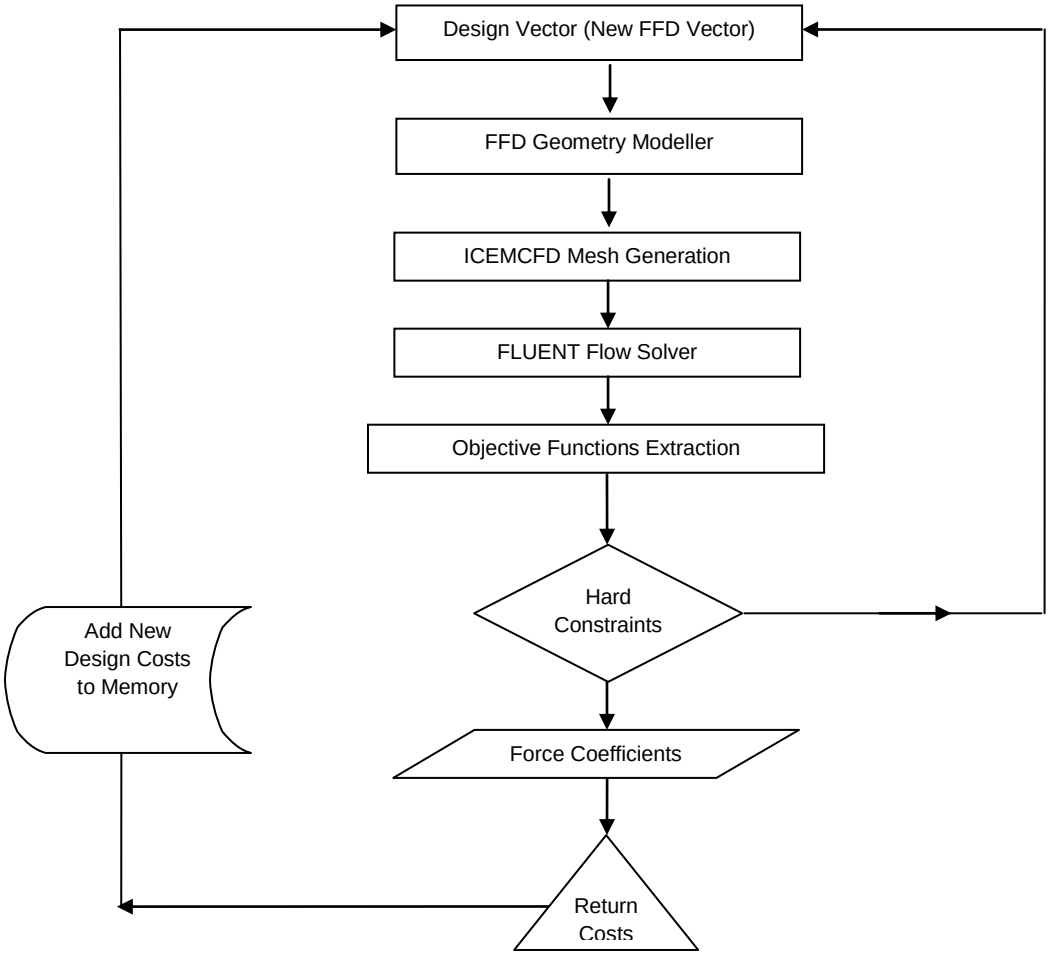

Representative Tail Plane Profile Optimisation Flow Chart

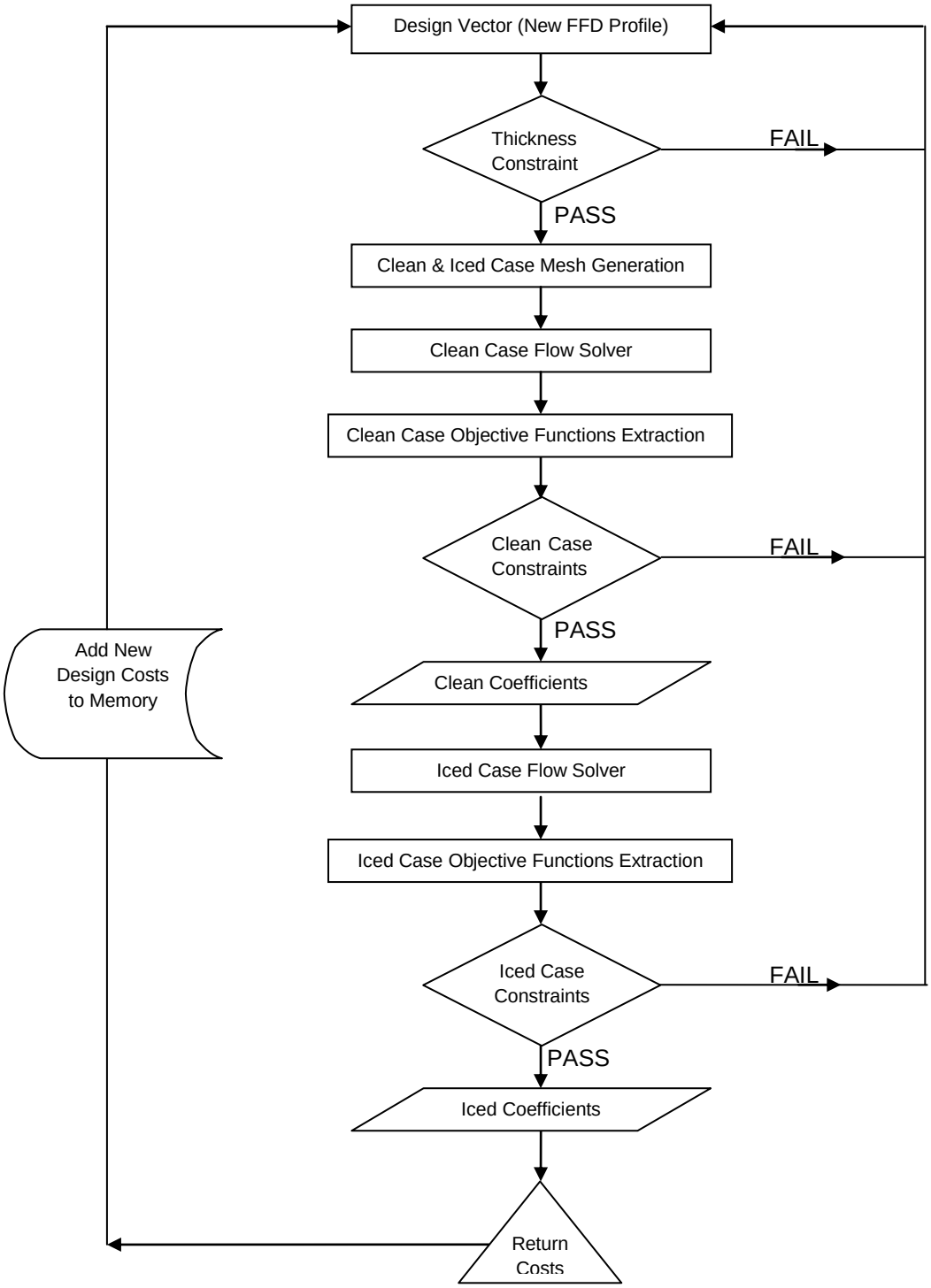

Anti Icing Optimisation Flow Chart